C6770 NMR Spectroscopy of Biomolecules

Lukáš Žídek, Radovan Fiala, Pavel Kadeřávek

January 18, 2021

ii

Contents

Lecture 1a
NMR as a tool for structural biology

1.1 Aim of the course

The aim of our course (C6770 NMR Spectroscopy of Biomolecules) is to give students interested in structural biology an insight into methods of NMR spectroscopy applicable to biologically important molecules (mostly proteins and nucleic acids). Principles of methods are explained in details, but using classical physics instead of quantum mechanics. It should be emphasized that classical physics describes NMR correctly as long as we discuss macroscopic samples, consisting of large numbers of molecules. Graphical description and explanation in text is preferred to derivations based on series of plain equations. The theoretical background is limited, those interested in the theory of nuclear magnetic resonance (based on quantum mechanics) may choose the course C5320 Theoretical concepts of NMR.

Most topics of our course, except for NMR spectroscopy of nucleic acids, are described very well in Cavanagh et al., Protein NMR spectroscopy, 2nd. ed., Academic Press 2006. However, the book is based on the quantum mechanical approach and is not easy to read for a beginner without a solid physical background. General ideas and technical issues are explained in Keeler, Understanding NMR spectroscopy, 2nd. ed., Wiley 2010, and in Levitt: Spin dynamics, 2nd. ed., Wiley 2008. Both books are written for non-experts and present NMR in a very understandable manner, but they do not cover applications to proteins and nucleic acids. The mentioned limitations of the available literature where the major motivation to write this study text. The intention was to complement the lectures by writing a short review of NMR techniques applicable to biomacromolecules. The main purpose of the lectures is to explain the basic ideas in an interactive manner. The text should summarize the topics in a more fluent form and to provide a broader context.

1.2 Structure and structure determination

It should not surprise anybody that *the structure* is what a structural biologist is mostly interested in. Therefore, we have a good reason to start our discussion of nuclear magnetic resonance with the topic of *structure determination*. There are of course good reasons to start somewhere else (e.g., to show applications where no other method can compete with NMR), but I feel an obligation to acknowledge the importance of the structural information right at the beginning.

Before we start talking about structure determination, we should ask what the word *structure* means. The question may sound silly but it is really useful to define this term clearly if we wish to avoid possible confusions. When structural biologists talk about *structure* they usually refer to a model of little balls representing atoms and sticks representing covalent chemical bonds connecting the atoms. The way how the atoms are connected is described by the chemical term *configuration*. Limitations of the described model are obvious. The model is rigid and cannot describe molecular motions that are always present or chemical reactivity of the molecule.

Macromolecules of our interest, i.e., proteins and nucleic acids, are composed of a small number of basic building blocks, *residues*. Configuration is almost completely described by the *sequence* of the residues in the studied molecule. Configuration of the individual building blocks is well defined and depends very little on the actual position of the residue in the macromolecule. In other words, the sticks have a certain length and fit to holes drilled into the balls,

and there is very little that we can do about it. Even the way how to assemble the individual residues is given, so our task is only to find out how to join the residues together. Various *sequencing techniques* have been designed in order to determine the order of residues in a particular macromolecular chain. Once we build the chain of residues, and do some little adjustments like connecting correct disulfide bridges in proteins, the (chemical) configuration of our molecule is defined.

Knowing the configuration, we have enough information to draw a pretty scheme of our macromolecule, in the same way as the authors of the organic chemistry textbooks describe somewhat smaller molecules. Note that organic chemists call such pictures "structures", they use the term *structure* at a level equivalent to *configuration*. In the case of small molecules, the drawing is giving is a fairly good idea about the shape of the molecule (described by the ball-and-stick model). The situation is different if the molecule has a size of a protein. Why? It is possible to rotate more or less freely about most chemical bonds without changing the configuration. An astronomic number of possible ball-and-stick models can be generated by the rotation about various bonds. If we need to refer to one of them, we use the term *conformation*. Now it should be clear that the term *structure* is typically a synonym of *conformation* in structural biology, unlike in organic chemistry (where *structure* often refers to *configuration*).

Now, when we know that *structure determination* is nothing else than the process of finding correct conformation of the studied molecule, we can briefly discuss mathematical description of the structures. Position of every ball in our model can be described by three *coordinates*. Very often, the familiar Cartesian x, y, and z coordinates are used. Cartesian coordinates are very transparent but they also present some problems. If the molecule moves or rotates a little bit, the numbers describing its Cartesian coordinates completely change. It is difficult to say if two molecules are identical just by looking at their Cartesian coordinate lists. Another way of numerical description of the molecule is to list all bond length, angles between bonds, and torsions about the bonds (in terms of so-called *dihedral angles* or *torsion angles*.[1] The latter way represents *internal coordinates* of the molecule, independent of the position or orientation of the whole molecule. It should not surprise you that if six *external coordinates* (three defining position of the molecule in the chosen coordinate system and three describing overall orientation of the molecule with respect to the axes) are added to the internal coordinates, we obtain a list of numbers exactly as long as the list of Cartesian coordinates. The internal coordinates can be divided into those describing configuration of the molecule (i.e., bond length and bond angles) and those describing conformation (torsion angles). This is useful because configuration can be taken as granted and the whole structure can be described by torsion angles only.

1.3 Macromolecular structure from interatomic distances

Positions of individual atoms in biologically important macromolecules are most typically determined by techniques that somehow depend on diffraction of waves: X-ray crystallography, electron microscopy, neutron diffraction. The general requirement is that the wavelength must be similar to the distances between atoms (or shorter). Obviously, NMR spectroscopy does not meet this criterion. There are waves used in NMR spectroscopy, as we discuss later , but their wavelength is several decimeters. How can such waves provide information about atomic distances. The answer is: *NMR is an indirect method*. This is a big disadvantage because NMR structure determination is less straightforward and based on less complete data than when structures are solved using diffraction techniques. But the indirect nature of NMR structure determination is also a great advantage because limitations of diffraction techniques do not apply to NMR spectroscopy. Let us now compare the direct and indirect approaches to the structure determination. Instead of equations and technical argument, we use a story.

Imagine you are a sailor and you visit a beautiful Pacific island with friendly people. You wish to live there for ever. You burn your yacht, crash your smartphone, and build a shanty. After couple of days, you find out that the inhabitants do not have any map of their land. You decide to draw one for them.

There are several ways how to draw a map. For example, you can make a hot-air balloon, inflate it, sail over your island, and draw a map when watching the landscape from the balloon's basket. Or you can just walk from one site to another one, count your steps and measure distances between caps, bays, mountains, and other sites that should appear in the map.

The first approach requires long preparation but makes drawing the map rather easy. It resembles the diffraction techniques. The second approach does not need any preparation. You can start striding immediately. However, it

---

[1]Note that mathematical definitions of torsion and dihedral angles differ in sign.

takes a long time to walk between all sites and the distances measured in this way will not be too precise. It is also not so straightforward to construct a map from distances as to draw what you see from the sky. You have to draw circles of radii corresponding to the measured distances. Positions of the important points are given by intersections of the circles and every error in the measured distances makes the intersections less accurate. Accuracy can be improved if you use more circles for every point, but it would be time consuming to compete with the first approach.

The latter approach resembles NMR structure determination. The NMR methods discussed in our course are applied to molecules in solution.[2] You just need to dissolve your molecule in a buffer and add some heavy water as a sort of internal standard. However, the measurement itself requires a whole set of different experiments, and often takes several weeks. Like in the case of the sailor, the more experiment you run, the more accurate structural model you obtain. Analysis of the measured data is also more tedious than it was in the case of crystallography. Finally, it is very hard to determine structure of molecules larger than approximately 25 kDa. Not only the measured spectra are more complex, but it is difficult to get any signal at all. Currently, NMR is used as a structure determination method for small proteins, individual domains of large proteins, and structurally interesting fragments of nucleic acids. Approximately 15 % structures in the databases were obtained from NMR data.

In order to explain how NMR structure determination really works, we have to modify the sailor's story a little bit. We let our sailor use a more sophisticated means of measuring distances by giving him a set of walkie-talkies, tunable to different frequency channelsl (Figure 1.1). The sailor can give them to his friends living at various sites of the island. Each of these "radio-operators" can estimate how far her or his neighbors are by evaluating signal intensity. The procedure is simple. A guy sitting in a certain town tries to tune in all his fellows that he can hear, and writes down how strong the signal is (your operator locates the position of your mobile phone in a similar manner). Then the sailor collects the notes from every walkie-talkie and begins drawing the map.

The process of NMR structure determination is very similar to the walkie-talkie tale. We make the atomic nuclei transmit radio waves and then we measure how much of the signal has been passed to the nuclei in their vicinity. But such an experiment is not where we usually start. It certainly helped the sailor if he first made something like a telephone directory of his walkie-talkie operators: a list of their names and transmitting frequencies of the devices given to them. It is almost a rule that the NMR structure determination (actually, any NMR study of a biologically interesting macromolecule) starts with "writing a telephone directory". It is not so easy because nuclei do not have their frequencies written on their backs. We have a list of nuclei defined by the amino-acid (or nucleotide) sequence in one hand and a list of measured frequencies in the other hand. It is our task to find which frequency belongs to which nucleus. There is a whole suite of NMR experiments designed just for this purpose and analysis of their results is a routine well known to anybody who uses NMR as a structure determination tool. The process of writing "nuclear phone directory" has been given a self-explanatory name *assignment*. Only when the assignment is done, the structural data starts to make sense.[3] It can take longer to assign frequencies to (almost) all nuclei than to collect information about distances among nuclei. If you later feel that I spend too much time talking about the assignment experiments which tell us nothing about the structure,[4] please, be patient a remember what I just told you.

1.4 List of applications

We have described NMR as a method of structure determination, working reasonably well for smaller proteins and nucleic acid fragments. However, NMR is a much more flexible technique. Other applications are perhaps even more useful than building a structural model. In many cases, the assignment provides a basis for a variety of structural and functional studies. What looked just as an additional effort in the context of structure determination, opens doors to many interesting experiments. Let us now list at least some of them.

- *Is my protein folded?* We start our overview with a very simple but very useful application. It is an experiment telling us if the prepared protein has a well-defined structure, is only partially folded, or is present as a random

---

[2]NMR spectroscopy of biomacromolecules in solid state is a rapidly developing field and is already able to provide structure with atomic resolution.

[3]In theory, we do not need to assign frequencies to nuclei in advance. Structural model can be obtained just from a set of internuclear frequencies. However, protocols following this idea are currently less successful than the "orthodox approaches" described in the rest of this book.

[4]This is not quite fair, useful structural information can be obtained already from the assigned frequencies.
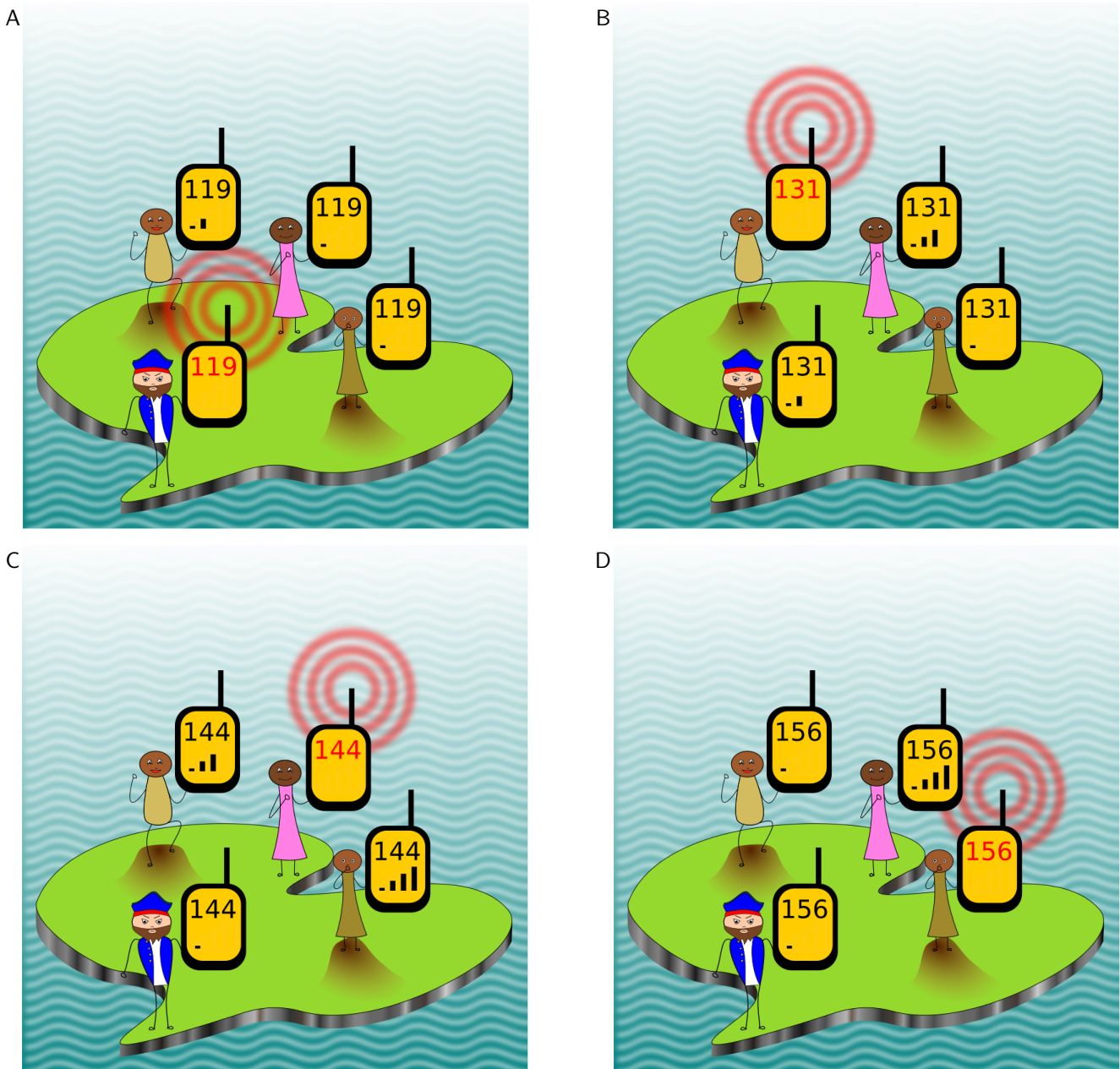
Figure 1.1: Walkie-talkie method of distance measurement. Technically, you decided to use PMR 446 (personal mobile radio operating at 446 MHz). Your walkie-talkies are tuned to four frequencies (four channels) that distinguish individual devices: 446.11875 MHz, 446.13125 MHz, 446.14375 MHz, and 446.15625 MHz. The transmitted and received frequencies are shown on the walkie-talkie displays in red and black, respectively (for better visibility, only three digits following 446 MHz are displayed). When switched to the receiver mode, the displays show also the strength of the received signal (the ▄▄▅▆ indicator).

coil. This information can be obtained in several minutes. The spectra provide atomic resolution (unlike the circular dichroism spectra, giving only percentage of secondary structure elements). The atomic resolution may seem useless when the assignment is not yet available, but it allows us to count signals corresponding to observed amino acids. If we count as many signals as we expect, and if their distribution is typical for a well folded protein, we know that the protein is likely to be prepared correctly. What I have said should already convince you that this experiment is a very useful test of the sample. It is always run prior to more complex NMR experiments. It is also a good idea to record a simple NMR spectrum before we try to crystallize a protein (if the protein is not too large).

- *3D structure determination* has been already described in Section 1.2.

- *Specific structural details.* We already know that NMR data are different from data provided by diffraction techniques. Each NMR frequency can be attributed to an individual nucleus (and to the effects of its neighbors). On the other hand, diffraction of X-rays at each atom contributes to all reflections in a predictable way. This is a great advantage of X-ray crystallography. The diffraction pattern can be back-transformed into the electron density map of the molecule. However, the local nature of the NMR data can be an advantage under certain circumstances. There are cases when we are not interested so much in the whole structure but we would like to learn more about some detail (e.g., mutated active center of an enzyme, or binding site occupied by various ligands). We can save time and look just at the interesting site instead of solving the structure completely. Of course, the assignment must be known in advance, it is only the structural part of the study that can be simplified.

- *Intermolecular interactions.* Once the assignment is completed, interactions of a protein with another molecule (I call it "ligand" in the following text but it can be almost anything: metal ions, small molecules, other proteins, nucleic acids) can be monitored very quickly. We take the protein and titrate it with the ligand. After each addition of the ligand, a simple NMR experiment is run. Such experiments do not need to take more than an hour. A qualitative information at the atomic-level resolution is obtained immediately from the spectra. Nuclei that change frequency upon addition are likely to be close to the binding site. A real structural information requires distance measurements, like when determining the whole structure. But NMR makes our life easier again. It is possible to distinguish intramolecular and intermolecular distances using a clever combination of isotope labeling and design of the NMR experiment. This approach eliminates many ambiguities and produces highly reliable information about intermolecular contacts.

- *Molecular motions.* Crystal structures and EM images of proteins reflect protein flexibility to some degree. Less defined electron density may indicate internal motions. Missing loops are likely to be flexible. NMR methods tell us much more about the molecular dynamics. *Hydrodynamic behavior* of macromolecules may seem not too interesting from a biological point of view. Still, it is useful to know how a molecule moves in solution because the hydrodynamic properties depend on the size and shape of the molecule. This type of information is useful when we need to check if a molecule is monomer or dimer, if it is present in complex with another large molecule or not, etc. *Internal motions* are often essential for the biological function of biomolecules. Motions on various time scales can be distinguished and described quantitatively with atomic resolution. Motions on the time scale of seconds (and slower) can be studied in real time as you can expect. More interestingly, very fast motions (faster than 10^{-9} s) can be described relatively easily in terms of their amplitude and often frequency (at atomic resolution, of course). It is also an advantage of NMR that the signals affected by the fast motions are averaged but not missing. Various experiments have been designed to study slower, microsecond to millisecond, motions.

- *Kinetics and thermodynamics.* The fact that NMR can be applied to kinetic studies has been already mentioned in the previous paragraph. It is very easy to monitor molecular processes at various temperatures. Activation energies can be obtained at least in some cases. In principle, NMR spectroscopy can also provide thermodynamic data such as binding constants. However, the typical concentration range used in NMR experiments (higher than $100\,\mu$M) is rather high to study interactions with high affinities.

- *In vivo measurements.* Mild conditions of the NMR measurements offer the possibility to study molecules in living cells. Major limitation is relatively low sensitivity of the method and high complexity of the molecular

mixture inside the cell. Small molecules have been studied in applications like metabolic profile monitoring or intracellular pH measurements. It is currently also possible to measure *in vivo* NMR spectra of proteins and nucleic acids, although at higher than physiological concentrations. This allows us to estimate how are molecules influenced by the cellular environment and to check if spectra obtained *in vitro* are the same as those measured *in vivo*. Recently published *in vivo* studies already addressed important biological issues.

- *Spatial resolution.* So far, we looked at applications where NMR spectra were measured in the entire volume of the sample. It is also possible to monitor distribution of certain type of nucleus in space. *Magnetic resonance imaging*, used in medical diagnostics, is a typical example. Requirements for spectral and spatial resolutions can be combined, and *in situ* spectra (limited to a small volume) can be measured.

1.5 When can a structural biologist use NMR

I have tried to describe NMR as a wonderful method offering so much useful information and you may ask why it is not used more frequently by biochemists and biologists. I must admit that NMR has also its requirements and that some of them can be tough for a particular biological macromolecule. The common source of the limitations is an inherently low sensitivity. So, how should a biomolecular sample look like to be ready for an NMR study in general (and for structure determination, in particular)?

- *Solubility.* Sensitivity of the method requires relatively high concentrations. Samples of 1 mM macromolecules promise good results, higher concentrations are better. Working with concentrations below 0.1 mM is a challenge.

- *Stability.* Not only the molecule of interest should be well soluble, but it should also stay in solution for a long time. Ideally, the sample survives for month at room temperature. Molecules that are decomposed in less than a week are not suited for a long-term study such as structure determination. Measurements at temperatures close to 0 °C are possible but sensitivity is much worse (especially for large molecules).

- *Stable isotope labeling.* We do not see all nuclei in NMR. Almost all hydrogen and all phosphorus nuclei are active but only every hundredth nucleus of carbon is visible. The most abundant isotope ^{12}C is stable and silent in NMR experiments. Natural samples contain about 1 % of the isotope ^{13}C. It is also stable but can be observed in NMR experiments. Finally, trace amounts of a third isotope are present in Nature. The third isotope, ^{14}C, is created by cosmic rays in atmosphere, undergoes a radioactive decay, and is silent in NMR experiments. Unfortunately, the natural amounts of ^{13}C can be observed only in the most sensitive NMR experiments. The situation is even worse for nitrogen, and oxygen is completely useless for biomolecular application. Therefore, artificial molecules of proteins and nucleic acids are often prepared for NMR experiments by replacing the most abundant, NMR silent, isotope ^{12}C with the NMR active isotope ^{13}C. Also, ^{14}N is replaced by a more suitable ^{15}N. This effects NMR spectroscopy to proteins that are expressed in well behaving host organisms (often bacteria) and to the synthetically available molecules.

- *Scaling up production.* It follows from the previous paragraph, that proteins for NMR studies must be prepared in milligram amounts and with completely changed ratio of isotopes. Fortunately, *recombinant* methods of molecular biology nicely fit our needs. As most proteins are prepared in a recombinant form anyway, protein sample preparation does not present any extraordinary requirements. Samples of nucleic acids are not obtained so easily and labeling with NMR active isotopes is relatively expensive in this case.

- *Size.* Sensitivity of the NMR methods for large molecules is very poor. It is not molecular mass but rate of tumbling in solution that is critical. Large rigid molecules (or rigid molecules in more viscous solvents, e.g. in cold water) tumbles slowly and give weaker NMR signal. The sensitivity can be regained by using special tricks. Molecules of a relative mass close to one million have been successfully studied. On the other hand, the process of full structure determination is very difficult and has been applied to only few monomeric proteins larger that ~30 kDa so far.

- *Separation from impurities.* Purity of the NMR sample is usually not a big problem. Obviously, signals of impurities are observed in the spectra, may obscure signals of our interest, and should be eliminated. Paramagnetic

compounds (typically various metal ions) should be avoided or removed from the sample. In theory, molecular oxygen dissolved in water may interfere as a paramagnetic molecule, but its presence causes no problems when working with large molecules. Bacterial contamination represents more serious danger than chemical impurities. Addition of an antimicrobial agent, such as sodium azide, is necessary to keep samples stable for a long time.

- *Salt content.* High ionic strength should be avoided for purely technical reasons. A decrease of sensitivity can be noticed with concentration of salt above $100\,\mathrm{mM}$. Higher than $0.5\,\mathrm{M}$ salt concentrations should not be used at all. NMR spectroscopists just do not like salty stuff.

Lecture 1b
NMR as a physical phenomenon

1.6   Spin and magnetic moment

Nuclear magnetism is a phenomenon exact description of which requires an advanced physical theory of *quantum electrodynamics*. Yet, we can use very simple pictures to understand the basic ideas. Let us start with a really naïve model of the hydrogen atom shown in Figure 1.2A. Let us imagine an electron orbiting a proton like our Earth orbits Sun. The electron is charged and its circular motion is equivalent to the electric current (electric current in a wire is nothing else than traveling electrons). This circular current induces magnetic field like in an electric motor. But this is not all. The Earth is also spinning about its own axes. Let us assume for a moment that the electron is spinning in the same manner. The *spin* is also a circular motion and induces its own magnetic field. If we pull the electron out of the atom, the orbital motion (and the orbital magnetism) disappears, but the spin (and the spin magnetism) remains. If we put the electron inside a magnet, we can observe its spin magnetism (actually, this is how the spin of electrons was discovered).

Magnetism of the electrons is quantitatively described by the *magnetic moment*. It is a vector property. Magnitude of the magnetic moment describes strength of the magnetic field generated by the electron, and the direction of the magnetic moment defines orientation of this magnetic field. The magnetic moment is directly proportional to the *angular momentum*.[5] Behavior of the magnetic moment and of the angular momentum is therefore similar (except for the numeric value) and we will inspect both vectors together.

As any vector, magnetic moment or angular momentum can be decomposed into three perpendicular components oriented along the x, y, and z axes. Perhaps a more convenient way of description is the spherical representation, where the radius of the sphere defines the magnitude and two angles define direction in the same way as geographical latitude and longitude define the position on the Earth's surface.

How does a spinning electron move in a magnetic field? Well, in a similar way as a spinning top moves in the gravitation field of Earth. If you steal such a toy from children and set it spinning, there is a little chance that the axis of rotation is precisely perpendicular to the Earth's surface. More often, the axis is slightly askew. Gravitation pulls the spinning top down, but it does not fall to the ground immediately. Instead, the angular momentum rotates the spinning axis so that it undergoes a slow *precession* motion. You do a similar thing when you ride your bicycle. Your body does not stay straight up but it is swinging from left to right. Thanks to the angular momentum of your wheels you do not fall down, you are only forced to continually change direction. It should not surprise you that magnetic moments of free electrons are precessing in static homogeneous magnetic fields.

In order to proceed in our description of electrons in a magnetic field, we must borrow some results from quantum theory.[6] So far we have not noticed any difference between behavior of the electrons and our everyday experience. One might get a feeling that we do not need quantum theory at all. This feelings disappear as soon as we realize one big difference between electrons and macroscopic rotating bodies such as the Earth or the spinning top. Spinning of the electron cannot be stopped. It cannot be accelerated or slowed down. The angular momentum of the spinning top

---

[5]Angular momentum is a vector oriented along the axis of rotation and its absolute value is rmv, were r is radius of the circular orbit and m and v are mass and velocity of the electron, respectively.

[6]It is interesting that quantum mechanics itself does not explain why the spin exists. Only in combination with the special theory of relativity, the quantum theory predicts spin as a necessary property of particles like electrons.
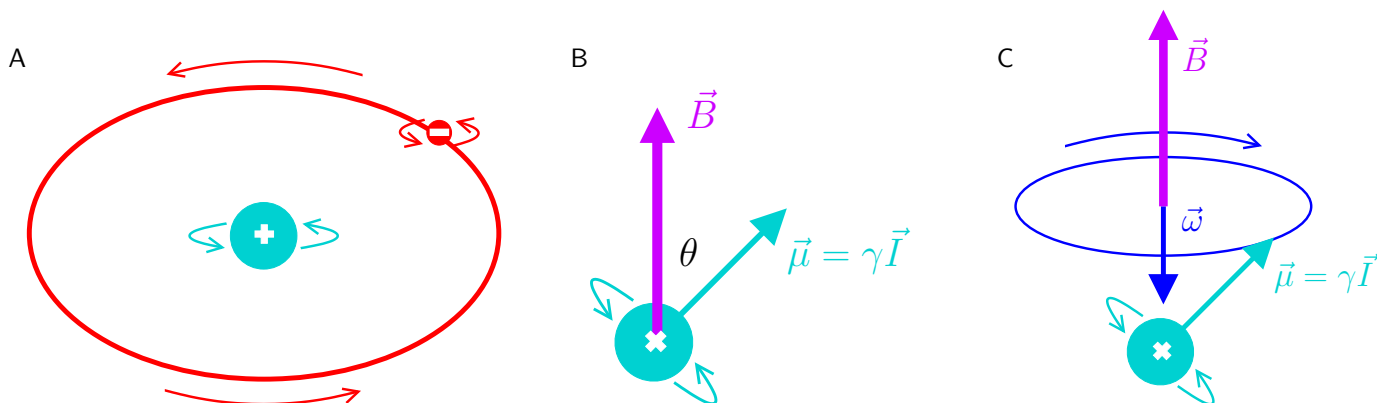
Figure 1.2: A, A naïve model of hydrogen atom. B, A magnetic particle in a homogeneous magnetic field $\vec{B}_0$. C, Precession of a magnetic dipolar moment in a homogeneous magnetic field $\vec{B}_0$.

is introduced by external forces of our fingers but the angular momentum of the electron is an inherent property of the particle. It is even misleading to take the spin as a kind of rotation motion. Experiments and theory show that electrons are not spinning, they simply *have spin*. I agree that the idea of an angular momentum[7] without physical rotation is very strange but we have to live with it.

Another consequence of the quantum theory that deserves our attention is the relation between the electron's spin and magnetic moment. In the classical physics, the proportionality constant is equal to one half of the charge-to-mass ratio. Quantum theory gives a value twice as big in the first approximation. Further corrections are needed to account for interactions of the electron with its own electromagnetism, but these effects are small and can be easily calculated. In the case of electron, the quantum theory can predict the magnetic moment with an astonishing precision of eleven digits.

Quantum theory of course describes electron and its spin in more details. For example, it tells us that only some physical quantities can be measured simultaneously. It also shows that two particular orientations of the magnetic moment in a magnetic fields are special. They are called stationary states and traditionally labeled α and β. We do not need such details for the description of NMR because we are not interested in isolated particles but in macroscopic samples. It is not only unnecessary, but confusing and physically incorrect (but unfortunately frequent in the literature[8]) to apply quantum theory of single particles to NMR samples.

1.7 Nuclear magnetism

In spite of our deep interest in atomic nuclei, we talked about electrons so far. The only reason was that electrons behave as simple particles, nicely described by quantum electrodynamics. Because the word "simple" may suggest various things, physicists call electron and other well-behaving particles *Dirac particles*.[9] On the other hand, nuclei are *composite particles* and their theoretical description is more complex. Even the nucleus of the hydrogen atom, a single proton, is a composite particle. Protons and neutrons consist Dirac particles, *quarks*. Each quark possesses its own spin and magnetic moment. Quarks are held together by very strong interactions, mediated by particles called *gluons*. Calculation of the magnetic moments of protons and neutrons, and consequently of the whole nuclei, is very difficult, as the resulting magnetic moment is a combination of spin and orbital moments of quarks and gluons. One of the following three general results can be obtained.

---

[7]The word "spin" is just a short name of the inherent angular momentum of a particle – do not confuse it with the angular momentum describing orbital motion of an electron around the nucleus.

[8]Quantum theory can be used to describe macroscopic samples but it must incorporate the statistical approach. The textbooks recommended in Section 1.1 use the quantum theory correctly.

[9]Paul Dirac laid the foundations for the development of quantum electrodynamics.

1. The magnetic moments are canceled completely and the nucleus does not show any magnetism. The most abundant isotope of carbon, ^{12}C, composed of six protons and six neutrons, is a typical example.

2. The magnetic moments are combined such that the magnetic behavior of the nucleus resembles magnetic behavior of a Dirac particle. The nucleus has the same spin as electrons.As uqntum theory describe this type of particles with the spin quantum numbers $\pm\frac{1}{2}$, a term *spin-1/2 nuclei* is used. It follows from the theory that these nuclei have spherically symmetric electric field, which is a great advantage for NMR measurements. Typical examples are isotopes ^{1}H, ^{13}C, ^{15}N, ^{31}P.

3. The third category includes all other combinations. Such nuclei have larger angular momenta (spins) and asymmetric electric fields. They are not suitable for biomolecular NMR investigations. The most abundant isotope of nitrogen (^{14}N) is an example.

It follows from the previous discussion that we can ignore the first and third type of nuclei[10] and treat nuclei of the second type as *Dirac-like particles.* Such an approach leads to correct qualitative conclusions but the numerical values must be taken as empirical constants.

Now it is a good time to turn our attention to quantitative issues. Fortunately, we do not need heavy math to understand biomolecular applications NMR spectroscopy.[11] It is good to remember three simple equations relating four physical quantities (i) spin or angular momentum $\vec{I}$, (ii) magnetic moment $\vec{\mu}$ and its (iii) energy E and (iv) angular precession frequency $\vec{\omega}$ in a magnetic field of *magnetic induction* $\vec{B}$ (Figure 1.2B,C):

$$\vec{\mu} = \gamma\vec{I}, \tag{1.1}$$
$$E = -\vec{B}\cdot\vec{\mu} = -\gamma\vec{B}\cdot\vec{I}, \tag{1.2}$$
$$\vec{\omega} = -\gamma\vec{B}, \tag{1.3}$$

where the symbol γ describes the proportionality constant between spin and magnetic moment, known as the *magnetogyric ratio.*

We have already discussed relation between $\vec{\mu}$ and $\vec{I}$ (Eq. 1.1) for electron and nuclei. The value of γ is provided by quantum mechanics with a great precision for Dirac particles and should be determined experimentally for Dirac-like particles, including nuclei.

Eq. 1.2 defines energy of the magnetic moment in a magnetic field. The classical physics shows that a magnet in a magnetic field has the lowest energy if its magnetic moment is oriented along the magnetic field (parallel with the vector of the magnetic induction $\vec{B}$. The expression $\vec{B}\cdot\vec{\mu}$ is a short version of the sum $B_x\mu_x + B_y\mu_y + B_z\mu_z$ (B_x is the x component of the vector $\vec{B}$ etc.). Traditionally, the z axis is defined by the direction of the magnetic field $\vec{B}_0$ inside the strong magnet of the NMR spectrometer. Therefore, the B_z component of $\vec{B}_0$ must be equal to the total length of the vector,[12] B_0, while B_x and B_y must be equal to zero. Eq. 1.2 can be simply written as

$$E = -B\mu_z = -\gamma B_0 I_z = -\gamma B_0 I \cos\theta, \tag{1.4}$$

where θ is the angle between the magnetic moment $\vec{\mu}$ and the vector of magnetic induction $\vec{B}$.

Finally, Eq. 1.3 shows that the angular precession frequency $\vec{\omega}$ is proportional to the external magnetic field and that the proportionality constant is again γ. Note that the angular precession frequency is presented as a *vector quantity* in Eq. 1.3. The magnitude $|\omega|$ is the speed of the precession (in the units of radian per second, precession frequency in the units of Hertz is $|\omega|/(2\pi)$), whereas the direction of $\vec{\omega}$ defines axis of the precession motion. The minus sign reminds us that the axis of precession is oriented opposite to the magnetic induction.

In summary, Eqs. 1.1–1.3 tell us that the spin and magnetic moment are intrinsic properties of the nucleus but the energy E and precession frequency $\vec{\omega}$ obviously depend on the external magnetic field.

---

[10]Only the nucleus of heavy hydrogen (deuterium) ^{2}H is somewhat exceptional. Its electric field is not spherically symmetric, but is relatively small and is observed in some biomolecular applications.

[11]Much more mathematics is needed if we ask *why* the NMR experiment works as they do. Another course at Masaryk University, C5320 Theoretical concepts of NMR, tries to ask such questions.

[12]Total length or magnitude, usually called absolute value or amplitude in physical literature, is labeled simply by the letter symbolizing the vector written without the arrow (B_0 in our case), or by the letter surrounded with the absolute value symbols ($|B_0|$).
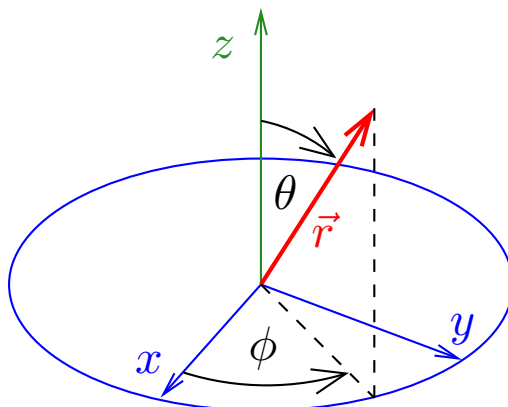
Figure 1.3: Orientation of a vector $\vec{r}$ (red) described by spherical coordinates ϕ, θ (black) and by the Cartesian coordinates x, y, z. The longitudinal direction (z) is shown in green, the transverse plane (xy) is shown in blue.

1.8   Nuclei in the test-tube

After discussing the nuclear magnetism as a phenomenon, we can look at it from a more practical point of view. We are now interested not in microscopic processes inside isolated atoms but in a measurable macroscopic quantity describing magnetism of the whole sample. Such quantity is called *total magnetization* and labeled with symbol $\vec{M}$. As we moved from microscopic particles to macroscopic samples, classical (non-quantum) physics should be sufficient to describe what we observe.

In physics, magnetization is defined as the *sum of magnetic moments per unit volume.* Magnetic moments of the same nucleus in different molecules have the same magnitude but different orientation. The orientation in a coordinate frame formed by axes x, y, z is described by two angles (Figure 1.3), (i) the angle θ between the magnetic moment and the z axis induction vector of the external magnetic field $\vec{B}$ (analogy of geographic latitude), and (ii) the angle ϕ describing the *azimuth*, i.e., the angle telling us how much is the component of the vector perpendicular to z rotated from the direction y in the xy plane (analogy of geographic longitude). Therefore, the result of addition of many little vectors of magnetic moments of individual nuclei depends on their angles θ and ϕ.

Real chemical and biological samples contain huge numbers of nuclei. The only practical approach to such a large collection of nuclei is a statistical description. Let us ask a typical statistical question: What are the most probable angles θ and ϕ? The answer depends on the magnetic field, describing forces acting on the magnetic moments. In the following paragraphs, we explore three types of magnetic environments.

1.9   No magnetic field

First, we can consider a sample of a biologically interesting molecule sitting on our laboratory bench (Figure 1.4A). If we ignore magnetism of the Earth and all other magnetic fields that surround us every day, the nuclear magnetic moments can be described as completely uncorrelated vectors, oriented randomly, pointing to all directions in space with the same probability (Figure 1.4B). No wonder that such sample has a zero total magnetization.

1.10   Static magnetic field

Second, we put the sample inside a static, homogeneous magnetic field defined by the magnetic induction vector $\vec{B}_0$ and ask again: What are the most probable angles θ and ϕ if the axis z is given by the direction of $\vec{B}_0$? The answer is simple for ϕ: all values of ϕ (all azimuths) are equally probable because the energy of a magnetic moment in $\vec{B}_0$ does not depend on ϕ (Eq. 1.4). As a consequence, components of magnetic vectors perpendicular to $\vec{B}_0$ (along x and y axes in our coordinate frame) are uniformly distributed and therefore they sum to zero. Only the components of
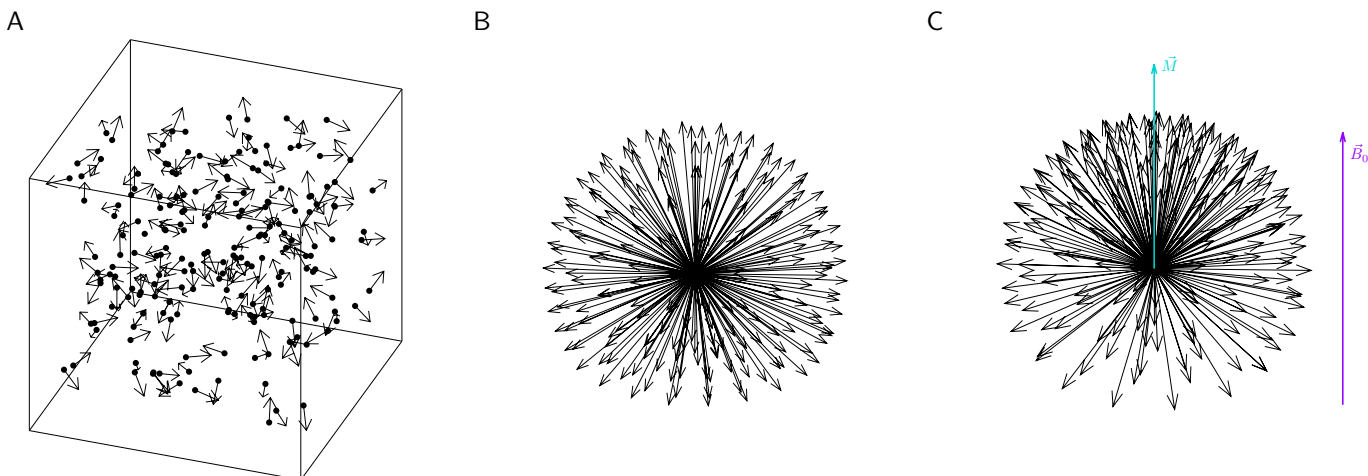
A

B

C

Figure 1.4: A, a schematic representation of an NMR sample. Dots represent molecules, arrows represent magnetic moments (only one magnetic moment per molecule is shown for the sake of simplicity, like e.g. in compressed $^{13}C^{16}O_2$). B, Distribution of magnetic moments in the absence of a magnetic field. The molecules are superimposed to make the distribution of magnetic moments visible. C, distribution of magnetic moments (black arrows) in a homogeneous magnetic field $\vec{B}_0$. The cyan arrow represents the macroscopic magnetization. Even if all black arrows precess with the same frequency about $\vec{B}_0$, the cyan arrow remains static.

magnetic moments parallel with $\vec{B}_0$ depend on $\vec{B}_0$. These components are described only by the angle θ. Therefore, we have to statistically analyze θ in order to evaluate the only non-zero component of the sum of magnetic moments, the component along the z axis of our coordinate frame.

On one hand, we have seen (Eq. 1.4) that energy of the magnetic moment in a magnetic field depends on the angle θ. Eq. 1.2 shows that the orientation of the magnetic moment parallel with $\vec{B}_0$, i.e. orientation with $\theta = 0$, has the lowest energy. One might expect that magnetic moments of nuclei should have this most favored orientation, at least in the classical physics. On the other hand, there is only one orientation with $\theta = 0$ (the magnetic moments pointing to the "northern pole"), but there are many possible orientations of magnetic moments for $\theta = 90\,°$ (magnetic moment pointing to the "equator"). We can see that we obtained two contradictory answers: if we ignore statistics and consider only energy, the most probable θ is zero, if we ignore energy and consider only statistics, the most probable θ is $90\,°$. The correct balance between energy and statistics is described by the Boltzmann law. Nuclei are not isolated from the rest of the world. They interact with the environment full of randomly moving molecules. This stochastic motion is manifested as the *temperature*, and represents a rich source of energy for the nuclear magnets. According to the Boltzmann law, fraction of magnetic moments in each orientation is indirectly proportional to the exponent of the ratio of the magnetic energy to the thermal energy. If we study biological molecules in liquid solutions, we work at temperatures high compared to the magnetic energies of nuclei in the strongest magnets. Therefore, the exponent in the Boltzmann law is a very small number and the exponential dependence is very close to a linear relation. Going through the somewhat tedious calculation[13] yields the average value of $\cos\theta$ at the thermal equilibrium:

$$\overline{\cos\theta^{\mathrm{eq}}} = \frac{|\mu||B_0|}{3k_{\mathrm{B}}T}, \tag{1.5}$$

where $k_{\mathrm{B}} = 1.38 \times 10^{-23}\,\mathrm{JK}^{-1}$ is the Boltzmann constant and T is the thermodynamic equilibrium. For the sake of simplicity, we assumed that the molecule contains only one type of nuclei with a magnetic moment, for example protons. As shown in Figure 1.4C, the distribution of magnetic moments is *polarized* in the direction of $\vec{B}_0$ (most favored orientation of a magnetic moment).

If we use the value of $|\mu|$ provided by quantum mechanics ($\sqrt{3}\gamma\hbar/2$, where $\hbar$ is the Plank constant divided by 2π,

---

[13]The following equation is derived in Course C5320 Theoretical concepts of NMR and the derivation is presented in the study material for the course.
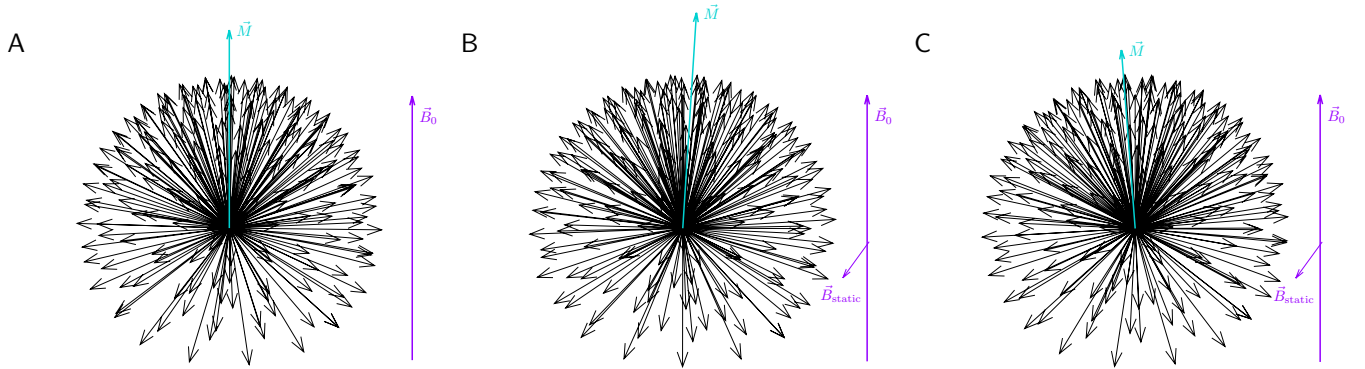
A B C

Figure 1.5: Distribution of magnetic moments in the presence of an external homogeneous magnetic field $\vec{B}_0$ (vertical violet arrow) is such that the macroscopic magnetization of nuclei (shown in cyan) is oriented along $\vec{B}_0$ (A). Application of an another static magnetic field $\vec{B}_1$ rotates magnetization away from the original vertical orientation down in a clockwise direction (B). However, the magnetization also precesses about $\vec{B}_0$. After a half-turn precession (C), the clockwise rotation by the additional magnetic field $\vec{B}_1$ returns the magnetization towards its original vertical direction. Therefore, a static field cannot be used to turn the magnetization from the vertical direction to a perpendicular orientation.

$\hbar = 1.054 \times 10^{-34}\,\mathrm{J\,s}$), we can express the z component of magnetization at the equilibrium as

$$M_z^{\mathrm{eq}} = \mathcal{N}|\mu|\overline{\cos\theta^{\mathrm{eq}}} = \mathcal{N}\frac{\gamma^2\hbar^2}{4k_{\mathrm{B}T}}, \tag{1.6}$$

where $\mathcal{N}$ is the number of magnetic nuclei per unit volume.

The x and y components of magnetization

$$
\begin{aligned}
M_x^{\mathrm{eq}} &= \mathcal{N}|\mu|\overline{\sin\theta^{\mathrm{eq}}} \cdot \overline{\cos\phi^{\mathrm{eq}}}, \tag{1.7}\\
M_y^{\mathrm{eq}} &= \mathcal{N}|\mu|\overline{\sin\theta^{\mathrm{eq}}} \cdot \overline{\sin\phi^{\mathrm{eq}}} \tag{1.8}
\end{aligned}
$$

are equal to zero because $\cos\phi$ and $\sin\phi$ average to zero when all values of ϕ are equally probable. The magnetization vector pointing in the direction z tells us that the magnetic moments are polarized along the z axis (so-called *longitudinal polarization*).

Note that we added moments undergoing precession and obtained a macroscopic magnetization that does not move at all (Figure 1.4C). Although all summed magnetic moments precess at the same frequency and the total magnetization is not zero in this case, the rate of precession cannot be measured.

1.11 Creating a signal

We see that having a magnet is not enough to measure precession frequency. We also need something that would disturb the macroscopic magnetization from its equilibrium orientation along $\vec{B}_0$. Not surprisingly, this "something" is again a magnetic field. Let us try to orient the additional field, described by the induction $\vec{B}_1$, perpendicular to the original external field (now we need to distinguish two independent external fields, the original field $\vec{B}_0$ and the new one $\vec{B}_1$). The magnetic force of $\vec{B}_1$ would pull the magnetic moments from their equilibrium orientations. Unfortunately, static $\vec{B}_1$ would not work as we wish. It is shown in Figure 1.5. The magnetic moments precess around $\vec{B}_0$, so they would feel the force of $\vec{B}_1$ pulling them from their equilibrium orientation at the beginning but back to the equilibrium orientation a fraction of microsecond later. The static $\vec{B}_1$ would perhaps introduce fast fluctuations but not net change in the total magnetization.

Obviously, $\vec{B}_1$ must be synchronized with the precession caused by $\vec{B}_0$. For example, the magnetic field $\vec{B}_1$ could be a field that rotates at the frequency which *resonates* with the precession frequency of nuclear magnetic moments. This is why we talk about nuclear magnetic *resonance*. In such case, the precessing magnetic moment would feel a
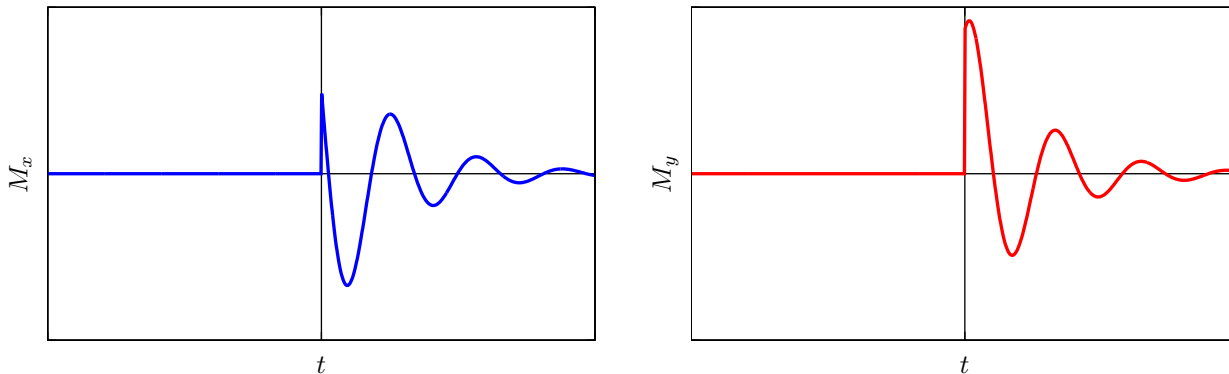
Figure 1.6: Values of M_x (blue) and M_y (red) components of a magnetization vector rotating with the initial phase of $60°$. The values decay due to a loss of coherence.

constant pull in one direction. This direction would precess together with the magnetic moment but would always point away from the equilibrium orientation. It is difficult to imagine the effect of the synchronized $\vec{B}_1$. Physicists like to make things simpler and so they introduced a coordinate system rotating together with the precessing magnetic moment. It is like jumping on a carousel that rotates with the precession frequency. Once we jump on it, the magnetic moments seem not to move any more and also $\vec{B}_1$ looks like a static field (Figure 1.7A). If $\vec{B}_1$ is static, it must have the same effect as $\vec{B}_0$, it must introduce a circular (precession) motion of the magnetic moments. The total magnetization is not parallel to $\vec{B}_1$ but perpendicular to it. So, it does not stay in its original position, defined by $\vec{B}_0$ but starts to rotate about a new axis defined by $\vec{B}_1$. The rotation of the magnetization is result of the additional precession introduced by $\vec{B}_1$, and has the same frequency as the new precession. Outside the rotating frame, we observe two superimposed rotations about two perpendicular axes. In our spherical representation of vectors, the tip of the arrow symbolizing the total magnetization draws spirals on a spherical surface. Such motion has been given a name *nutation* by astronomers.

I must admit that current technology does not allow us to rotate magnets at the precession frequency of nuclei. Fortunately, a magnetic field oscillating in one direction has a very similar effect if it is much weaker than $\vec{B}_0$ (Figure 1.7B). Radio waves represent a readily available source of a magnetic field oscillating in one direction with a frequency resonating with the precession frequency of the magnetic moments. Application of a radio wave for a well chosen period of time, known as the *radio-wave pulse*, thus rotates the magnetization vector from the z direction to the xy plane. After the pulse, the magnetic moments are not polarized vertically, but horizontally (Figure 1.7C). The direction of the horizontal, or *transverse* polarization then rotates with the precession frequency of the polarized magnetic moments. In other words, the M_x and M_y components of the magnetization vector oscillate as cosine and sine functions with the frequency equal to the precession frequency of individual nuclei. The cosine and sine functions are actually shifted in time by a phase factor depending on the phase of the radio wave, as shown in Figure 1.6.

We should stress that the *radio-wave pulse* did not create the transverse (horizontal) polarization from an unpolarized distribution. It only rotated the already existing longitudinal (vertical) polarization induced by the much stronger static field $\vec{B}_0$. Therefore, the magnitude of the magnetization rotating in the xy plane is proportional to $|B_0|$ according to the Boltzmann law (Eq. 1.6).

Bringing the magnetization to the xy plane is called *creation of coherence* in the NMR literature. The term *coherence* has its origin in statistical quantum mechanics, discussed in detail in Course C5320 Theoretical concepts of NMR. At this moment, we use the word "coherence" as a synonym for transverse polarization (we extend its meaning when we take into account mutual interactions between nuclei). The coherence is preserved as long as the magnetic moments move together, *coherently*. It does not take too long (usually seconds or less) to lose the coherence and, finally, to restore the equilibrium distribution of magnetic moments. The loss of coherence and return to the
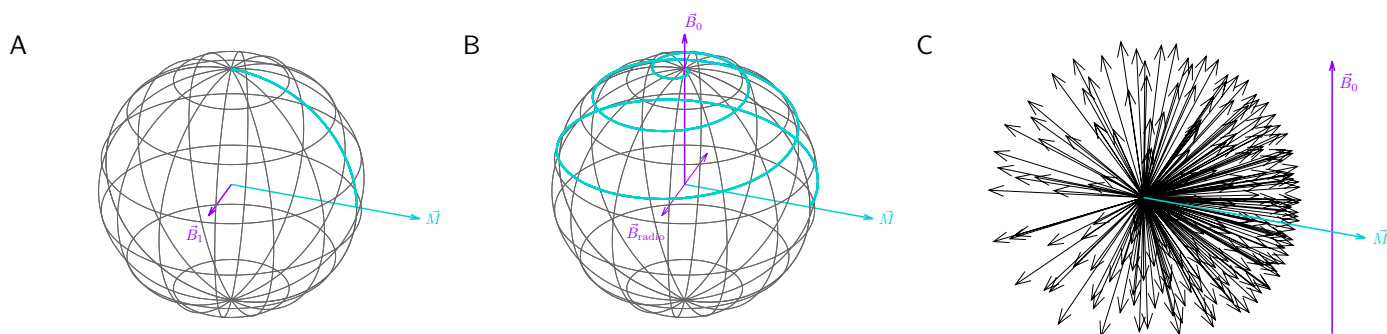
Figure 1.7: Effect of the radio waves on the bulk magnetization (A, in the rotating coordinate frame; B, in the laboratory coordinate frame) and distribution of magnetic moments after application of the radio-wave pulse (C). The thin purple line shows oscillation of the magnetic induction vector of the radio waves, the cyan trace shows evolution of the magnetization during irradiation. If the perpendicular magnetic field oscillates with a frequency equal to the precession frequency of magnetization, it rotates the magnetization clockwise then it is tilted to the right, but counter-clockwise when the magnetization is tilted to the left. Therefore, the magnetization is more and more tilted down from the original vertical direction. The total duration of the irradiation by the radio wave was chosen so that the magnetization is rotated to the plane perpendicular to $\vec{B}_0$ (cyan arrow). Note that the ratio $|\vec{B}_0|/|\vec{B}_{\text{radio}}|$ is much higher in a real experiment.

equilibrium are known as *relaxation*. We discuss relaxation in more detail later in our course. Before doing so, we explain other issues important for NMR spectroscopy and often ignore the relaxation effects for the sake of simplicity. However, we should never forget that relaxation exists and influences all NMR experiments.

Lecture 2
NMR as a method reflecting chemistry

2.1 Nuclei are affected by their environment

We discussed a very simple situation in the previous lecture. Nuclei were placed into a homogeneous magnetic field of the magnet sitting in our laboratory. The result was a precession motion at a frequency given (1) by the internal structure of the nucleus and (2) by the strength of our magnet. The observable magnetization, tilted to the transverse plane by a pulse of a radio wave, rotated et the same frequency. Clearly, such frequency carried no information about the molecule built of atoms containing our nuclei. The chemical and biological applications are only possible because the molecular environment modifies the magnetic field felt by the nuclei. We will look at the most interesting effects of the molecular environment in this section.

2.2 Interactions with close nuclei

Magnetic dipolar moments of the nuclei experience not only the external magnetic fields. The nuclei themselves are also sources of little magnetic fields. The effective magnetic field perceived by a certain nucleus is modified by its nuclear neighbors. The effect of a close nucleus depends on mutual orientation of both nuclei, i.e., the observed nucleus (shown in cyan in Figure 2.1) and its neighbor (shown in green in Figure 2.1) modifying the field felt by the observed nucleus. Let us suppose that the neighbor's magnetic moment is pointing up (vertical green arrow in Figure 2.1). If the neighbor is placed in direction perpendicular to the induction of the external field (Figure 2.1A), the magnetic field generated by the neighbor at the site of the observed nucleus is oriented opposite to the external field, and the effective field is decreased. If the neighbor is positioned in the direction of the external field, its magnetic moment creates a field that is added to the external field (Figure 2.1C). Quantitatively, the field created by the neighbor nucleus is proportional to $3\cos^2\theta - 1$, where θ is the angle between a line connecting the nuclei and the direction of the external field. Graphically, the direction of the neighbor's field is described by the shape of the magnetic induction lines of the neighbor's magnetic dipole. The effects are exactly opposite if the neighbor's magnetic moment is pointing down. This type of interaction is called *dipole-dipole coupling* (or *dipolar coupling*) in the NMR literature.

The effects of the close nuclei can be observed directly as shifts of precession frequency if the molecules are ordered in space (in crystals, or at least partially in liquid crystals). If the molecule freely rotates and if the rate of the rotation is the same in all directions (*isotropic rotation*), the position of the neighbor varies in time and the effects of the neighbor's magnetic field average to zero (if we calculate the average value of $\cos^2\theta$ for all possible values of θ, we find that is equal to 1/3, and therefore the average of $3\cos^2\theta - 1$ is zero). Does it mean that no information about the molecular structure can be obtained? Not at all. The fluctuating electromagnetic fields resulting from the molecular tumbling can be viewed as electromagnetic waves (or photons) of certain frequency. The frequency of molecular rotation changes randomly as the molecule collides with other molecules, and once a while it matches the precession frequency of the neighbor nucleus. When this happens, the x and y components of the magnetic induction of the stochastic waves generated by the molecular rotation resemble the radio waves applied by us: frequency of oscillation in the xy plane resonates with the precession frequency of the close nucleus and rotates its magnetization as shown in Figure 1.7 until a next collision changes the frequency of the molecular rotation. Such exchange of energy between
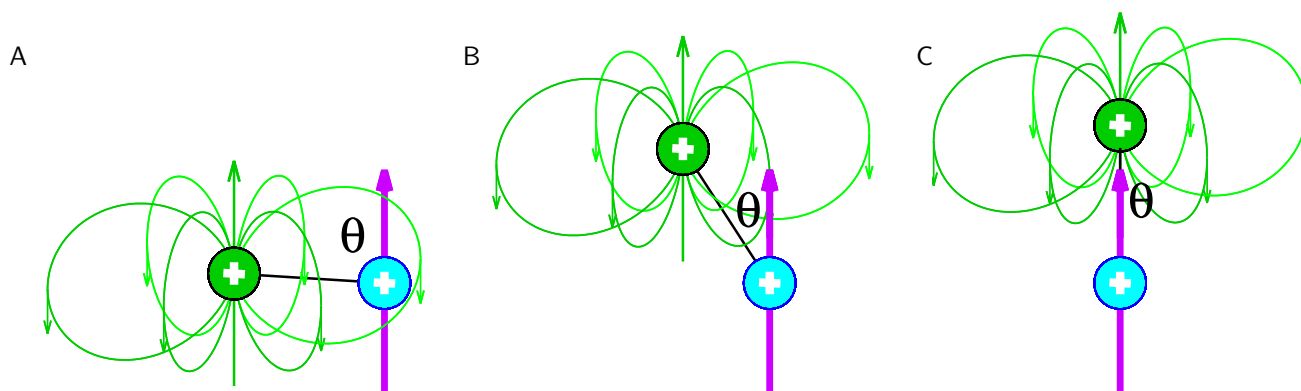
Figure 2.1: A, Classical description of interaction of a spin magnetic moment of the observed nucleus (shown in cyan) with a spin magnetic moment of another nucleus (shown in green). The thick purple arrow represents $\vec{B}_0$, the thin green induction lines represent the magnetic field $\vec{B}_2$ of the green nucleus (the small green arrows indicate its direction). The black line represents the internuclear vector $\vec{r}$. As the molecule rotates, the cyan nucleus moves from a position where the field of the spin magnetic moment of the green nucleus $\vec{B}_2$ has the opposite direction than $\vec{B}_0$ (A), through a position where $\vec{B}_2$ is perpendicular to $\vec{B}_0$ (B), to a position where $\vec{B}_2$ has the same direction as $\vec{B}_0$ (C).

nuclei is more probable if the nuclei are closer in space. Distances between nuclei can be estimated by measuring the efficiency of the described energy exchange, known as the *nuclear Overhauser effect* in the NMR literature. The interactions with magnetic moments of nuclear neighbors thus represent the physical nature of the allegory about the sailor and his walkie-talkie method (Section 1.3). Later we also show that dipole-dipole interactions varying due to the molecular motions cause *relaxation* (loss of coherence and return to equilibrium distribution of magnetic moments).

2.3 Interactions with electrons

Every nucleus in a molecule is surrounded by electrons. The magnetic fields of electrons significantly modify the field felt by the nucleus. Interactions with the spin magnetic moments of electrons are not so important because most electrons are paired and their spin magnetic moments canceled.[1] What is more interesting is the effect of the *orbital* magnetic moments. The orbital magnetism is induced by the external magnetic field and is always oriented against it. The external field is *shielded* by the paired electrons. Therefore, the precession frequency of a nucleus is decreased by orbital magnetic moments of electrons of the same atom (Figure 2.2A). Nuclei are also influenced by orbital magnetic moments of electrons of other atoms. The effect then depends on the orientation of the whole molecule in the magnetic field (Figure 2.2B,C). The precession frequency can be slowed down (shielding) but also speeded up (deshielding). The orientation of the molecule in the magnetic field influences the interaction with the orbital magnetic moments of electrons in a similar manner as described for the dipole-dipole interactions in Section 2.2, including relaxation. However, the isotropic molecular tumbling does not eliminate the shielding. As a result, the precession frequency is shifted even in perfectly spherical molecules. This phenomenon is known as the *chemical shift* (chemical because it does not reflect nuclear properties but molecular structure). Chemical shift is a sensitive probe of the structure of the molecule because it depends on the distribution of electrons in the molecule. Empirical values are routinely used as the key identifiers in the process of determining chemical configuration of small organic molecules. Unfortunately, interpretation of subtle chemical shift variations is very difficult and the use of chemical shifts in structure determination of biomacromolecules is limited.

---

[1]Unpaired electrons are mostly observed in proteins containing metal ions. They affect nuclei through the same mechanism as described in Section 2.2, but the interaction is much stronger.
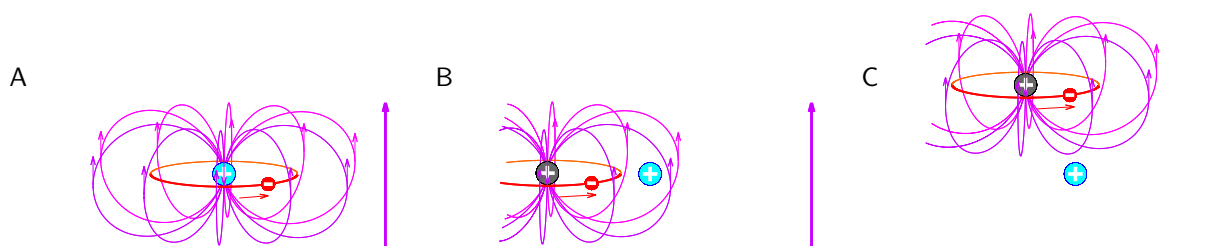
Figure 2.2: A, Classical description of interaction of an observed magnetic moment with the orbital magnetic moment of an electron of the same atom. The observed nucleus and the electron are shown in cyan and red, respectively. The thick purple arrow represents $\vec{B}_0$, the thin purple induction lines represent the magnetic field of the electron (the small purple arrows indicate its direction). The electron in $\vec{B}_0$ moves in a circle shown in red, direction of the motion is shown as the red arrow. The field of the orbital magnetic moment of the electron in the same atom decreases the total field in the place of the observed nucleus (the small purple arrow in the place of the cyan nucleus is pointing down). B, Interaction of an observed magnetic moment with the orbital magnetic moment of an electron of the another atom (its nucleus is shown in gray). In the shown orientation of the molecule, the field of the orbital magnetic moment of the electron in the other atom increases the total field in the place of the observed nucleus (the small purple arrow close the cyan nucleus is pointing up). C, As the molecule rotates, the cyan nucleus moves to a position where the field of the orbital magnetic moment of the electron in the other atom starts to decrease the total field (the induction lines reverse their direction in the place of the cyan nucleus).

2.4 Interactions between nuclei mediated by electrons

We described how magnetic moments modify the external magnetic field felt by their nuclear neighbors. The little magnetic moments of nuclei also interact with the magnetic moments of electrons forming bonds between atoms. Therefore, nuclei interact not only directly, as described in Section 2.2, but also through a cascade of interactions with magnetic moments of electrons forming chemical bonds between them. This type of interaction is known as the *J-coupling*.

The origin of the *J*-coupling is interesting. The dominant component of the *J*-coupling is the *Fermi contact interactions*, which can be explained as follows. It is not surprising that magnetic moments of nuclei interact with spin magnetic moments of electrons, but this is just a regular dipole-dipole interaction. We already learned in Section 2.2 that the shape of the magnetic field of a nuclear dipole is described by magnetic induction lines of the dipole, and that the numerical value is given by $3\cos^2\theta - 1$, which averages to zero if the nucleus freely rotates in the external magnetic field (Figure 2.3A–C). This is true, but with one exception, depicted in Figure 2.3D.

If the electron is present *exactly* at the nucleus, the vector of the electron spin magnetic moment $\vec{\mu}_e$ has the same direction as $\vec{B}_e$ and the magnetic energy is proportional to the scalar product of the vectors of the magnetic moments of the electron and the nucleus ($-\vec{\mu}_n \cdot \vec{\mu}_e$). This energy is lowest when the magnetic moments are parallel, and obviously does not depend on the orientation of the molecules (the scalar product is scalar, not a vector). Therefore, this interaction is often called *scalar coupling*. The exact co-localization of electron and nucleus may look strange in our classical (non-quantum) discussion of NMR, but the interaction between the nucleus and electron *inside* the nucleus can be simulated by a hypothetical current loop giving the correct magnetic moment when treated classically. The direction of the magnetic induction lines *inside such loop* (*inside the nucleus*) is *parallel* with the magnetic moment of the electron.

When we discussed interactions between nuclear magnetic moments in Section 2.2, we did not pay any attention to the field inside the nucleus because no other nucleus can be found there, nuclei are always separated in molecules. But this restriction does not apply to electrons! The shape of the atomic s-orbital suggests that the electron can be found with non-zero probability exactly at the position of the nucleus (Figure 2.3E).

Let us now look at a pair of two nuclei connected by a single bond, interacting with two electrons with non-zero probability to be present exactly at the positions of the nuclei (Figure 2.3F,G). The electrons in pairs that form chemical bonds have the opposite spin (red arrows in Figure 2.3F,G). It has the following consequence.

If the magnetic moment of the neighbor (shown in green in Figure 2.3F,G) is pointing up (Figure 2.3F), it makes

the $-z$ orientation (pointing down) of the spin magnetic moment of the electron at the place of the cyan nucleus more favorable. Such a magnetic moment is a source of a magnetic field $\vec{B}_e$ oriented in the $-z$ direction at the site of the cyan nucleus. Any magnetic field causes precession of magnetic moments. The magnetic moment of the cyan nucleus would precess about an axis given by the vector of the angular frequency $\vec{\omega}_e = -\gamma\vec{B}_e$. For a magnetic field pointing down, this corresponds to a counterclockwise precession if γ of the cyan nucleus is positive. The described precession caused by the electron's field is added to the much faster precession caused by $\vec{B}_0$. As the electron generates a field in a direction opposite to $\vec{B}_0$, the electron's field *slows down* the precession. To make a long story short, the $+z$ orientation of the neighbor's magnetic field *decreases* the precession frequency of the observed nucleus.

If the magnetic moment of the neighbor is pointing down (Figure 2.3G), the effect is opposite. The electron co-localized with the observed nucleus *increases* precession frequency of the magnetic moment of the observed nucleus (the field of the electron $\vec{B}_e$ has the same direction as $\vec{B}_0$).

We have analyzed only the vertical direction of nuclear magnetic moments when discussing Figure 2.3F,G. Other directions have similar effects, they introduce additional counterclockwise precession for nuclei with $\gamma > 0$ (and clockwise precession for nuclei with $\gamma < 0$). However, if the precession frequencies of the cyan and green nuclei differ, the horizontal polarization of the green nucleus rotates quickly in a coordinate frame of the cyan nucleus. Therefore, the effect of the horizontal polarization of the green nucleus on the precession frequency of the cyan nucleus fluctuates rapidly and is quickly averaged to zero.

The described electron-mediated interactions of course depend on the electron distribution in the molecule. The existence of an interaction so closely related to the chemical structure is obviously very useful. When we discuss the NMR methodology in details, we find out that the J-couplings are the corner stones of almost all modern NMR techniques.

2.5 Evolution of coherences

The coherence, introduced by the $\vec{B}_1$ field, evolves under the influence of magnetic fields acting on the observed nucleus, and the macroscopic magnetization of the sample varies. In order to track the changes, it is useful to decompose the overall magnetization into individual contributions rotating with different frequencies.

- First, we distinguish magnetizations of different nuclides (^{1}H, ^{13}C, ^{15}N, ^{31}P) because the magnetization vector rotates about $\vec{B}_0$ with the frequency $\vec{\omega}_0 = -\gamma\vec{B}_0$ (Eq. 1.3) and each nuclide is characterized by a unique value of γ.

- Second, we distinguish magnetizations of the same nuclides in different chemical groups because they are surrounded by different distributions of electrons resulting in different chemical shifts. As a consequence, precession frequencies ω_0 and frequency offsets Ω of magnetic moments of the same nuclide in different groups slightly vary.

- Third, we distinguish magnetizations of the same nuclides in different chemical groups coupled via covalent bonds to nuclei with different polarizations. As shown in Figure 2.3, polarization along $\vec{B}_0$ of a J-coupled neighbor slows down the precession frequency (Figure 2.3F) whereas polarization against $\vec{B}_0$ of a J-coupled neighbor speed up the precession frequency (Figure 2.3F). In other words, evolution of transverse polarization (coherence) of the observed nucleus *correlates* with the longitudinal polarization of the neighbour.

The correlation underlying the third distinction is not easy to grasp. An attempt to explain it is present in Table 2.1. In the second column of the table, four magnetic moment distributions of two nuclei are drawn. We assume that the nuclei are different nuclides with very different precession frequencies, e.g. the left nucleus is ^{1}H (proton) and the right nucleus is ^{13}C (or ^{15}N).

The first row (labeled "In-phase") shows distributions immediately after applying a 90° pulse a frequency very close to the ^{1}H precession frequency. The drawings are oriented so that the magnetic field is pointing to the right. Traditionally, the direction of $\vec{B}_1$ is used to define the x axis of the rotating coordinate frame introduced in Section 1.11. According to a convention described in Section 4.4 the axis of rotation is the same as direction of $\vec{B}_1$ for protons and other nuclei with positive γ. Therefore, the ^{1}H magnetic moments are polarized towards us (direction $-y$) after the pulse. In the second column, most polarized magnetic moments of ^{1}H are colored in cyan and magnetic moments of
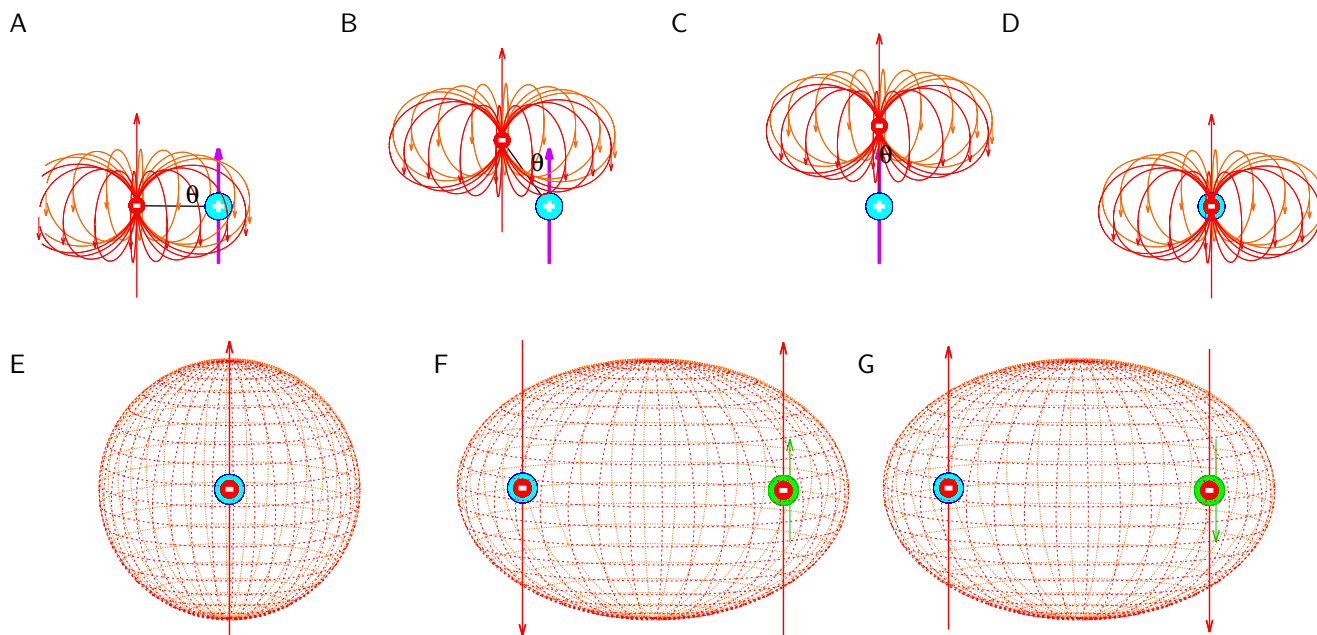
Figure 2.3: *J*-coupling. A–C, magnetic fields of an electron (red induction lines) outside the nucleus (cyan), influencing the nucleus as expected for regular dipole-dipole interactions. D, magnetic field of an electron localized at the position of the nucleus. E, probability of finding an electron in the hydrogen atom at particular coordinates is described by the probability density. The probability density described by the orbital 1s (depicted as a sphere) has a non-zero value at the position of the nucleus (shown in cyan). Therefore, there is a non-zero probability of finding electron (red circle) exactly at the site of the nucleus. The field produced at the site of the nucleus by the electron's magnetic moment (red arrow) does not depend on the orientation of the atom if the positions of the nucleus and electron coincide. Therefore, the interaction of the nucleus with the electron is not averaged to zero if the atom rotates isotropically. F and G, the probability density described by the sigma orbitals (depicted as an ellipsoid) in molecules has also non-zero values at the sites of nuclei. The spin states of the electrons in the bonding sigma orbital are opposite (indicated by the opposite direction of the red arrows) and perturbed by the magnetic moment of the nuclei. The parallel orientations of magnetic moments is energetically favorable for a nucleus and an electron sharing its position. As a consequence, precession frequency of the cyan nucleus is lower in Panel F and higher in Panel G (see text for details).

^{13}C (not influenced by the radio wave and therefore keeping their equilibrium distribution) in the *same molecules* are colored in green. We see that there is no obvious correlation between orientations of magnetic moments shown in cyan and in green. Before we discuss diagrams in other columns, we look at the second row.

After the 90° pulse, the distribution of proton magnetic moments evolves. The transverse polarization of ^{1}H rotates due to the presence of $\vec{B}_0$ modulated by the chemical shift (*chemical shift evolution*). The apparent speed of rotation in the rotating coordinate frame depends on the exact choice of the radio wave frequency (which defines the frequency of the rotating coordinate frame). To simplify our analysis, let us assume that the radio wave has exactly the same frequency as the precession frequency of the observed proton. Therefore, the most polarized magnetic moments would not rotate in the rotating coordinate frame and stay in the $-y$ direction (pointing to us in the view used in Table 2.1) if there were no coupling between the nuclei.

However, the nuclei *are* coupled. Protons coupled to ^{13}C with magnetic moment pointing up precess slower (counterclockwise in the rotating coordinate frame) and protons coupled to ^{13}C with magnetic moment pointing down precess faster (clockwise in the rotating coordinate frame). As a result, the originally polarized magnetic moments of ^{1}H (cyan arrows in the second row) spread in a belt surrounding the "equator" in our drawings. At certain time, the polarization of ^{1}H is lost completely. A rigorous calculation of this time would require careful statistical analysis of all magnetic moments. We can simplify this task by dividing molecules into two groups: the first one with positive z components of ^{13}C magnetic moments and the second one with negative z components of ^{13}C magnetic moments. In the former groups, the proton magnetic moments would precess slower, in the latter one, the proton magnetic moments would precess faster. If we neglect a slight preference of the $+z$ orientation of ^{13}C magnetic moments, we can assume

that proton magnetic moments in the second group precess exactly like those in the first group, but in the opposite direction in the rotating frame. Therefore, it is sufficient to track "half-magnetization vectors" in the two groups and calculate the total magnetization as their sum. Immediately after the 90° pulse, directions of the "half-magnetization vectors" are the same (differences in precession frequencies due to ^{13}C did not have time to show up). Then, one "half-magnetization vectors" rotates clockwise and the other one counterclockwise. So they must point in mutually opposite directions after some time and this is the time we are looking for. Let us call it t_0.

When the directions of "half-magnetization vectors" are opposite, the total magnetization is zero. The polarization is lost. However, the distribution is still coherent! If we follow the rotation of the "half-magnetization vectors" further, we find out that at the time $2t_0$ both "half-magnetization vectors" have the same orientation again and the polarization is restored. The distribution of magnetic moments at t_0 is just another type of coherence, present only in samples with coupled nuclei. In such samples, the magnetic moment distribution oscillates regularly between a coherence with maximum polarization and a coherence with zero polarization. The rate of the oscillation is given by a constant $J = 1/(2t_0)$. To distinguish the different types of coherences, the former one, associated with measurable proton magnetization, is called *in-phase*, and the latter one, associated with zero proton magnetization, is called *anti-phase*.

One feature of the anti-phase coherence is zero polarization. Another feature is shown in the second row of Table 2.1, where fractions of proton magnetic moment oriented most to the right (x direction in our coordinate system) are colored in cyan. Now, the distributions of the magnetic moments of the nuclei are *correlated*, the right direction of the cyan arrows correlates with the up direction of the green arrows, the left direction of cyan arrows correlates with the down direction of the green arrows.

In the third column of Table 2.1, the highlighted magnetic moments are divided based on the distribution of the magnetic moments of ^{13}C. The top and bottom parts of the diagram show distributions in molecules where the ^{13}C magnetic moments are closer to $+z$ and $-z$ direction, respectively. In the case of the in-phase coherence, the proton magnetic moments are polarized in the $-y$ direction (the cyan cluster of magnetic moments with the most frequent orientations). The anti-phase coherence corresponds to the distribution when the average orientation of the half population of proton magnetic moments precessing slower (top) is exactly opposite to the average orientation of the half population of proton magnetic moments precessing faster (bottom).

To avoid tedious drawing the distributions, we introduce simple arrows (the last two columns in Table 2.1) specifying directions of the magnetic moments of protons attached to ^{13}C with the magnetic moment pointing up (dashed arrow) and pointing down (solid arrow). Such arrows correspond to the "half-magnetization vectors", discussed above. The depicted distributions and "half-magnetization arrows" remind us that coherences have their directions. The direction of the in-phase coherence is naturally the direction of the polarization. The direction of the anti-phase coherence is given by the dashed arrow, describing distribution of proton magnetic moments correlated with the ^{13}C the magnetic moments pointing up.

In the following sections, we use the solid and dashed "half-magnetization" arrows to analyze evolution of coherences in various modules of pulse sequences. Here, we only mention the effects of the chemical shift and J-coupling in the absence of radio-wave pulses:

- *Chemical shift* causes transverse polarization of nuclei in different chemical groups to rotate about $\vec{B}_0$ with different frequencies (Figure 2.4). The size of transverse magnetization is preserved (except for relaxation effects, neglected here), only the direction changes. Any direction in the xy plane can be expressed as a linear combination of x and y components of the magnetization. Both components oscillate as the magnetization rotates, and these oscillations are detected as the NMR signal. Accordingly, the in-phase coherence can be decomposed into x and y components. Chemical shift does not convert in-phase coherences to anti-phase coherences or vice versa.

- *J-coupling* makes transverse polarization and magnetization of nuclei in the same chemical group to disappear and reappear periodically (Figure 2.5). This can be described as an oscillation between "visible" in-phase coherences and "invisible" coherences. The consequence is an oscillation of the NMR signal given by the value of the interaction constant J.

- Simultaneous effects of the chemical shift and the J-coupling is presented in Figure 2.6.

Note that although the anti-phase coherence is "invisible", the polarization is hidden in it. As shown in Figures 2.5 and 2.6, the polarization is completely converted to the anti-phase coherence after a time period equal to $t_0 = 1/(2J)$

(snapshots number 6). However, at time $2t_0 = 1/J$ after excitation (snapshots number 12), the magnetization is recovered, now in the opposite direction ($+y$).

2.6 NMR experiment

After discussing the physical phenomena important for understanding nuclear magnetic resonance, we proceed to more technical issues. The use of NMR spectroscopy in chemistry and structural biology relies on our ability to measure precession frequencies of nuclear magnetic moments in the studied molecules. We already know that this requires a strong static homogeneous magnetic field and a much weaker magnetic field oscillating with frequencies close to the measured precession frequencies. By accident, the required frequencies are in the same range as those used in frequency modulated broadcasting. We see that the instrument able to measure precession frequencies, the *NMR spectrometer*, must contain three components: magnet (as a source of the static magnetic field $\vec{B}_0$), radio transmitter (as a generator of the oscillating field $\vec{B}_1$), and radio receiver (as a detector).

Scenario of the basic NMR experiment is rather simple. We put our sample inside a strong homogeneous magnet and let it reach thermal equilibrium. Then we switch on our radio transmitter for a precisely defined time period. This event is called the *radio-frequency pulse*. Duration of the pulse should be such that the pulse rotates the total magnetization just by $90°$ in order to achieve the highest sensitivity.[2] Finally, we switch off the transmitter and turn on the radio receiver. Our sample is now a source of magnetic field oscillations. These oscillations have frequencies very close to the frequency of the applied radio pulse (only nuclei resonating with this frequency were excited from their equilibrium states), but not exactly identical. Slight variations in frequency have their origin mostly in the electron shielding (the chemical shift). Nuclei in different chemical moieties are shielded to different extent and feel slightly different magnetic field (see Section 2.1). Now we see why the external field $\vec{B}_0$ must be very homogeneous. Variations of $\vec{B}_0$ would cause the precession frequencies to vary as well. Even relatively small variability in the inherent frequencies of nuclei would completely mask the tiny shielding effects of electrons.

The megahertz radio frequency is *modulated* by the variable shielding, causing deviations ranging from zero up to several kilohertz. In the same manner, megahertz radio waves are modulated with the audio frequencies in the FM radio broadcasting. The megahertz frequency serves as a *carrier* for the kilohertz frequencies generated by the electron environment of nuclei in the case of NMR or by vibrations of musical instruments or human voice in the case of the radio. The NMR receiver does the same job as an ordinary radio receiver. It subtracts the carrier frequency from the signal (technical details are discussed in Section 4.6). The remaining lower frequencies called *frequency offsets* Ω, are converted to a digital signal and recorded. The saved file has the same format as a typical audio record. If plotted, it shows a sum of sine (or cosine) curves. The amplitude of oscillations gradually decreases, as the nuclear magnetic moments lose their coherence, and as they return back to their equilibrium distribution. NMR spectroscopists use the term *free induction decay*, or simply *FID*, for the damped oscillating signal. When the system of nuclei arrives sufficiently close to the equilibrium, a new experiment can start. Waiting for the return to equilibrium is typically slightly longer than one second in the case of biological macromolecules.
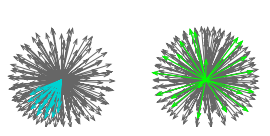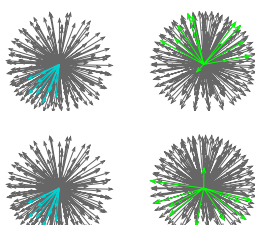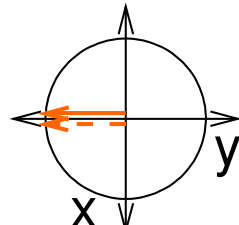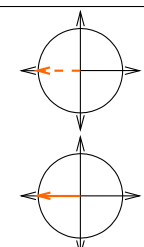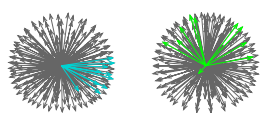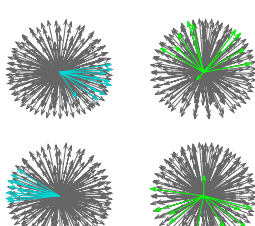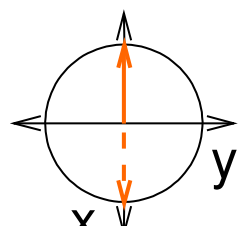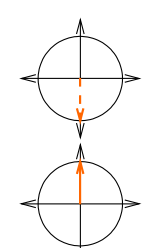
The output of the NMR experiments is an audio record. We can therefore easily *listen* to the NMR data. Well, listening is not a typical way of analyzing chemical data. We would like to present our records in some graphical representation. Simple plotting does not make us happy. The damped sine curves interfere and several sinusoids already produce a mess. Fortunately, the signal, recorded as a function of time, can be easily converted to a *spectrum*, which is a function of frequency. We now examine the procedure leading to nice looking spectra in some detail.
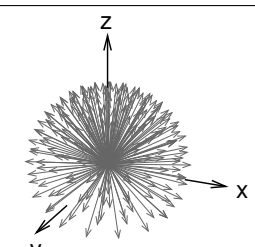
2.7 From oscillations to spectrum: Fourier transformation

Certain people, including the author of this text, have hard time to remember their shoe size. Some shops take this handicap into account. They keep a special device, a board with the footprints of various sizes. Imagine somebody really silly, who starts with the smallest size and keeps comparing his foot with the footprints on the board to the largest size. He ranks each trial on a scale of comfort ranging from zero to 100%. Clearly, the shoe size that fits

---

[2]We learn soon that the first pulse is followed by a whole sequence of carefully timed pulses in all biomolecular experiments.

Table 2.1: Examples of two graphical representations of in-phase and anti-phase coherences: as distributions and as arrows (used in Figure 3.1). Cyan arrows represent magnetic moments resonating with the applied radio wave (magnetic moments of ^{1}H in our example) most aligned along the $-y$ direction. Green arrows represent magnetic moments that do not resonate with the radio frequency (magnetic moments of ^{13}C or ^{15}N in our example) in the same molecules. The solid and dashed orange arrows presented in the last two columns correspond to partial distributions of proton magnetic moments, shown in cyan in the third column. The direction of the arrow is given by the average direction of the cyan arrows, the type (dashed or solid) of the arrow is given by the average direction of the green arrows in the third column (up or down, respectively). The orientation of axes in the schematic drawings of the magnetic moment distributions is shown below the table.

Coherence	depicted as distributions: selected molecules with $\vec{\mu}$ of ^{1}H closest to $-y$ (in-phase) or closest to x (anti-phase)	decomposed distributions based on $\vec{\mu}$ of ^{13}C/^{15}N being closer to $+z$ vs. to $-z$ in the selected molecules	depicted as arrows	decomposed arrows
In-phase				
Anti-phase				

Figure 2.4: Coherence evolution due to the chemical shift. Several snapshots of coherence evolving in the xy plane are shown in the circles in the middle. Evolution of the x and y components of the in-phase (red) and anti-phase (blue) coherences are plotted above and below the snapshots, respectively. The in-phase coherence (blue bar) coincides with the transverse polarization of magnetic moments (cyan arrow), size of which is preserved in the presence of the chemical shifts. The anti-phase coherence does not evolve.
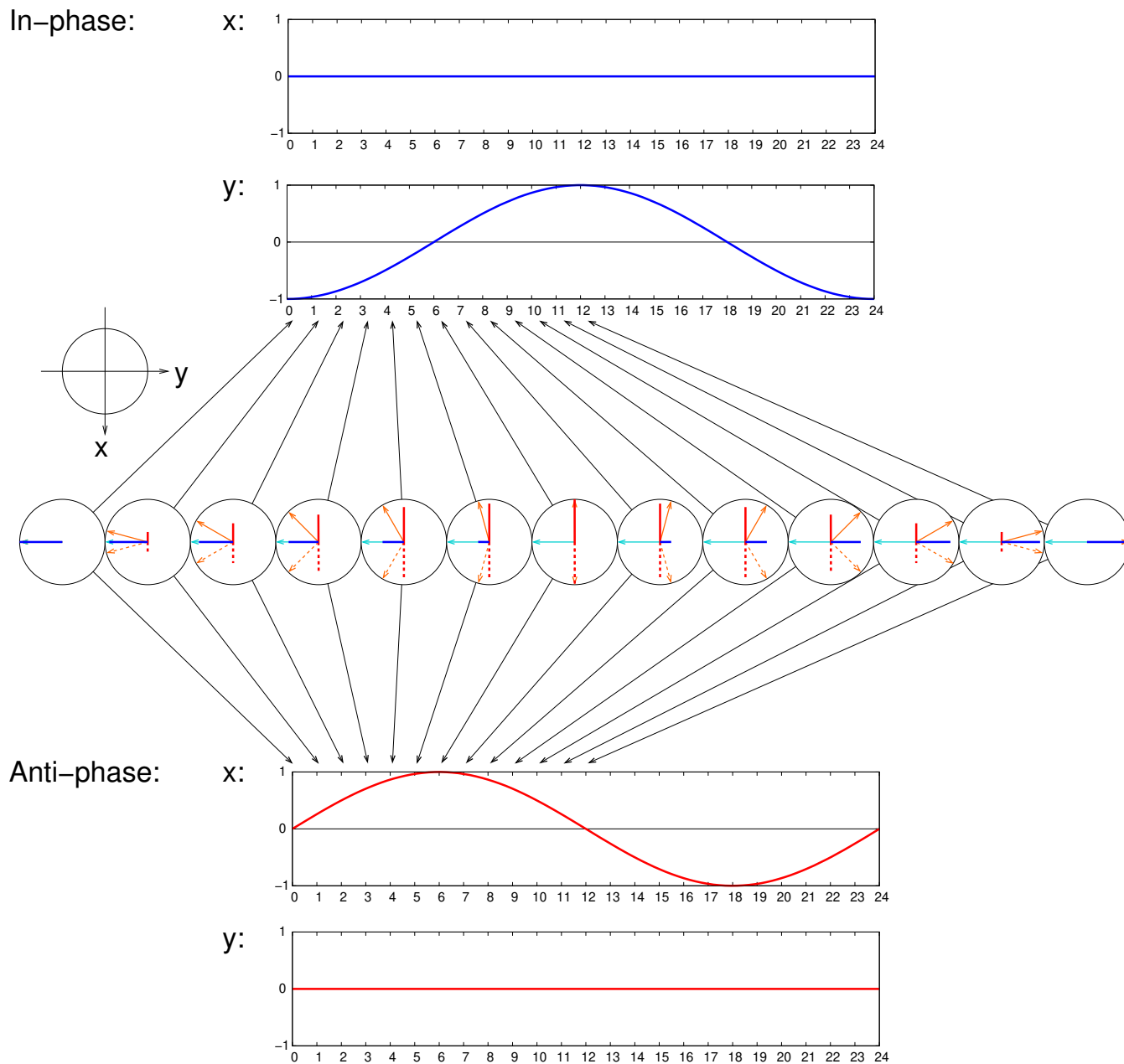
Figure 2.5: Coherence evolution due to the J-coupling. Several snapshots of coherence evolving in the xy plane are shown in the circles in the middle. Evolution of the x and y components of the in-phase (red) and anti-phase (blue) coherences are plotted above and below the snapshots, respectively. The in-phase coherence (blue bar) evolves into the anti-phase coherence (red bars). The orientation of the anti-phase coherence is given by the direction of the dashed bar. The direction of the transverse polarization in the absence of the J-coupling is shown as the cyan arrow. The solid and dashed arrows, used in this text to describe evolution of coherences, are shown in orange. The blue and red bars, representing the in-phase and anti-phase coherences, are projections of the orange arrows to the directions parallel and perpendicular to the cyan arrow.

Figure 2.6: Coherence evolution due to the chemical shift and J-coupling. Several snapshots of coherence evolving in the xy plane are shown in the circles in the middle. Evolution of the x and y components of the in-phase (red) and anti-phase (blue) coherences are plotted above and below the snapshots, respectively. The in-phase coherence (blue bar) evolves into the anti-phase coherence (red bars). The orientation of the anti-phase coherence is given by the direction of the dashed bar. The direction of the transverse polarization in the absence of the J-coupling is shown as the cyan arrow. The solid and dashed arrows, used in this text to describe evolution of coherences, are shown in orange. The blue and red bars, representing the in-phase and anti-phase coherences, are projections of the orange arrows to the directions parallel and perpendicular to the cyan arrow.

Figure 2.7: The basic principle of Fourier transformation presented for experimental data (red) and five testing functions (blue). Experimental data multiplied by the testing functions are displayed as magenta dots, sums (integrals) of the products as magenta lines. The sums are plotted in the right diagram and connected with the green lines.

his foot gets high comfort mark, perhaps two closest sizes get some low mark, and the other sizes are ranked as zero comfort. This is roughly the same procedure as used by computers converting FID to a spectrum.

The procedure described in the previous paragraph closely resembles *Fourier transformation*. Fourier transformation does not compare footprints but sine (or cosine) curves (Figure 2.7). Instead of the board with various footprints, Fourier transformation works with a set of testing sine (or cosine) functions of gradually increasing frequency. Each trial represents calculating product of the tested curve (experimental data points shown in red in Figure 2.7) with one of the testing curve (blue curves in Figure 2.7). In case of different frequencies, the oscillations are uncorrelated and the products at individual points (shown in magenta in Figure 2.7) oscillate around zero. The total product (sum over all points) is equal or very close to zero. On the other hand, if the frequency of the tested curve matches the frequency of the testing curve, the oscillations coincid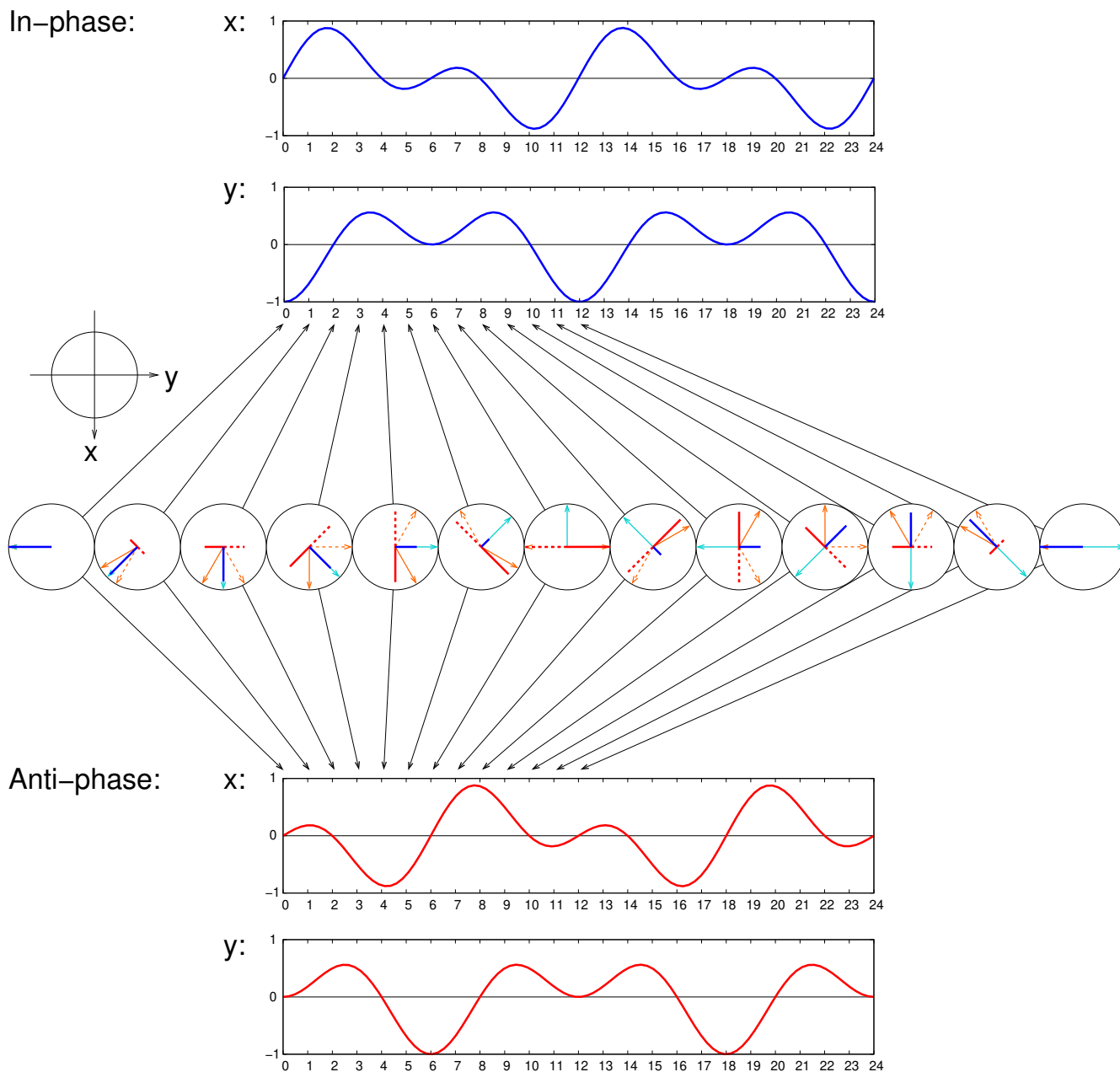e and we obtain some positive number as the product at each point (with the exception of points where both curves pass zero). The total product is a large number. Then we plot the total product as a function of frequency of the testing curve (green plot in Figure 2.7). The obtained plot has the familiar shape of a resonance curve with a peak at the frequency that matched the frequency of the testing curve. We obtained a *spectrum*.

The really attractive feature of Fourier transformation is its *additivity*. Two or more cosine curves oscillating at different frequencies just show two or more peaks in the spectrum. Figure 2.8 documents that the additivity allows us to convert a signal that is very difficult to interpret (three interfering cosine curves in the left plot) to a spectrum clearly showing presence of three frequencies and allowing us to read their values with a good accuracy (maxima of three peaks in the right plot). The width of each peak is given by the damping rate – the faster a cosine curve decays, the broader the resonance peak is.

Interactions described in Sections 2.2–2.4 affect the shape of the spectrum in a clear manner, as listed below and depicted in Table 2.2.

- *Dipole-dipole interactions* make the peak broader (contribute to relaxation) but do not shift the average frequency (peak maximum).

- *Chemical shift* shifts the average frequency (peak maximum) and its dependence on molecular orientation makes

Figure 2.8: Signal (left) and frequency spectrum (right) with three precession frequencies.

the peak broader (contributes to relaxation). The size of the shift is given by the electron distribution in the molecule and is linearly proportional to B_0 (because the effect is shielding B_0). Therefore it is presented in relative units (ppm). In principle, the chemical shift should be equal to $(\omega_0 + \gamma B_0)/(-\gamma B_0)$. In practice, it is reported relative to a reference signal from a standard compound $(\omega_0 - \omega_{0,\text{ref}})/\omega_{0,\text{ref}}$.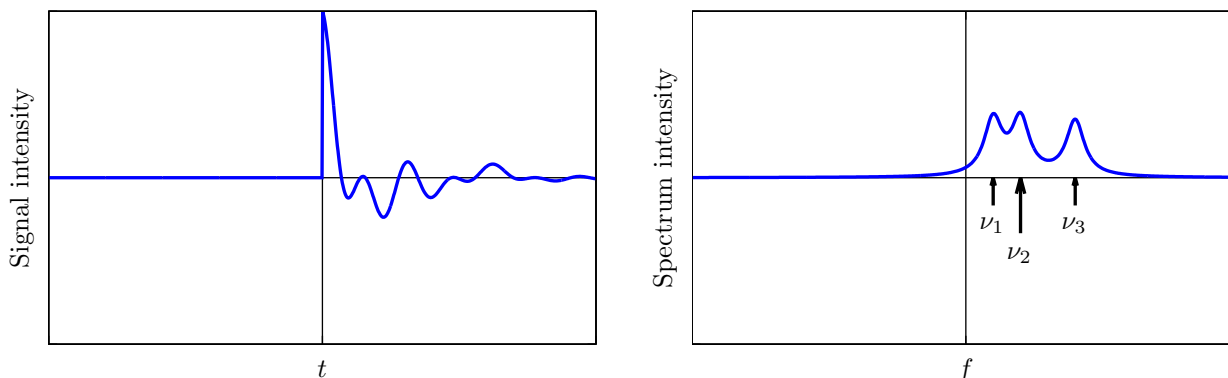 The standards used in biochemistry are sodium 3-(trimethylsilyl)propane-1-sulfonate $(^{13}\text{C}^1\text{H}_3)_3\text{SiCH}_2\text{CH}_2\text{CH}_2\text{SO}_3\text{Na}^+$, liquid ammonia $^{15}\text{NH}_3$, and 85% phosphoric acid $\text{H}_3{}^{31}\text{PO}_4$. Chemical shift is the value reported in the literature as a property of the given compound. It is given by the molecular structure, is influenced by chemical and physical conditions (temperature, ionic strength, pH) but does not depend on the experimental setup (on B_0 or frequency of radio waves used in the experiment). As $-\gamma B_0$ is negative for nuclei with positive γ, peaks of the most shielded nuclei (with low values of the chemical shift and positive Ω) appear in the right-hand side of the spectrum, i.e. the Ω values increase from left to right, and the chemical shift values increase from right to left (Figure 2.9). As the spectrometers do not distinguish sign of the frequency, the chemical shift values *also increase from right to left* in spectra of nuclei with negative γ, and Ω values increase from right to left, which is, strictly speaking, inconsistent with the general convention used in physics.

- *J-coupling* splits the peak to a doublet[3] but does not contribute to broadening (does not change as the molecule tumbles[4]) The appearance of additional frequency in the spectrum (observing two peaks instead of one) is a direct consequence of the oscillation[5] between "visible" in-phase coherence and "invisible" anti-phase coherence, presented in Figures 2.4 and 2.6. Frequencies of individual peaks of the doublets are the same as rotation frequencies of the solid and dashed arrows introduced in Section 2.5 (Figure 2.9). If one nucleus is coupled to more nuclear magnetic moments, more complex *multiplets* appear in the spectra.[6] The frequency differences (splittings) are given by the electron distribution in the molecule and do not change with B_0 (*J*-coupling does not depend on the external field). Therefore they are presented in units of frequency (Hz).

In summary, frequencies observed in a signal converted to a spectrum by Fourier transformation are given by a combination of three effects: the external magnetic field, chemical shift, and *J*-coupling. The signs of the frequencies (senses of rotation of coherences described by the solid and dashed arrows introduced in Section 2.5) depend on signs

---
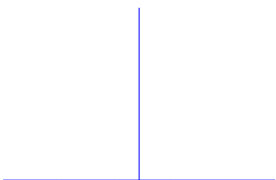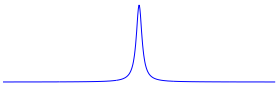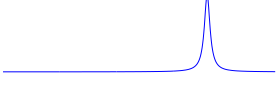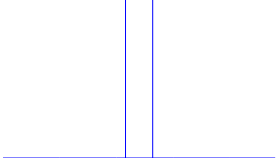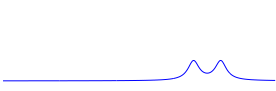
[3]This is true for Dirac-like nuclei with sufficiently different precession frequencies.

[4]*J*-coupling does not contribute to peak broadening via molecular tumbling, but it may cause relaxation (broaden the peaks) if the structure of the molecule and/or distribution of magnetic moments changes during the experiment.

[5]The mathematical relation between sine/cosine oscillations and the number of peaks in the spectrum obtained by Fourier transformation is discussed in more detail in Section 4.6.

[6]E.g., spectrum of three mutually coupled nuclei consists of three quartets (doublets of doublets), i.e., of twelve peaks. However, the central peaks may overlap if the interactions with both neighbors are of similar size, and the quartet may look like a triplet with doubled intensity of the middle peak.

Table 2.2: Effects of interactions of magnetic moments with magnetic fields in the molecule on the shape of a spectrum. The external magnetic field is assumed to be ideally homogeneous, the molecular tumbling isotropic, the data acquisition is supposed to be continuous and infinitely long.

Interaction	mechanism	effect		spectrum
		coherent	relaxation	
none (bare nucleus)				
dipolar coupling	direct dipole-dipole interaction through space	no	yes	
chemical shift	shielding by electrons (orbital magnetic moment)	yes	yes	
J-coupling	mediated by electrons in covalent bonds	yes	no	
all	combination of all	yes	yes	

of γ and Ω. Figure 2.9 shows the evolution for all combinations of positive and negative γ and Ω and also summarizes (sometimes confusing) conventions used in NMR spectroscopy.
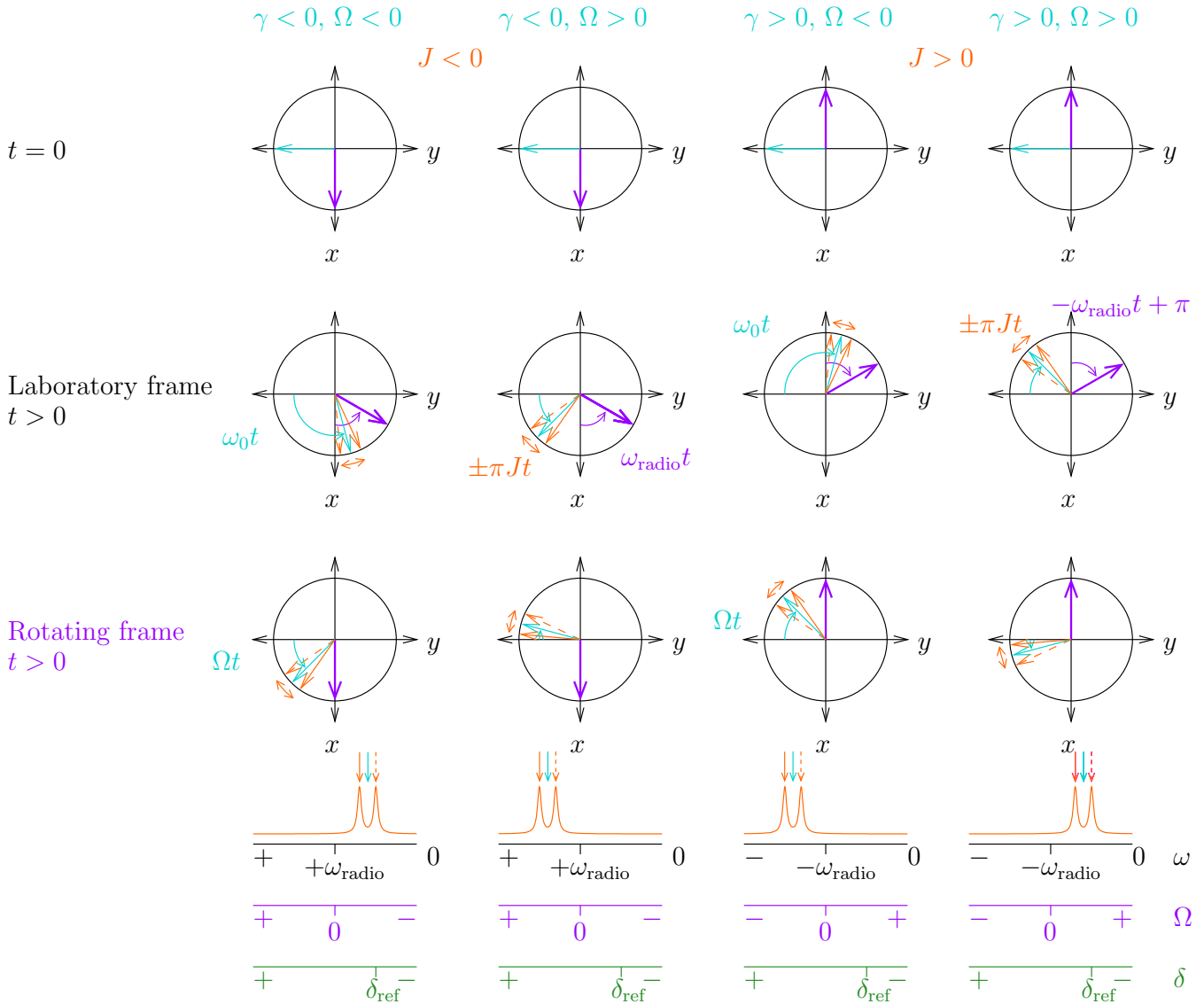
Figure 2.9: Conventions used in NMR spectroscopy when describing the effect of radio-wave pulses and the evolution of coherences, and when presenting the spectra. Evolution of coherences symbolized by the solid and dashed orange arrows (introduced in Table 2.1) for nuclei with different signs of γ and Ω is shown in the circles. The first row of circles represents the polarization immediately after applying a very short $90°$ radio-wave pulse (at $t = 0$). The second and third row show directions of coherences and of $\vec{B}_1$ at time t the laboratory and rotating coordinate frame, respectively. The direction of the transverse polarization in the absence of the J-coupling is shown as the cyan arrow. The z axis is defined by the direction of $\vec{B}_0$. The oscillating radio-wave magnetic field is decomposed into two counter-rotating components. The purple arrows indicate the direction of the resonant component $\vec{B}_1$ ($+\vec{B}_{\text{radio}}$ for $\gamma < 0$ and $-\vec{B}_{\text{radio}}$ for $\gamma > 0$). The absolute value of $\vec{B}_0$ is supposed to be much greater that the amplitude of $\vec{B}_1$. Note the convention to add a phase of $180°$ to the direction of $\vec{B}_1$ (i.e., to revert the direction) for $\gamma > 0$. The resulting spectra (after Fourier transformation and applying the necessary phase correction, which is $90°$ in the presented cases), are plotted below the circles. Arrows above the spectra assign individual peaks to the solid and dashed arrows. Note the convention to plot the frequency axis from the right to the left for nuclei with $\gamma < 0$.

Lecture 3
Correlated spectroscopy

3.1 Spin alchemy

Section 1.11 introduced a very valuable servant, radio waves. The oscillating field of a short pulse of the radio wave helped us to disturb equilibrium distribution of nuclear magnetic moments and created an observable signal. The magic power of the radio-wave pulses is much greater than simply exciting magnetic moments from their equilibrium. Combinations of exactly spaced pulses allow us to create, destroy, and convert polarizations of nuclei with an ease that overcomes all dreams of alchemists. This is why the modern NMR methodology is sometimes described as *spin alchemy*. The sequences of radio-wave pulses and delays, called simply *pulse sequences* in the NMR literature, may be very complex. However, they are built from relatively simple building blocks or modules. Knowledge of the basic modules allow us to understand, analyze, and design very sophisticated pulse sequences. In this lecture, we learn the most important modules.

Another goal of this lecture is to introduce the idea of *correlated spectroscopy*. Biomacromolecules like proteins or nucleic acid fragments consists of many atoms. Atomic-resolution description of their structure, dynamics, and interactions cannot be derived simply from frequencies identified in a spectrum obtained from a signal recorded as described in Sections 2.6–2.7. The biomolecular applications of NMR are based on our ability to correlate the frequencies observed in the spectra.

3.2 Excitation

We start with the very fundamental *excitation module*. It is very simple, consisting of a single 90° pulse. We know that a single 90° pulse applied to a sample with the equilibrium distribution of magnetic moments turns the magnetization vector from the vertical orientation to the xy plane. The obtained horizontally polarized sample is not at the equilibrium, it is *excited*. Coherence is created and rotation of the horizontal (transverse) magnetization vector at the precession frequency of the observed nucleus can be detected.

The excitation pulse also plays an important role in the formal description of polarization and magnetization. The magnetic induction $\vec{B}_1$ of the radio wave defines the x axis of our rotating coordinate system, as $\vec{B}_0$ defines the z axis (of rotating and laboratory coordinate frames). However, the orientation of the $\vec{B}_1$ axis is somewhat arbitrary because the phase of the radio wave is not well defined (it depends on length of the cables, distance of the transmitter antenna from the sample, various instrumental time delays etc.). Unfortunately, the typical convention (see Figure 2.9) is a bit confusing. We assume that the phase is 180° for nuclei with $\gamma > 0$ (e.g. ^{1}H or ^{13}C) and 0° for nuclei with $\gamma < 0$ (e.g. ^{15}N). Then, the nutation frequency is $\vec{\omega}_1 = +\gamma\vec{B}_1 = +|\gamma|\vec{B}_1$ (opposite convention to the precession frequency!) for nuclei with $\gamma > 0$ and $\vec{\omega}_1 = -\gamma\vec{B}_1 = +|\gamma|\vec{B}_1$ (the same convention as the precession frequency) for nuclei with $\gamma < 0$. A practical consequence is that an ideal excitation pulse generates a pure $-y$ component of magnetization for nuclei with any sign of γ.
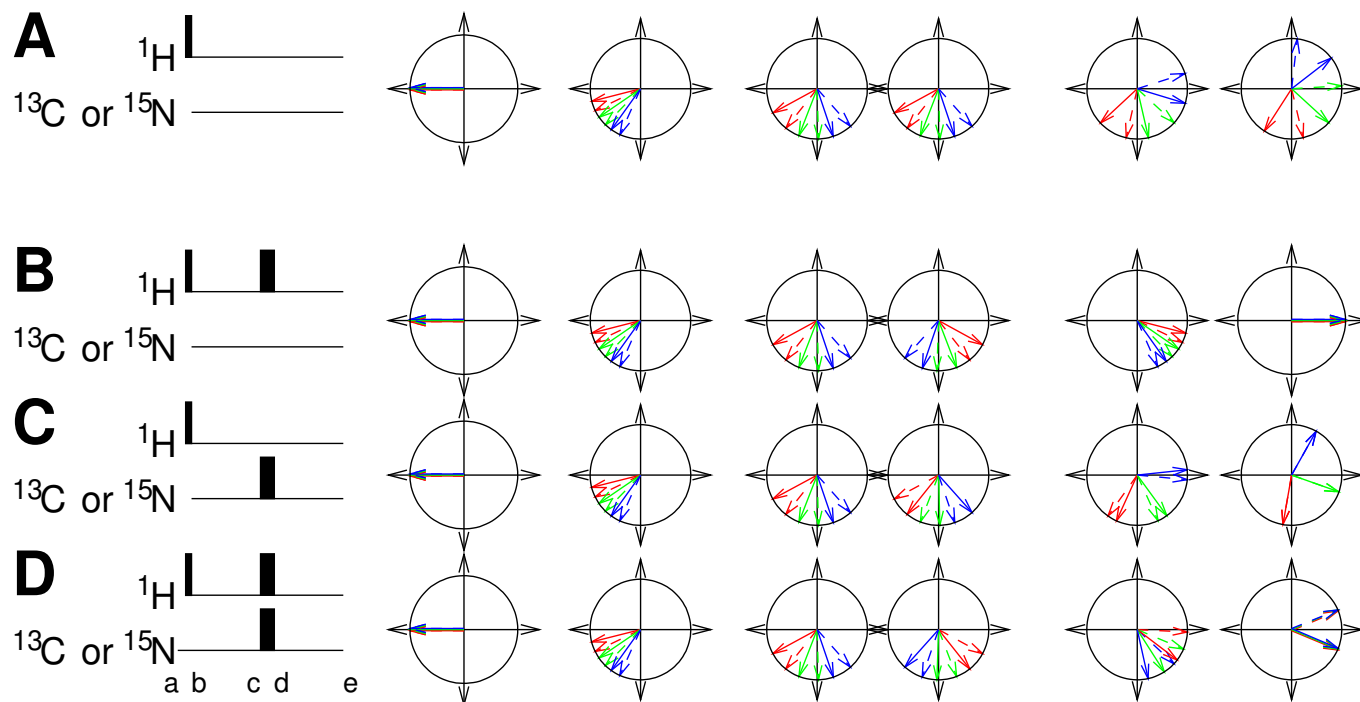
Figure 3.1: Left, schematic drawings of the pulse sequences of echoes. 90° and 180° radio-wave pulses are depicted as narrow and wide bars, respectively. Letters below the pulse sequences refer to the columns in the right section of the figure. Right, analysis of spin echoes for ^{1}H and ^{13}C (^{15}N) in an isolated –CH– (or –NH–) group. In individual rows, evolution of magnetization vectors in the xy plane is shown for three protons (distinguished by colors) with slightly different precession frequency due to the different chemical shifts δ. The protons are bonded to ^{13}C. The magnetic moment distributions are represented by solid and dashed arrows using the convention introduced in Table 2.1. The first column shows magnetization vectors at the beginning of the echo (after the initial 90° pulse at the proton frequency, letter b below the pulse sequences), the second column shows magnetization vectors in the middle of the first delay τ, the third and fourth columns, respectively, show magnetization immediately before and after the 180° pulse(s) in the middle of the echo (letters c and d below the pulse sequences, respectively), the fifths column shows magnetization vectors in the middle of the second delay τ, the sixth column shows magnetization vectors at the end of the echo (letter e below the pulse sequences). Row A corresponds to an experiment when no 180° pulse is applied, row B corresponds to the echo with the 180° pulse applied at the proton frequency, row C corresponds to the echo with the 180° pulse applied at the ^{13}C frequency, and row D corresponds to the echo with the 180° pulses applied at both frequencies. The x-axis points down, the y-axis points to the right.

3.3 Echoes

Now we explore symmetric modules called *echoes*, built of two delays of the same length τ. The delays may be separated by 180° pulses acting on individual nuclei. Schematic drawings of the modules are presented in the left section of Figure 3.1. In a model compound containing coupled ^{1}H and ^{13}C nuclei, three combinations of 180° pulses are possible: a pulse resonating with the ^{1}H frequency (Figure 3.1B), a pulse resonating with the ^{13}C frequency (Figure 3.1C), and both such pulses applied at the same time (Figure 3.1D). Let us analyze what effects these three modules have when applied just after the excitation pulse acting on ^{1}H. A graphical analysis is shown in the right section of Figure 3.1. The first row (Figure 3.1A) shows a combined effect of chemical shift and J coupling in the absence of any 180° pulse. It was discussed already in Section 2.5. Figure 3.1A extends the previous discussion to a molecule containing three ^{1}H–^{13}C groups. Analysis during modules including one or two 180° pulses is presented in the following sections.

3.4 Refocusing echo

.

Let us start with the echo involving a 180° pulse is applied to the excited nucleus (Figure 3.1B). We know that the

magnetic moment distribution polarized in the $-y$ direction rotates with the frequency offset Ω (the difference between the frequency of the radio waves and the precession frequency modulated by the chemical shift), and is further split into two components. One (represented by the dashed arrow) is accelerated and the other one (represented by the solid arrow) is slowed down by the effect of ^{13}C. The third column of circles in Figure 3.1 shows the directions of the arrows right before applying the 180° pulse. The slower arrow rotated by angle of $(\Omega - \pi J)\tau$, while the faster arrow rotated by angle of $(\Omega + \pi J)\tau$. The 180° pulse flips the arrows by rotation about the x axis. The flipped arrows form a mirror image to the original ones with respect to the xz plane. The dashed arrow is less advanced after flipping. But it still rotates in the same direction with a higher frequency. In a similar way, the solid arrow is more advanced but rotates with a lower frequency. The angles between arrows in the third column and the original direction $-y$ are the same as the angles between arrows in the fourth column and the direction $+y$. Therefore, solid and dashed arrows meet in the original y direction at the end of the echo (the sixth column). The dashed arrow had a little longer way to go, but being faster it caught on the slower solid arrow exactly at the end of the module. Note that both arrows pass the y axis in that moment regardless of the actual Ω value. This is why the module is called an "echo". Can you see the magic? Effects of both chemical shift and scalar coupling are canceled at the end of the echo. The 180° pulse now acts as a *refocusing pulse*: effects of the chemical shift and scalar coupling are refocused at the end of the echo.

3.5 Decoupling echo

What if the 180° pulse is applied to the other nucleus, which was not excited (^{13}C in our example)? Again, we know the evolution up to the pulse. What happens if we invert the distribution of ^{13}C magnetic moments by the 180° pulse right in the middle (Figure 3.1C)? The faster fraction of proton magnetic moments that was accelerated by ^{13}C magnetic moments pointing down is now slowed down because the protons are coupled to ^{13}C with magnetic moments pointing up, and vice versa. In our graphical representation, solid arrows become dashed and the dashed arrows become solid. The originally slower fraction of proton magnetic moments would rotate faster after the 180° pulse and would catch the originally accelerated fraction just at the end of the module (Figure 3.1C). Now we see another magic. The nuclear magnetic moments interact and there is no way how we can turn off their interaction. But we can play a trick with the magnetic moments and prepare the same distribution as we would have obtained if no coupling were present. This is why the described inversion 180° pulse has been given the name *decoupling pulse*.

3.6 Simultaneous echo

We know how to refocus both chemical shift and scalar coupling and we know how to refocus evolution of the coupling only. How can we refocus just the chemical shift evolution? The answer is the echo with two 180° pulses, each hitting one of the nuclei (Figure 3.1D). The proton pulse flips arrows representing proton coherences and the ^{13}C pulse inverts longitudinal polarizations of ^{13}C nuclei (solid arrows change to dashed ones and vice versa). As a result, the average direction of dashed and solid arrows is refocused at the end of the echo but the difference due to the coupling is preserved (the handicapped arrows were made slower by the inversion of longitudinal polarization of ^{13}C). The magic is here again. The same scalar coupling evolution is observed as it would be at the and of a delay long 2τ with no pulses applied and no chemical shift evolution present.

3.7 Polarization transfer

The three described echoes give us what looks like a supernatural power. We turn on and off physical interaction as we want, at least seemingly. Some applications are obvious, like measurement of the chemical shift without complications introduced by the coupling. I would like to show you another application of great importance. It is a real alchemy, we are going to change protons to carbon nuclei, of course at the level of magnetic properties.

The pulse sequence module presented in Figure 3.2A is an extension of the third echo (Figure 3.1D). The trick requires that the dashed and solid arrows evolve to exactly opposite directions. In other words, that the distribution of the magnetic moments is the *anti-phase coherence* (see the second row of Table 2.1). It can be achieved by choosing the total length of echo equal to $1/(2J)$ which means $\tau = 1/(4J)$. Then, the solid and dashed arrows in the sixth circle
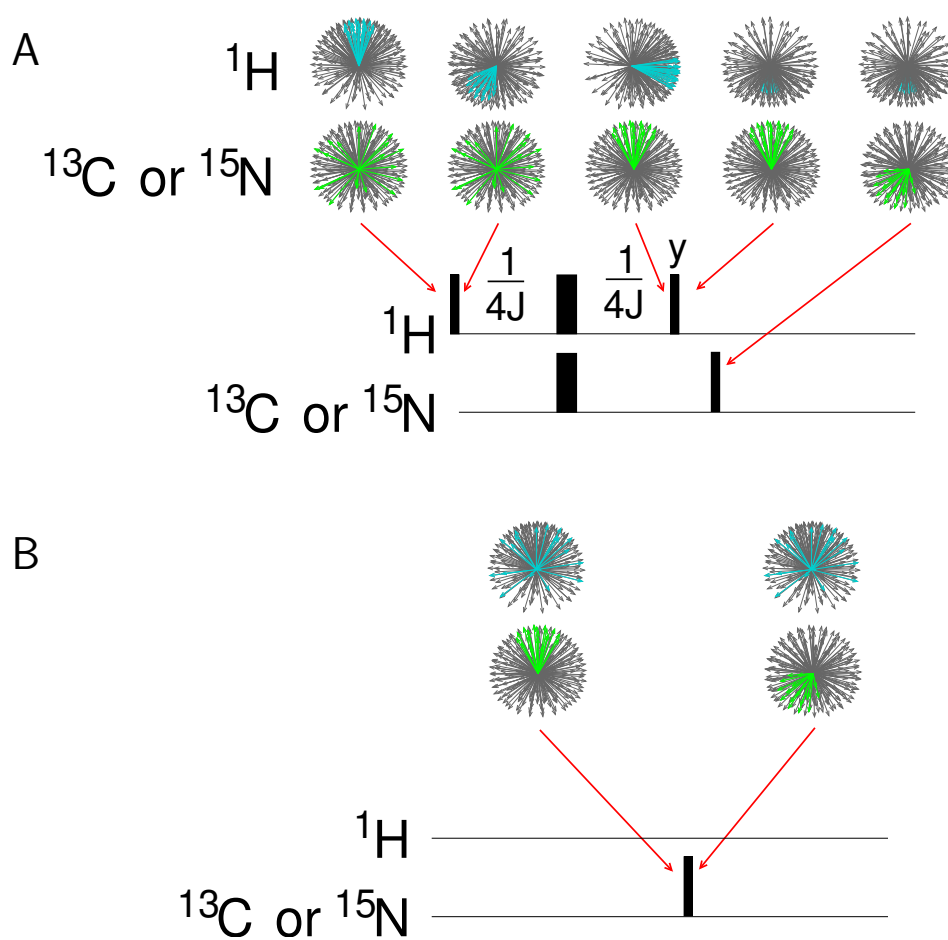
Figure 3.2: INEPT pulse sequence applied to ^{1}H and ^{13}C or ^{15}N (A) and direct excitation of ^{13}C or ^{15}N (B). The narrow and wide rectangles represent 90° and 180° radio wave pulses, respectively. The label y above the pulse indicates irradiation by a radio wave with the phase shifted by 90° relative to the first pulse in the sequence. Distributions of magnetic moments are shown schematically above the pulse sequences for time instants labeled by the red arrows. The distributions are shown in a coordinate frame with the z axis pointing up and the x axis pointing to the right.

of Figure 3.1D evolve to the $+x$ and $-x$ directions, respectively. In the moment when the chemical shift is refocused but the J-coupling is showing its full glory, two 90° pulses are applied, one at the ^{1}H frequency and the other one at the ^{13}C frequency. As the solid and dashed arrows, describing distribution of proton magnetic moments, are aligned along $\pm x$, the magnetic field of the radio waves cannot be applied in the x direction of the rotating coordinate frame. The desired radio-wave magnetic field oriented in the y direction can be obtained by shifting the phase of the radio wave by 90° from that of the excitation pulse. In the NMR literature, pulse of a radio wave with 90° phase shift is called simply a y-pulse. Phase of the ^{13}C pulse is arbitrary. The proton 90° pulse rotates the distribution of proton magnetic moments so that the cyan arrows in the second row of Table 2.1 are aligned along the $\pm z$ direction. The ^{13}C 90° pulse rotates the distribution of ^{13}C magnetic moments. This of course creates transverse polarization of the ^{13}C magnetic moments. But we are now interested in a different effect.

The fractions of the ^{13}C magnetic moments represented by the green arrows in the second row of Table 2.1 rotated by the ^{13}C 90° pulse become distributed around the $+y$ and $-y$ direction. Such distribution is an "invisible" ^{13}C anti-phase coherence. It immediately starts to rotate about $\vec{B}_0$ with the ^{13}C precession frequency (modulated by the ^{13}C chemical shift). As ^{13}C nuclei are coupled to ^{1}H, the two green distributions *also* evolve in a similar manner as described in Section 2.5 for the cyan distribution of proton magnetic moments. The green and cyan distributions are correlated. Therefore, the green cluster coupled to the cyan cluster that happened to be pointing down evolves faster than the other green cluster. As a consequence, the green clusters with originally opposite populations (anti-phase coherence) starts to redistribute and after $t = 1/(2J)$ they merge into a distribution polarized in a single direction. The ^{13}C in-phase coherence is created. In such a way, the distribution of ^{13}C magnetic moments oscillates between "invisible" anti-phase and "visible" in-phase coherences, in addition to the overall rotation with the ^{13}C frequency offset. This process resembles the evolution started from the proton in-phase coherence described in Section 2.5, with the following differences.

- The overall rotation is modulated by the chemical shift of ^{13}C (not of ^{1}H).

- The ^{13}C in-phase coherence oscillates as a sine curve because the evolution started from the anti-phase coherence (i.e., from a zero contribution of the in-phase coherence, as the sine curve starts from the zero value). In contrast, the ^{1}H in-phase coherence oscillated as a cosine curve after the excitation of ^{1}H because the evolution started from the in-phase coherence (i.e., from a maximum contribution of the in-phase coherence, as the cosine curve starts from the maximum).

- The transverse polarization of ^{13}C magnetic moments correlated with proton magnetic moments during the echo depends on the equilibrium distribution of *proton* magnetic moments because proton was excited. The original equilibrium distribution is approximately proportional to the value of γ which is four times higher for ^{1}H than for ^{13}C. Therefore, the size of the measured signal is four times higher that the signal measured in an experiment with a direct excitation of ^{13}C (a ^{13}C 90° pulse immediately followed by detection, Figure 3.2B). It gave the module a name *INEPT* (insensitive nuclei enhanced by polarization transfer). The sensitivity improvement is even bigger (tenfold) in the case of ^{15}N.

The original purpose of the described trick was to improve sensitivity of carbon measurements: as discussed above, the dependence on the magnetogyric ratio results in a four-fold increase of the signal.[1] An application much more important in biomolecular NMR is the topic of the next section.

3.8 HSQC

Let us build the following pulse sequence from the modules that we learned: Excitation of ^{1}H, INEPT to ^{13}C, decoupling echo, INEPT to ^{1}H, and acquisition (Figure 3.3). During the first INEPT, the proton polarization is converted to the anti-phase ^{13}C coherence, the second INEPT converts the anti-phase ^{13}C coherence back to the in-phase proton coherence.

What looks like a useless exercise at the first glance, is actually a basic form of a very important pulse sequence. One advantage of the pulse sequence is that protons are excited at the beginning and protons are directly detected

---

[1] In reality, the ^{13}C 90° pulse also generates coherence corresponding to the direct excitation of ^{13}C. However, this coherence can be filtered out of the signal by phase cycling, described in Section 4.9.
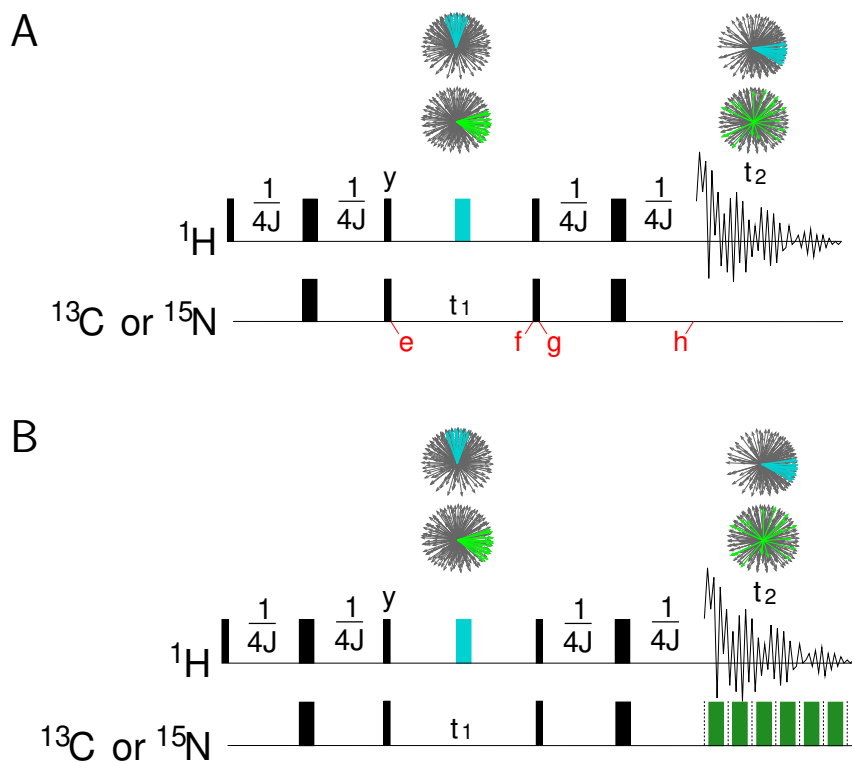
Figure 3.3: HSQC experiment. A, basic HSQC pulse sequence. B, general idea of the decoupling in the direct dimension. The decoupling pulses applied to proton and to ^{13}C (or ^{15}N) are shown in cyan and green, respectively. Other symbols are used as explained in Figure 3.2.
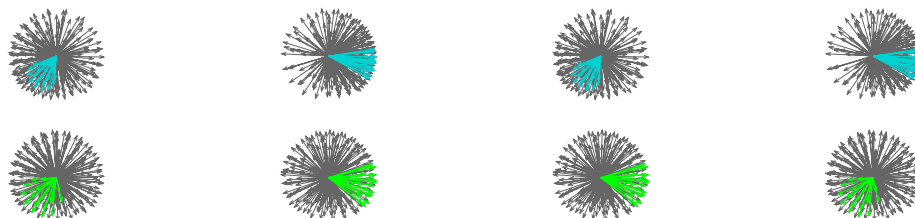
Figure 3.4: Schematic representation of multiple quantum coherences. Correlations of magnetic moment distributions are depicted by color coding sets of magnetic moments of coupled ^{1}H (cyan) and ^{13}C or ^{1N}N (green) nuclei in the same molecules. In the absence of radio waves, the magnetic moment distributions oscillates between individual multiple quantum coherences with the frequency offsets $\Omega_{\mathrm{H}} + \Omega_{\mathrm{C}}$ and $\Omega_{\mathrm{H}} - \Omega_{\mathrm{C}}$ (or $\Omega_{\mathrm{H}} + \Omega_{\mathrm{N}}$ and $\Omega_{\mathrm{H}} - \Omega_{\mathrm{N}}$)

in the end. We discussed in Section 3.7 that the signal depends on the original polarization of the excited nucleus, which is proportional to the magnetogyric ratio γ, and that, as a consequence, exciting protons instead of ^{13}C yields four-fold improvement in the sensitivity. The signal amplitude is also proportional to the absolute value of the detected magnetic moment and to the frequency of the rotation.[2] As both parameters are approximately proportional to γ, the signal is proportional to γ^3. The noise is proportional $\sqrt{\gamma}$,[3] therefore the signal-to-noise ratio, which is the true measure of sensitivity, is proportional to $\gamma^{3/2}$. The resulting theoretical improvement in sensitivity, compared to the direct detection, is 32-fold for ^{13}C and 315-fold for ^{15}N.

The sensitivity enhancement is already impressive, but the HSQC pulse sequence offers more. The described pulse sequence allows us to measure both ^{1}H frequency and ^{13}C (or ^{15}N) frequency in a single experiment and in a correlated manner. Let us now try to understand how is it possible.

We emphasized in Section 3.7 that it is important to apply the radio waves with a phase corresponding to $\vec{B}_1$ perpendicular to the direction of the solid and dashed arrows describing anti-phase polarization. This is why we had to apply the second proton 90° pulse with a 90° phase shift (as a "y" pulse). Therefore, the effect of the second ^{13}C 90° pulse also depends on the length of the delay between the ^{13}C 90° pulses. If we apply the second pulse immediately after the first one, all ^{13}C anti-phase coherence is converted back to the proton in-phase coherence. If we wait, the arrows symbolizing the distribution of magnetic moments rotates start to rotate about $\vec{B}_0$. The rate of the rotation is the ^{13}C frequency offset, given by the ^{13}C chemical shift. It is useful to decompose the solid and dashed arrows into two directions in the xy plane, one parallel to the ^{13}C $\vec{B}_1$ field and the other perpendicular. Our NMR experiment relies on two facts: (i) only the perpendicular component is affected by the second ^{13}C pulse, applied in the x direction, and (ii) how much of the arrow is in the perpendicular direction depends on the length of the delay between ^{13}C 90° pulses (t_1 in Figure 3.3). Let us know explain both facts in more detail.

- *Only perpendicular component, affected by the second ^{13}C pulse, yields the signal.* The second ^{13}C pulse rotates the perpendicular components of the arrows to the $\pm z$ direction and the parallel components stay in the xy plane. The simultaneous proton pulse creates proton anti-phase coherence from the perpendicular components, which evolves to the "visible" in-phase coherence in a reversed process to what was described in Section 3.7. The magnetic moment distribution corresponding to the parallel components of the arrows are converted to *multiple quantum coherences*, correlated distributions of ^{1}H and ^{13}C magnetic moments (Figure 3.4) that rotate in the xy plane and do not contribute to the signal (are not converted to the observable proton polarization in the given experiment). The fact that only *single-quantum* (not multiple quantum) coherences contribute to the signal is encoded in the name of the experiment: Heteronuclear Single-Quantum Coherence spectroscopy (HSQC).

- *The signal depends on the delay t_1 in Figure 3.3.* The INEPT resulted in arrows perpendicular to $\vec{B}_1$ of the first ^{13}C pulse (direction $\pm x$). The perpendicular component therefore evolves following a cosine function with the argument $\Omega_C t_1$, where Ω_C is the carbon frequency offset and t_1 is the length of the delay between the ^{13}C pulses. As a result, the amount of proton anti-phase coherence converted to proton polarization is modulated by cosine of the ^{13}C frequency offset. This amount represents the *amplitude* of the signal, the length of the transverse magnetization vector that rotates during the measurement and generates electromotive force in the detector.

The critical trick is to repeat the measurement many times while incrementing the delay t_1 in the middle. We then obtain a whole array of 1D spectra, of cosine curves with *frequencies modulated by the proton chemical shift*. The spectra stored in a digital form, not as a continuous function, but as a list of values of voltage measured at discrete time points labeled t_2. The spectra have the same frequency (proton frequency offset Ω_H), but different amplitude. As t_1 grows, the argument in $\cos(\Omega_C t_1)$ also increases and therefore the amplitude is *modulated* by $\cos(\Omega_C t_1)$. The array of the spectra can be stored as two *two-dimensional* digital data, a table of signal intensities measured for all combination of t_1 and t_2 values.

To sum up, we obtain a *two-dimensional signal*, which is *frequency modulated by the proton chemical shift in t_2* and *amplitude modulated* by the ^{13}C chemical shift in t_1. An example is shown in Figure 3.5. The acquired two-dimensional array is then converted to a *two-dimensional spectrum* by applying the Fourier transformation twice, once with t_2 as the time variable, and once with t_1 as the time variable.

---

[2]The signal is an electromotive force (voltage) induced by an oscillating flux of the magnetic field (generated by the rotating transverse magnetization) through the detector loop. The electromotive force is proportional to the change of the flux in time. If Φ oscillates as
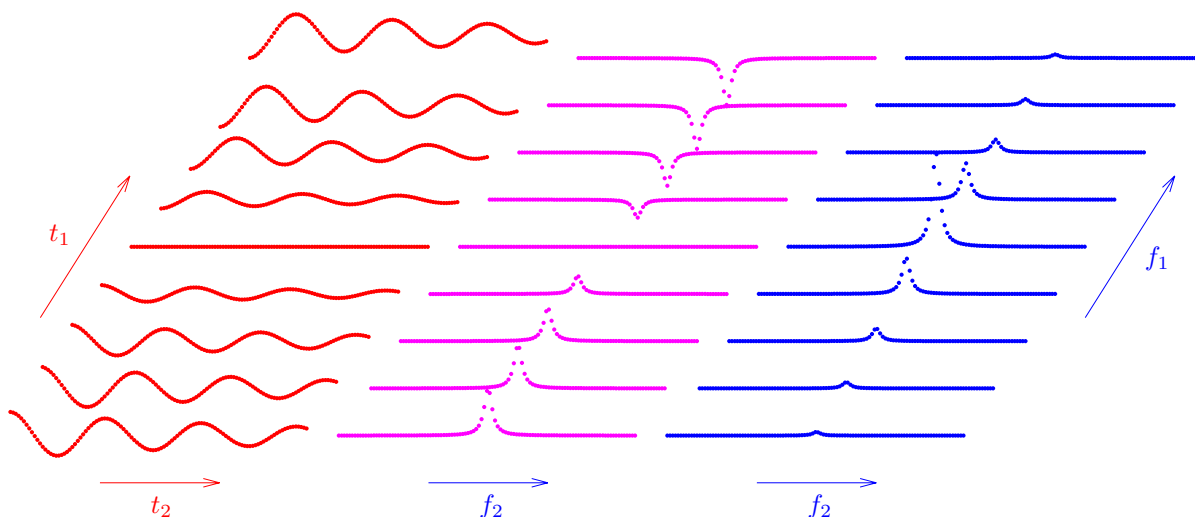
Figure 3.5: Principle of 2D spectroscopy. The recorded signal is shown in red, the result of the first Fourier transformation in magenta, and the final spectrum, obtained by two Fourier transformations, in blue.

The obtained information is quite different from what we learn from separate one-dimensional ^{1}H and ^{13}C spectra. The ^{13}C frequency can be measured only because ^{1}H and ^{13}C nuclei are coupled. Therefore, the described experiment works selectively for carbons directly bonded to protons and for protons directly bonded to carbons. But the coupling introduces also some problems because it splits frequencies of both nuclei due to the oscillations between in-phase and anti-phase coherences. The splitting of peaks caused by the J-coupling is an undesired complication in most spectra. It is easy to remove the effect of coupling from the indirect dimension – simply by applying a decoupling echo during the incremented delay (the cyan pulse in Figure 3.3). This trick cannot be played when we directly record the spectrum. We need to remove the coupling effect at each moment during the acquisition, not just at the and of some delay. We need to use a brute force approach. We do not apply just one decoupling echo, we apply *many* little decoupling echoes, each as short as possible. The result is that the coupling is *always* refocused if we ignore tiny evolution during each little echo. Note that we do not apply a separate pulse any more. The sample is now bombarded by a long *train of decoupling pulses* during the whole acquisition (Figure 3.3B). Power of these pulses must be moderate because energy is absorbed by the sample for a long time, and the sample could get overheated.

Unfortunately, during the described series of many 180 ° pulses various imperfections accumulate. Therefore such a train of pulses is never applied in practice. Great effort has been dedicated to designing sequences of relatively weak pulses having the best possible performance. Pulses rotating magnetization by angles different from 180 ° or 90 ° are used and their phases are varied in complicated manners. Decoupling can be optimized either for the width of the range of the affected frequencies or for the highest efficiency. One of the most popular decoupling trains, known as GARP, has been designed with the help of numerical optimization to meet the former requirement, other decoupling trains (e.g. MLEV) provide better efficiency (lower residual scalar coupling) in a somewhat narrower range of frequencies. Obviously, all decoupling methods discussed here require that the decoupled and observed nuclei must differ in the resonance frequency so that they can be manipulated separately.

The area of pulse train applications is not limited to the decoupling. Polarization transfer based on pulse trains will be an important topic of our later discussion (in Section 6.4).

$\Phi(t) = \Phi_0 \sin(\omega t)$, its change is the time derivative $\mathrm{d}\Phi(t)/\mathrm{d}t = \omega\Phi_0 \cos(\omega t)$, where both Φ_0 and ω are proportional to γ.

[3]Square of the noise is proportional to the window of detected frequencies, which depends linearly on γ.

Lecture 4
Technical issues

4.1 Content of the lecture

Up to now, we tried to understand the basic principles of NMR spectroscopy without going into technical details. Anybody who intends to actually *run* an NMR experiment must learn the technical issues at some point. In our course, we are getting to this point right now. This lecture is dedicated to technical details that are critical for optimal performance of NMR experiments. Parameters of basic elements of pulse sequences are discussed in the following sections. The number of parameters that must be controlled and of the technical tricks that are routinely applied to obtain high quality spectra is large, and the time of our lectures is limited. Therefore, only really fundamental technical issues are discussed in the class. Additional technical details are also included in the following text so that an interested reader can gain a deeper insight. Sections discussing such more advanced topics are labeled with the asterisks.

4.2 Delays

Delay is a very easy trick of spin alchemy, it is simply waiting and doing nothing. The nuclei only feel $\vec{B}_0$ modulated by their environment during the waiting periods. Evolution of transverse magnetization during a delay was discussed in Section 2.5 and depicted graphically in Figure 3.1A. The only parameter describing the delay is thus its *length*. In multidimensional experiments, we distinguish *constant delays* and *incremented delays*, introducing amplitude modulation by chemical shift[1] in the indirect dimensions. Length of the incremented delays must be defined very precisely.

The fact that we do not measure time continuously in the indirect dimensions, but only in discrete time increments, and that the number of the increments is limited, has important consequences:[2]

- *Consequence of recording spectra for discrete time increments.* As shown in Figure 4.1A, the same set of discrete data points (blue dots) spaced by the time increment Δt fits equally well the cosine curve with the angular frequency offset Ω_1 and the cosine curve with the angular frequency offset $\Omega_1 + 2\pi/\Delta t$. This documents that angular frequency can be distinguished only within a window of the width of $2\pi/\Delta t$, i.e. in the range from $-\pi/\Delta t$ to $+\pi/\Delta t$. If the frequency is measured in Hz, the window width is $1/\Delta t$, ranging from $-1/(2\Delta t)$ to $+1/(2\Delta t)$.

- *Consequence of limited number of time increments.* As shown in Figure 4.1B, termination of data acquisition before the signal decays to the noise results in artificial wiggles around peaks in the spectrum. The wiggles are suppressed if the acquired signal is multiplied by a function that decays to zero prior to the Fourier transformation. This trick, called *apodization*, is applied almost always in multidimensional spectra.

---

[1] *J*-coupling also modulates the signal if decoupling is not applied.

[2] The same actually applies to the directly detected signal. It is converted to a digital form (i.e., to a discrete series of data points) and the acquisition time is also limited.

A
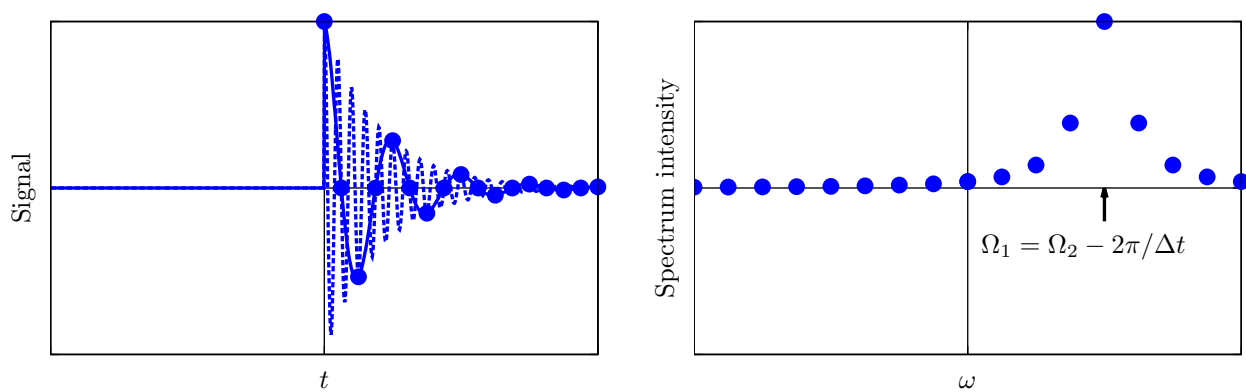
B
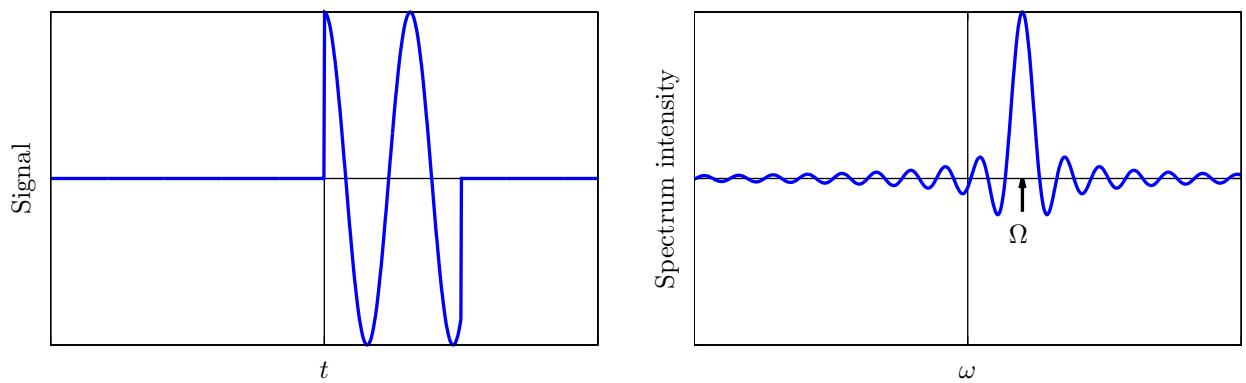
Figure 4.1: Consequences of recording spectra for discrete time increments (A) and of limited number of time increments (B).
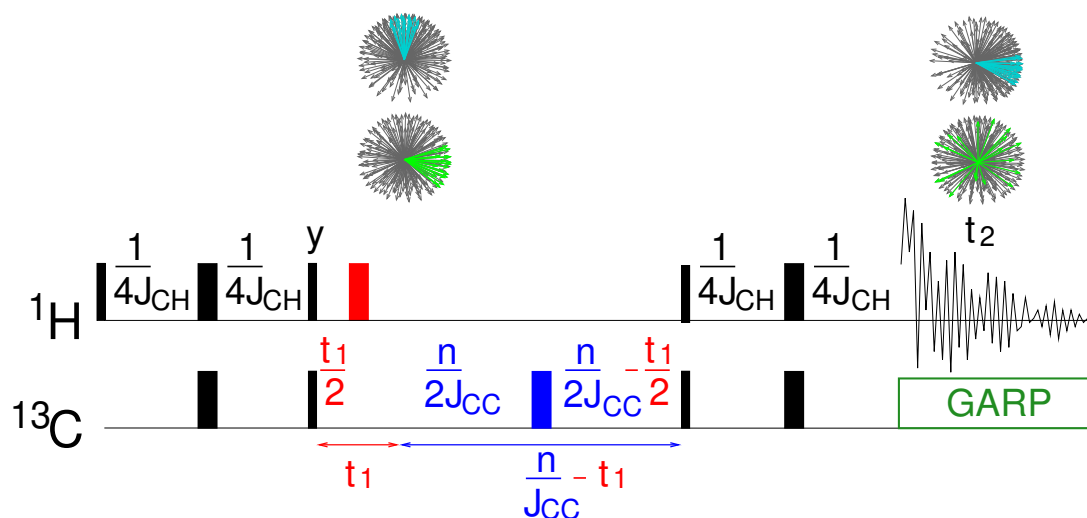
Figure 4.2: ^{1}H,^{13}C HSQC experiment with constant-time J_{CC} evolution in the indirect dimension. The symbols are used as explained in Figure 3.3.

4.3 Constant time evolution*

The constant and incremented delays can be combined. A simple example, known as *constant time evolution* is presented in Figure 4.2. The depicted pulse sequence addresses one limitation of the HSQC experiment, namely the J-coupling between ^{13}C nuclei. If a molecule contains several J-coupled ^{13}C nuclei with similar chemical shifts, the effect of the ^{13}C-^{13}C J-coupling cannot be eliminated by the decoupling echo because we cannot selectively invert distribution of the magnetic moments of the coupled partner. A solution is to combine the evolution period t_1 (a decoupling echo of incremented duration shown in red in Figure 4.2) with a simultaneous echo affecting all ^{13}C nuclei (blue). The simultaneous echo is actually formed by a single 180 ° pulse of a radio wave with frequency sufficiently close to precession frequencies of all ^{13}C nuclei. If the total length of the echo is an integer multiple of J_{CC}, where J_{CC} is the ^{13}C-^{13}C coupling constant (assumed to be identical for all carbon pairs), the original ^{13}C coherence (anti-phase in our case) is restored at the end of the echo. It is because the in-phase and anti-phase ^{13}C coherences evolve as $\cos(\pi J t)$ during both echoes[3] of the complete length of $t = n/J_{CC}$, and therefore $\cos(\pi J t) = \cos(n\pi) = \pm 1$ (no modulation by t_1). The chemical shift of ^{13}C evolves during the decoupling echo, resulting in the modulation by $\cos(\Omega_C t_1$, but it is refocused during the simultaneous echo. Therefore, the modulation by $\cos(\Omega_C t_1$ is preserved. When analyzing the effect of the J-couplings of ^{13}C with ^{1}H, we follow two lines: "^{1}H" and "^{13}C". The first (red) echo is decoupling, the second one (blue) is refocusing (now we do not consider the ^{13}C-^{13}C J-coupling), therefore the analyzed ^{13}C-^{1}H J-coupling does not have any effect at the end of the second echo. In summary, we were able to keep the modulation by the chemical shift of ^{13}C and remove the effects of both ^{13}C-^{1}H and ^{13}C-^{13}C J-couplings, without actually decoupling the second one.

Another, very frequent, application of the constant time evolution is the incorporation of the incremented delay t_1 (introducing modulation of the signal by the frequency of ^{15}N) into a rather long INEPT transferring polarization between ^{15}N and ^{13}C in triple resonance experiments, discussed in Section 5.4. An example is presented in Figure 5.5.

---

[3]No pulse is applied to ^{13}C during t_1 (see the red arrow below the pulse sequence in Figure 4.2), therefore both ^{13}C chemical shift and the J-coupling between ^{13}C evolve freely. During the following simultaneous echo (blue arrow below the pulse sequence in Figure 4.2), the evolution due to the ^{13}C chemical shift is refocused, but the evolution due to the J-coupling is preserved.

4.4 Pulses

The pulse of radio waves is the fundamental element of NMR experiments as we learned in Section 1.11. Each pulse of an NMR experiment must be precisely defined by setting the following parameters.

- *Frequency* of the radio wave is the first important parameter of each pulse, the unit is Hertz. It is chosen to match the precession frequency of magnetic moments of the observed nucleus, therefore it depends on the magnetic induction B_0 (cf. Eq. 1.3). Spectrometers used for biomolecular applications are equipped with magnets of the induction $9\,T$–$24\,T$ (the highest value available in 2020 was $28\,T$), it corresponds to $400\,MHz$–$1\,GHz$ for protons (values for ^{13}C and ^{15}N are four-times and ten-times lower, respectively).

- *Phase* is another fundamental, although somewhat arbitrary parameter of the radio wave. The absolute phase is not clearly defined, it depends on exact timing, length of the cables etc. As mentioned in Section 3.2 and shown in Figure 2.9, the phase of the radio wave applied during the first pulse is assumed to be $180\,°$ and $0\,°$ for nuclei with $\gamma > 0$ and $\gamma < 0$, respectively, so that the rotation axis (direction of $\vec{\omega}_1$) is oriented along the x axis regardless of the sign of γ. The relative phase (difference in phase compared to the first pulse) is well defined and should be set precisely. A change of the phase of the actual radio wave oscillating in certain direction has a similar effect as applying a field in a different direction in the rotating coordinate system: the phase shifts of $0\,°$, $90\,°$, $180\,°$, and $270\,°$ correspond to a $\vec{\omega}_1$ in the x, y, $-x$, and $-y$ directions, respectively. Therefore, the pulses with phase shifts of $0\,°$, $90\,°$, $180\,°$, and $270\,°$ are are traditionally labeled as x, y, $-x$, and $-y$ pulses in the literature, respectively.

- *Phase modulation* The pulse can be divided into a certain number of short rectangular pulses (Figure 4.3). Phase of the short pulses can be varied during irradiation (Figure 4.3B–D). A gradual change of the phase is nothing else than another oscillation. This trick allows us to modify frequency of $\vec{B}_1$ without re-tuning the actual carrier frequency generated by the synthesizer.

  Power of the radio wave P (energy of the radiation per unit time) is proportional of the square of its amplitude $|\vec{B}_1|$. The absolute unit of power is Watt, a relative logarithmic unit decibell (dB) is often used in practice. The relative power is often calculated as attenuation of some reference (maximum) power. The relative and absolute units are related by the following equations.

$$20 \log_{10} \frac{|\vec{B}_1|_2}{|\vec{B}_1|_1} = 10 \log_{10} \frac{|\vec{B}_1|_2^2}{|\vec{B}_1|_1^2} = 10 \log_{10} \frac{P_2}{P_1} = \text{attenuation/dB}. \tag{4.1}$$

  Typical power for excitation pulses ranges between $10\,W$ and $1000\,W$, this is the number we need to know to set up the experiment. However, we are not interested in the power in Watts, but in the effect on the magnetization vector. Therefore, we do not report power in Watts when we describe the NMR experiment in the literature. Instead, we present the frequency ω_1 (more accurately $\omega_1/(2\pi)$) in kHz. The actual value of the power determines the length of the pulse, as discussed bellow.

- *Length* (duration) of the radio-wave pulse must be chosen so that the pulse has a desired effect. If the radio-wave frequency exactly matches the precession frequency, the total angle of rotation (*flip angle*) is a product of γ, B_1 (proportional to the square root of the power as discussed above), and duration t_p. Once we choose the power, B_1 is defined. We must calibrate the time t_p (length of the pulse) to achieve the desired effect. Pulses with $\gamma B_1 t_p = \pi/2$ (i.e., $90\,°$) cause maximum excitation (ideally complete conversion of M_z to $-M_y$), pulses with $\gamma B_1 t_p = \pi$ (i.e., $180\,°$) turn M_z to the opposite direction $-M_z$. The flipped M_z corresponds to the inverted distribution of magnetic moments.[4] A pulse of a flip angle equal to $360\,°$ returns magnetization to its original position. The length of the $360°$ pulse is the inverse value of $\omega_1/(2\pi)$, i.e. of the aforementioned equivalent of power in units of Hz. Apparently, the same effect (flip angle) can be achieved by increasing B_1 or t_p. However, this is true only *on resonance*, when the radio-wave frequency exactly matches the precession frequency. If the

---

[4]The Boltzmann law seems to require that the temperature is lower than absolute zero (or higher than infinity) under such circumstances. But do not panic, the Second Law of Thermodynamics is not violated because the inverted populations are not in thermal equilibrium.
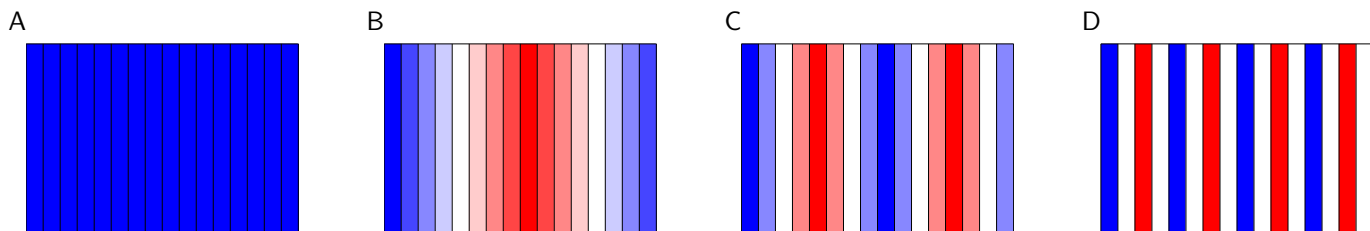
Figure 4.3: Phase-modulated pulses. A radio wave irradiation is divided into 16 pulses of different phases, distinguished by different colors. The blue and red colors correspond to $0°$ and $180°$ phases (x and $-x$ pulses), respectively, whereas white corresponds to $90°$ and $270°$ phases ($\pm y$ pulses). Magnetic moments irradiated by the pulses B, C, and D experience additional frequency of one, two, and four cycles per the pulse length, respectively. For example, if the pulse length is $100\,\mu s$, the pulses B, C, and D, respectively, resonate with the frequency higher by $10\,\mathrm{kHz}$, $20\,\mathrm{kHz}$, and $40\,\mathrm{kHz}$ than the carrier frequency.

radio-wave frequency differs from the precession frequency, effects of long pulses deviate more from the desired performance than those of short ones. Therefore, we often choose the highest possible power to be able to shorten the pulse as much as possible. The limits are rather technical. The energy of the radio waves is absorbed by the sample and temperature may increase if the instrument is not able to cool the sample efficiently (note that $1000\,\mathrm{W}$ is a typical power of a microwave oven). Sample may overheat or even get evaporated! Eventually, the transmitter coil could be burned which would not make the lab manager happy. Therefore, the pulses cannot be so short that the deviations from the resonance would be negligible. We discuss the consequences of being *off-resonance* in Section 4.5.

- *Amplitude modulation.* So-far, we discussed only *rectangular* pulses, generated simply by switching the radio transmitter on and off. We can also increase the power gradually,[5] so that the radio-pulse is *amplitude modulated* like in the AM broadcasting. As the amplitude, forming an envelope of the pulse, has a certain shape, the term *shaped pulses* is used for the amplitude-modulated pulses. Careful choice of the shape can lead to a pulse which affects almost ideally magnetic moments in a certain region of frequency offsets and has a negligible effect on magnetic moments with frequency offsets outside this region. Such selective performance is discussed in Section 4.5. In combination with the phase modulation, we have the liberty to affect various ranges of frequencies selectively.

4.5 Offset effects

If the radio-wave frequency exactly matches the precession frequency of a certain nucleus, the effect of the pulse is pretty clear. The frequency offset Ω is zero and $\vec{B}_0$ has no effect on the evolution. The effect of $\vec{B}_1$ on a system in equilibrium can be described simply as a rotation about the x axis in the rotating coordinate system, as shown in Figure 4.4A.

If a precession frequency of a certain nucleus slightly differs from the radio-wave frequency of $\vec{B}_1$, the evolution of the magnetization vector during the pulse is not easy to describe. In a coordinate frame rotating with the same frequency as $\vec{B}_1$ (i.e., axis z is defined by the direction of $\vec{B}_0$ and axis x is defined by the direction of $\vec{B}_1$), the magnetization rotates about two axes, as shown in Figure 4.4B. One axis is $\vec{B}_1$ (or more precisely $\vec{\omega}_1$), the other one is $\vec{\Omega}$, with the magnitude given by the *frequency offset* and direction given by $\vec{B}_0$. Formally, such motion can be described as a rotation about an *effective field* $\vec{B}_{\mathrm{eff}}$, defined in Figure 4.4B. As a consequence, the orientation of the magnetization is *not* perpendicular to both $\vec{B}_1$ and $\vec{B}_0$. The difference between the on-resonance and off-resonance pulses (the difference between Figure 4.4A and Figure 4.4B) is called the *offset effect*.

Due to the offset effects, signals (oscillating induced electromotive forces) of different nuclei differ in amplitude and phases, which decreases sensitivity and introduces distortions of spectra. But the offset effects have also some positive consequences. Variation of power (combined with the corresponding change of length in order to keep the same flip angle) allows us to introduce certain selectivity. We start with a non-selective pulse that should excite two nuclei,

---

[5]In practice, the pulse is composed of a certain number of short rectangular pulses differing in the amplitude of the radio wave.

Table 4.1: Dependence of excitation efficiency on frequency offsets for various amplitude modulations of radio wave pulses. The lengths and amplitudes (shapes) are plotted in the real ratios, blue and red correspond to the phase of $0°$ and $180°$, respectively. The efficiency of excitation is plotted in blue, ranging from zero ($M_z = M^{\mathrm{eq}}$, $M_x = M_y = \sqrt{M_x^2 + M_y^2} = 0$, magnetization vector in the z direction, no excitation) to one ($M_z = 0$, $\sqrt{M_x^2 + M_y^2} = M^{\mathrm{eq}}$, magnetization vector in the xy plane). The deviations of the x and y components of the magnetization vector from the desired $-y$ direction are plotted in red. The range of the frequency offsets is $-30\,\mathrm{kHz}$ to $+30\,\mathrm{kHz}$. The arrows above the plot indicate average frequency offsets of $^{13}\mathrm{C}^{\alpha}$ (assumed to be on-resonance, light green), carbonyl $^{13}\mathrm{C}$ (red), and methyl $^{13}\mathrm{C}$ (dark green) at $111.75\,\mathrm{T}$ (corresponding to the proton resonance frequency of $500\,\mathrm{MHz}$). The lengths and amplitude of the hard rectangular pulse correspond to $10\,\mu\mathrm{s}$ and $|\omega_1| = 25\,\mathrm{kHz}$. The lengths ($64.5\,\mu\mathrm{s}$) and amplitude ($|\omega_1| = 9.675\,\mathrm{kHz}$) of the selective rectangular pulse are chosen so that the frequency offset of carbonyl $^{13}\mathrm{C}$ ($15\,\mathrm{kHz}$) is equal to $\sqrt{15}|\omega_1|$. The lengths of the Q5 and EBURP2 pulses ($300\,\mu\mathrm{s}$ both) were chosen so that the aliphatic $^{13}\mathrm{C}$ nuclei are excited and carbonyl $^{13}\mathrm{C}$ magnetic moments remain in the equilibrium. The amplitudes of the Q5 and EBURP2 pulses were set so that the pulses rotate the magnetization by $90°$ when applied on resonance. NMR-Sim (Pavel Kessler) was used to calculate the effects of shaped pulses.

Name	shape	offset-dependent effect
rectangular (hard)		
rectangular (selective)		
Q5		
EBURP2		
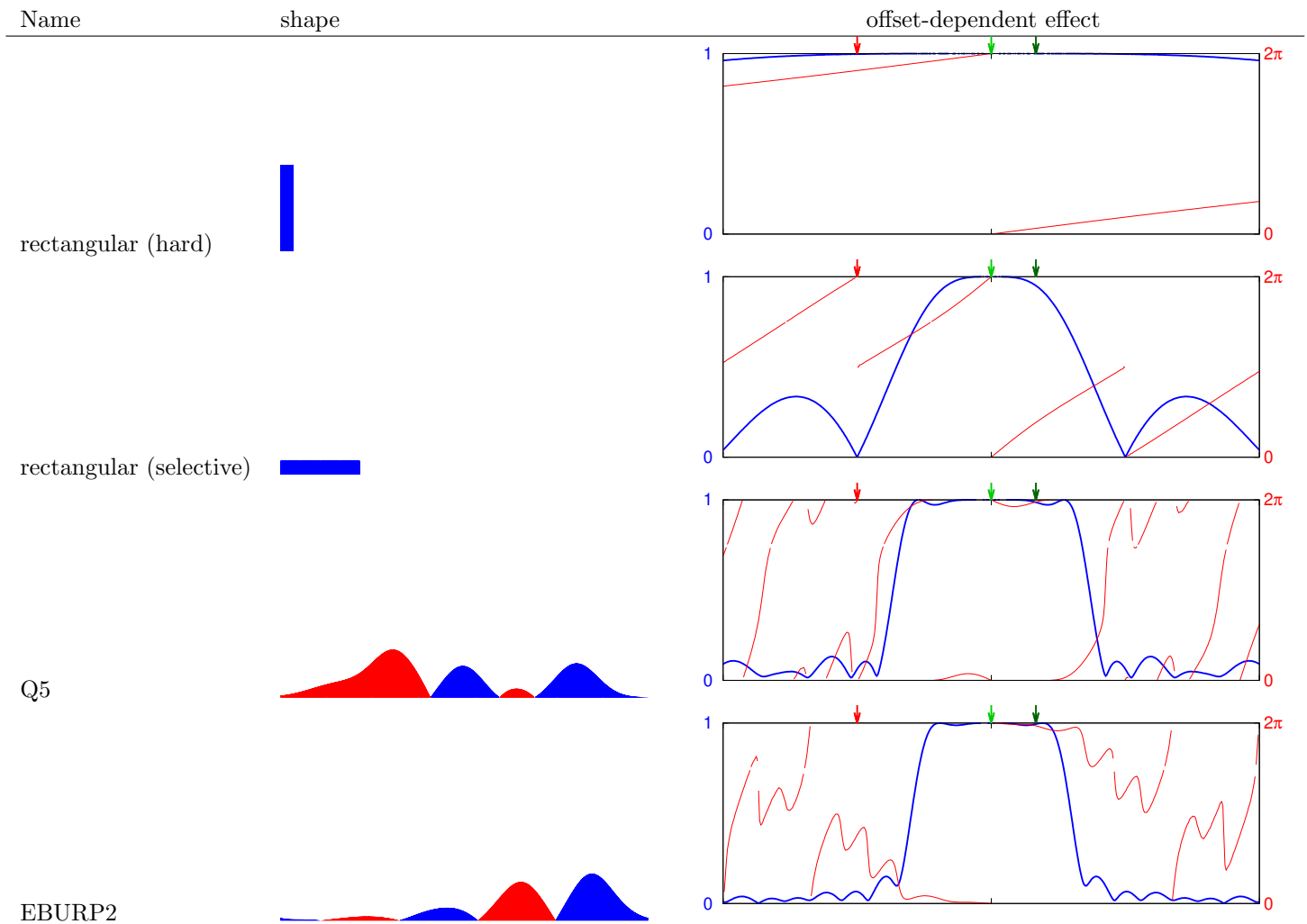
Table 4.2: Dependence of inversion efficiency on frequency offsets for various amplitude modulations of radio wave pulses. The lengths and amplitudes (shapes) are plotted in the real ratios, blue and red correspond to the phase of $0°$ and $180°$, respectively. The efficiency of inversion is plotted in blue, ranging from zero ($M_z = M^{eq}$) to one ($M_z = -M^{eq}$). The range of the frequency offsets is $-30\,kHz$ to $+30\,kHz$. The arrows above the plot indicate average frequency offsets of $^{13}C^{\alpha}$ (assumed to be on-resonance, light green), carbonyl ^{13}C (red), and methyl ^{13}C (dark green) at $111.75\,T$ (corresponding to the proton resonance frequency of $500\,MHz$). The lengths and amplitude of the hard rectangular pulse correspond to $20\,\mu s$ and $|\omega_1| = 25\,kHz$. The lengths ($57.7\,\mu s$) and amplitude ($|\omega_1| = 4.33\,kHz$) of the selective rectangular pulse are chosen so that the frequency offset of carbonyl ^{13}C ($15\,kHz$) is equal to $\sqrt{3}|\omega_1|$. The lengths of the Q3 and IBURP2 pulses ($250\,\mu s$ and $300\,\mu s$, respectively) were chosen so that the aliphatic ^{13}C nuclei are inverted and carbonyl ^{13}C magnetic moments remain in the equilibrium. The amplitudes of the Q3 and IBURP2 pulses were set so that the pulses rotate the magnetization by $180°$ when applied on resonance. NMR-Sim (Pavel Kessler) was used to calculate the effects of shaped pulses.

Name	shape	offset-dependent effect
rectangular (hard)		
rectangular (selective)		
Q3		
IBURP2		
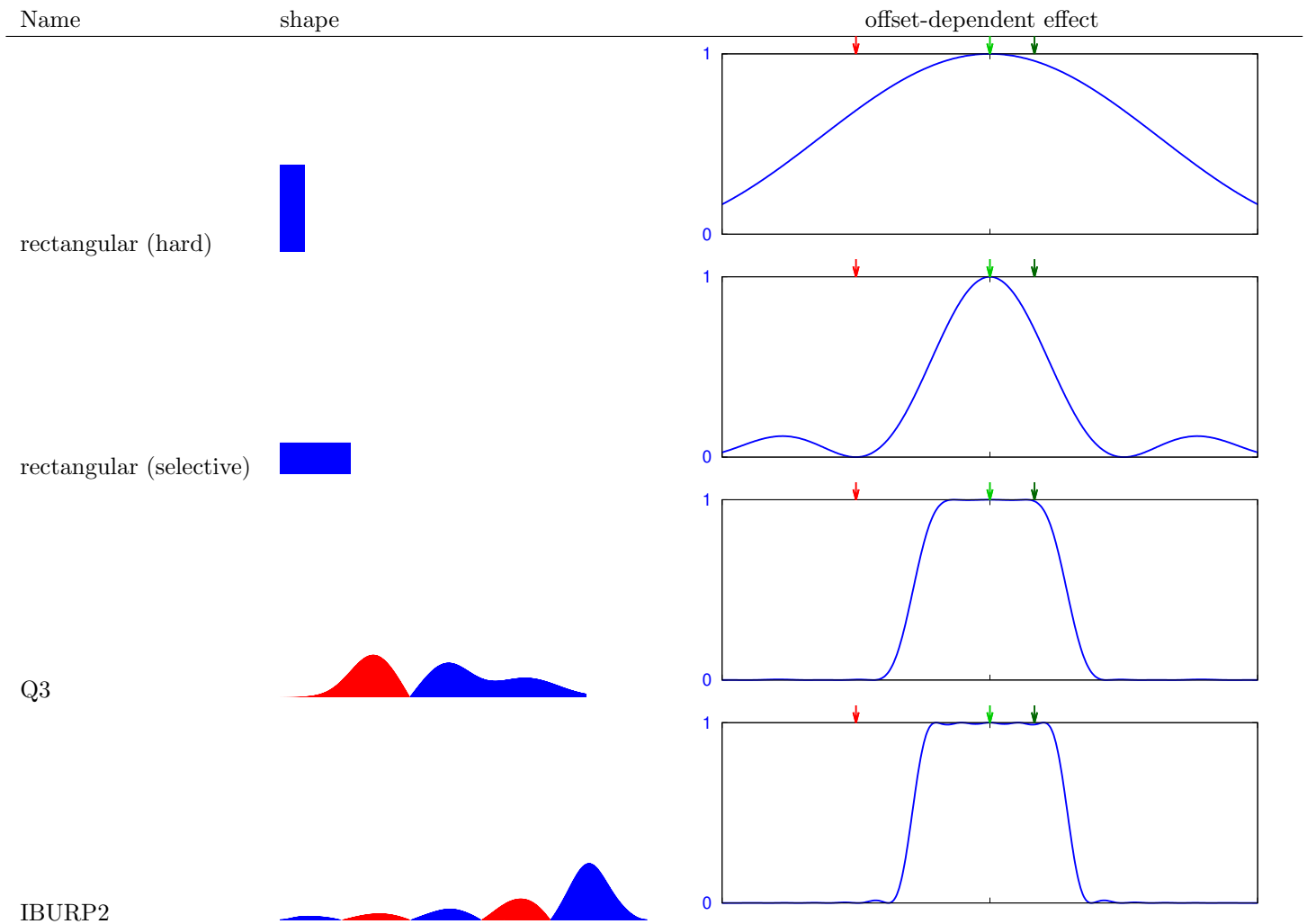
Table 4.3: Dependence of refocusing efficiency on frequency offsets for various amplitude modulations of radio wave pulses. The lengths and amplitudes (shapes) are plotted in the real ratios, blue and red correspond to the phase of $0°$ and $180°$, respectively. The efficiency of inversion is plotted in blue, ranging from zero ($M_y = -M^{eq}$) to one ($M_y = M^{eq}$). The deviations of the x and y components of the magnetization vector from the desired y direction are plotted in red. The range of the frequency offsets is $-30\,\text{kHz}$ to $+30\,\text{kHz}$. The arrows above the plot indicate average frequency offsets of $^{13}\text{C}^{\alpha}$ (assumed to be on-resonance, light green), carbonyl ^{13}C (red), and methyl ^{13}C (dark green) at $111.75\,\text{T}$ (corresponding to the proton resonance frequency of $500\,\text{MHz}$). The lengths and amplitude of the hard rectangular pulse correspond to $20\,\mu\text{s}$ and $|\omega_1| = 25\,\text{kHz}$. The lengths ($57.7\,\mu\text{s}$) and amplitude ($|\omega_1| = 4.33\,\text{kHz}$) of the selective rectangular pulse are chosen so that the frequency offset of carbonyl ^{13}C ($15\,\text{kHz}$) is equal to $\sqrt{3}|\omega_1|$. The lengths of the Q3 and REBURP pulses ($250\,\mu\text{s}$ and $300\,\mu\text{s}$, respectively) were chosen so that the aliphatic ^{13}C nuclei are refocused and rotation of the carbonyl ^{13}C magnetization is unaffected. The amplitudes of the Q3 and REBURP pulses were set so that the pulses rotate the magnetization by $180°$ when applied on resonance. NMR-Sim (Pavel Kessler) was used to calculate the effects of shaped pulses.
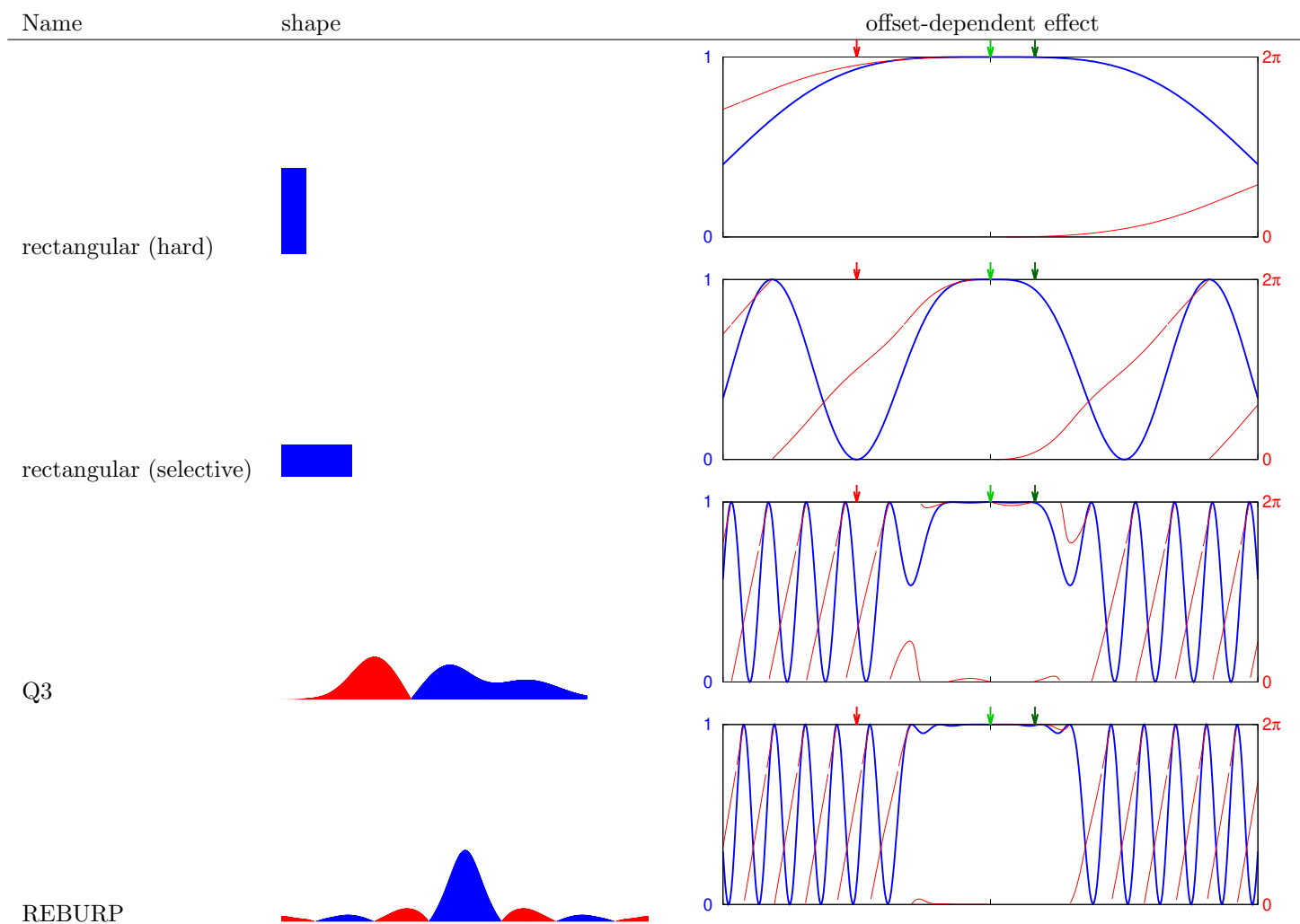
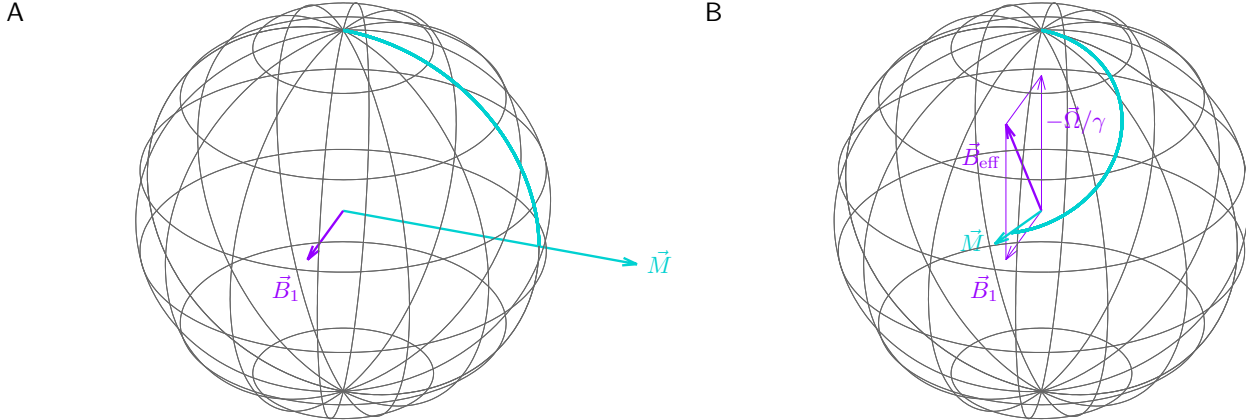| Name	shape	offset-dependent effect
rectangular (hard)		
rectangular (selective)		
Q3		
REBURP		

A

B

Figure 4.4: Evolution of the magnetization vectors with precession frequency exactly matching the used radio frequency (left) and slightly off-resonance (right). The evolution is shown in a coordinate frame rotating with $\vec{\omega}_{\mathrm{rot}} = -\vec{\omega}_{\mathrm{radio}}$.

e.g. $^{13}\mathrm{C}^\alpha$ and carbonyl $^{13}\mathrm{C}$, simultaneously. If the pulse is applied with a high power, the condition $|B_1| \gg |\Omega/\gamma|$ is fulfilled sufficiently for a broad range of frequency offsets Ω. Within this range of frequencies, $\vec{B}_{\mathrm{eff}}$ is close enough to $\vec{B}_1$ and magnetization vectors of all nuclei are rotated close to the desired orientation. Pulses of lower powers have this "on-resonance window" narrower. In the case of $^{13}\mathrm{C}^\alpha$ and carbonyl $^{13}\mathrm{C}$, the window must cover 140 ppm to affect both types of nuclei efficiently. Let us now suppose that we wish to rotate magnetization of certain nuclei (e.g. $^{13}\mathrm{C}^\alpha$) by 90 ° and leave other nuclei (e.g. carbonyl $^{13}\mathrm{C}$) untouched. In other words, we are looking for a pulse that rotates $^{13}\mathrm{C}^\alpha$ magnetization by 90 ° and carbonyl $^{13}\mathrm{C}$ magnetization by 360 °. The solution is presented in Figure 4.5. Finding of the correct value of $|B_1| = |\Omega|/(\sqrt{15}\gamma)$, or $|\omega_1| = |\Omega|/\sqrt{15}$, for the given Ω (120 ppm in the case of $^{13}\mathrm{C}^\alpha$ and carbonyl $^{13}\mathrm{C}$, corresponding e.g. to 60 kHz at 11.75 T) is just a matter of applying the Pythagorean theorem. Figure 4.6 shows a similar solution for a 180 ° pulse selectively inverting longitudinal polarization of carbonyl $^{13}\mathrm{C}$ but not of $^{13}\mathrm{C}^\alpha$. In this case, the condition is $|B_1| = |\Omega|/(\sqrt{3}\gamma)$, or $|\omega_1| = |\Omega|/\sqrt{3}$.

Figure 4.6 suggests that a pulse with $|\omega_1| = |\Omega|/\sqrt{3}$ and resonating exactly with the carbonyl precession frequency can be used to selectively decouple carbonyl $^{13}\mathrm{C}$ during an incremented delay when the signal is modulated by the $^{13}\mathrm{C}^\alpha$ frequency (in a similar fashion as the cyan pulse in t_1 in Figure 3.3 decouples $^{15}\mathrm{N}$). The longitudinal polarization of carbonyl $^{13}\mathrm{C}$ should be inverted and transverse polarization (or anti-phase coherence) of $^{13}\mathrm{C}^\alpha$ should be returned to its original direction. This is true, and we discuss pulse sequences containing such decoupling later (see e.g. Figure 5.5). However, there is a caveat here. If a selective carbonyl pulse of a duration t_p is applied, the $^{13}\mathrm{C}^\alpha$ coherence is returned to its original direction (Figure 4.6. If the selective carbonyl pulse is *not* applied, the $^{13}\mathrm{C}^\alpha$ coherence rotates with its frequency offset Ω). Therefore, application of the pulse reduces the total rotation during the incremented delay by Ωt_p. This reduction corresponds to a phase shift in the modulation (sometimes called the *Bloch-Siegert shift of the second kind*).[6]

We should admit that the selection described in Figures 4.5 and 4.6 is rather rough as no sharp border exists between "on-resonance" and "off-resonance". The offset effects increase gradually and the efficiency of the pulse ($\sqrt{M_x^2 + M_y^2}/M$ for excitation, $-M_z/M$ for inversion, see Tables 4.1 and 4.2, respectively) gradually decreases (with additional oscillations). Therefore, only magnetic moments with relatively narrow and sufficiently distant frequency

---

[6]It is not difficult to calculate the phase shift in our case. The selective pulse rotates the carbonyl magnetization by 180 ° = π rad. Therefore, $\omega_1 t_\mathrm{p} = \pi$ and $t_\mathrm{p} = \pi/\omega_1$. As mentioned above, the radio wave power is chosen so that $|\omega_1| = |\Omega|/\sqrt{3}$. Consequently, $t_\mathrm{p} = \pi/\omega_1 = \pm\sqrt{3}\pi/\Omega$, showing that the "missing" angle of the rotation of the $^{13}\mathrm{C}^\alpha$ coherence is $\Omega t_\mathrm{p} = \pm\sqrt{3}\pi$.

A

B

Figure 4.5: Evolution of the magnetization vectors with precession frequency exactly matching the used radio frequency (left) and with a frequency offset Ω (right), for $\omega_1 = \Omega/\sqrt{15}$. If ω_1 rotates magnetization of the former nucleus by $90\,^\circ$, then $\omega_{\text{eff}} = \sqrt{1+15}\,\Omega = 4\Omega$ rotates magnetization of the latter nucleus by $4 \times 90\,^\circ = 360\,^\circ$, i.e., by the full circle. The evolution is shown in a coordinate frame rotating with $\vec{\omega}_{\text{rot}} = -\vec{\omega}_{\text{radio}}$. In both cases, magnetization rotates about the thick purple arrow with the angular frequency proportional to the length of the arrow.

offsets can be distinguished. Fortunately, this is true only for *rectangular* pulses, generated simply by switching the transmitter on and off. The *amplitude modulated*, or *shaped pulses* provide much better selectivity. Careful choice of the shape (or, more efficiently, computer optimization) can lead to a pulse which efficiency is almost constant in a certain region of frequencies and than it rapidly fades out. Performance of amplitude-modulated pulses providing selective excitation, inversion, and refocusing is compared in Tables 4.1–4.3. The effects of the pulses presented in Tables 4.1–4.3 are calculated for a typical example of selectively manipulated nuclei in biomacromolecules, for ^{13}C in aliphatic and carbonyl groups in proteins. The tables show that different amplitude modulations can be used for similar purposes with slightly different outcomes.

4.6 Quadrature detection and demodulation

Precession of the magnetization vector in the sample induces a signal oscillating with the same frequency ω_0 in the coil of the NMR probe. The signal generated in the coil and amplified in the preamplifier is split into two channels, labeled a and b here. The signal in each channel is mixed with a reference wave supplied by the radio-frequency synthesizer. The reference waves have the same frequency $-\omega_{\text{radio}}$ in both channels, but their phases are shifted by $90\,^\circ$. Let us assume that the signal oscillates as a cosine function $\cos(\omega_0 t)$ and that the reference wave in the first channel is a cosine wave $\cos(-\omega_{\text{radio}} t)$ and that the reference wave in the second channel is a sine wave $\sin(-\omega_{\text{radio}} t)$. Mathematically, splitting the signal and mixing it with the reference wave can be described as

$$\cos(\omega_0 t) \rightarrow \begin{cases} \frac{1}{2}\cos(\omega_0 t) \rightarrow & \frac{1}{2}\cos(\omega_0 t)\cos(-\omega_{\text{radio}} t) & \text{channel } a \\ \frac{1}{2}\cos(\omega_0 t) \rightarrow & \frac{1}{2}\cos(\omega_0 t)\sin(-\omega_{\text{radio}} t) & \text{channel } b \end{cases} \tag{4.2}$$

Basic trigonometric identities show that the result of mixing in the first channel is a sum of a high-frequency cosine wave $\cos((\omega_0 - \omega_{\text{radio}})t)$ and a low-frequency cosine wave $\cos((\omega_0 + \omega_{\text{radio}})t) = \cos(\Omega t)$, while the result of mixing in the second channel is a difference of the corresponding sine waves:

$$\frac{1}{2}\cos(\omega_0 t)\cos(-\omega_{\text{radio}} t) = \frac{1}{4}\cos((\omega_0 - \omega_{\text{radio}})t) + \frac{1}{4}\cos((\omega_0 + \omega_{\text{radio}})t), \tag{4.3}$$
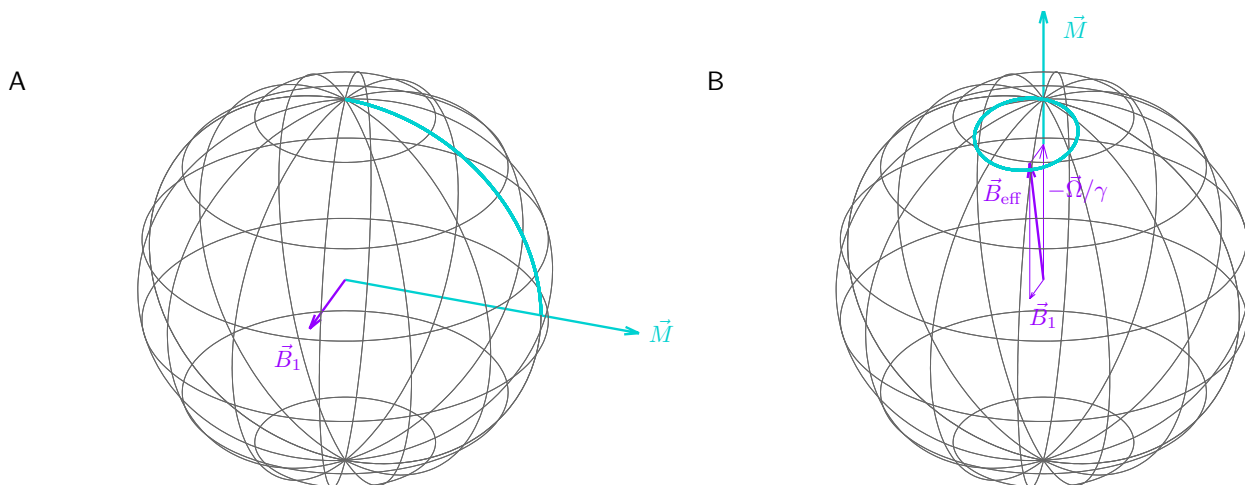
A

B
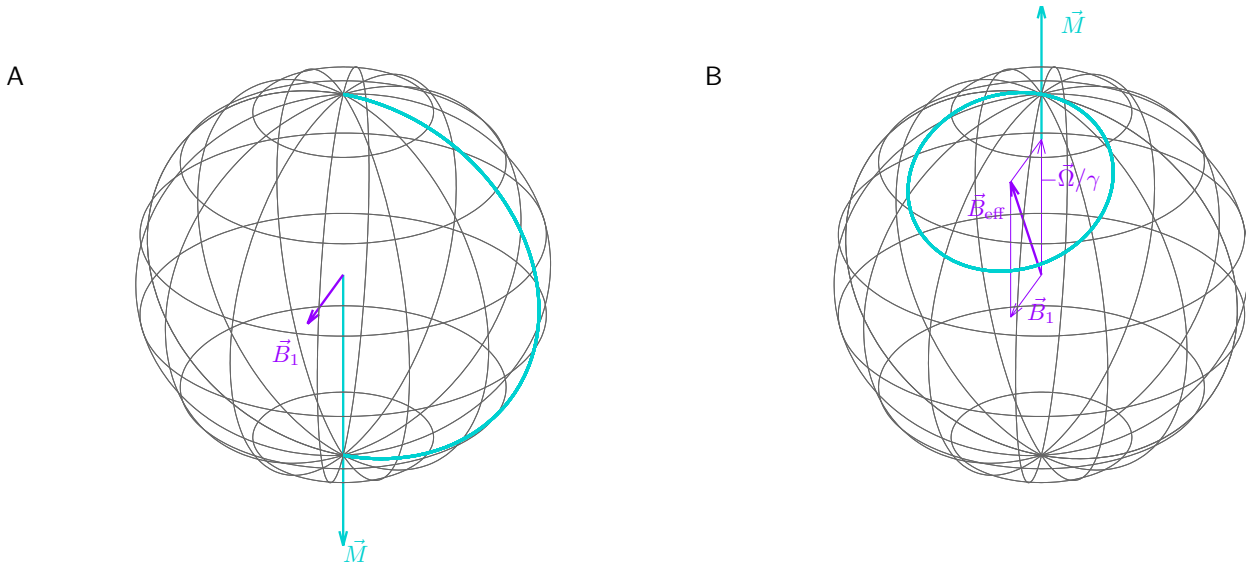
Figure 4.6: Evolution of the magnetization vectors with precession frequency exactly matching the used radio frequency (left) and with a frequency offset Ω (right), for $\omega_1 = \Omega/\sqrt{3}$. If ω_1 rotates magnetization of the former nucleus by $180°$, then $\omega_{\mathrm{eff}} = \sqrt{1+3}\,\Omega = 2\Omega$ rotates magnetization of the latter nucleus by $2 \times 180° = 360°$, i.e., by the full circle. The evolution is shown in a coordinate frame rotating with $\vec{\omega}_{\mathrm{rot}} = -\vec{\omega}_{\mathrm{radio}}$. In both cases, magnetization rotates about the thick purple arrow with the angular frequency proportional to the length of the arrow.

$$\frac{1}{2}\cos(\omega_0 t)\sin(-\omega_{\mathrm{radio}}t) = \frac{1}{4}\sin((\omega_0 - \omega_{\mathrm{radio}})t) - \frac{1}{4}\sin((\omega_0 + \omega_{\mathrm{radio}})t). \tag{4.4}$$

The high-frequency waves are filtered out by a low-pass filter, resulting in signals oscillating with a low frequency $\omega_0 + \omega_{\mathrm{radio}} = \Omega$. The procedure, similar to the demodulation in an ordinary radio receiver, thus produces audio signals in both channels

$$\cos(\omega_0 t) \rightarrow \begin{cases} \frac{1}{2}\cos(\omega_0 t) \rightarrow & \frac{1}{2}\cos(\omega_0 t)\cos(-\omega_{\mathrm{radio}}t) & \rightarrow \frac{1}{4}\cos(\Omega t) & \text{channel } a \\ \frac{1}{2}\cos(\omega_0 t) \rightarrow & \frac{1}{2}\cos(\omega_0 t)\sin(-\omega_{\mathrm{radio}}t) & \rightarrow \frac{1}{4}\sin(\Omega t) & \text{channel } b \end{cases} \tag{4.5}$$

The signal also has some amplitude, therefore, we replace the factor of $1/4$ by an amplitude A and write

$$a = A\cos(\Omega t) \qquad\qquad b = A\sin(\Omega t). \tag{4.6}$$

The described manipulation is called *quadrature detection* and the unit performing it is called the *receiver*. The outputs of the receiver are converted to digital data (series of numbers describing values of the signal at discrete, equally spaced time points). It is convenient to treat the outputs of the individual channels as a real and imaginary component of a single complex number, but physically they are stored just as series of two numbers in the computer.

A very useful trick is to play with the order of the stored numbers. The four basic options are

data storing option:	conventionally labeled:
$a, \; b$	x
$b, -a$	y
$-a, -b$	$-x$
$-b, \; a$	$-y$

The given storage option is described as the *receiver phase* in the literature. It is not an accident that the same symbols are used for the phase of the radio wave transmitted during the pulse and for the receiver phase. Choosing the right storage option (setting the receiver phase) allows us to remove the effect of changing the pulse phase. For example, a signal recorded immediately after an ideal $90°$ pulse of phase x (by definition) oscillates as $a = A\sin(\Omega t), b = -A\cos(\Omega t)$ (the magnetization starts to rotate from the $-y$ direction). If we run the same

experiment but with the y phase of the first pulse, the signal oscillates as $a = A\cos(\Omega t), b = A\sin(\Omega t)$. However, if we use the option y to store the data, the record is the same as in the previous experiment: $b = A\sin(\Omega t), -a = -A\cos(\Omega t)$. We see that the same signal is obtained if the receiver phase matches the transmitter phase.

The motivation to store both sine- and cosine-oscillating data is that the cosine function itself does not tell us if Ω is positive or negative because $\cos(\Omega t) = \cos(-\Omega t)$. In other words, we do not know if the true ω_0 is slightly higher or lower than ω_{ref}. This ambiguity is reflected by the Fourier transformation which produces a spectrum with two peaks, one is true and one is false (Figure 4.7A). To resolve the ambiguity and to identify the correct peak, we need both $\cos(\Omega t)$ and $\sin(\Omega t)$. A *complex* variant of the Fourier transformations converts the pair of $\cos(\Omega t)$ and $\sin(\Omega t)$ into a spectrum with a single peak at the right Ω, and produces also an imaginary component which is usually discarded (Figure 4.7B).

4.7   Complex signal in the indirect dimension(s)

The incrementation of t_1 in the HSQC experiment, as presented in Figure 3.3, introduces amplitude modulation of the signal by the ^{13}C (or ^{15}N) frequency offset and consequently allows us to obtain a 2D correlated spectrum. The cosine dependence of amplitude on Ω_{C} cannot distinguish the sign of Ω_{C}, as explained in Section 4.6. It is therefore desirable to obtain both cosine and sine modulations also in the indirect dimension.

It is possible to introduce the complex numbers in the indirect dimension by repeating the measurement twice for each value of t_1, each time with a different phase of the radio waves applied during a 90° ^{13}C pulse. We describe the procedure for the pulse sequence shown in Figure 4.8A. First we acquire the signal with the same phase (x by definition) of both 90° ^{13}C pulses. As described in Section 3.8, only the $\pm y$ components (perpendicular to the direction of B_1) of the arrows symbolizing anti-phase ^{13}C coherence contribute to the signal. These components are modulated by $\cos\Omega_{\mathrm{C}}t_1$. We store the outputs of the quadrature receiver channels a and b as records r_1 and r_2, respectively. Then, we repeat the acquisition with the phase of the first pulse shifted by 90° (phase y) and store the outputs of the channels a and b as records r_3 and r_4, respectively. The y pulse creates anti-phase coherence described by arrows in the $\pm x$ direction, but the second pulse selects the $\pm y$ components. Such selected coherence, shifted by 90° from the former one, oscillates as $\sin\Omega_{\mathrm{C}}t_1$ and can be used as an imaginary component of the signal. We than increase t_1 and repeat the cycle. This approach, known as *hypercomplex* or *States-Haberkorn-Ruben* method, provides both cosine and sine amplitude modulation in the indirect dimension. If we label these modulated amplitudes A_{c} and A_{s}, we can describe the acquired signal as

$$\left.\begin{array}{ll}
r_1 = A_{\mathrm{c}}a = \cos(\Omega_{\mathrm{C}}t_1)\cos(\Omega_{\mathrm{H}}t_2) & \text{channel } a, \text{ pulse } x \\
r_2 = A_{\mathrm{c}}b = \cos(\Omega_{\mathrm{C}}t_1)\sin(\Omega_{\mathrm{H}}t_2) & \text{channel } b, \text{ pulse } x \\
r_3 = A_{\mathrm{s}}a = \sin(\Omega_{\mathrm{C}}t_1)\cos(\Omega_{\mathrm{H}}t_2) & \text{channel } a, \text{ pulse } y \\
r_4 = A_{\mathrm{s}}b = \sin(\Omega_{\mathrm{C}}t_1)\sin(\Omega_{\mathrm{H}}t_2) & \text{channel } b, \text{ pulse } y
\end{array}\right\} (A_{\mathrm{c}} + \mathrm{i}A_{\mathrm{s}})(a + \mathrm{i}b), \tag{4.7}$$

or in a table

x/y	receiver	acquired as	stored as records r_j
$+x$	$+x$	$a : A_{\mathrm{c}}\sin(\Omega_{\mathrm{H}}t_2)$	$r_1, r_2 = A_{\mathrm{c}}\sin(\Omega_{\mathrm{H}}t_2), A_{\mathrm{c}}\cos(\Omega_{\mathrm{H}}t_2)$
		$b : A_{\mathrm{c}}\cos(\Omega_{\mathrm{H}}t_2)$	
$+y$	$+x$	$a : A_{\mathrm{s}}\sin(\Omega_{\mathrm{H}}t_2)$	$r_3, r_4 = A_{\mathrm{s}}\sin(\Omega_{\mathrm{H}}t_2), A_{\mathrm{s}}\cos(\Omega_{\mathrm{H}}t_2)$
		$b : A_{\mathrm{s}}\cos(\Omega_{\mathrm{H}}t_2)$	

We must be careful when processing the hypercomplex data. In the case of 1D spectra, processing of the signal treated as series of complex numbers is simple. Complex Fourier transformation converts the data to the spectrum, stored again as a complex number, but only the real part is interesting. Symbolically,

$$a + \mathrm{i}b \longrightarrow X + \mathrm{i}Y, \tag{4.8}$$

where X is the desired real spectrum and Y is its imaginary counterpart.

In the case of a hypercomplex 2D signal, applying the complex Fourier transformation twice is not what we want:

$$(A_{\mathrm{c}} + \mathrm{i}A_{\mathrm{s}})(a + \mathrm{i}b) \longrightarrow (A_{\mathrm{c}} + \mathrm{i}A_{\mathrm{s}})(X_2 + \mathrm{i}Y_2) \longrightarrow (X_1 + \mathrm{i}Y_1)(X_2 + \mathrm{i}Y_2) = X_1 X_2 - Y_1 Y_2 + \mathrm{i}(X_1 Y_2 + Y_1 X_2). \tag{4.9}$$

A
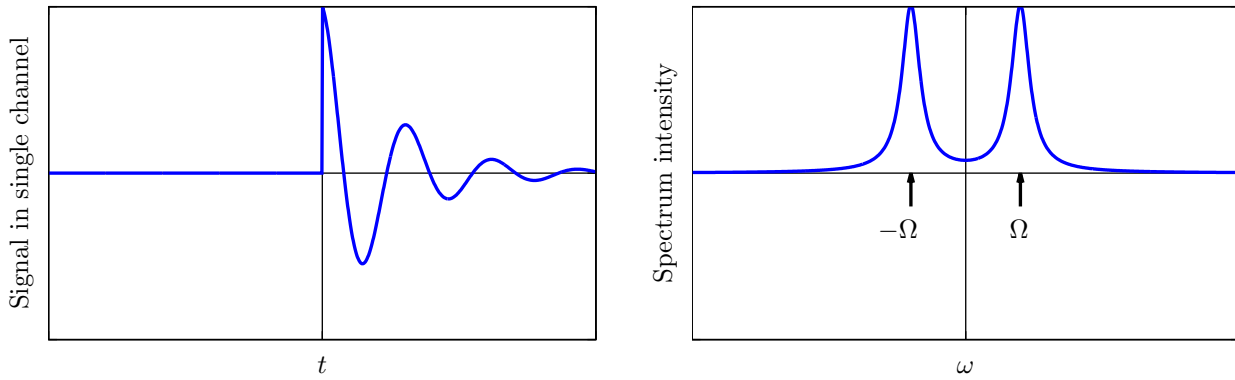
B
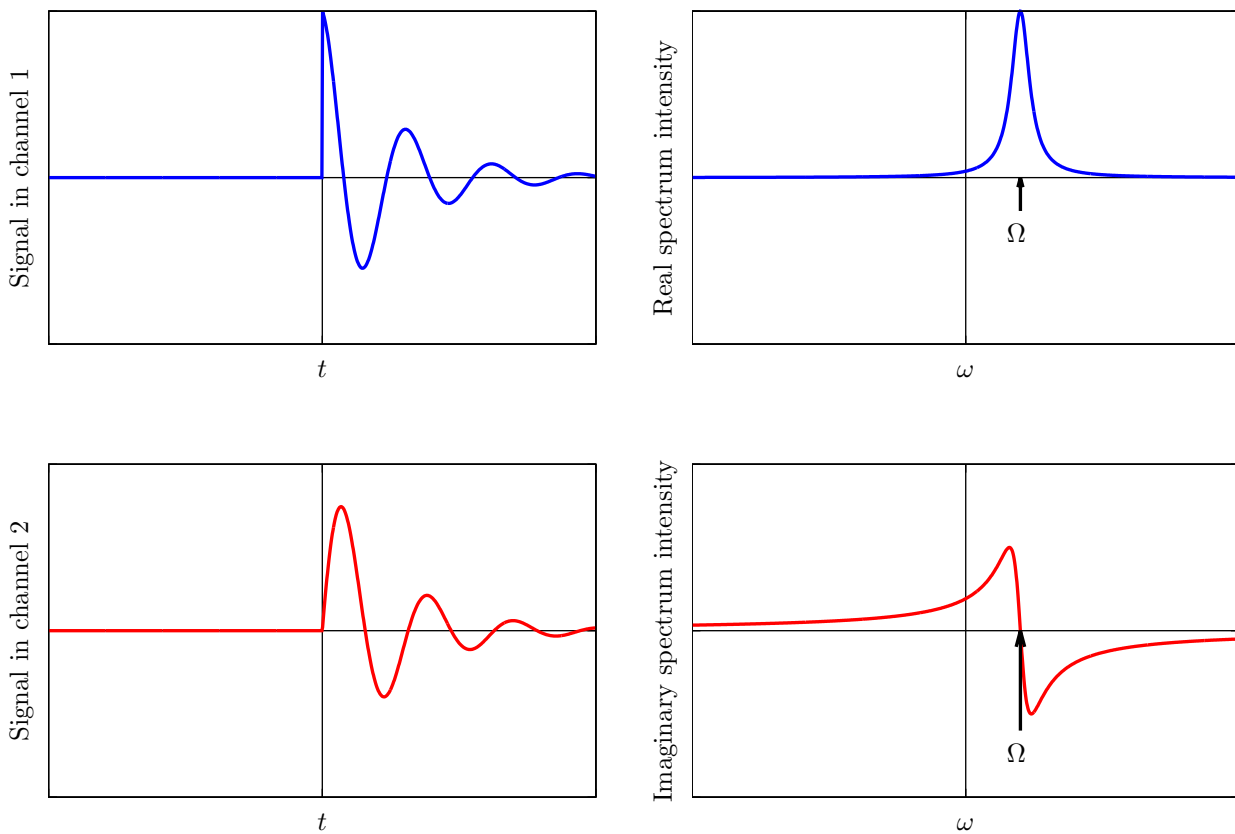
Figure 4.7: Fourier transformation of signal detected using a single channel (A) and two channels (B). Left panels show outputs of the receivers, right panels show spectra obtained by Fourier transformations. Data treated as real and imaginary numbers are shown in blue and red, respectively. The correct frequency offset is Ω.

What is stored as the real component of the signal is actually a mixture of the desired real peaks $X_1 X_2$ and "double-imaginary" peaks $Y_1 Y_2$ of ugly shapes. The correct procedure is to do the Fourier transformation in t_2, discard the imaginary part of the spectrum, and do the Fourier transformation in t_1:

$$(A_\mathrm{c} + \mathrm{i}A_\mathrm{s})(a + \mathrm{i}b) \longrightarrow (A_\mathrm{c} + \mathrm{i}A_\mathrm{s})(X_2 + \mathrm{i}Y_2) \longrightarrow (A_\mathrm{c} + \mathrm{i}A_\mathrm{s})X_2 \longrightarrow (X_1 + \mathrm{i}Y_1)X_2 = X_1 X_2 + \mathrm{i}Y_1 X_2. \tag{4.10}$$

4.8 Time-proportional phase incrementation*

Positive and negative frequencies can be also discriminated in the following manner. Let us assume that the time increment Δt in a reference experiment not distinguishing positive and negative frequencies has been chosen so that all angular frequencies are within the range $-\pi/\Delta t$ to $+\pi/\Delta t$ (cf. Section 4.2). Then the following changes are applied

- The number of increments is doubled and the increment is shortened to $\Delta t/2$. This increases the spectral width to the range from $-2\pi/\Delta t$ to $+2\pi/\Delta t$, but all really occurring frequencies are in the central region from $-\pi/\Delta t$ to $+\pi/\Delta t$.

- The phase of the 90° pulse before or after the incremented period is increased by 90° in each time increment.

The result can be analyzed as follows. Incrementation of the 90° pulse phase decreases the argument of the modulating function by 90°, from $\Omega k \Delta t/2$ to

$$\Omega k \frac{\Delta t}{2} - k\frac{\pi}{2} = \left(\Omega - \frac{\pi}{\Delta t}\right)k\frac{\Delta t}{2}, \tag{4.11}$$

i.e., all frequencies are decreased by one quarter of the spectral width. Therefore, all really occurring frequencies are shifted from the central region to the range from $-2\pi/\Delta t$ to 0, where all angular frequencies have the same sign. The other half of the spectrum (from 0 to $+2\pi/\Delta t$ is empty and can be discarded. Then, we obtain a spectrum with the same number of points as originally, but with the same sign of the frequencies.

This procedure is known as *time-proportional phase incrementation* (TPPI). The States-Haberkorn-Ruben method (Section 4.7) and TPPI are actually very similar. In both cases, the frequency discrimination requires doubling of the experimental time (repeated measurement in the case of the States-Haberkorn-Ruben method and doubling increments in the case of TPPI). The even and odd increments in the TPPI method are equivalent to the cosine and sine modulation:

$$\cos\left(\Omega k \frac{\Delta t}{2} - k\frac{\pi}{2}\right) = \cos\left(\Omega k \frac{\Delta t}{2}\right)\cos\left(k\frac{\pi}{2}\right) + \sin\left(\Omega k \frac{\Delta t}{2}\right)\sin\left(k\frac{\pi}{2}\right) = \begin{cases} \pm\cos\left(\Omega k \frac{\Delta t}{2}\right) & \text{for even } k \\ \pm\sin\left(\Omega k \frac{\Delta t}{2}\right) & \text{for odd } k \end{cases}. \tag{4.12}$$

The advantage of TPPI is that artifacts known as *axial peaks* (discussed in Section 4.12) are moved to the edge of the spectrum. TPPI is often combined with the States-Haberkorn-Ruben method by setting the phase of the 90° pulse to $x, y, -x, -y$ and the receiver phase to $x, x, -x, -x$ for the subsequent time increments.

4.9 Phase cycling

We discussed in Sections 4.7 and 4.8 how changing the pulse phase *between* acquisitions of *separately stored* records provides complex modulation in the indirect dimension. In real experiments, phases are often changed when acquiring data that are then summed and stored as a single record. This trick is known as *phase cycling* and it is applied in order to suppress unwanted signals. The unwanted signals may be due to magnetic moments really present in the sample (of water protons, of ^{13}C or ^{15}N nuclei without protons attached) or due to various artifacts.

When phase cycling is applied, the experiments are repeated for each increment of t_1 with different phases of some radio-wave pulses, and the acquired signals are combined. Repeating the measurements of course extends the overall time of the experiments. However, this drawback is not as serious as it may appear. In many cases, the sensitivity of

A

B

ϕ_1=x,−x,x,−x,x,−x,x,−x ϕ_2=x,x,−x,−x,x,x,−x,−x

ϕ_1=y,−y,y,−y,y,−y,y,−y ϕ_3=x,x,x,x,−x,−x,−x,−x

receiver phase: x,−x,−x,x,x,−x,−x,x
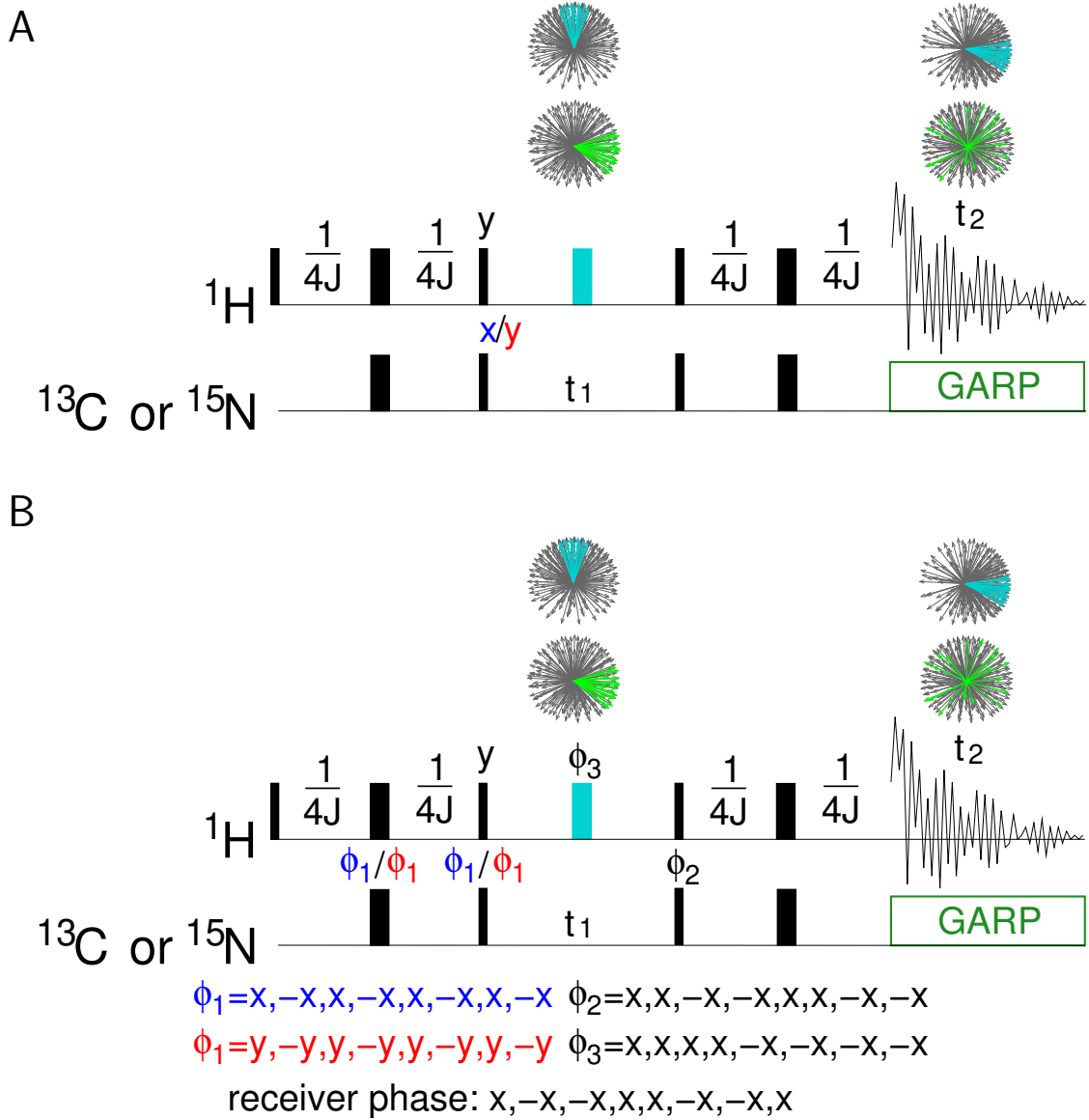
Figure 4.8: A, Recording hypercomplex HSQC spectra. The label x/y indicates repeated acquisition with the phase of the given pulse set first to $0\,°$ (x) and than to $90°$ (y), in order to obtain a cosine-modulated and sine-modulated 1D records for each t_1 increment. B HSQC experiment with phase cycling. The pulses with cycled phases are labeled ϕ_1, ϕ_2, ϕ_3, and the actual phases during the cycles are listed below the sequence. In order to add signals with the same signs, the individual signals are acquired with receiver phases indicated below the sequence. Other symbols are used as explained in Figure 3.3.

the measurement requires to sum results of several measurements anyway, in order to achieve a sufficient signal-to-noise ratio. Usually, the signals recorded with individual settings of the phases are not stored separately but directly added to the data acquired with the preceding phase setting. Phase of the desired signal acquired with different phases of the pulses may vary. Therefore, the phase of the acquired signal has to be adjusted before it is added to the sum of the signals recorded in the previous runs. As described in Section 4.6, signal with the same phase can be obtained by changing the *receiver phase* (the way how outputs of individual channels of the receiver are stored).

In the example shown in Figure 4.8B, the phases of ^{13}C (or ^{15}N) 90° pulses are cycled in order to suppress the signal of protons not attached to ^{13}C (or ^{15}N), e.g. of protons in water or in buffer components, that are not enriched in ^{13}C (or ^{15}N). Let us first analyze the evolution of the wanted polarizations of protons attached to ^{13}C (or ^{15}N), converted to the anti-phase ^{13}C (or ^{15}N) coherence and back by two INEPT modules. The phase of the first 90° pulse is shifted by 180° after every run, which inverts direction of the arrows describing the anti-phase coherence and finally changes the sign of the signal (i.e., shifts the signal by 180°). The phase of the second 90° pulse is cycled in a same manner and with the same effect, but after every second run. The result of such two nested phase cycles is that the phases of signal acquired in the second, third, sixth, and seventh runs are shifted by 180° and has to be adjusted, which is achieved by storing the data in a manner described by the receiver phase $-x$. The undesired polarization of protons in water or buffer of course does not sense the changes of ^{13}C (or ^{15}N) pulses and produces signal with the same phase. Alternation of the receiver phase between x and $-x$ thus cancels every two consecutive signals of the uncoupled protons.

When the phase cycling is applied in a two-dimensional experiment, as discussed in this section, we should carefully distinguish different purposes of repeating the data acquisition:

- In order to apply *phase cycling* and to *improve signal-to-noise ratio*, the signal is acquired repeatedly with various phases of certain radio-wave pulses. The individual signals are called *transients* or *scans* in the NMR literature. Usually, transients (scans) are not stored separately, but combined (summed after necessary phase adjustment). Quadrature receivers of standard NMR spectrometers supply two output signals with phases shifted by 90°, therefore each transient represents a *complex signal* with *real* and *imaginary* component.

- In order to introduce the *second dimension*, the signal is acquired repeatedly with increasing (or decreasing) length of the delay t_1. The individual signals are called *increments* in the NMR literature. The increments are stored separately as an *array* of one-dimensional data (data matrix). Each increment is stored as two records (sums of transients) with phases shifted by 90°, providing (after appropriate phase correction) *real* and *imaginary* component of the data in the *direct dimension*.

- In order to achieve *frequency discrimination* in the *indirect dimension* (using the States-Haberkorn-Ruben method described in Section 4.7), each increment is recorded twice with a different phase of a certain pulse. The individual increments are called *cosine modulated* and *sine modulated* in the NMR literature. The States-Haberkorn-Ruben method of frequency discrimination is based on changing a pulse phase (like phase cycling), but (unlike phase cycling) data collected with different phases are stored separately. The real components of the cosine- and sine-modulated increments provide the real and imaginary component of the data in the *indirect dimension* as described in Section 4.7.

The most common applications of phase cycling are described in the following sections.

4.10   Quadrature artifacts and CYCLOPS*

Phase cycling is important in suppressing various instrumental artifacts. For example, two channels of the receiver are never identical. They differ in the amplitudes (*imbalance*) and in the background *direct current*. Instead of the perfect signal

$$A\sin(\Omega t), -A\cos(\Omega t) \tag{4.13}$$

we obtain an imperfect signal

$$D + (A + \Delta)\sin(\Omega t), -D + (A - \Delta)(-\cos(\Omega t)). \tag{4.14}$$
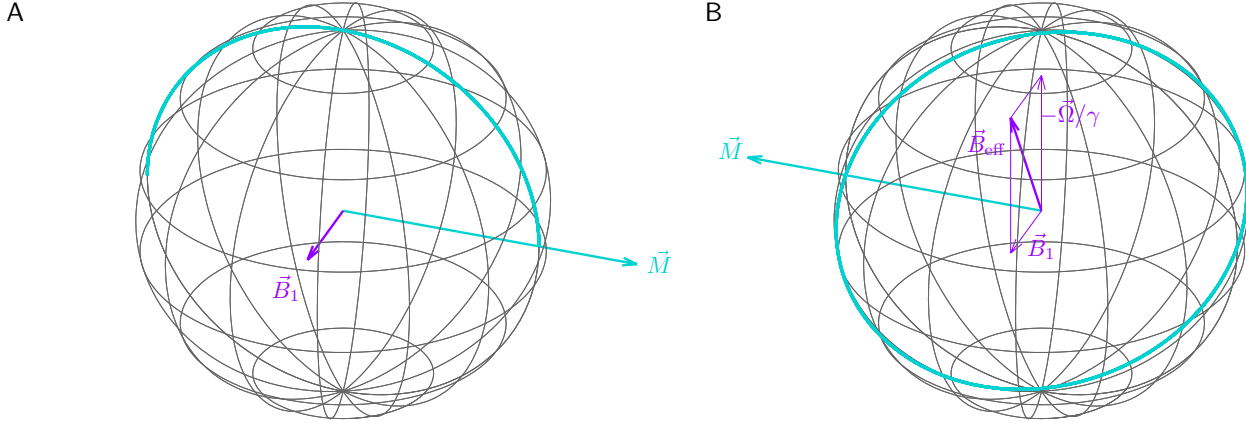
A

B

Figure 4.9: Evolution of refocusing $180°$ pulse on magnetization vectors with precession frequency exactly matching the used radio frequency (A) and with a frequency offset Ω (B), for $\omega_1 = \Omega/\sqrt{3}$. If ω_1 rotates magnetization of the former nucleus by $180°$, then $\omega_\mathrm{eff} = \sqrt{1 + 3\Omega} = 2\Omega$ rotates magnetization of the latter nucleus by $2 \times 180° = 360°$, i.e., by the full circle. The evolution is shown in a coordinate frame rotating with $\vec{\omega}_\mathrm{rot} = -\vec{\omega}_\mathrm{radio}$. In both cases, magnetization rotates about the thick purple arrow with the angular frequency proportional to the length of the arrow.

The consequence of the direct current D is a presence of so-called *quadrature glitch* (an artificial peak at $\Omega = 0$) and the consequences of the imbalance Δ are so-called *quadrature images* (artificial peaks at the false frequency $-\Omega$).

The imperfections can be removed by cycling the phases of the transmitter (during the excitation pulse) and of the receiver simultaneously, this phase cycle is called *CYCLOPS*:

transmitter	acquired as	receiver	stored as	
$+x$	$a: +D + (+A + \Delta)\sin(\Omega t)$	$+x$	$+D + (+A + \Delta)\sin(\Omega t),$	$-D + (-A + \Delta)\cos(\Omega t)$
	$b: -D - (+A - \Delta)\cos(\Omega t)$			
$+y$	$a: +D + (+A + \Delta)\cos(\Omega t)$	$+y$	$-D + (+A - \Delta)\sin(\Omega t),$	$-D + (-A - \Delta)\cos(\Omega t)$
	$b: -D + (+A - \Delta)\sin(\Omega t)$			
$-x$	$a: +D - (+A + \Delta)\sin(\Omega t)$	$-x$	$-D + (+A + \Delta)\sin(\Omega t),$	$+D + (-A + \Delta)\cos(\Omega t)$
	$b: -D + (+A - \Delta)\cos(\Omega t)$			
$-y$	$a: +D - (+A + \Delta)\cos(\Omega t)$	$-y$	$+D + (+A - \Delta)\sin(\Omega t),$	$+D + (-A - \Delta)\cos(\Omega t)$
	$b: -D - (+A - \Delta)\sin(\Omega t)$			
		sum:	$4A\sin(\Omega t),$	$-4A\cos(\Omega t)$

4.11 Pulse imperfections and EXORCYCLE*

Phase cycling also removes imperfection of pulses. For example, each $180°$ pulse has a limited power and it affects ideally only magnetic moments exactly *on resonance* (with the precession frequency exactly matching frequency of the applied radio waves). All other magnetic moments experience some offset effects, as discussed in Section 4.5. The extreme cases of ideal performance (*on resonance*) and no effect (*off resonance*) are presented in Figure 4.9A and B, respectively. Let us now analyze how phase cycling affects the offset effects.

Let us analyze as an example a signal of uncoupled proton detected after a refocusing echo (Figure 3.1B). If the $180°$ pulse is applied *on resonance*, the echo refocuses the magnetization to M_y (see Section 3.4), which then yields a signal oscillating as $-A\sin(\Omega t)$ in channel a (detecting the M_x component of the magnetization vector) and as $A\cos(\Omega t)$ in channel b (detecting the $-M_y$ component). If the $180°$ pulse is applied *off resonance*, it does not have
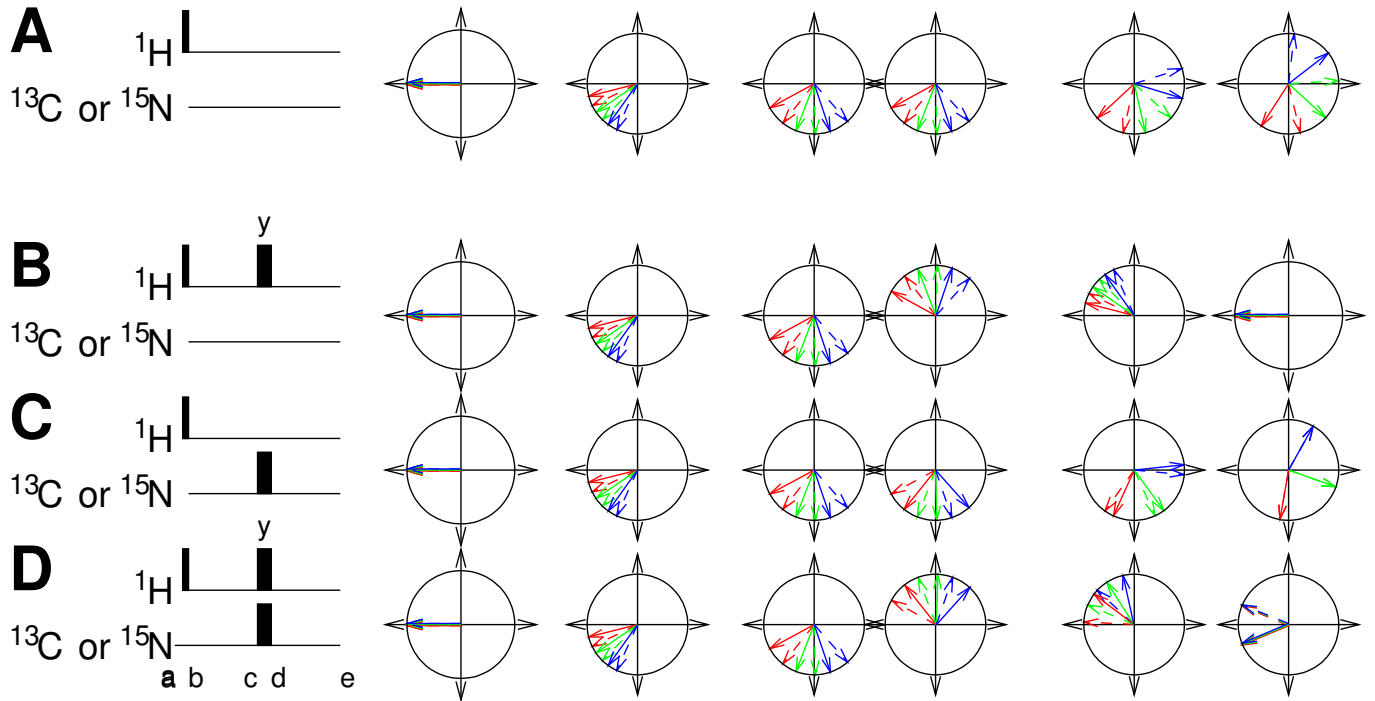
Figure 4.10: Spin echoes with the 180° ^{1}H pulse applied with a 90° the phase shift, as a y pulse. The symbols are explained in Figure 3.1. Note that 180° ^{1}H $-x$ and $-y$ pulses have the same effect as the $-x$ and $-y$ pulses, respectively, and that all phases of the 180° ^{13}C (or ^{15}N) have the same effect.

any effect and the magnetization freely evolves during the echo. Therefore, the detected signal is not a function of the time t (measured from switching the receiver on), it is a function of time $t + 2\tau$, where τ is the length of the one of the delays constituting the echo. The *off-resonance* signal thus yields a signal oscillating as $A\sin(\Omega t + \phi)$ in channel a and as $-A\cos(\Omega t)$ in channel b, where $\phi = 2\Omega\tau$ is a constant phase shift, distorting the signal.

What if we repeat the experiment with the phase of the 180° pulse shifted by 90° (a "y" pulse)? If a 180° y pulse is applied *on resonance*, it flips the M_x components to $-M_x$ in the middle of the echo and leaves M_y as M_y (Figure 4.10). At the end of the echo, the magnetization is refocused in the $-y$ direction. Therefore the signal oscillates as $A\sin(\Omega t)$ in channel a and as $-A\cos(\Omega t)$ in channel b during the detection. Again, the magnetic moments that are *off resonance* are not influenced by the pulse and yield a signal oscillating as $A\sin(\Omega t + \phi)$ in channel a and as $-A\cos(\Omega t)$ in channel b, as described above.

The following analysis shows that the desired on-resonance signal is preserved and the undesired phase-shifted off-resonance signal is canceled if the transmitter phase cycles as x, y and the receiver phase cycles as $x, -x$

On resonance:

transmitter	receiver	acquired as	stored as
$+x$	$+x$	$a : -A\sin(\Omega t)$	$-A\sin(\Omega t), +A\cos(\Omega t)$
		$b : +A\cos(\Omega t)$	
$+y$	$-x$	$a : +A\sin(\Omega t)$	$-A\sin(\Omega t), +A\cos(\Omega t)$
		$b : -A\cos(\Omega t)$	
		sum:	$-2A\sin(\Omega t), 2A\cos(\Omega t)$

Off resonance:

transmitter	receiver	acquired as	stored as
$+x$	$+x$	$a: +A\sin(\Omega t + \phi)$	$+A\sin(\Omega t + \phi), -A\cos(\Omega t + \phi)$
		$b: -A\cos(\Omega t + \phi)$	
$+y$	$-x$	$a: +A\sin(\Omega t + \phi)$	$-A\sin(\Omega t + \phi), +A\cos(\Omega t + \phi)$
		$b: -A\cos(\Omega t + \phi)$	
		sum:	0

Another common imperfection is inaccurate calibration of the pulse. A miscalibrated $180°$ pulse rotates the magnetization vector too much or too little. For example, if the $180°$ x pulse in Figure 3.1B is longer by Δt_p, it does not flip $-M_y$ exactly to M_y, but it yields $M_y\cos(\omega_1\Delta t_\mathrm{p}) + M_z\sin(\omega_1\Delta t_\mathrm{p})$. If the same miscalibrated $180°$ pulse is applied with a phase shifted by $180°$ (as a $-x$ pulse), it rotates M_y in the opposite direction and the unwanted M_z component thus has the opposite orientation: $M_y\cos(\omega_1\Delta t_\mathrm{p}) - M_z\sin(\omega_1\Delta t_\mathrm{p})$. If this happens in a more complex pulse sequence, where a $90°$ y pulse is applied after the echo, the artificial M_z components is converted to M_x and yields an undesired signal, shifted by $90°$ from the desired one. Fortunately, the unwanted M_x component can be removed by cycling the transmitter as $x, -x$ without changing the receiver phase, as shown below.

Desired M_y:

transmitter	receiver	acquired as	stored as
$+x$	$+x$	$a: -A\cos(\omega_1\Delta t_\mathrm{p})\sin(\Omega t)$	$-A\cos(\omega_1\Delta t_\mathrm{p})\sin(\Omega t), +A\cos(\omega_1\Delta t_\mathrm{p})\cos(\Omega t)$
		$b: +A\cos(\omega_1\Delta t_\mathrm{p})\cos(\Omega t)$	
$-x$	$+x$	$a: -A\cos(\omega_1\Delta t_\mathrm{p})\sin(\Omega t)$	$-A\cos(\omega_1\Delta t_\mathrm{p})\sin(\Omega t), +A\cos(\omega_1\Delta t_\mathrm{p})\cos(\Omega t)$
		$b: +A\cos(\omega_1\Delta t_\mathrm{p})\cos(\Omega t)$	
		sum:	$-2A\cos(\omega_1\Delta t_\mathrm{p})\sin(\Omega t), 2A\cos(\omega_1\Delta t_\mathrm{p})\cos(\Omega t)$

Undesired M_z ($\longrightarrow M_x$ after application of a $90°$ y pulse):

transmitter	receiver	acquired as	stored a...
$+x$	$+x$	$a: -A\sin(\omega_1\Delta t_\mathrm{p})\sin(\Omega t)$	$-A\sin(\omega_1\Delta t_\mathrm{p})\sin(\Omega t), -A...$
		$b: -A\sin(\omega_1\Delta t_\mathrm{p})\cos(\Omega t)$	
$-x$	$+x$	$a: +A\sin(\omega_1\Delta t_\mathrm{p})\sin(\Omega t)$	$+A\sin(\omega_1\Delta t_\mathrm{p})\sin(\Omega t), +A...$
		$b: +A\sin(\omega_1\Delta t_\mathrm{p})\cos(\Omega t)$	
		sum:	0

The phase cycles suppressing offset and miscalibration effects are combined into a four-step cycle removing various "ghost peaks", called EXORCYCLE:

transmitter:		receiver:	
	x		x
	y		$-x$
	$-x$		x
	$-y$		$-x$

4.12 Axial peaks*

Another source of undesired signals is relaxation (return to the equilibrium distribution of magnetic moments). For example, magnetic moments of uncoupled protons in the HSQC experiments (Figure 4.8) after the first INEPT module are polarized in the direction y (they are not affected by the $90°$ y pulse). During t_1, they start to redistribute due to the relaxation and the equilibrium longitudinal (vertical) polarization starts to build up. As a consequence, a certain M_z component is created. It is inverted to $-M_z$ by the cyan pulse in Figure 3.3, but it is not modulated by any frequency during t_1 (it does not rotate about $\vec{B}_0$). The next proton $90°$ pulse flips the artificial $-M_z$ component it to $+M_y$, its evolution is refocused during the second INEPT, and it yields a signal oscillating with proton frequency during t_2. However, amplitude of this signal is not modulated by the ^{13}C or ^{15}N frequency. Therefore, the Fourier transformation converts this signal to an *axial peak*, i.e. a peak at zero ^{13}C or ^{15}N frequency in the two-dimensional spectrum. The origin of the axial peak closely resembles the miscalibration artifacts (unwanted M_z component
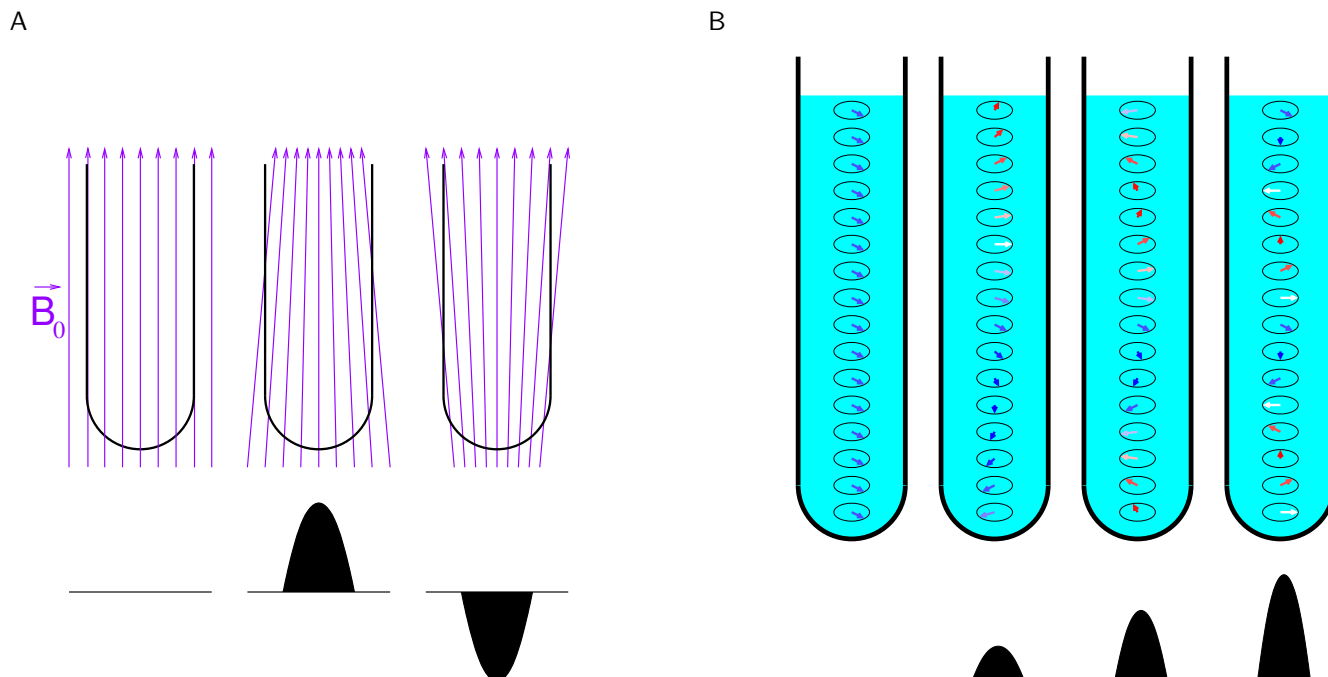
A

B

Figure 4.11: Magnetic field gradients in the vertical (z) direction. A, magnetic induction lines and the corresponding schematic drawings of the gradients (used to present the gradients in pulse sequence diagrams) are shown in purple and black, respectively. B, local transverse polarizations (magnetization) at different positions in the sample tube for increasing gradients (indicated by the black schematic drawings below the sample tubes). The arrows representing the transverse polarization (magnetization) vectors are color-coded so that blue corresponds to M_x, red corresponds to $-M_x$, and white corresponds to $\pm M_y$. The round shape of the gradient symbols indicates that the gradients were applied with smoothly changing magnetic field inhomogeneity.

converted to measurable signal by a 90° pulse). Therefore, the axial peaks are removed by the same cycle as the miscalibration artifacts (by cycling the transmitter as $x, -x$ without changing the receiver phase). In Figure 4.8B, this cycle is combined (nested) with cycling the 90° pulses discussed in Section 4.9.

4.13   Pulsed field gradients

Resonance frequencies of nuclei depend on properties of the molecule (inherent properties of nuclei and interactions of nuclei with their microscopic environment) and on the external magnetic field. The external magnetic field is what we control and the molecular properties is what we study. We try to keep the external magnetic field as homogeneous as possible so that all nuclei feel the same external field $\vec{B}_0$ and their frequencies are modulated by their molecular environment only. Now we learn a trick of the spin alchemy which is based on violating this paradigm.

It is possible to create a magnetic field that is inhomogeneous in a controlled way. We will discuss an example when the field is linearly increasing along the z axis (Figure 4.11). A *linear gradient of magnetic field* (or simply "a gradient" in the NMR jargon) is applied in the z direction. The nuclei close to the bottom of the sample tube feel a weaker magnetic field and have a lower resonance frequency while the nuclei close to the top feel a stronger field and have a higher resonance frequency in such case. We can say that *frequency carries information about position along the z axis*. In the NMR experiments, the gradients are applied for a limited time, as short *pulses* of magnetic field perturbation. Therefore, they are described as *pulsed field gradients* in the NMR literature. Moreover, the gradients are usually not applied as a sudden perturbation of a given strength (magnetic field change per unit distance), but the inhomogeneity is increased and then decreased smoothly (cf. the shape of symbols representing gradients in Figure 4.11).

If the gradient in the z direction is applied when the total magnetization vector rotates in the xy plane, nuclei at different height of the sample acquire different frequencies of rotation. In the individual slices, the coherence is
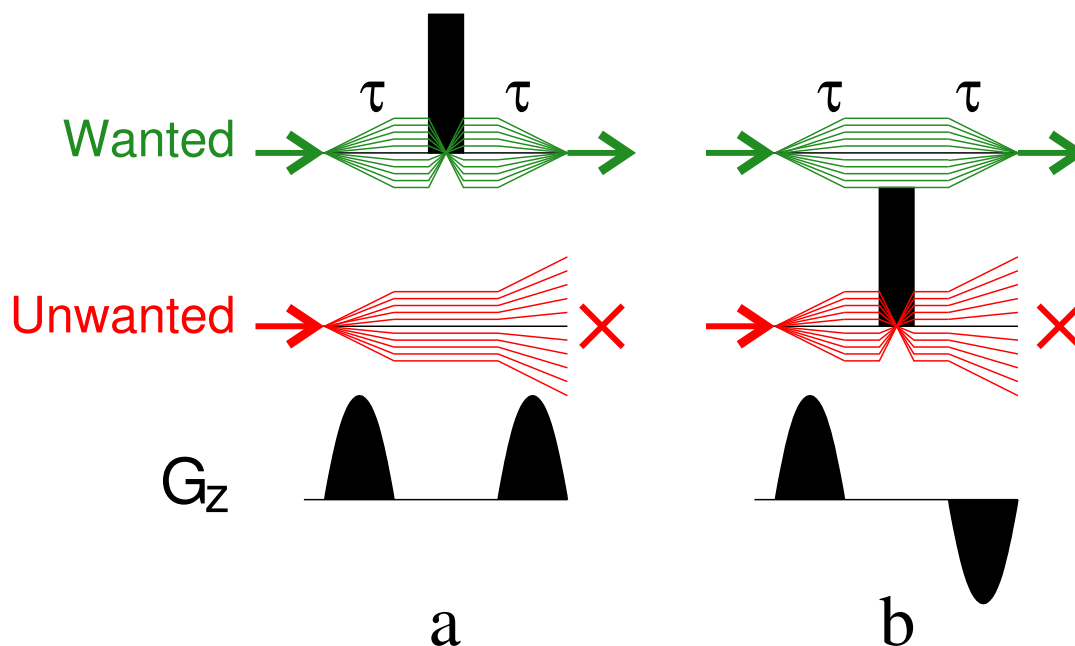
Figure 4.12: Gradient echoes. Black rectangles and round shapes indicate pluses of radio waves and magnetic field gradients, respectively. Evolution of the phase of the desired and undesired transverse coherence (describing direction of the corresponding transverse polarization) is shown as green and red lines, respectively. Values of the phase at different positions in the sample tubes correspond to the distances of the green and red lines from the central black line.

preserved. But after a while, vectors of local transverse polarization (magnetization) rotating at different frequencies in *different slices* of the sample would point to all possible directions and they would no longer add up to a measurable total magnetization. The gradient destroys the bulk (macroscopic) *transverse* magnetization and the NMR signal. The longitudinal polarizations are not influenced.

At the first glance, it seems that dephasing of coherences and the consequent loss of the signal are completely useless and should be avoided in NMR experiments. It is not true, gradients are very useful if they are applied correctly. The first trick is to apply gradients that destroy coherences we are not interested in. Such gradients have *cleaning* effects and remove unwanted contributions from the spectra.

Another trick is to recover the magnetization back. If we apply the same gradient for the same time, but in the opposite direction $(-z)$, later in the pulse sequence, the magnetic vectors are refocused and the signal appears again. We see how an *echo* can be created from two opposite gradients. There are also other ways of creating gradient echoes, presented in Figure 4.12. Instead of using two opposite gradients, two identical gradients can be applied during the refocusing echo (described in Section 3.4), one in the first half of the echo and the other one in the other half (echo "a" in Figure 4.12). The gradients do nothing else but adding another source of frequency variation, on the top of the chemical shift and scalar coupling effects. Magnetic moments of the nuclei affected by the 180° pulse in the middle of the echo get always refocused, no matter what was the origin of the frequency variability. On the other hand, magnetic moments of nuclei not affected by the 180° pulse (e.g., ^{13}C or ^{15}N nuclei if radio ways are applied at the proton frequency) feel two identical gradients and get dephased. We see the selective cleaning effect of the gradient echo, e.g. preserving the ^1H coherences but destroying unwanted ^{13}C coherences. Gradients incorporated into the decoupling echo (described in Section 3.5) have exactly the opposite effect (echo "b" in Figure 4.12). In this spirit, gradients are frequently added to the echoes in the pulse sequence to clean imperfections of the used pulses.

Application of a cleaning gradient and of gradient echoes in a real NMR experiment is presented in Figure 4.13A (magenta and cyan symbols, respectively). Note that the cleaning (magenta) gradient is applied when no coherence (transverse polarization) should be present. The cyan gradients are applied during the simultaneous echoes and refocus coherences that evolve due to the *J*-coupling.
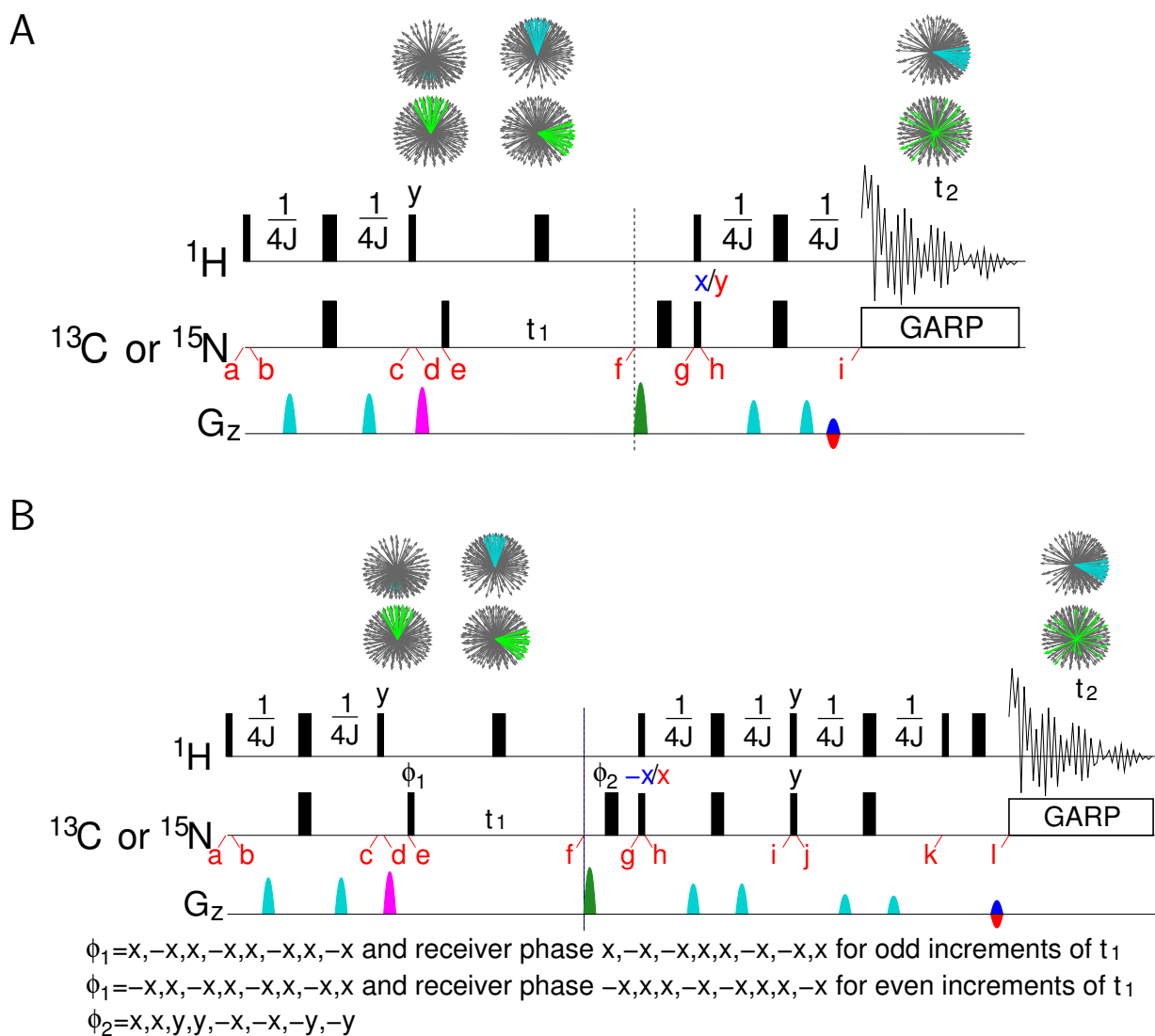
Figure 4.13: Gradient enhanced HSQC experiment (A) and its PEP version (B). Cleaning gradients and gradient echoes are shown in magenta and cyan, respectively. The heteronuclear gradient echo consists of a gradient shown in green, applied during the refocusing echo between time instants "f" and "g" (when the coherence evolves with the ^{13}C or ^{15}N frequency), and of another gradient applied during the last echo (when transverse polarization evolves with the proton frequency). The latter gradient is shown in blue and red, depending on the phase of the second ^{13}C or ^{15}N 90° pulse. Other symbols are used as explained in Figure 4.8

4.14 Frequency discrimination by pulsed field gradients*

Figure 4.13A also shows another, more tricky use of gradients implemented in an improved version of the HSQC experiment (blue/red and green symbols). The idea is to apply one gradient during the time when the desired coherence rotates with the frequency of ^{13}C (or ^{15}N) and another gradient during the time when the total magnetization rotates with the frequency of protons. In order to do it, we must generate a space in the pulse sequence by including a refocusing echo (a typical example of using refocusing echoes in situation when we need more space but do not want to change evolution). The two applied gradients are not identical, they change the magnetic fields to different extent. The deviations of the field must be exactly in the ratio of resonance frequencies of ^{13}C and ^{1}H. Then, the gradients form a *heteronuclear gradient echo.* Note what happens to various coherences of protons. The coherence which contributed to the polarization transferred to ^{13}C and back experiences the gradients as an echo and gets refocused. On the other hand, population of protons whose polarization was not transferred to ^{13}C (e.g. protons of water that are not ^{13}C-bonded) feels just two gradients of different strengths and its coherence is destroyed. The gradient echo makes the experiment selective for protons correlated with carbons and suppresses the signal of uncorrelated protons.

The green and blue/red gradients in Figure 4.13A have also and important impact on acquiring the hypercomplex data. The gradients are applied in echoes after t_1 and before t_2 when coherences rotate with the proton and ^{13}C (or ^{15}N) frequency offsets, respectively. The green gradient is applied only in one half of the echo, so the precession of the magnetic moments is not refocused, but made dependent on their position along the z axis. It is no longer the y component of the coherence at point "f" what is selected because individual magnetic moments rotated further by some angle ϕ_1 (see Figure 4.11B). This angle is proportional to γ_C and to the gradient strength, depends on the actual position of the magnetic moment, and adds as a phase to the coherence rotation angle $\Omega_C t_1$. As a consequence, the signal is modulated by $\overline{\cos(\Omega_C t_1 + \phi_1)}$, were the horizontal bar indicates that we have to sum values of the cosine all magnetic moments in the sample (differing because ϕ_1 depends on the vertical position). If no blue/red gradient were applied in Figure 4.13A, the signal would be negligible because ϕ_1 adopts all values between $0°$ and $180°$ (see Figure 4.11B), and the sum of the cosines of all angles (actually the average value of the cosine function) is zero. The blue/red gradient adds a similar phase ϕ_2 to $\Omega_H t_2$. We assume that ϕ_2 depends on the position exactly like ϕ_1 (i.e., that the molecules do dot diffuse to a different position in the short time between the gradients), so $\phi_1 = \phi_2$ if the gradient strengths are set to be in the ratio $\gamma_H : \gamma_C$. Therefore, the outputs of the channels of the quadrature receivers are

$$a : A\overline{\cos(\Omega_C t_1 + \phi_1)\cos(\Omega_H t_2 + \phi_2)}, \tag{4.15}$$

$$b : A\overline{\cos(\Omega_C t_1 + \phi_1)\sin(\Omega_H t_2 + \phi_2)}. \tag{4.16}$$

In order to see how the gradients refocus, we apply basic trigonometric relations:

$$a : \frac{A}{2}\overline{\cos(\Omega_C t_1 + \Omega_H t_2 + \phi_1 + \phi_2)} - \frac{A}{2}\overline{\cos(\Omega_C t_1 - \Omega_H t_2 + \phi_1 - \phi_2)}, \tag{4.17}$$

$$b : \frac{A}{2}\overline{\sin(\Omega_C t_1 + \Omega_H t_2 + \phi_1 + \phi_2)} - \frac{A}{2}\overline{\sin(\Omega_C t_1 - \Omega_H t_2 + \phi_1 - \phi_2)}. \tag{4.18}$$

Strengths of the green and blue gradients are set to be in the ratio $\gamma_H : \gamma_C$, so $\phi_1 = \phi_2$. The cosine function with $\phi_1 + \phi_2 = 2\phi_1$ averages to zero, and (returning to the products of goniometric functions)

$$a : \frac{A}{2}\cos(\Omega_C t_1 - \Omega_H t_2) = \frac{A}{2}\cos(\Omega_C t_1)\cos(\Omega_H t_2) + \frac{A}{2}\sin(\Omega_C t_1)\sin(\Omega_H t_2) = \frac{A_c}{2}\cos(\Omega_H t_2) + \frac{A_s}{2}\sin(\Omega_H t_2), \tag{4.19}$$

$$b : \frac{A}{2}\sin(\Omega_C t_1 - \Omega_H t_2) = \frac{A}{2}\sin(\Omega_C t_1)\cos(\Omega_H t_2) - \frac{A}{2}\cos(\Omega_C t_1)\sin(\Omega_H t_2) = \frac{A_s}{2}\cos(\Omega_H t_2) - \frac{A_c}{2}\sin(\Omega_H t_2). \tag{4.20}$$

Using terminology introduced in Section 4.7, complex Fourier transform of the acquired signal is

$$\longrightarrow \frac{1}{2}(A_c X_2 + A_s Y_2) + \frac{i}{2}(A_s X_2 - A_c Y_2) \longrightarrow \frac{1}{2}(X_1 X_2 + Y_1 Y_2) + \frac{i}{2}(Y_1 X_2 - X_1 Y_2). \tag{4.21}$$

This closely resembles Eq. 4.9, showing that the heteronuclear gradient echo in Figure 4.13A provides discrimination between positive and negative Ω_C *without recording each increment twice*, but with the undesired shape of the peaks due to the Y_1Y_2 contribution, as discussed in Section 4.7. The remedy is to repeat the acquisition with the usual 90° phase shift of the 90° ^{13}C (or ^{15}N) pulse (red "y" in Figure 4.13A) and with reversed direction of the second gradient (shown in red in Figure 4.13A). The signal modulation in the repeated experiment is

$$a: A\overline{\sin(\Omega_C t_1 + \phi_1)\cos(\Omega_H t_2 + \phi_2)} = \frac{A}{2}\overline{\sin(\Omega_C t_1 + \Omega_H t_2 + \phi_1 + \phi_2)} + \frac{A}{2}\overline{\sin(\Omega_C t_1 - \Omega_H t_2 + \phi_1 - \phi_2)}, \quad (4.22)$$

$$b: A\overline{\sin(\Omega_C t_1 + \phi_1)\sin(\Omega_H t_2 + \phi_2)} = -\frac{A}{2}\overline{\cos(\Omega_C t_1 + \Omega_H t_2 + \phi_1 + \phi_2)} + \frac{A}{2}\overline{\cos(\Omega_C t_1 - \Omega_H t_2 + \phi_1 - \phi_2)}. \quad (4.23)$$

Strengths of the green and red gradients are now set to be in the ratio $\gamma_H : -\gamma_C$, so $\phi_1 = -\phi_2$. The cosine function with $\phi_1 - \phi_2 = 2\phi_1$ averages to zero, and (returning to the products of goniometric functions)

$$a: \frac{A}{2}\sin(\Omega_C t_1 + \Omega_H t_2) = \frac{A}{2}\sin(\Omega_C t_1)\cos(\Omega_H t_2) + \frac{A}{2}\cos(\Omega_C t_1)\sin(\Omega_H t_2) = \frac{A_s}{2}\cos(\Omega_H t_2) + \frac{A_c}{2}\sin(\Omega_H t_2), \quad (4.24)$$

$$b: -\frac{A}{2}\cos(\Omega_C t_1 + \Omega_H t_2) = -\frac{A}{2}\cos(\Omega_C t_1)\cos(\Omega_H t_2) + \frac{A}{2}\sin(\Omega_C t_1)\sin(\Omega_H t_2) = -\frac{A_c}{2}\cos(\Omega_H t_2) + \frac{A_s}{2}\sin(\Omega_H t_2). \quad (4.25)$$

If we store the data with the y receiver phase $(b, -a)$, the result of both runs can be summarized as

x/y	receiver	acquired as	stored as records r_j
$+x$	$+x$	$a: +\frac{A_c}{2}\cos(\Omega_H t_2) + \frac{A_s}{2}\sin(\Omega_H t_2)$	$r_1, r_2 =$
		$b: +\frac{A_s}{2}\cos(\Omega_H t_2) - \frac{A_c}{2}\sin(\Omega_H t_2)$	$+\frac{A_c}{2}\cos(\Omega_H t_2) + \frac{A_s}{2}\sin(\Omega_H t_2), +\frac{A_s}{2}\cos(\Omega_H t_2) - \frac{A_c}{2}\sin(\Omega_H t_2)$
$+y$	$+y$	$a: +\frac{A_s}{2}\cos(\Omega_H t_2) + \frac{A_c}{2}\sin(\Omega_H t_2)$	$r_3, r_4 =$
		$b: -\frac{A_c}{2}\cos(\Omega_H t_2) + \frac{A_s}{2}\sin(\Omega_H t_2)$	$-\frac{A_c}{2}\cos(\Omega_H t_2) + \frac{A_s}{2}\sin(\Omega_H t_2), -\frac{A_s}{2}\cos(\Omega_H t_2) - \frac{A_c}{2}\sin(\Omega_H t_2)$

The records r_1, r_2, r_3, and r_4 are then combined to obtain the desired hypercomplex set:

$$\left. \begin{array}{rcl} r_1 - r_3 &=& A_c\cos(\Omega_H t_2) \\ -r_2 - r_4 &=& A_c\sin(\Omega_H t_2) \\ r_2 - r_4 &=& A_s\cos(\Omega_H t_2) \\ r_1 + r_3 &=& A_s\sin(\Omega_H t_2) \end{array} \right\} (A_c + iA_s)(\cos(\Omega_H t_2) + i\sin(\Omega_H t_2)). \quad (4.26)$$

The hypercomplex Fourier transformation is performed exactly as described by Eq. 4.10. The experiment presented in Figure 4.13A thus may seem equivalent to the States-Haberkorn-Ruben method introduced in Section 4.7. However, the States-Haberkorn-Ruben method is more sensitive. Although the hypercomplex data obtained by both methods are identical, including signal intensity, there is an important difference between them. When the States-Haberkorn-Ruben approach is applied, each record (r_1, r_2, r_3, and r_4), acquired with some noise σ, directly provides one component of the hypercomplex data. However, the experiment presented in Figure 4.13A provides such components as *combinations* (sums or differences) of two records with independent noise. Adding or subtracting data data with comparable but independent random noise increases the noise level by a factor of $\sqrt{2}$. Therefore, the *signal-to-noise* ratio of the data obtained as described in Figure 4.13A is lower by a factor of $\sqrt{2}$ than the data obtained as described in Figure 4.8.

4.15   Preservation of equivalent pathways*

In order to use gradients with the same theoretical sensitivity (neglecting relaxation) as provided by the States-Haberkorn-Ruben method, a trick known as *preservation of equivalent pathways* (PEP) can be employed. It is achieved

by inserting one more INEPT module followed by 90° ^{1}H pulse before detection (Figure 4.13B). This trick works only for isolated spin pairs such as ^{1}H-^{13}C or ^{1}H-^{15}N (e.g. not for CH$_2$ or NH$_2$ groups). As discussed in Section 3.8, the second pair of 90° ^{1}H and ^{13}C (or ^{15}N) pulses acts differently on y and x components of the ^{13}C (or ^{15}N) anti-phase coherences. The PEP method tracks both components and eventually converts them to measurable signal.

- The y component is converted to ^{1}H anti-phase coherence (time point "h" in Figure 4.13), which evolves to the "visible" ^{1}H in-phase coherence (x polarization) at point "i". In Figure 4.13A, signal detection starts at this moment. In Figure 4.13B, the proton x polarization is rotated to the $-z$ direction, where it survives the additional INEPT step, and is finally returned to the xy plane by the last 90° ^{1}H x pulse. The experiment presented in Figure 4.13B is repeated with the direction of the last (red) gradient and phase of the second ^{13}C (or ^{15}N) 90° pulse inverted. This results in alternation of the proton polarization between $-y$ and $+y$ direction at the beginning of detection (point "l").

- The x component is converted to "invisible" multiple-quantum coherence (the longitudinal polarization of proton magnetic moments correlated with the ^{13}C (or ^{15}N) transverse polarization is flipped to the xy). The multiple-quantum coherence is a special correlation between ^{1}H and ^{13}C (or ^{15}N) transverse polarizations, rotating with the sum and difference of their frequency offsets. The simultaneous echo refocuses both rotations and returns the multiple-quantum coherence to its original state. In Figure 4.13A, it is never recovered. In Figure 4.13B, the pair of 90° ^{1}H and ^{13}C (or ^{15}N) y pulses converts the multiple-quantum coherence to proton anti-phase coherence. The ^{13}C (or ^{15}N) pulse must have the y phase so that it affects the component which was untouched by the previous 90° pulse. The proton 90° pulse must also have the y phase to keep the proton magnetization in the xy plane. The created proton anti-phase coherence evolves to the in-phase coherence (x polarization) at the point "i". This pathway of polarization transfer is insensitive to the phase alteration of the second ^{13}C (or ^{15}N) 90° pulse, which does not affect the x component of the ^{13}C (or ^{15}N) in-phase coherence.

In summary, the PEP method produces signal composed of two components. The first component results in a signal produced by proton magnetization starting its rotation from $-y$ and y direction depending on the phase of the second ^{13}C (or ^{15}N) 90° pulse. The second component results in a signal produced by proton magnetization starting always from direction x. Schematically, the result (with the second component, recovered by PEP, shown in green) can be summarized as

$-x/x$	receiver	acquired as	stored as records r_j
$-x$	$+x$	$a : +A_{\rm s}\cos(\Omega_{\rm H}t_2) + A_{\rm c}\sin(\Omega_{\rm H}t_2)$	$r_1, r_2 =$
		$b : -A_{\rm c}\cos(\Omega_{\rm H}t_2)+A_{\rm s}\sin(\Omega_{\rm H}t_2)$	$+A_{\rm s}\cos(\Omega_{\rm H}t_2) + A_{\rm c}\sin(\Omega_{\rm H}t_2), -A_{\rm c}\cos(\Omega_{\rm H}t_2)+A_{\rm s}\sin(\Omega_{\rm H}t_2)$
$+x$	$+x$	$a : +A_{\rm s}\cos(\Omega_{\rm H}t_2) - A_{\rm c}\sin(\Omega_{\rm H}t_2)$	$r_3, r_4 =$
		$b : +A_{\rm c}\cos(\Omega_{\rm H}t_2)+A_{\rm s}\sin(\Omega_{\rm H}t_2)$	$+A_{\rm s}\cos(\Omega_{\rm H}t_2) - A_{\rm c}\sin(\Omega_{\rm H}t_2), +A_{\rm c}\cos(\Omega_{\rm H}t_2)+A_{\rm s}\sin(\Omega_{\rm H}t_2)$

If we subtract the signals detected with the "blue" and "red" setting in Figure 4.13B, we obtain the first component, and when we add them, we obtain the second component. After shifting the phase of the first component (i.e. replacing the order of the stored sums of records $r_1 + r_3$ and $r_2 + r_4$), we obtain a series of data with the same signal-to-noise ratio (doubled signal and noise scaled by $\sqrt{2}$) as in the experiment presented in Figure 4.8:

$$\left.\begin{array}{rcl} r_1 - r_3 &=& 2A_{\rm c}\cos(\Omega_{\rm H}t_2) \\ -r_2 + r_4 &=& 2A_{\rm c}\sin(\Omega_{\rm H}t_2) \\ r_2 + r_4 &=& 2A_{\rm s}\cos(\Omega_{\rm H}t_2) \\ r_1 + r_3 &=& 2A_{\rm s}\sin(\Omega_{\rm H}t_2) \end{array}\right\} 2(A_{\rm c} + {\rm i}A_{\rm s})(\cos(\Omega_{\rm H}t_2) + {\rm i}\sin(\Omega_{\rm H}t_2)). \tag{4.27}$$

66

Lecture 5
Protein heteronuclear techniques

5.1 Proteins and NMR

We spend a lot of time talking about proteins when we discuss applications of NMR to biologically interesting macro-molecules. Proteins are well-suited for NMR studies and most features of biomolecular NMR can be explained using proteins as a model case. What makes proteins so good for NMR? The answer is hidden in the *chemical configuration* of proteins.

Proteins are composed of amino-acid residues forming a linear chain. The residues are joint by amide bonds, the special term *peptide bond* is used in the context of proteins and peptides. Let us now compare the sketched chemical configuration with the pattern of magnetic interactions among atomic nuclei in a protein.

We learned two types of interactions between nuclei in Section 2.1. The direct, through-space or dipolar, interactions average to zero in common, i.e., isotropic, solutions and we do not need to care about them now. The J-coupling, mediated by electrons in chemical bonds, deserves our attention. The armory of spin alchemy allows us to control the effect of *heteronuclear* J-couplings easily. In the context of NMR, heteronuclear systems consist of nuclei which greatly differ in the precession frequency. Pairs like ^{1}H–^{13}C, ^{1}H–^{15}N, ^{13}C–^{15}N are clearly heteronuclear. Moreover, the frequencies of aliphatic, aromatic, and carbonyl ^{13}C are so different, that pairs of these carbon nuclei behave like heteronuclear systems in most experiments. The experiments based on the heteronuclear correlation include the HSQC spectroscopy, introduced in Section 3.8, and its extensions, discussed bellow. *Homonuclear* J-couplings are harder to control, and require other approaches than those based on the HSQC pulse sequence. Therefore, it is important to identify networks of the homonuclear J-couplings in proteins. When we define such interaction network, it is sufficient to consider directly bonded nuclei for most isotopes. Protons are exceptionally sensitive and J-couplings between protons separated by up to three bonds need to be taken into account. Nuclei forming a J-coupling network are described as a *spin system* (Figure 5.1).

What are the spin systems of proteins? The ^{15}N nuclei are isolated and well spread in the protein molecule (Figure 5.1A). Every amino acid contains at least one nitrogen atom and no N–N bonds are present. The aliphatic ^{13}C nuclei form an individual spin system for each residue, these spin systems are separated by peptide bonds (Figure 5.1B). Distribution of carbonyl ^{13}C (Figure 5.1C) resembles that of ^{15}N. The ^{13}C nuclei in aromatic side-chains form isolated spin systems (Figure 5.1D). Amide and aliphatic protons constitute an individual spin system for each residue like aliphatic ^{13}C nuclei. These spin systems are separated by carbonyl (Figure 5.1E). Spin systems of aromatic protons (cyan in Figure 5.1D) are separated from the aliphatic spin systems by γ-carbon.

The following features of the protein spin systems are the keys to the success of protein NMR spectroscopy:

- Spin systems of individual amino-acid residues in the polypeptide chain are *separated*. This allows us to analyze the individual residues separately, which greatly simplifies interpretation and facilitates the *side-chain assignment*, described in Section 6.8.

- Spin systems of individual amino-acid residues in the polypeptide chain are *connected by one-bond heteronuclear J-couplings*. Using spin echoes, we can explore the heteronuclear J-couplings selectively. For example, we can distinguish J-coupling of ^{15}N to carbonyl ^{13}C from the J-coupling between ^{15}N and aliphatic ^{13}C. This greatly facilitates the *sequential assignment*, described in Section 5.5.
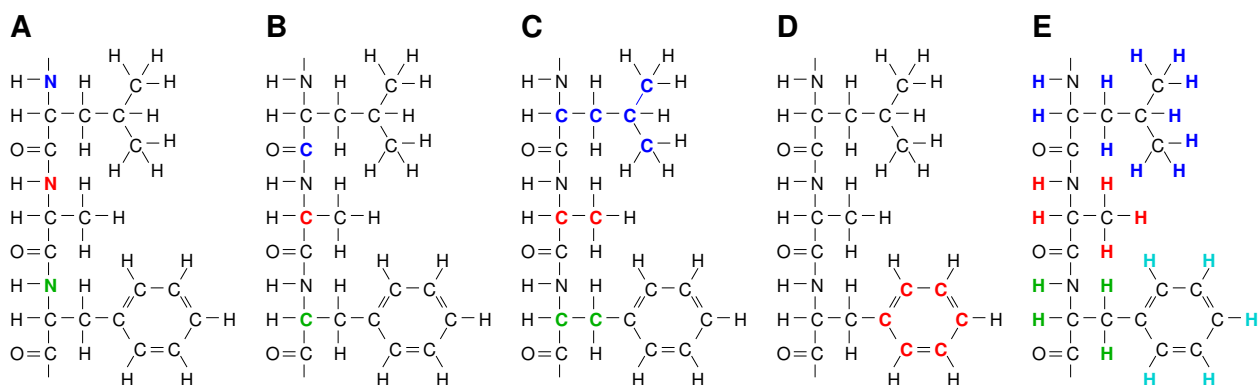
Figure 5.1: Spin systems in proteins. Isolated spin systems of the following nuclei in three consecutive residues are distinguished by different colors: ^{15}N (A), aliphatic ^{13}C (B), carbonyl ^{13}C (C), aromatic ^{13}C (D), and ^{1}H.

In the following sections, we explore the protein NMR experiments, starting from the simple ones and continuing with pulse sequences of increasing complexity.

5.2 One-dimensional proton spectra

The simple one-dimensional experiment that does not include more than excitation of protons and acquisition of their signal is the basic tool of NMR of small molecules. One-dimensional proton spectra are also acquired when studying proteins. However, the 1D protein spectroscopy relies on somewhat more sophisticated pulse sequences than the mentioned single-pulse experiment. The major reason is trivial: the biomolecular proton-detection experiments must address one important issue, presence of water. Concentration of water protons in pure water is $110\,\mathrm{M}$, five order of magnitude higher than concentration of protons in the studied proteins. The strong signal of water protons would obscure most of other signals in the spectrum without effective suppression. There are several ways to removing water signal from spectra:

- *Removing oscillations of water protons from already recorded spectra.* If the carrier frequency is chosen to match the water resonance frequency, the signal of water protons does not oscillate or oscillates with very low frequency offset of several Hertz – compared to kilohertz frequency offsets of other protons. The slow oscillation can be removed by filtering the recorded and digitized data. In pracice, a low-pass filter is applied to obtain a pure signal of water, and it is subtracted from the overall signal.

- *Presaturation* is a method of disqualifying water protons prior to excitation (Figure 5.2A). We irradiate the sample for a long time (approximately one second) with a weak radio-frequency field before we apply the $90°$ excitation pulse. The weak radiation selectively affects protons resonating at the carrier frequency, i.e., protons of water. The irradiated protons experience two opposite effects. On one hand, relaxation destroys coherence and drives the magnetic moments to the equilibrium distribution, polarized along z. On the other hand, the irradiating field continuously rotates the polarization from the z direction and thus restores coherence. Finally, the distribution of magnetic moments reaches a steady state with polarization depending on the ratios of ω_1 to the relaxation rates. If ω_1 is much greater than the relaxation rates, the steady state distribution is not polarized in any direction. Rotation of such distribution by the $90°$ excitation pulse does not create any transverse polarization. Therefore, signals of water protons do not appear in spectra. The major advantage of presaturation is its simplicity and the fact that is applied before excitation. As the acquisition starts immediately after the excitation $90°$ pulse, the signal intensity is proportional to the number of magnetic moments, i.e. to the protein concentration.
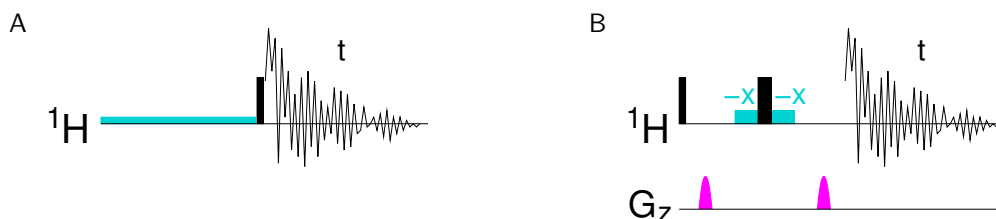
Figure 5.2: Presaturation (A) and WATERGATE (B) water suppression techniques. The radio waves selectively affecting protons of water are shown in cyan (a long very weak irradiation in panel A and a pair of selective 90° pulses with phase $-x$ in panel B). Cleaning gradients are shown in magenta.

- *WATERGATE* is an example of a more elaborate approach. The excitation pulse is followed by a refocusing echo with identical gradients in both delays (Figure 5.2B). Such sequence works as a gradient echo for all nuclei. What makes it a water suppression tool is a couple of selective 90° pulses surrounding the refocusing 180 ° pulse in the middle of the echo. If the 90° pulses are applied with a phase opposite to the phase of the 180 ° pulse, the effect of the refocusing echo is canceled. If the carrier frequency matches the water resonance frequency, protons of water feel two gradients, both of which destroy the water signal. All nuclei not affected by the selective 90° pulses experience a gradient echo and their signal get safely refocused.

We know how to get proton one-dimensional spectra, but what can we learn from them? On one hand, such simple experiments are very sensitive and very quick to run. We obtain a spectrum within several seconds or minutes. No isotope labeling is needed, so we can study proteins of any origin. On the other hand, we do not learn too much from the spectra. Thousands of relatively broad spectral lines heavily overlap, only a few protons are resolved. An example of such spectrum is presented in Figure 5.3. The peaks between -1 ppm and 5 ppm are signals of aliphatic protons, those with the lowest chemical shift values correspond to the methyl protons that are most shielded, some of them are well resolved. Peaks between 6 and 11 ppm are mostly signals of amide and aromatic protons.

In spite of the limited resolution, the one-dimensional spectra provide useful information: they serve as a quick check of quality and quantity of the protein sample (the first application in Section 1.4). An important signature of the 1D spectrum in Figure 5.3A is a broad distribution of the amide peaks covering the whole range of chemical shifts between 10 ppm and the aromatic region (approximately 6–7.5 ppm). The peaks of methyl groups also exhibit a broad distribution starting with negative chemical shifts. The large dispersion of signals tells us that the protein has a unique three-dimensional structure (probably is correctly folded). A comparison of chemical shift distribution of methyl groups in well-ordered and disordered (unfolded by thermal denaturation) protein is shown in Figure 5.3B.

As the spectrum shows peaks of all protons that are not exchanged rapidly with water, all impurities are visible. For example, the spectrum in Figure 5.3A revealed traces of glycerol. The 1D spectrum is also ideal for checking protein quantity because the area under the peaks is proportional to the concentration.[1] This does not apply to more advanced pulse sequences, where the magnetization has time to relax between excitation and detection. One-dimensional spectra are also useful when quick changes of protein structure are monitored (denaturation or folding studies), as documented in Figure 5.3B.

5.3 ^{1}H-^{15}N two-dimensional correlation (HSQC)

The two-dimensional HSQC experiment correlating ^{1}H and ^{15}N nuclei (Figure 5.4) is the basic element of the most popular strategy of protein investigation by NMR. The experiment is relatively sensitive (typical time requirements range between 15 minutes and two hours). Suppression of water signal is important. It is achieved by combination of the tricks introduced in Section 5.2 with phase cycling (Section 4.9) and pulsed-field gradients (Section 4.13).

As the amide protons slowly dissociate and exchange with the protons of water, it is useful to keep their magnetic moments in the equilibrium polarization during measurement. It is because sensitivity of the experiments is

---

[1]Strictly speaking, this is true only if water suppression is not based on additional radio wave pulses applied after excitation. As mentioned above, presaturation should be used if the spectra are used to determine protein concentration.

A
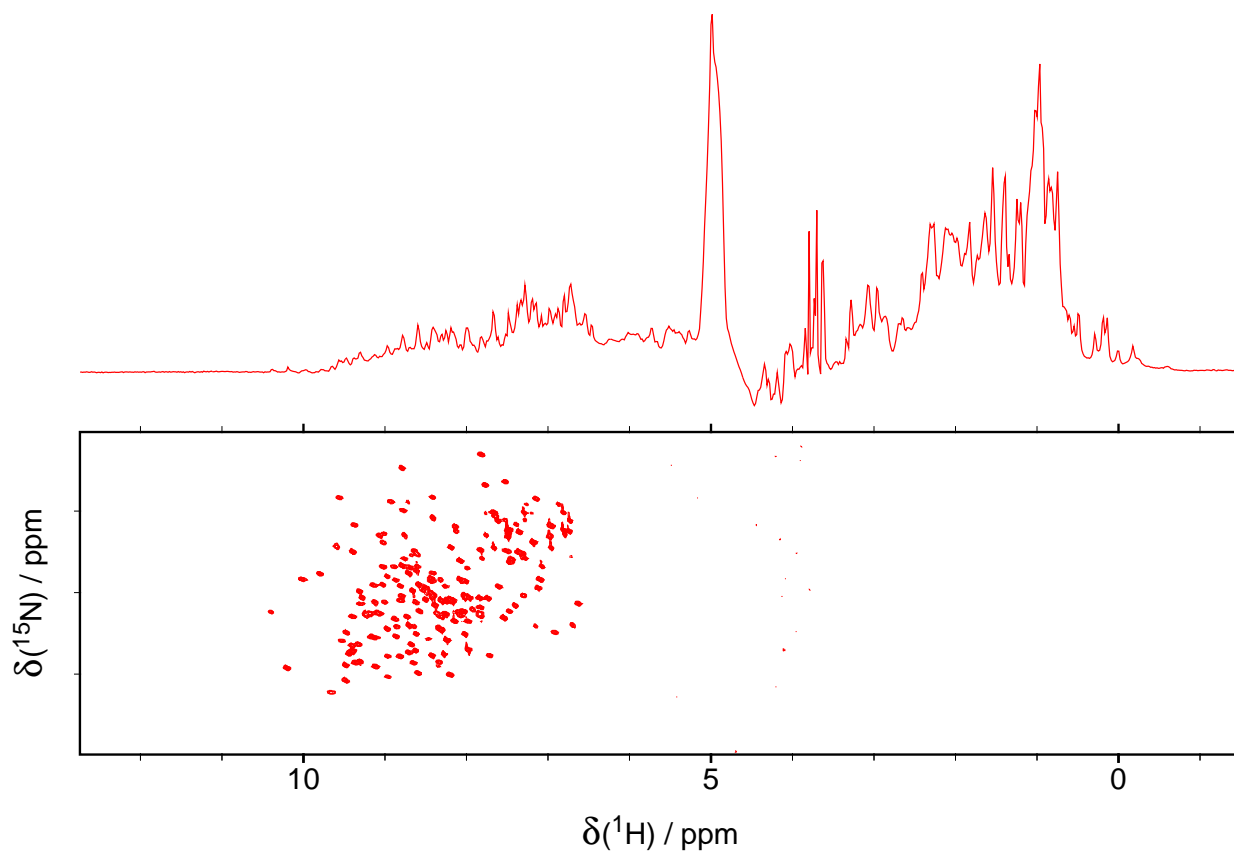
B
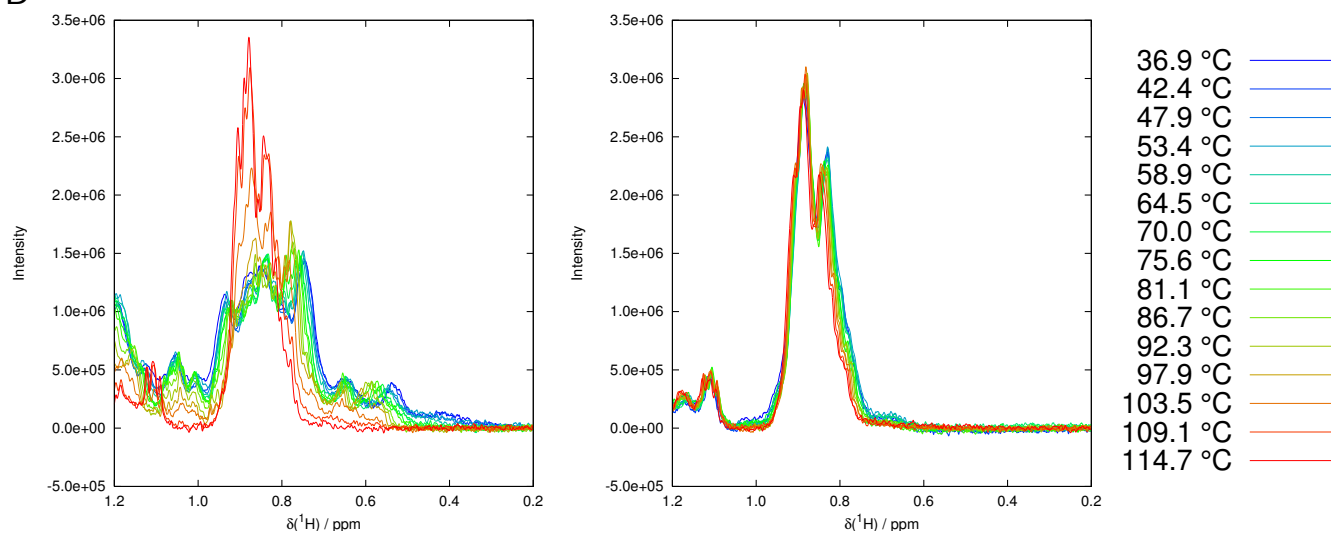
Figure 5.3: A, comparison of proton 1D (top) and ^{1}H-^{15}N 2D HSQC (bottom) spectra of the same protein (mouse Major Urinary Protein I consisting of 162 amino acids). The large peak in the 1D spectrum close to 5 ppm is incompletely suppressed signal of water, the sharp peaks between 3 and 4 ppm are signals of an impurity (glycerol not completely removed during sample preparation). B, methyl region of proton 1D spectra recorded during heating (left) and subsequent cooling (right) of barley Nonspecific Lipid Transfer Protein 1b. Native Protein (low temperatures in the left panel) has a wider distribution of chemical shifts and broader peaks than protein unfolded by thermal denaturation (high temperatures). The right panel shows that the denaturation is irreversible as the peaks remain sharp and the chemical shift distribution narrow after cooling the denatured sample.
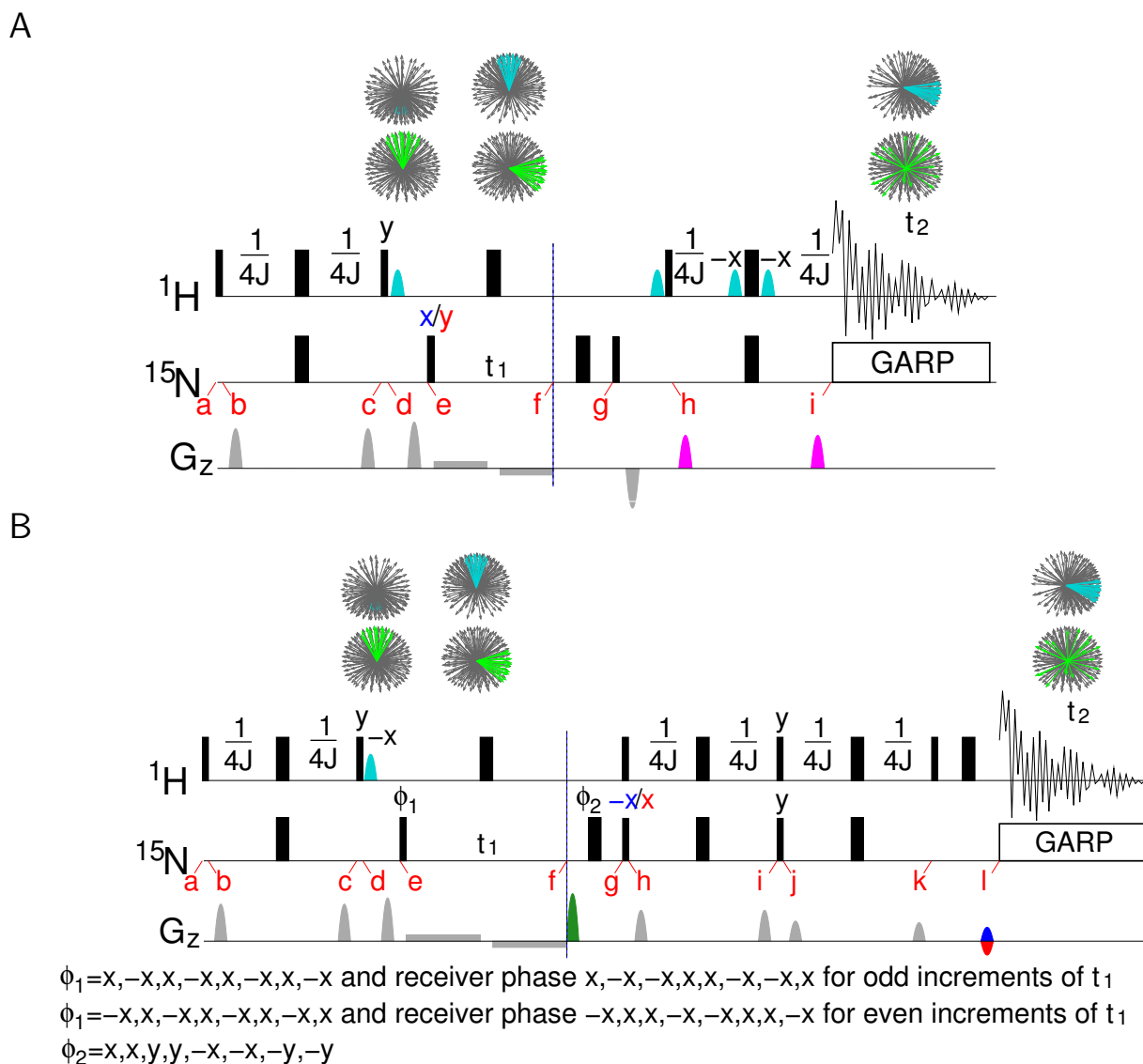
Figure 5.4: ^1H-^{15}N versions of HSQC experiments presented in Figure 4.13 with water suppression and water "flip-back" pulses. The cyan symbols represents weak $90°$ pulses of radio waves selectively affecting magnetic moments of water. The cyan pulses applied after time point d and before time point h are "flip-back" pulses controlling magnetic moments of water so that they are in their equilibrium polarization at the beginning of t_2. The cyan pulses applied after time points h and i are parts of the WATERGATE module, together with the gradients shown in magenta (cf. Figure 5.2B). Other symbols are used as explained in Figure 4.13

proportional to M_z prior to the first pulse. Therefore, amide protons, including those coming from water, should have their magnetic moments polarized along z at the beginning of the pulse sequence. The pulse sequences presented in Figure 5.4 include so-called "flip-back" pulses that control the polarization of water at the beginning of the measurement.

Another effect related to the water signal is the *radiation damping*. The concentration of water protons in protein samples is so high that its magnetization, if flipped to the xy plane, induces a large current in the receiver coil. This current, in turn, induces an oscillating magnetic field that cannot be neglected. As the frequency of the induced oscillating current is given by the precession frequency of magnetic moments of protons in water, the resulting field resonates with the precession, and rotates the water magnetization toward the z direction. In general, radiation damping may be useful as it re-established the equilibrium polarization of water. However, if the "flib-back" pulses are applied, radiation damping interferes with their effect. Therefore, we suppress radiation damping by applying pulsed-filed gradients immediately before and after $90°$ pulses and also during t_1 in the pulse sequences presented in Figure 5.4 (note that the weak gradients applied during t_1 form a gradient echo for the ^{15}N anti-phase coherence, but not for the proton transverse polarization).

Resolution in the two-dimensional ^{1}H-^{15}N HSQC spectra is dramatically improved in comparison to the one-dimensional spectra. Not only the signals are spread into two dimensions, but the number of peaks is greatly reduced (see Figure 5.3). Instead of thousands proton peaks of the one-dimensional spectra, only protons directly attached to nitrogen are visible. Since most residues have just one N–H group, namely the backbone amide, the ^{1}H-^{15}N correlation is a wonderful fingerprint of the protein. Dispersion of proton chemical shifts in the ^{1}H-^{15}N two-dimensional spectrum is a much better indicator of a regular fold of the protein than the 1D ^{1}H spectrum. Well-folded protein usually give a resolution that allows us to count the peaks. If the number of peaks corresponds to what we expect from the sequence, it is likely that the protein is complete and present in a single form. In order to predict the number of expected peaks, the following simple rules can be applied.

- Expect one peak for each residue with the exception of prolines and the N-terminal amino acid.[2]

- Add one peak for each tryptophan and arginine.

- Add two peaks for each asparagine and glutamine.

It is impossible to assign peaks to individual amino acids in the sequence just from the ^{1}H-^{15}N HSQC spectrum. Still, rough estimates of number of amino acids of a certain type can be made. Side-chain amides of asparagines and glutamines appear as pairs of peaks of the same ^{15}N frequency in the "upper right corner" of the spectrum.[3] Tryptophan indole protons (i.e., side-chain, not backbone) can be often identified as their signal are found in the "lower left corner" of the spectrum, separated from most backbone peaks. The only observable signal of the arginine side chain has a ^{15}N frequency outside the typical range of backbone ^{15}N. The spectral width usually covers only the backbone frequencies. It does not mean that the signals outside the spectral width are invisible. It is a special feature of working with digital data that signals outside the covered frequency range are *folded* into the spectrum. The apparent position of the folded peak depends on the chosen spectral width. The arginine side-chain peaks can be distinguished by slightly changing the spectral width – they "travel" along the ^{15}N axis while the unfolded peaks sit at their place.[4]

5.4 Triple resonance experiments

The tricks of transferring polarization and incrementing the length of a chosen delay can be applied twice in a pulse sequence. If the polarization is transferred via INEPT first from ^{1}H to ^{15}N and then (via another INEPT) to aliphatic ^{13}C (in position α) and modulation with ^{15}N and ^{13}C frequencies is introduced by appropriate delay incrementation,

---

[2]N–H group in the middle of backbone is a secondary amide but the N-terminal NH_3^+ is an amino group. Amino-protons readily dissociate and are exchanged with water protons before the spectrum is acquired. On the other hand, exchange half-times of amide protons vary from seconds to weeks. Therefore, amide protons appear in the spectrum but amino-protons do not.

[3]It is a tradition to plot NMR spectra with the chemical shift increasing from right to left and from top to bottom.

[4]Backbone peaks close to the edge can be also folded if the spectral width is too narrow. It is easy to distinguish folded backbone peaks of frequencies just outside the spectral with from the arginine side chain resonating approximately one spectral width away.
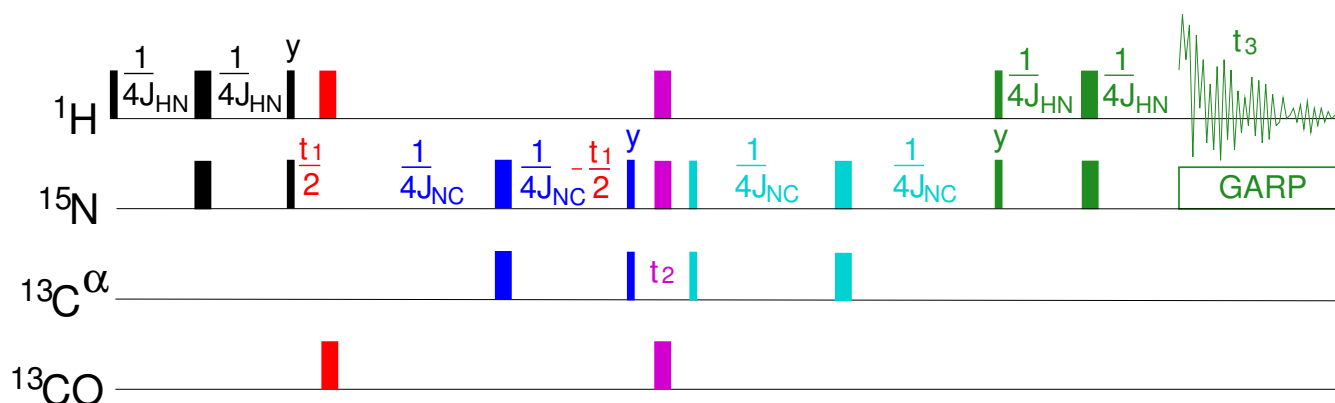
Figure 5.5: Basic idea of an HNCA triple resonance experiment. The pulse sequence can be viewed as and extension of the ^{1}H-^{15}N HSQC experiment consisting of two INEPT modules (black and green) and the t_1 delay introducing amplitude modulation by the ^{15}N frequency. Another pair of INEPT modules (blue and cyan) separated by another incremented delay t_2 (magenta) is inserted in the middle of the HSQC pulse sequence. The blue INEPT step is actually combined with t_1 to shorten the pulse sequence and reduce signal loss due to relaxation. This is a typical example of the constant-time evolution, introduced in Section 4.3. The blue and cyan INEPT modules transfer polarization from ^{15}N further to ^{13}C$^\alpha$, creating a more complex ^{13}C anti-phase coherence that evolves during t_2 with the ^{13}C$^\alpha$ frequency offset. Therefore, the signal gets amplitude-modulated by the ^{13}C$^\alpha$ chemical shift during t_2. Interactions with three neighbors of ^{13}C$^\alpha$ (^{1}H, ^{15}N, and carbonyl ^{13}C) are decoupled by the magenta 180° pulses, decoupling of the interaction with ^{13}C$^\beta$ is not applied in the presented pulse sequence (the J-couplings therefore evolves during t_2 which somewhat limits the resolution).

the ^{1}H-^{15}N-^{13}C correlation is measured. The described scenario is just an example of a *triple resonance experiment*, correlating nuclei of three different elements. The triple resonance experiments are three-dimensional, which allows further improvement of resolution. This improvement is not achieved for free. Triple resonance experiments require ^{15}N and ^{13}C isotope labeling of the sample. Time needed to measure a three-dimensional triple resonance spectrum typically varies between 10 hours and two days.[5] The sensitivity is lower because the ^{15}N-^{13}C scalar coupling is relatively weak and therefore requires long INEPT modules, when a significant fraction of the coherences relax. In spite of these drawbacks, triple-resonance experiments represent the standard approach to the assignment of frequencies in proteins consisting of 100–200 amino acids.

Although the resolution enhancement is useful, it is not the major benefit of the triple resonance experiments. The major virtue of the triple resonance experiments is the choice of the polarization transfer direction. The N–H groups can be correlated with their own C$^\alpha$ or with C$^\alpha$ of the preceding residue (using polarization transfer from ^{15}N to carbonyl ^{13}C and then to ^{13}C$^\alpha$). This opens a door to the assignment of peaks to the backbone nuclei.

5.5 Sequential assignment

This section is dedicated to the first step of any detailed study of proteins using NMR, to the *assignment of frequencies observed in spectra to nuclei in the molecule*. Our goal is to make a long list of nuclei with their frequencies. We will need the list in future, when we run NMR experiments focused on structure, motions, or other properties of the studied protein. We will use the list to identify atoms observed in the spectra as peaks at certain frequencies in the same way as we use a phone directory when we need to specify the person we want to call by a telephone number.

The first step in sorting observed frequencies and relating them to the known chemical configuration is the *sequential assignment*. We need to learn which of the observed resonance frequencies correspond to particular atoms in all residues in the amino-acid sequence. The most popular sequential assignment approach is based on the *triple resonance experiments*, introduced in Section 5.4. First we describe the general idea of the sequential assignment using an example of the simplest triple resonance experiments applied to a short peptide. Then we look at the standard experiments and at the problem of identifying sequential fragments in real-life samples.

---

[5]If sufficient concentrations of the protein are available, advanced techniques of data processing allow us to work with incomplete sets of increments and the measurement time can be reduced to values typical for 2D spectra.
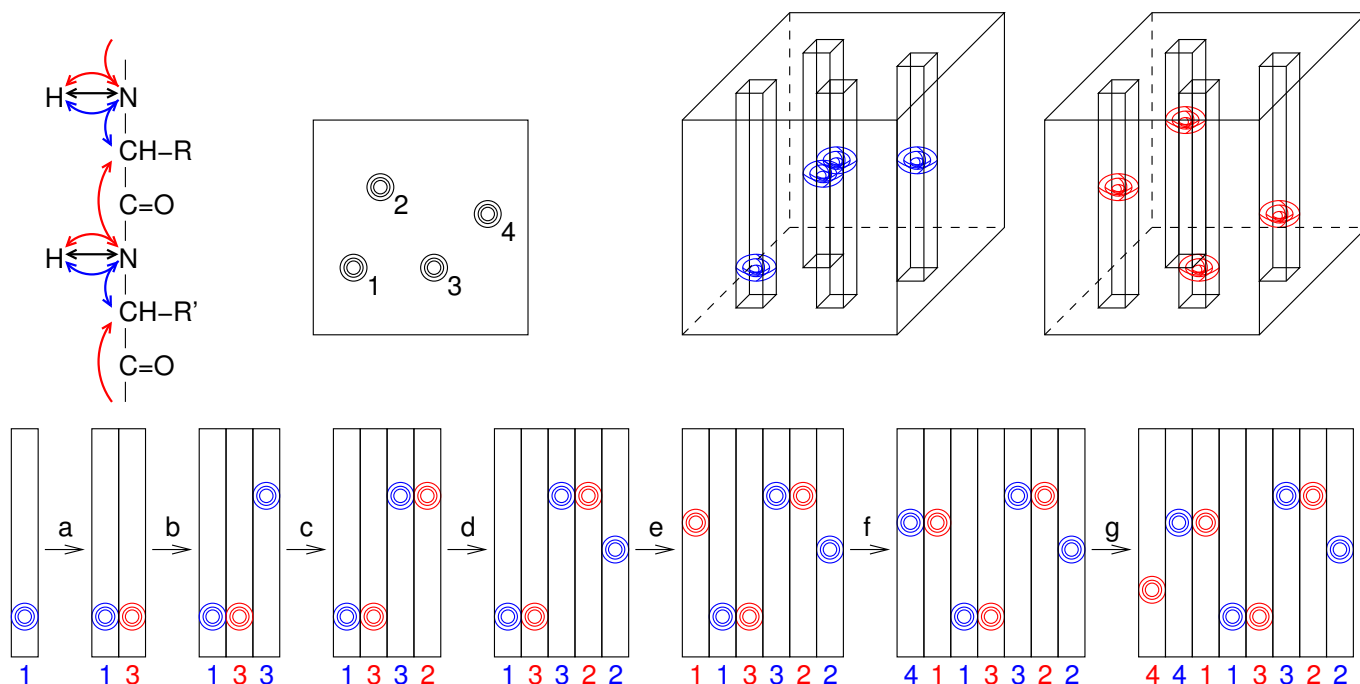
Figure 5.6: Principle of sequential assignment based on the combination of HNCA and HN(CO)CA. Details are discussed in the text.

The basic idea of the sequential assignment utilizing triple resonance experiments is summarized in Figure 5.6. In addition to the already discussed ^{1}H-^{15}N HSQC spectrum, we perform two 3D experiments. The arrows in the protein backbone fragment indicate three correlations. The black arrow corresponds to the backbone amide ^{1}H–^{15}N correlation, observed in the ^{1}H-^{15}N HSQC spectrum. The blue arrows mark the correlation observed in a triple resonance experiment employing polarization transfers from backbone amide ^{1}H to ^{15}N, than to ^{13}C of α-carbon, and back. It is a convention to name the triple resonance experiments based on the polarization transfer pathway. According to this convention, the blue experiment is described as HNCA (H–N–C$^\alpha$). The red arrow shows the correlation obtained in another triple resonance experiment, in HN(CO)CA.[6] The acronym indicates that polarization is transferred from backbone amide ^{1}H to ^{15}N, then to carbonyl ^{13}C, using a ^{13}C-^{13}C coupling to the α-carbon of the preceding amino acid, and back. The parentheses tell us that the polarization was passed to carbonyl ^{13}C but its frequency was not measured (i.e., frequency modulation with carbonyl ^{13}C frequency was not introduced).

The obtained spectra are shown in the upper half of the figure. The studied molecule was a penta-peptide, showing four peaks in the ^{1}H-^{15}N HSQC spectrum. Each peak corresponds to one backbone amide. We do not know which peak corresponds to which residue, so we give them some arbitrary numbers. The cubes in Figure 5.6 represent three-dimensional spectra obtained by the triple resonance experiment. The peaks in the HNCA spectrum are blue while the peaks in the HN(CO)CA spectrum are red. If we look at each cube from top and project the peaks to the base of the cube, we see a pattern identical to the black peaks in the two-dimensional ^{1}H-^{15}N HSQC spectrum. In other words, all peaks can be found in four columns above the ^{1}H-^{15}N correlation. The position of each peak in its column is given by the ^{13}C frequency of the α-carbon correlated to the particular backbone amide. The vertical positions differ between corresponding columns of the blue and red spectra because the blue spectrum (HNCA) shows correlation of ^{13}C$^\alpha$ with the amide of the same amino-acid but the red HN(CO)CA spectrum shows correlation of C$^\alpha$ with the amide of the following residue. Of course, for each peak in the blue spectrum, a peak with the same position must exist somewhere in the red spectrum.

---

[6]Planarity of the peptide bond makes the two-bond J coupling between ^{15}N and ^{13}C of α-carbon of the preceding residue relatively strong (~ 7 Hz). As a consequence, peaks shown in the red color in Figure 5.6 are often observed in the HNCA experiment as well. If the sensitivity is high enough to observe the peaks for all residues, the HNCA spectrum contains all information needed for the assignment. However, both HNCA and HN(CO)CA experiments are usually run.

The assignment process, shown in the bottom half of Figure 5.6, is nothing else than a search for peaks of the same vertical position. Let us start with the blue peak sitting above the amide labeled as "1". We find the same vertical position for the red peak sitting above the amide number 3. Let us cut the columns above the amide peaks labeled 1 and 3 from the cubes and place them side-by-side (step a). At this point we know that amide number 3 follows amide number 1 in the sequence. So let us look for amide 3 in the blue spectrum (step b). It has a red peak of the same vertical position above amide 2 (step c). We can add the blue peak above amide 2 (step d) but we cannot find any red peak of the same vertical position. We arrived at the end of the sequence, there is no amide following the α-carbon observed as the last blue peak. But we are not done yet. We did not begin with the first residue, we just started with a residue arbitrarily labeled as "number 1". So we must search for the residue preceding amide 1. We need to add the red peak number 1 (step e) and look for a blue peak with the same vertical position. It is the peak sitting above amide 4 (step f). Finally we add the red peak number 4 (step g) and our sequential assignment is complete. We see all five α-carbons (five different vertical positions corresponding to five frequencies of $^{13}C^{\alpha}$) in the final plot and we can read the sequence (in arbitrary numbers of the amide peaks) as 4-1-3-2.

The sequential assignment shown in Figure 5.6 worked pretty well. Problem starts if two different α-carbons have identical frequency. The assignment is ambiguous. This is why improved experiments were designed. One of them, known as HNCACB, extends the correlation to β-carbons. An extra INEPT is added to pass polarization from $^{13}C^{\alpha}$ to $^{13}C^{\beta}$. It is not a four-dimensional experiment, the polarization transfer is set to be only 50 % efficient. The polarization is split between $^{13}C^{\alpha}$ and $^{13}C^{\beta}$ before the carbon frequency is measured, and joint again before it is transferred back to amide protons. As a result, two carbon peaks appear in each column (with the exception of glycines), one at the $^{13}C^{\alpha}$ frequency, the other one at the $^{13}C^{\beta}$. A complementary correlation with the C^{α} and C^{β} of the preceding residue is achieved in the CBCA(CO)NH[7] experiment. What are the advantages of employing the β-carbons?

- The probability that both $^{13}C^{\alpha}$ and $^{13}C^{\beta}$ have identical frequency in two residues is much lower than the probability that two α-carbons have the same frequency.

- The range of $^{13}C^{\beta}$ frequencies is much broader (approximately from 15 to 75 ppm) than the range of $^{13}C^{\alpha}$ frequencies (40 to 75 ppm).

- Typical frequencies of β-carbons are different for different types of amino acids.

There are also some disadvantages of the HNCACB and CBCA(CO)NH experiments, compared to HNCA and HN(CO)CA:

- HNCACB and CBCA(CO)NH are less sensitive. First, polarization is split between two carbons, so each peak has only half intensity. In addition, HNCACB and CBCA(CO)NH are more complex than HNCA and HN(CO)CA and their sensitivity is therefore even worse due to the relaxation.

- Frequency of $^{13}C^{\alpha}$ is measured more precisely in HNCA and HN(CO)CA because a narrower spectral width is needed.

As a consequence of the discussed advantages and disadvantages, the full set of triple resonance experiments is usually measured. The sequential assignment relies mostly on the HNCACB and CBCA(CO)NH spectra while the HNCA and HN(CO)CA help when sensitivity or resolution of $^{13}C^{\alpha}$ is critical.

5.6 Degenerated sequencing

As mentioned in Section 5.5, the typical frequencies of β-carbons vary for different types of amino acids. Alanines can be distinguished by $^{13}C^{\beta}$ frequency lower than 25 ppm. There is a group of amino acids with $^{13}C^{\beta}$ frequency between

---

[7]Did you expect HN(CO)CACB? The different acronym shows that a different polarization transfer pathway was used. Going from amide proton down to β-carbon *via* carbonyl would be too long, the experiment would be less sensitive. CBCA(CO)NH is a "one-way" experiment. H^{α} and H^{β} are excited, and polarization is transferred to the aliphatic carbons, carbonyl, nitrogen, and finally to the amide proton. The pulse sequence is rather tricky. The HN(CO)CACB experiment is also used in some cases. For example, protons attached to carbons are replaced by deuterons when larger proteins are studied in order to reduce the dipole-dipole interactions and thus suppress relaxation. Therefore, the sequence cannot start by the excitation of H^{α} and H^{β}.

25 and 36 ppm (glutamic acid, glutamine, histidine, tryptophan, lysine, arginine, methionine, proline, valine, and reduced cysteine). Another group of residues have $^{13}C^\beta$ resonating between 36 and 45 ppm (aspartic acid, asparagine, phenylalanine, tyrosine, leucine, isoleucine, and cysteine forming disulfide bridges). Threonine and serine have $^{13}C^\beta$ frequency in a range typical for $^{13}C^\alpha$ (55 to 70 ppm) and glycine has no β-carbon. We see that the triple resonance experiment cannot sequence a protein unambiguously, but that a degenerated sequence, with the 20-letter amino-acid alphabet reduced to five letters, can be obtained. A hypothetical sequence

```
P   A   C   D   E   F   G   H   I   K   L   M   N   Q   R   S   T   V   W   Y
```

can be read as

```
O   A   O   X   O   X   G   O   X   O   X   O   X   O   O   U   U   O   O   X
```

where U=(S or T), O=(C,E,H,K,M,P,Q,R,V, or W) and X=(D,F,I,L,N, or Y). Some residues can be further distinguished by higher $^{13}C^\alpha$ frequencies (isoleucine, valine, proline) but this indication is less reliable. On the other hand, $^{13}C^\alpha$ close to 45 ppm is really unique.

The partial sequencing is used routinely. It is never possible to obtain sequential connectivity for the whole protein unambiguously. For example, proline always breaks the sequential assignment based on the described experiments, as it has no amide protons. The real-life sequential assignment is a combination of establishing connectivity in short fragments, identifying them based on the degenerated sequencing, and looking for bridges between them.

Lecture 6
Protein homonuclear techniques

6.1 Weak and strong J-coupling

After discussing the experiments based on selective manipulations of different nuclides, we turn our attention to NMR techniques designed to explore *homonuclear systems*. First we discuss experiments based on homonuclear J-coupling. We start by asking how the J-coupling between nuclei of the same nuclide differs from the J-coupling between different nuclides.

If the nuclei of the same type (nuclide) differ in chemical shift (they are present in different chemical groups and therefore influenced by different distributions of electrons in their proximity), then their mutual J-coupling has the same effect as described in Section 2.5. The only difference is that cyan and green do not distinguish distributions of magnetic moments of protons and ^{13}C (or ^{13}N) nuclei, but of two protons in different chemical groups. If the differences in frequencies of J-coupled nuclei are not significantly lower than their interaction constant J, the coupling has a more complex effect on the spectrum. To understand the difference, we should return to the explanation of the origin of the J-coupling, presented in Section 2.4.

We have shown in Section 2.4 that the magnetic moment of the J-coupled nucleus oriented in a certain direction makes the *opposite direction* of a magnetic moment of an electron at the site of the observed nucleus more favorable. As a result, the magnetic moment of nucleus 2 directly covalently bonded to nucleus 2 induces a counterclockwise[1] "secondary precession" (nutation) of the magnetic moment of nucleus 1 about the direction given by the magnetic moment of nucleus 1. This is shown for the magnetic moments of nucleus 2 oriented in the z and $-z$ direction in Figure 2.3, but it should be true for *any orientation*. What is then special about the z direction?

If the precession frequencies of nuclei 1 and 2 differ, the horizontal polarization of nucleus 2 rotates in a coordinate frame of the observed nucleus 1. Let us consider nucleus 1 resonating with the radio wave ($\Omega_1 = 0$) coupled to nucleus 2 with a different precession frequency and therefore $\Omega_2 \neq 0$. If $|\Omega_2| \gg 2\pi J$, the vector describing polarization (magnetization) of nucleus 2 makes many cycles of rotation about the z axis before conversion of the in-phase coherence of nucleus 1 to the anti-phase coherence starts to be significant. Therefore, the effect of the horizontal polarization of nucleus 1 on nucleus 2 fluctuates rapidly and is quickly averaged to zero. The oscillations between "visible" and "invisible" coherences of the observed nucleus are influenced only by the vertical (longitudinal) polarization of the neighbor. This is called *weak coupling* in the NMR literature.

If the precession frequencies of nuclei 1 and 2 are similar, the magnetization vector of nucleus 2 rotates slowly and the anti-phase coherence of nucleus 1 evolves significantly already during the first cycle of rotation of the magnetization vector of nucleus 2. As a consequence, the rotational averaging is not complete and the horizontal polarization of the neighbor also influences the spectrum. The interaction between such nuclei is known as a *strong coupling*. A correct interpretation of the strong coupling is very important when spectra of smaller compounds are analyzed by an organic chemist. The strong coupling also influences spectra of proteins, but usually does not have an impact on the interpretation.

---

[1]The sense of rotation is counterclockwise for nuclei with $\gamma > 0$ connected by a single covalent bond. The change of sign of γ reverts the sense of rotation. In addition, the sense of rotation is opposite for a coupling between nuclei separated by two chemical bonds, but the same for nuclei three bonds apart.

6.2 COSY*

A spectrum showing homonuclear correlation of two protons can be obtained very easily (Figure 6.1A), by running an experiment consisting of only two 90° pulses and called simply COSY (COrrelated SpectroscopY). After an excitation 90° pulse, the signal amplitude is modulated by the chemical shift and J-coupling evolution by incrementing the delay t_1. The second 90° pulse (with the "x" phase) acts on both interacting protons, like the pair of 90° pulses at the end of INEPT (Section 3.7). This pulse

1. returns the y components of polarizations (in-phase coherences) of both nuclei to the invisible z magnetizations,

2. converts the x component of anti-phase coherences to invisible multiple-quantum coherences (note that the "solid and dashed arrows" in the $\pm x$ directions are not affected, but the pulse rotates the polarization of the *neighbour* to the xy plane, creating the multiple-quantum coherences),

3. converts the y component of anti-phase coherence of the first proton into the $-y$ component of the anti-phase coherence of the second proton and vice versa (exactly like the last two 90° pulses of INEPT),

4. leaves the x components of polarizations (in-phase coherences) untouched.

Only the last two components contribute to the signal. The signal is created by coherences of both protons rotating in the xy with the frequency offsets (given by chemical shifts) and further oscillating between "visible" in-phase coherences (magnetizations) and "invisible" anti-phase coherences. Moreover, the amplitude of the signal is modulated by the same processes during t_1. The result is a spectrum with rather complex shapes of peaks. It should not surprise us that a simple experiment yields a complex spectrum. The tricks of spin alchemy (echoes) suppress effects of individual interactions to simplify the spectra, and we did not applied any echo in Figure 6.1A.

The complex pattern of the spectrum carries useful information, but we are not going to discuss it. We just stress the most important feature: because the second 90° exchanged anti-phase coherences of the protons, the spectrum shows coherences of protons that interact via the J coupling.

6.3 Magnetic equivalence

The extreme case of a strong coupling is a pair of nuclei with the same chemical shift (and not differing in interactions with other nuclei). Such nuclei are called *magnetically equivalent.*

Evolution of the coherences of magnetically equivalent nuclei is interesting. As frequencies of both nuclei are the same, we can work in a rotating coordinate frame that is on-resonance for both nuclei. If a 90° pulse creates polarizations of in the $-y$ direction, they do not rotate (i.e., they rotate with a zero frequency offset). However, the *individual* magnetic moments precess at different frequencies depending on the orientation of the magnetic moment of the neighbor nucleus because the nuclei are coupled.

In order to simplify discussion of the J-coupling between magnetically equivalent, we decompose the magnetic moments vectors into their x, y, and z components. As mentioned in Section 6.1, the z component of the magnetic moment of directly bonded nucleus 2 induces a counterclockwise rotation of the x and y components of the magnetic moment of nucleus 1 about the z axis. This conclusions can be generalized to all components of both nuclei (nucleus 1 also influences nucleus 2). There are six combinations of mutually interacting perpendicular components in a pair of nuclei. In order to analyze such a complex system, we explore rotations for a very short time $\mathrm{d}t$, i.e. by a very short angle $\mathrm{d}\alpha = \omega \mathrm{d}t$, where ω is proportional to the size of the given perpendicular component of the neighbor's magnetic moment. As an example, we analyze the mutual effect of the x component of the magnetic moment of nucleus 1 and z component of the magnetic moment of nucleus 2. Rotation of a vector $\vec{a}$ oriented in the x direction by a small angle α about z does not change the x coordinate of the vector significantly because $\cos(\mathrm{d}\alpha) \approx 0$ for very small $\mathrm{d}\alpha$. However, the y coordinate of the vector increases from zero to $v\mathrm{d}\alpha$ because $\sin(\mathrm{d}\alpha) \approx \mathrm{d}\alpha$ for very small $\mathrm{d}\alpha$ (if the angles are expressed in radians). We can therefore write the evolution of the coordinates as $(a_0, 0, 0) \rightarrow (a_0, a_0\mathrm{d}\alpha, 0)$, or, in terms of the changes in time, as $(\mathrm{d}a_x/\mathrm{d}t, \mathrm{d}a_y/\mathrm{d}t, \mathrm{d}a_z/\mathrm{d}t) = (0, a_0\mathrm{d}\alpha/\mathrm{d}t, 0) = (0, a_0\omega, 0)$. In our case, a_0 is equal to the x component of the magnetic moment of nucleus 1 and ω is proportional to the z component of the magnetic moment of nucleus 2 at the given time. We can therefore write the change as $(\mathrm{d}\mu_{1x}/\mathrm{d}t, \mathrm{d}\mu_{1y}/\mathrm{d}t, \mathrm{d}\mu_{1z}/\mathrm{d}t) = (0, g\mu_{1x}\mu_{2z}, 0)$,
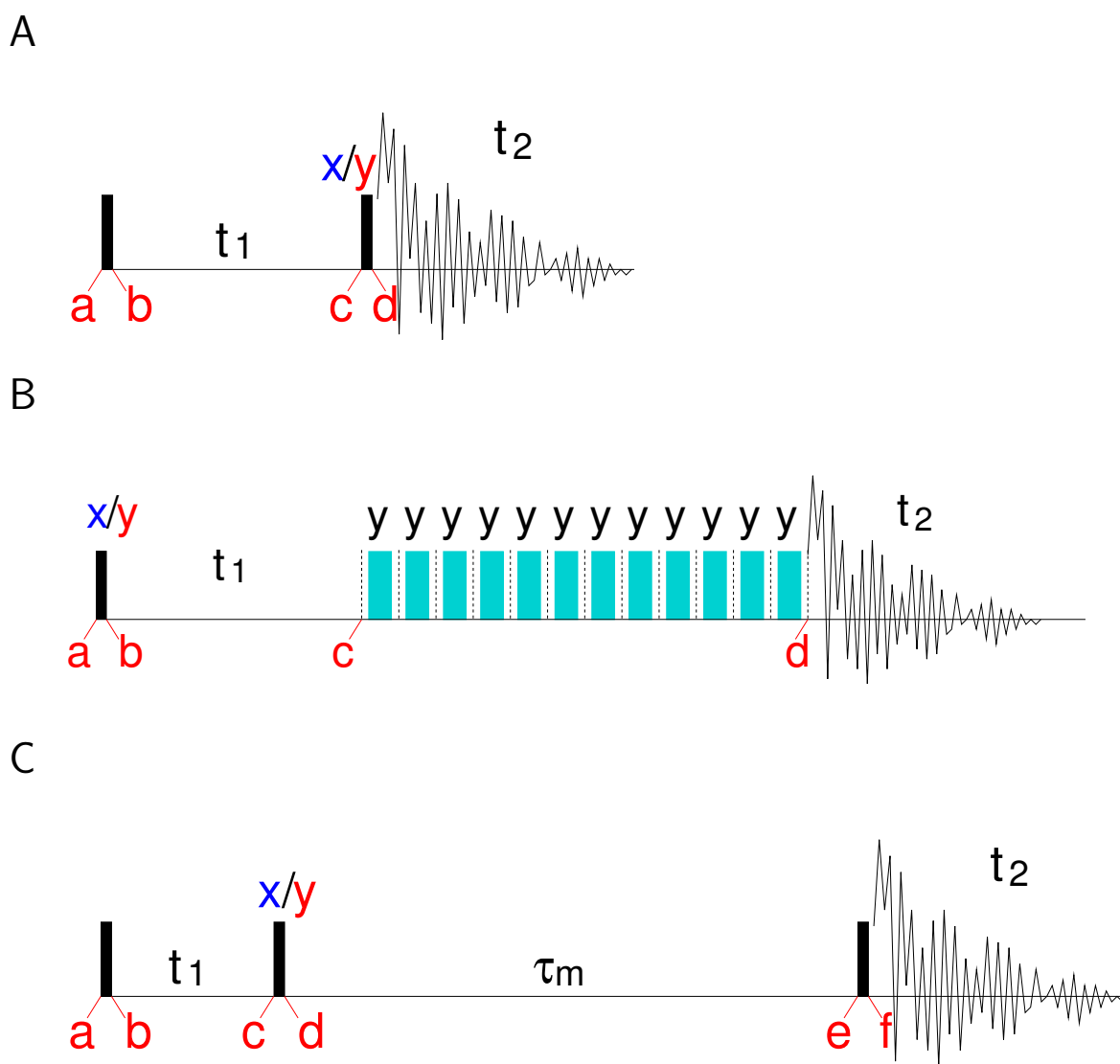
A

B

C

Figure 6.1: Homonuclear correlation experiments: COSY (A), TOCSY (B), and NOESY (C). The TOCSY mixing train is depicted as a series of 180° y pulses (wide cyan bars), more elaborate pulse trains are used in practice. Other symbols are used as explained in Figure 3.3.

where g is the proportionality constant (coupling). Nucleus 2 is also influenced by nucleus 1. A similar analysis for a small rotation of μ_{2z} about μ_{1x} provides $(\mathrm{d}\mu_{2x}/\mathrm{d}t, \mathrm{d}\mu_{2y}/\mathrm{d}t, \mathrm{d}\mu_{2z}/\mathrm{d}t) = (0, -g\mu_{1x}\mu_{2z}, 0)$. The expression for all perpendicular combinations are written in the following table

Combination	μ_{1x}, μ_{2y}	μ_{1x}, μ_{2z}	μ_{1y}, μ_{2x}	μ_{1y}, μ_{2z}	μ_{1z}, μ_{2x}	μ_{1z}, μ_{2y}
change of $\vec{\mu}_1$	$0,0,-g\mu_{1x}\mu_{2y}$	$0,+g\mu_{1x}\mu_{2z},0$	$0,0,+g\mu_{1x}\mu_{2y}$	$-g\mu_{1y}\mu_{2x},0,0$	$0,-g\mu_{1y}\mu_{2z},0$	$+g\mu_{1y}\mu_{2x},0,0$
change of $\vec{\mu}_2$	$0,0,+g\mu_{1x}\mu_{2y}$	$0,-g\mu_{1x}\mu_{2z},0$	$0,0,-g\mu_{1x}\mu_{2y}$	$+g\mu_{1y}\mu_{2x},0,0$	$0,+g\mu_{1y}\mu_{2z},0$	$-g\mu_{1y}\mu_{2x},0,0$
change of $\vec{\mu}_1 + \vec{\mu}_2$	$0,0,0$	$0,0,0$	$0,0,0$	$0,0,0$	$0,0,0$	$0,0,0$

The last line of the table reveals a remarkable fact. Although the two magnetic moments influence each other, the sums $\mu_{1x} + \mu_{2x}$, $\mu_{1y} + \mu_{2y}$, and $\mu_{1z} + \mu_{2z}$ do not change (their time derivatives are equal to zero). As the bulk magnetization $\vec{M} = \vec{M}_1 + \vec{M}_2$ consists of magnetic moments of both nuclei, its components M_x, M_y, and M_z keep their original values in the coordinate frame rotating with the resonance frequency. The practical consequence is that the J-coupling does not have any impact on the spectrum. It explains why we see just one peak (not two peaks) in a spectrum of water, despite the fact that water contains two protons strongly interacting via the J coupling.

6.4 Isotropic mixing

The fact that the overall magnetization of magnetically equivalent nuclei does not change during evolution has a very interesting implication. Let us imagine that we can selectively excite just one of the equivalent nuclei. This may seem impossible, but we later describe how we can achieve something at least very similar to selectively created polarizations in a magnetically equivalent system. If nucleus 1 is polarized in the $-y$ direction and nucleus 2 is left with its equilibrium distribution of magnetic moments, the original in-phase $-y$ coherence of nucleus 1 evolves to the anti-phase x coherence. In the case of a heteronuclear pair, analyzed in Section 2.5, we observed oscillations between "visible" in-phase and "invisible" anti-phase coherences. What happens in the case of a magnetically equivalent pair? The components of total magnetization, including M_y component must remain constant. In order to keep the magnetization constant, a y component of the magnetization of nucleus 2 must be generated to compensate for the loss of the contribution of nucleus 1. To make a long story short, if one of magnetically equivalent nuclei is excited, its polarization is also transferred to its partner.

The described polarization transfer among magnetically equivalent nuclei is not limited to the y components of magnetization. It applies to the x and z components as well because magnetic moments are influenced by *all directions* of the neighbor's magnetic moments. Therefore this type of polarization transfer is known as *isotropic mixing*.

The isotropic mixing is even more interesting in larger homonuclear systems when not all nuclei are mutually coupled. For example, $^1\mathrm{H}^\delta$ and $^1\mathrm{H}^\zeta$ in phenylalanine interact with $^1\mathrm{H}^\epsilon$ via an efficient three-bond J-coupling, but $^1\mathrm{H}^\delta$ interacts only negligibly with $^1\mathrm{H}^\zeta$ (they are separated by five bonds). If $^1\mathrm{H}^\delta$ is selectively excited and coherences evolve as in a magnetically equivalent system, the original in-phase $-y$ coherence of $^1\mathrm{H}^\delta$ evolves and magnetization of $^1\mathrm{H}^\epsilon$ is converted to the y polarization of $^1\mathrm{H}^\epsilon$, which contributes to the total M_y. But the sum of y components of $^1\mathrm{H}^\delta$ and $^1\mathrm{H}^\epsilon$ is *not* constant because $^1\mathrm{H}^\epsilon$ is also coupled to $^1\mathrm{H}^\zeta$. The y component of $^1\mathrm{H}^\epsilon$ polarization is further transferred to the y polarization of $^1\mathrm{H}^\zeta$. It is the total M_y of all three protons that does not change. The described transfer of the y polarization to all three nuclei of the spin system has a very useful consequence: *all* signals of the spin system are correlated in the spectra, not only those of directly coupled nuclei.

6.5 TOCSY

The discussion in Section 6.4 may lead to the conclusion that isotropic mixing is not very useful in correlated spectroscopy of proteins. Either the system *is* magnetically equivalent but then all nuclei have identical frequency and there is no correlation to be observed (like the three protons in methyl groups), or the system is *not* magnetically equivalent and the isotropic mixing does not work. Clearly, we meet the later case in proteins. Aliphatic carbon (or proton) frequencies are not identical, the differences are large enough to destroy the coherences in the xy plane very quickly.

The spin alchemist never gives up. The seemingly incompatible requirements of resolved frequencies and isotropic mixing are fulfilled with the help of pulse trains similar to those used for decoupling. The only difference is that the pulse train now affects all nuclei. The sequence of very short echoes hitting both nuclei of any pair in the spin

system acts as a sequence of the *simultaneous echoes*. Therefore, the chemical shift is kept refocused during the whole pulse train but the coupling is active. This is exactly what we wanted, all nuclei have apparently identical (i.e., zero) frequency offset, and they are coupled as in a magnetically equivalent spin system.

The described trick is combined with the incremented evolution of t_1 in a pulse sequence called TOCSY (TOtally Correlated SpectroscopY), presented in Figure 6.1B. Spin systems of nuclei with different chemical shifts evolve as described in Section 6.1. Then, a series of short echoes is applied. Let us assume that the TOCSY pulse train is applied with the 90° phases of the radio waves ("y" pulses).[2] As a consequence, the pulses keep the y components of the magnetization intact and rotate other coherences about the y axis. During the pulse train, the y polarizations of all nuclei are mixed as described in Section 6.4. Because the trains contain many (hundreds) of pulses, the imperfections of the pulses and stochastic molecular motions randomize the direction of the polarizations in the xz plane (an effect similar to the loss of coherence in the xy plane during evolution in the $\vec{B}_0$ field). Therefore, we assume that only the y coherences, "locked" in the y direction of the rotating frame, survive the TOCSY mixing pulse train and contribute to the signal.[3] The amplitude of the signal is modulated by the frequency offsets in t_1. For example, if polarization of phenylalanine $^1\text{H}^\delta$ stays in the $-y$ direction at the end of t_1 and polarizations of $^1\text{H}^\epsilon$ and $^1\text{H}^\zeta$ just happen to evolve to the x direction during t_1, the only polarization entering the mixing train is that of $^1\text{H}^\delta$. During the train, the polarization is transferred to $^1\text{H}^\epsilon$ and $^1\text{H}^\zeta$, so three polarizations evolve during t_2 with frequencies of $^1\text{H}^\delta$, $^1\text{H}^\epsilon$, and $^1\text{H}^\zeta$. However, intensities of all three signals correspond to the magnitude of the y polarization of $^1\text{H}^\delta$. As t_1 is incremented, the amplitudes of the signals are modulated by frequency offsets of all three protons. Therefore, correlations in individual spin systems show in the spectra as *cross-peaks* at the frequency offsets of all nuclei in both dimensions (e.g. six peaks for three nonequivalent aromatic protons of phenylalanine).

6.6   NOESY

So far, we have discussed correlated spectroscopy based on the J-coupling. Now we explore correlated spectroscopy utilizing another interaction, the direct *dipole-dipole coupling* introduced in Section 2.2. As discussed in Section 2.2, the effects of the dipole-dipole coupling on precession frequencies are canceled to zero in isotropic liquids. Nevertheless, the dipole-dipole interactions contribute to the relaxation. In this section, we explain how the relaxation can be employed to introduce correlation in the spectra.

The basic NOESY experiment is a sequence of three pulses separated by two delays (Figure 6.1C). Each pulse rotates magnetization by 90° about the x axis in the coordinate frame rotating about the z axis with the precession frequency of the observed nucleus. The first pulse brings the magnetization to a direction perpendicular to the external static field $\vec{B}_0$, under which influence it rotates with the precession frequency of the nucleus. The second pulse continues the rotation by another 90°. The effect of the second pulse also depends on the length of the incremented delay t_1. We assume that we observe two protons, one exactly on resonance ($\Omega_1 = 0$) and the other one with such a frequency offset Ω_2 that it rotates by 90° during each increment of t_1 (in other words, the increment is $\pi/(2\Omega_2)$).

We first analyze evolution of two protons that are far apart and their magnetic moments do not interact. If the first 90,° pulse is sufficiently strong, we can assume that both nuclei are polarized in the $-y$ direction at the end of the pulse. In the coordinate frame rotating with the precession frequency of proton 1, polarization of proton 2 rotates during t_1 in the xy plane with the frequency offset Ω_2. It is useful to decompose the magnetization vector of proton 2 ($\vec{M}_2$) into the M_{2x} and M_{2y} component. The M_{2y} component evolves from its original negative value following a cosine function ($\cos(\Omega_2 t_1)$) as the magnetization rotates. Evolution of the M_{2x} component is described by a sine function ($\sin(\Omega_2 t_1)$). Only the M_{2y} component is affected by the second pulse, applied in the x direction (the same phase as the first pulse). As a result, the $-y$ magnetization is rotated further to the $-z$ direction, the $-y$ magnetization is returned to the $+z$ direction, and the $\pm x$ magnetization stays in the xy plane.

The second pulse in our sequence is followed by another delay. It is usually relatively long, let us set its duration to 0.2 s in our example. What happens to the magnetization rotated to the $-z$ direction? The external field $\vec{B}_0$ has no net effect, so it should stay intact during the delay. But we should be careful because the magnetization in the $-z$ direction does not correspond to the equilibrium distribution of magnetic moments. Therefore, *relaxation* should be also considered. Due to the relaxation, the magnetic moments polarized in the $-z$ direction slowly redistribute

---

[2]180° pulses are depicted in Figure 6.1B, but more elaborate pulse trains are used in reality.

[3]If the other coherences are not destroyed completely, their contribution can be removed by phase cycling.

to the equilibrium $+z$ polarization. A typical rate constant of this process is $1\,\mathrm{s}^{-1}$. The return to the equilibrium distribution during $0.2\,\mathrm{s}$ with the rate of $1\,\mathrm{s}^{-1}$ can be calculated as $1 - \mathrm{e}^{-1\times 0.2} \approx -0.64$. Details of such calculations will be discussed later, in lectures dedicated to relaxation. Now we just accept the result, telling us that a large portion of magnetization (64 %) stays in the $-z$ direction.

And what about the M_{2x} component, that stayed in the xy plane? It continues to rotate about the z axis but relaxation reduces its size. This component corresponds to the transverse polarization. In large rigid molecules, the transverse polarization relaxes much faster than the longitudinal one. If we assume an exponential decay with a rate constant of $20\,\mathrm{s}^{-1}$, we can calculate the loss of the M_{2x} component as $\mathrm{e}^{-20\times 0.2} \approx 0.02$. For the sake of simplicity, we neglect the 2 % leftover and assume that the M_{2x} component decayed during the delay completely.

The third pulse would then rotate the $\mp z$ component to the $\pm y$ direction and the receiver would detect rotation of the magnetization about the z axis with the frequency offset of the observed nucleus. Directions of the magnetization vectors of both protons at certain time points marked in Figure 6.1C are listed below for the first four increments of t_1.

Increment	proton 1				proton 2			
	at c	at d	at e	at f	at c	at d	at e	at f
0	$-y$	$-z$	$-z$	$+y$	$-y$	$-z$	$-z$	$+y$
1	$-y$	$-z$	$-z$	$+y$	$+x$	$+x$	0	0
2	$-y$	$-z$	$-z$	$+y$	$+y$	$+z$	$+z$	$-y$
3	$-y$	$-z$	$-z$	$+y$	$-x$	$-x$	0	0

Magnetization of proton 1 stays in the y direction at the beginning of t_2, it corresponds to the amplitude modulation with a zero frequency offset. Magnetization of proton 2 at the beginning of t_2 (at point f) oscillates between $+y$ and $-y$ as expected for an amplitude modulation with the nonzero frequency offset Ω_2. The amplitude of the detected signal is modulated by the frequency offset Ω_2 because the fraction of magnetization which did not experience the second pulse relaxed almost completely during τ_m. We obtain a two dimensional spectrum with amplitude modulation in the indirect dimension. However, there is no *correlation* in the spectrum. The signal of proton 1 does not oscillate in t_1 or t_2, and the signal of proton 2 is modulated in t_1 with a frequency equal to the frequency of signal oscillation in t_2 (the frequency offset Ω_2).

In order to achieve correlation, protons 1 and 2 must be close enough in space so that their magnetic moments can interact directly (dipolar coupling). Let us now explore what happens in such a case to the z component of the magnetization during τ_m. Proton 1 is always polarized in the $-z$ direction, which is not the equilibrium polarization. Actually, the z component of the magnetization of proton 1 is exactly opposite to its equilibrium value: $M_{1z}(\mathrm{d}) = -M_{1z}^\mathrm{eq}$ Therefore, its magnetic moments are redistributed during τ_m to return to the equilibrium. This is the process of relaxation, driven by local magnetic fields. If proton 2 is close in space, interactions with its magnetic moments also contribute to the relaxation. The result of the relaxation is that the z component of the magnetization of proton 1 at the time point e in Figure 6.1C is somewhere between $-M_{1z}^\mathrm{eq}$ and M_{1z}^eq. Where exactly, it depends (also) on the magnetic moment distribution of proton 2 because what matters is the deviation of the total magnetization $\vec{M}_1 + \vec{M}_2$ from the equilibrium.[4] But the distribution (polarization) of proton 2 oscillates as t_1 increases. Therefore, the exact amplitude of the signal of proton 1, proportional to the actual value of $M_{1z}(\mathrm{e})$, oscillates with the frequency of proton 2! As a result, we observe a *cross-peak* in the spectrum at the frequency Ω_1 in t_2 and Ω_2 in t_1. Proton 1 of course influences proton 2 in the same manner. So we see another cross-peak at Ω_1 in t_1 and Ω_2 in t_2.

The described dependence of the longitudinal polarization of one nucleus on the longitudinal polarization of another

---

[4]The behavior of magnetic moments during the pulse sequence presented in Figure 6.1C resembles the following experiment. Imagine the temperature of our laboratory is $20\,°\mathrm{C}$. We put an iron block cooled to $-20\,°\mathrm{C}$ on a bench. The temperature of the block starts to increase until it reaches $20\,°\mathrm{C}$. We repeat the experiment several times and record the temperature after ten minutes. The temperature should be the same in all experiments. This is an analogy of the evolution of the longitudinal polarization of proton 1 during τ_m. Then we repeat the experiment with another block of iron, cooled to various temperatures: $-20\,°\mathrm{C}$, $0\,°\mathrm{C}$, $20\,°\mathrm{C}$, $0\,°\mathrm{C}$. Now the temperature recorded in subsequent experiments should oscillate. This resembles the effect of the t_1 incrementation on the longitudinal polarization of proton 2. In the third series of experiments, we use two iron blocks, one cooled always to $0\,°\mathrm{C}$, and the other one cooled to different temperatures: $-20\,°\mathrm{C}$, $0\,°\mathrm{C}$, $20\,°\mathrm{C}$, $0\,°\mathrm{C}$. We place the blocks on the bench so that they touch each other, and record the temperatures of both blocks after ten minutes. Now the blocks exchange heat and thus influence each other's temperature. For example in the third experiment, when the temperatures of the first and second blocks are $-20\,°\mathrm{C}$ and $20\,°\mathrm{C}$, respectively, the first block should warm up faster and its recorded temperature should be more positive (closer to $20\,°\mathrm{C}$) than in the first experiment. We see that the exchange of heat introduces variation of the recorded temperature of the first block, in a manner reflecting how we vary the initial temperature of the second block. This is an analogy of the evolution of longitudinal polarization of protons coupled by the dipole-dipole interactions.

nucleus close in space is know as the *nuclear Overhauser effect (NOE)*. Therefore, the correlated spectroscopy based on the dipole-dipole interaction is called *NOESY (NOE SpectroscopY)*.

Since the dipole-dipole coupling depends on the distance between the interacting magnetic moment, the exact fraction of the z-magnetization modulated by the frequency of the neighbor depends on how far the nuclei are in space. This a fundamentally different correlation than that observed in the COSY and TOCSY spectra. We can summarize:

- NOESY spectrum tells us which nuclei are close in space

- COSY spectrum tells us which nuclei are connected by covalent bonds

- TOCSY spectrum tells us which nuclei belong to the same spin system

As spin systems well overlap with individual amino acids of a protein (Figure 5.1), and as certain atoms of neighbor amino acids are close in space in all conformations (e.g., amide proton is close to α proton of the preceding residue), a combination of TOCSY and NOESY spectra can be used to perform sequential assignment. This alternative to the triple resonance experiments was the major approach to sequential assignment before the techniques of labeling of proteins with ^{13}C and ^{15}N were developed. A serious drawback of the assignment based on TOCSY and NOESY experiments is limited resolution of the 2D spectra. Therefore, proteins consisting of more than 100 amino acids are difficult to assign using the TOCSY and NOESY spectra.

6.7 Heteronuclear-edited homonuclear correlation

As mentioned in Section 6.6, the 2D spectra showing homonuclear correlation (COSY, TOCSY, NOESY) start to be too crowded for proteins consisting of more than 100 amino acids (Figure 6.2A). Therefore, the homonuclear experiments are combined with heternuclear correlation when applied to larger proteins. Such 3D experiments are called *heteronuclear-edited*, or *isotope-edited*. Examples of three experiments combining TOCSY and NOESY with the HSQC pulse sequence are shown in Figure 6.3.

The TOCSY-HSQC and NOESY-HSQC experiments (Figure 6.3A,C) are seamless combinations of pulse sequences presented in Figures 4.8 and 6.1. Note that the z-polarizations[5] are mixed in the version of the TOCSY-HSQC experiment presented in Figure 6.3A (the mixing train is sandwiched by 90° pulses). The NOESY and TOCSY sequences can be combined with HSQC also in the reversed order (starting with HSQC). In the case of ^{15}N-edited versions, the advantage of the reversed order is that frequencies of all protons are detected in the direct dimension (which offers better resolution), while only a narrow range of amide proton frequencies is measured in the indirect dimension. However, water suppression is more difficult when starting with HSQC.

Two slices cut from an ^{15}N-edited NOESY-HSQC spectrum are plotted in Figure 6.2B,C. The plots document that the 3D NOESY-HSQC experiment provides a good resolution even at a ^{15}N frequency corresponding to the most crowded central region of the ^{1}H-^{15}N HSQC spectrum (Figure 6.2C).

In the experiment presented in Figure 6.3B, the TOCSY block is inserted in the middle of the HSQC sequence. It allows us to employ isotropic mixing of ^{13}C nuclei connected by single bonds. Stronger coupling constants make the polarization transfer more efficient. Note that additional simultaneous echoes need to be included before and after the mixing train because we have to mix in-phase (not anti-phase) coherences. These INEPT steps are shorter than $1/(4J)$ because two or three protons are attached to ^{13}C. In such cases, the in-phase and anti-phase coherence oscillate more rapidly as functions $\cos(\pi Jt)\sin(\pi Jt)$ and $\cos^2(\pi Jt)\sin(\pi Jt)$, respectively. Therefore, the length of the simultaneous echo must be shortened in order to get sufficient polarization transfer for all chemical groups. Using the naming convention of the triple resonance experiments, the pulse sequence in Figure 6.3B is called HC(C)H-TOCSY (the acronym HCCH-TOCSY is also used in the literature).

The TOCSY-HSQC and NOESY-HSQC experiments can be used to obtain the sequential assignment as discussed for TOCSY and NOESY. However, the triple resonance experiments relying on much more diverse ^{13}C chemical shifts provide spectra that are easier to interpret. Therefore, the TOCSY-HSQC and NOESY-HSQC spectra are usually used as a complementary source of information.

---

[5]Not the y-polarizations, that were mixed in the pulse sequence presented in Figure 6.1.
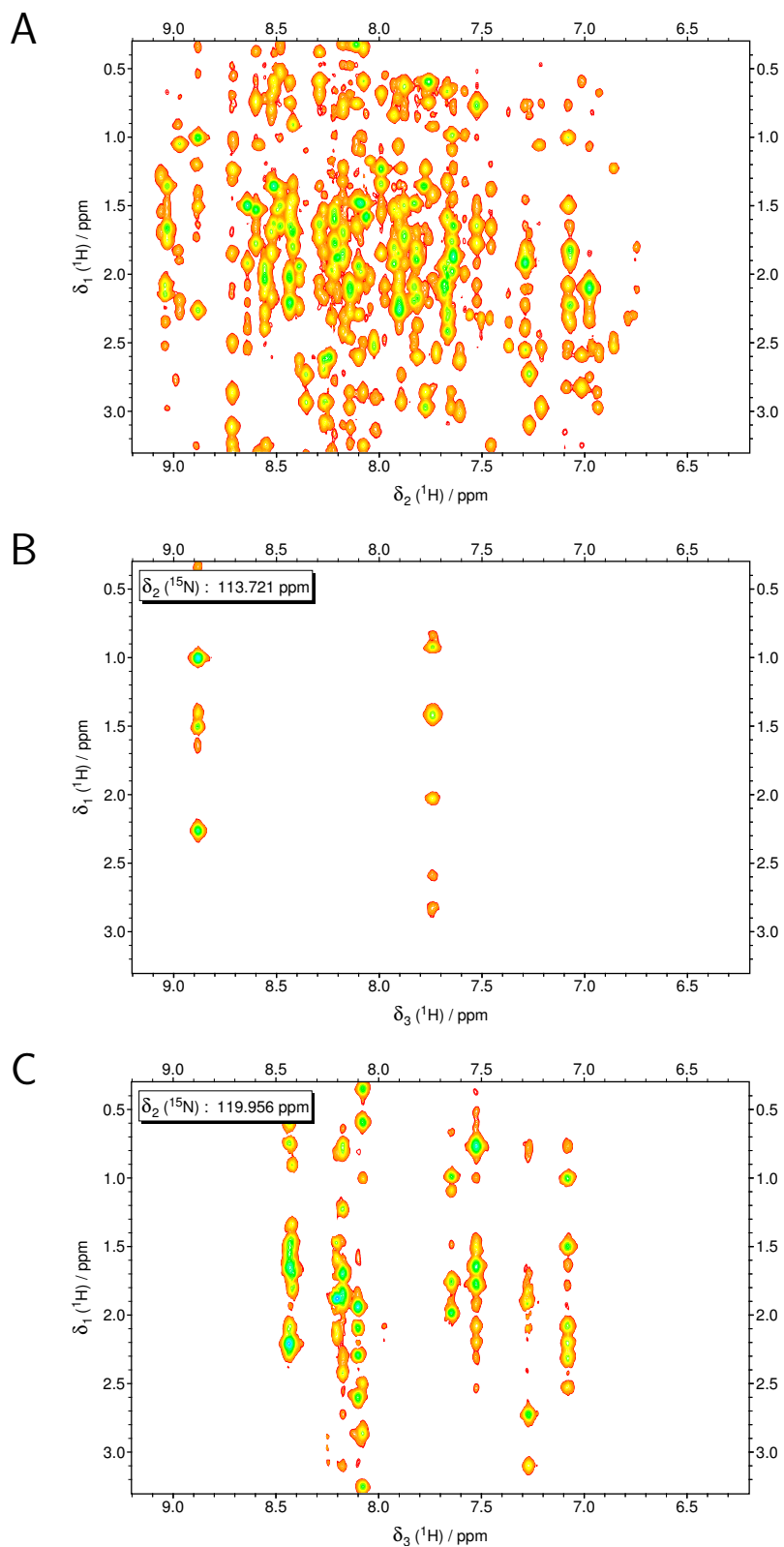
Figure 6.2: 2D NOESY spectrum (A) and two slices cut from a 3D NOESY-HSQC spectrum (B,C) of a protein consisting of 100 residues (N-terminal domain of δ-subunit of RNA polymerase from *Bacillus subtilis*.

All experiments presented in this section allow us to assign side-chain protons, as discussed in Section 6.8. HC(C)H-TOCSY is particularly useful because it provides also ^{13}C chemical shifts. The major application of the NOESY-HSQC experiments is measurement of distances between atoms. In principle, the intensity of NOESY cross-peaks decreases with the sixth power of the distance between the interacting nuclei. Therefore, peak intensities can be converted to the interatomic distances, that serve as a very important restraint in structure calculation. More details are discussed in Section 7.2.

6.8 Side-chain assignment

The triple resonance experiments, introduced in the previous lecture, allowed us to assign frequencies of peaks in spectra to nuclei in the corresponding residues in the amino acid sequence. When the sequential assignment is completed, it is time to think about assigning the remaining frequencies to the atoms of the side chains. As the side chains coincide with separated spin systems (Figure 5.1), *homonuclear correlation* plays an important role in the side-chain assignment. Heteronuclear correlations are also used, but only as an auxiliary tool as described in Section 6.7.

The fundamental experiment for the side-chain assignment is HC(C)H-TOCSY, described in Section 6.7 and presented graphically in Figure 6.3B. What correlations are observed in the HC(C)H-TOCSY spectrum? All proton frequencies, measured in two independent dimensions, are correlated because polarizations were mixed between the delay t_1 introducing modulation by proton frequency in the first indirect dimension and direct proton observation during t_3. The proton frequency offset modulating the amplitude during t_1 is correlated only to the ^{13}C frequency of the directly attached carbon. On the other hand, the proton frequency directly observed in t_3 is correlated to ^{13}C frequencies of all carbons (polarizations were mixed between the delay t_2 introducing modulation by ^{13}C frequency in the second indirect dimension, and acquisition of the proton signal).

The process of the side-chain assignment is summarized in Figure 6.4. The figure shows a hypothetical HC(C)H-TOCSY spectrum containing peaks of a single amino acid valine. We can look at slices of the spectrum cut at various ^{1}H or ^{13}C frequencies.

The side-chain assignment process starts with the ^{13}C frequencies of α-carbon and β-carbon, known from the sequential assignment (row a in Figure 6.4). If we take a plane cut at the ^{13}C frequency of α-carbon (62 ppm in our case), we see a diagonal peak (with the same proton frequencies in both dimensions of the plane) corresponding to the α-proton, and a series of signals with the same frequency of the directly observed proton (axis F3) and with frequencies of all other protons in the spin system in the other (indirect) dimension, labeled as F1 in the figure. The same pattern should be found on a plane cut at the ^{13}C$^\beta$ frequency (30 ppm), with the difference that the diagonal peak corresponds to the β-proton frequency. The slices cut at ^{13}C$^\alpha$ and ^{13}C$^\beta$ give us new information, frequencies of ^{1}H$^\alpha$ and ^{1}H$^\beta$ assigned unequivocally (4.0 and 2.0 ppm, respectively), and list of frequencies of the remaining protons (0.8 and 1.0 ppm). We know from the valine structure that this amino acid contains also two methyl groups with protons labeled ^{1}H$^{\gamma 1}$ and ^{1}H$^{\gamma 2}$, but we do not know which frequency belongs to which atom.

We can verify our assignment by cutting the spectrum in a perpendicular direction, at the frequency of ^{1}H$^\alpha$ and ^{1}H$^\beta$ (row b). Again, we see a series of peaks along the F3 dimension, but now at the ^{13}C frequency of the carbon directly attached to the chosen proton.

Then, we can cut the spectrum at one of the frequencies of the methyl protons (at 1.0 or 0.8 ppm, see row c). In each slice, we see a series of peaks along the F3 dimension at the ^{13}C frequency of a methyl carbon. The slices show that the protons with the resonance frequency of 1.0 ppm are attached to the carbon resonating at 18 ppm, and the protons with the resonance frequency of 0.8 ppm are attached to the carbon resonating at 22 ppm.

Finally, we verify the assignment in the slices cut at the methyl carbon frequencies (row d). Note that all protons were assigned to the directly bonded carbons but we do not know which methyl group should be labeled as $\gamma 1$ and which is $\gamma 2$ according to the standard nomenclature. We obtained a *full nonstereospecific assignment*.

The HC(C)H-TOCSY pulse experiment has some limitations. Spin systems of aliphatic and aromatic nuclei are usually treated separately as the frequency difference between the aromatic and aliphatic nuclei is large for both protons and carbons. We can use the HC(C)H-TOCSY pulse sequence to correlate carbons and protons of aromatic rings, but the connectivity of each ring to the corresponding side chain must be obtained from another experiment.

Also, the HC(C)H-TOCSY spectra are relatively crowded. The analysis can be facilitated by combination of the HC(C)-TOCSY part of the pulse sequence with the polarization transfer to the amide nitrogen and proton. We
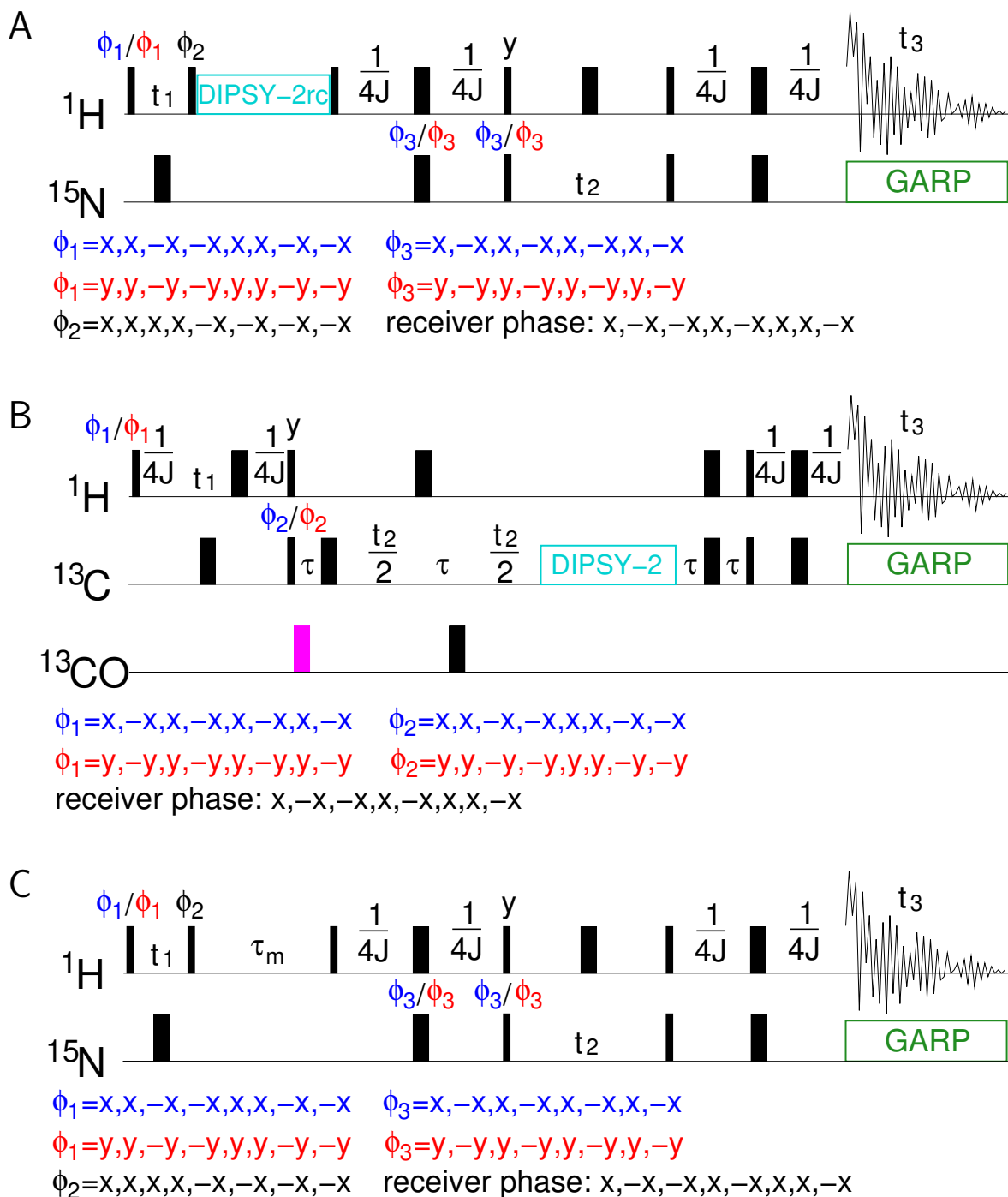
Figure 6.3: 3D Heteronuclear-edited experiments providing homonuclear correlation: TOCSY-HSQC (A), HC(C)H-TOCSY (B), and NOESY-HSQC (C). The isotropic mixing trains are shown as cyan boxes. The magenta pulse corrects phase distortions introduced by the other pulse applied at the carbonyl ^{13}C frequency. Note that the t_1 and t_2 incremented delays are combined with the INEPT transfer modules in HC(C)H-TOCSY. The delay τ is set to $0.6J/(4J)$. Other symbols are used as explained in Figure 3.3.
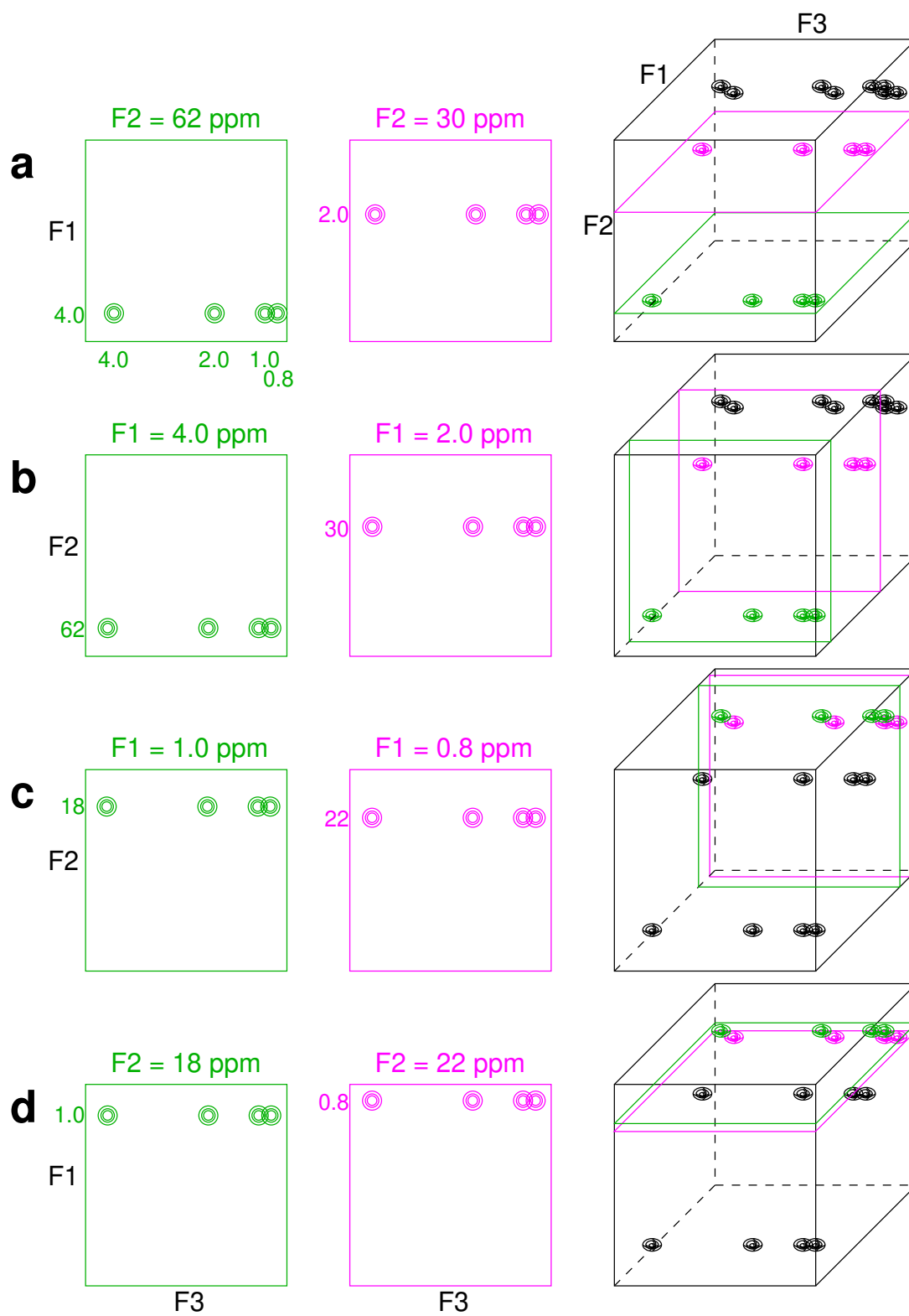
Figure 6.4: Principle of side-chain assignment using the HC(C)H-TOCSY experiment.

obtain spectra similar to those recorded by the triple resonance experiments during the sequential assignment, but with all carbon (or proton) peaks in the indirect dimension. Disadvantage of this attractive approach is relatively low sensitivity. In spite of all improvements, the HC(C)H-TOCSY spectrum remains the most complete source of information and is used when the fancy experiments fail to give unambiguous data.

Before we leave the area of assignments, we should mention nuclei that escaped our traps so far. We did not talk about detection of backbone carbonyl atoms – it can be achieved easily by the HNCO triple resonance experiment (identical to HNCA with a different carrier frequency). Side-chain amides of glutamine and asparagine appear in the ^{1}H-^{15}N HSQC spectra and can be correlated to the corresponding residues by the CBCA(CO)NH experiment. The side-chain NH group of arginine is also visible in the ^{1}H-^{15}N HSQC spectra and can be assigned from the HNCACB spectra (the terminal NH$_2$ groups of arginines are not observed as they exchange protons with water too quickly). Experiments allowing assignment of other side-chain atoms are available, but they are used rarely. The assignment obtained from the standard experiments is sufficient for most following studies, including structure determination.

Lecture 7
From spectra to protein structure

7.1 Content of the lecture

When the resonance frequencies observed in the NMR spectra are assigned to individual atoms of our molecule, we can start acquisition of spectra that provide parameters for structure determination. Information about three-dimensional structure can be derived from various types of experimental data. In the following sections, we describe the process of structure calculation based on the information derived from NOESY spectra. In sections labeled with asterisks, we also discuss measurement of structural parameters that are employed less often.

7.2 Distances and nuclear Overhauser effect

Measurement of internuclear distances (Figure 7.1) was the first method of building three-dimensional structure of large molecules and it remains to serve as the most important tool of NMR structure determination. We have introduced the general idea already in Section 1.3. The distance measurements is based on evaluating the nuclear Overhauser effect (NOE), as explained in Section 6.6. The actual pulse sequence used most frequently to internuclear obtain distances in proteins, $^{13}C/^{15}N$-edited NOESY-HSQC, was presented in Section 6.7.

   When we analyze the NOESY spectra, we are interested not only in the frequencies but also in the intensities of the cross-peaks. While the frequency identifies the interacting nuclei, the intensity measures strength of the interaction. It is known that the interaction between magnetic dipoles quickly decreases with the their distance r (the decrease follows the sixth power of $1/r$). Based on this "r^{-6} law", only nuclei closer than approximately 0.5 nm should show a measurable cross-peak. Also, it should be possible to measure the interatomic distances, using the e.g. following proton pairs of known and fixed distance as a reference:

geminal protons in methylene H–C–H	0.17 nm
vicinal protons in aromatic ring H–C=C–H	0.25 nm
H_i^α and H_{i+3}^N protons in α-helix	0.34 nm
meta protons in aromatic ring H–C=CH–C–H	0.42 nm

Unfortunately, there are at least three reasons why the distance measurement is not as accurate as we would expect.

- The experimental error of evaluating the intensities, especially in crowded regions of spectra.

- Proton pairs are not isolated but form a network of interacting magnetic dipoles. The perturbation of magnetic moment distribution due to direct dipole-dipole interactions with magnetic moments of the interacting partner propagates further to the neighbors of the affected nucleus (so-called *spin diffusion*). The intensity of cross-peaks is therefore not simply proportional to r^{-6}.

- Possible molecular motions. The observed intensity is then an average of what we would obtain for individual frozen conformations.

   The listed obstacles provide explanation why the evaluated internuclear distances alone do not define the structure accurately. The structure determination protocol is based on combining a large set of relatively inaccurate distances
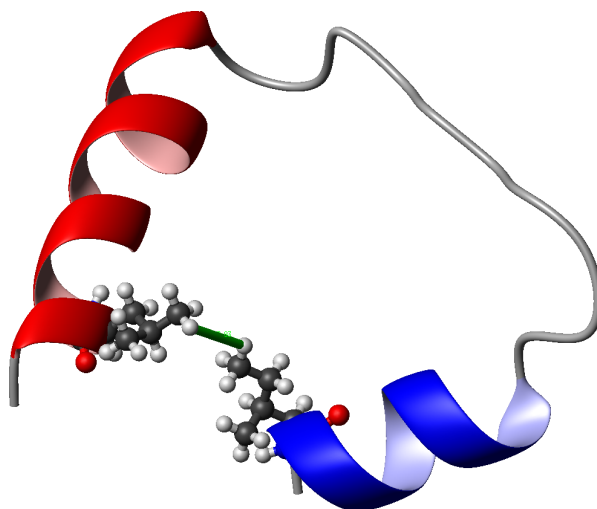
Figure 7.1: Distance between protons in two residues that are close in space but far in the sequence represents a structural restraint contributing to the description of the global protein fold.

with some computational method. Among the determined distances, those between nuclei far in sequence are most useful. Such distances are called *long-range restraints*.

7.3 Torsion angles and three-bond J-couplings[*]

Conformation of a macromolecule is given by torsion angles. In theory, exact determination of all torsion angles along a protein backbone would provide the global fold and addition of side-chain torsion angles would finish the structure determination. Unfortunately, torsion angles are really local parameters, there is nothing like the *long-range* NOE in the case of torsion angles. If we try to form the backbone according to the measured torsion angles, small experimental errors quickly accumulate and the information about the overall shape of the molecule gets lost. The structure determination strategy cannot be based on torsion angles but the torsion angles are still useful as a complement to NOE and may help to refine the solved structure, as discussed in Section 7.5.

Torsion angles are often obtained from three-bond J-couplings. This type of interaction does not depend on the orientation with respect to the external magnetic field, it reflects just the distribution of electrons forming chemical bonds. One-bond J-coupling is mostly given by the bond length, two-bond J-coupling is also affected by the bond angle. Bond lengths and angles are rather uniform and one- and two-bond J-couplings are not very interesting.[1] Three-bond J-couplings depend also on the torsion angles. The dependence reflects the periodic nature of torsion angles, with maxima corresponding to the planar arrangement of the three inspected bonds. Arithmetic and graphical expressions of the relation between torsion angles and three-bond J-couplings are known as *Karplus equation* and *Karplus curve*, respectively (Figure 7.2).

Measuring the J-couplings may look like a simple task: just do not use decoupling and measure distances between individual peaks of the signal split to a doublet. Unfortunately, three-bond couplings are relatively small and cannot be resolved in such a simple experiment. There are two general strategies of obtaining couplings smaller than the peak-width.

The first strategy utilizes evaluation of the signal intensity rather than (unresolved) frequency. A simple example called the *spin echo difference* experiment reveals the essence of the approach (Figure 7.3). We run two experiments. The first pulse sequence contains a simultaneous echo similar to that used in INEPT. Magnetization evolves into the anti-phase coherence during the echo and the measurable signal decreases. The other experiment represents a control. The pulse sequence contains a refocusing echo, during which no signal is lost due to the J-coupling. Value of

---

[1]The one- and two-bond angles are also partially affected by the changes of electron distribution associated with torsion angle changes. Their values are sometimes used as an auxiliary qualitative information.
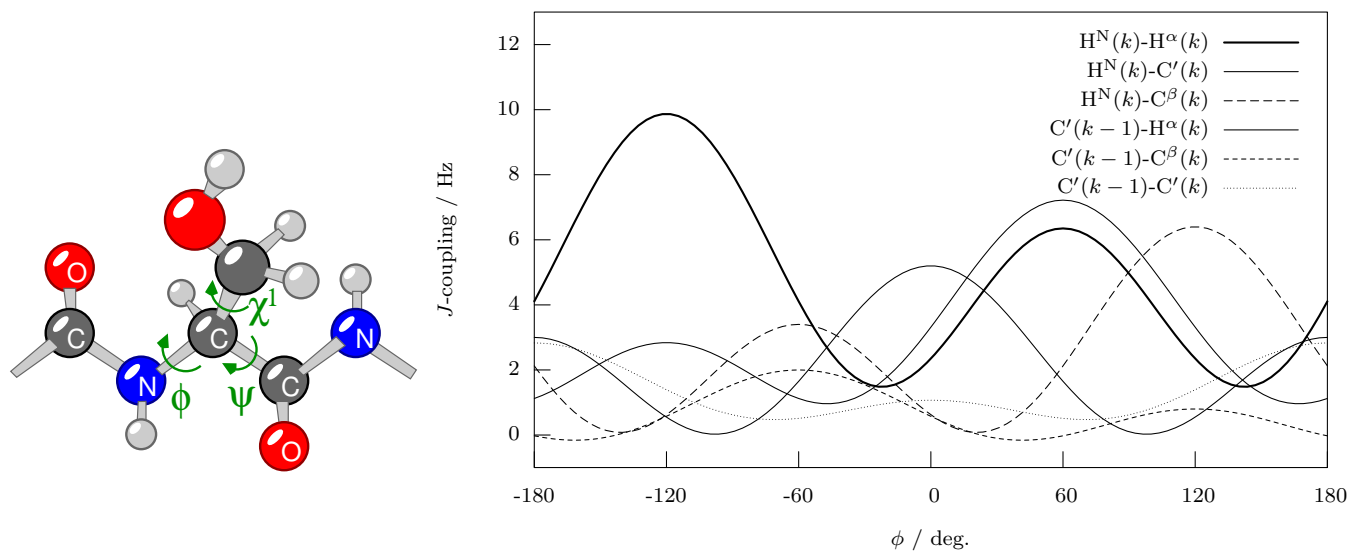
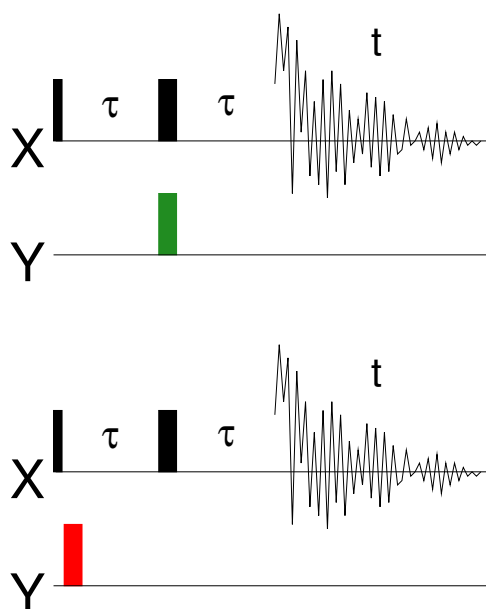Figure 7.2: Dependence of various ^3J-coupling constants on the bakcbone torsion angle ϕ.

Figure 7.3: Spin echo difference experiment. The measured J-coupling between nuclei labeled X and Y evolves during the simultaneous echo (top). A refocusing echo (bottom) is applied to obtain a reference intensity not influenced by the measured J-coupling. In order to perform the reference experiment at the same conditions, the 180° pulse applied to the coupled nucleus Y is not omitted, but moved to the beginning of the sequence (red rectangle).
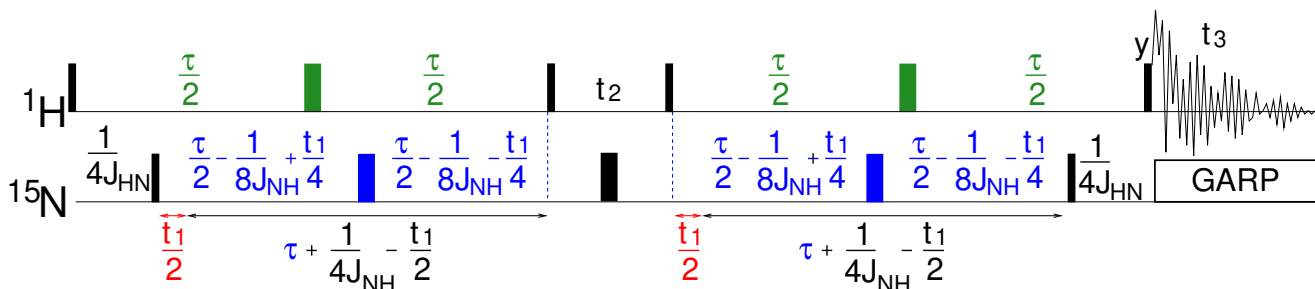
Figure 7.4: HNHA experiment. The measured J-coupling between amide proton and α-proton evolves during the echoes shown in green.

the coupling constant can be easily calculated from the ratio of signals obtained in the two experiments because the magnetization evolves under the influence of the coupling as $\cos(2\pi J\tau)$, where 2τ is the length of the echo and J is the measured coupling constant.

In order to obtain resolution required for proteins, a 3D experiment called HNHA is applied instead of the discussed pair of 1D experiments. Correlation of the detected amide proton with ^{15}N is used to improve resolution by modulating the signal with the ^{15}N frequency. The ^{1}H-^{15}N correlation is achieved using another way of transferring polarization than INEPT, and the studied system, consisting of three nuclei, is more complex than we are used to. It is not our goal to explain technical details of the polarization transfer in the HNHA experiment. Instead, we discuss what can be understood by analyzing individual lines of the pulse sequence, and what is also directly related to the purpose of the measurement.

We start analyzing the line labeled ^{15}N. We note that the blue blocks of the pulse sequence combine polarization transfer with the incremented delay t_1 in the manner of *constant time evolution*. This trick is described in Section 4.3 and also implemented in the pulse sequence presented in Figure 5.5. Each blue block can be decomposed into an incremented delay $t_1/2$ and a decremented refocusing echo, shown in red and black below the pulse sequence, respectively. Any refocusing echo, regardless of possible incrementation or decrementation, cancels the effect of chemical shift evolution. As a consequence, the signal is modulated by $\Omega_N t_1$ (where Ω_N is the frequency offset of amide ^{15}N).

We continue by analysing the line labeled ^{1}H. For the amide and alpha protons (^{1}H^N and ^{1}H$^\alpha$, respectively), the green blocks represent two simultaneous echoes (note that all pulses affect both protons). If the delay $\tau/2$ is equal to $1/(4J)$, where J is the ^{1}H^N-^{1}H$^\alpha$ J-coupling constant, the echoes with the adjacent 90° pulses act as INEPT modules. Apart from the correlation with ^{15}N magnetic moments,[2] we converted the in-phase ^{1}H^N and ^{1}H$^\alpha$ coherences to the anti-phase coherences of *the other proton* at the beginning of t_2. In such a case, we obtain signal oscillating with Ω of ^{1}H^N in t_3 modulated by Ω of ^{1}H$^\alpha$ in t_2, and wise versa. This corresponds to *cross-peaks* in the 3D spectrum.

So far, we discussed the pulse sequence as if τ were set to a well known value of $1/(2J)$. But the purpose of the experiment is to *measure an unknown value of J*, which depends on the torsion angle. And the torsion angle may differ in different amino-acid residues. If J is smaller than $1/(2\tau)$, a portion of the in-phase coherence is preserved and contributes to the signal. This contribution introduces modulation by Ω of ^{1}H^N in t_2 for the signal evolving with Ω of ^{1}H^N in t_3 and modulation by Ω of ^{1}H$^\alpha$ in t_2 for the signal evolving with by Ω of ^{1}H$^\alpha$ in t_3. Such modulation corresponds to the *diagonal peaks* in the 3D spectrum. As the polarization is transferred twice, with the $\sin(\pi J\tau)$ dependence on the three-bond proton-proton coupling, the intensity of the diagonal peak and cross-peak is proportional to $\cos^2(\pi J\tau)$ and $\sin^2(\pi J\tau)$, respectively. Therefore, the value of J can be calculated from the ratio of the peak intensities, which is equal to $\tan^2(\pi J\tau)$, where τ is the known and well chosen duration of the polarization transfer.

The other strategy is abbreviated as E.COSY (Exclusively COrrelated SpectroscopY). The E.COSY experiments include frequency measurement in the absence of decoupling, but no just by omitting the decoupling pulse train in *any* pulse sequence. The pulse sequences are carefully designed so that small couplings are resolved with a help of a large, usually one-bond, coupling. In the case of proteins, the three-bond $^3J(H^NH^\alpha)$ coupling (dependent on the backbone torsion angle ϕ), is measured most often using a slightly modified HNCA pulse sequence called HNCA-J (Figure 7.5).

First, polarization is transferred to ^{13}C$^\alpha$ by two INEPT blocks, exactly like in the standard HNCA experiments.

---

[2] We can ignore that polarization is transferred to ^{15}N when we discuss the effect of the ^{1}H^N-^{1}H$^\alpha$ J-coupling, but not when we design the pulse sequence. In particular, the phases of the 90° pulses must be set accordingly.
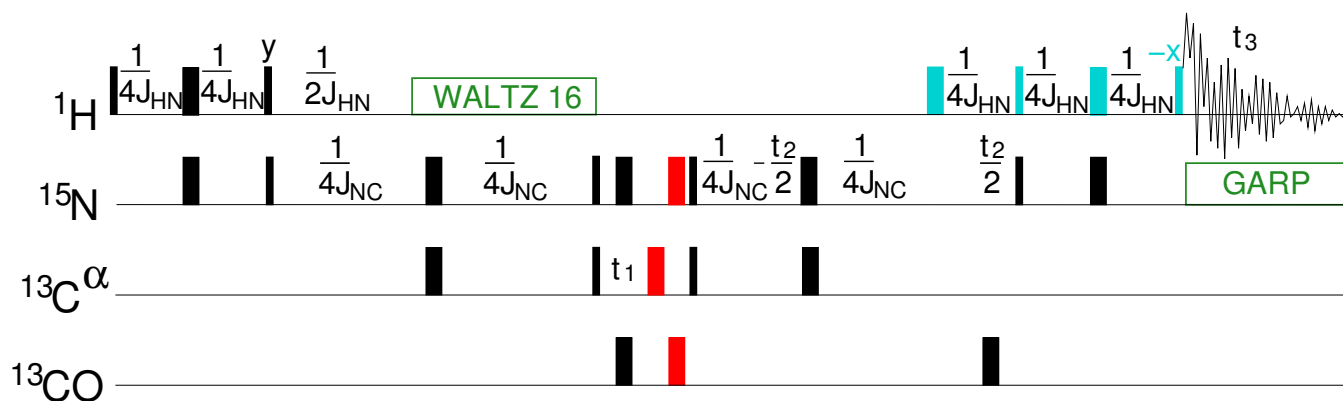
Figure 7.5: HNCA-J experiment. The total flip angle of the cyan pulses is $360\,°$. The green box labeled WALTZ 16 is a train of decoupling pulses (with a similar effect as GARP), applied so that the ^{1}H^N-^{15}N J coupling evolves only during the preceding delay with a length corresponding to $1/(2J((H^N N))$.
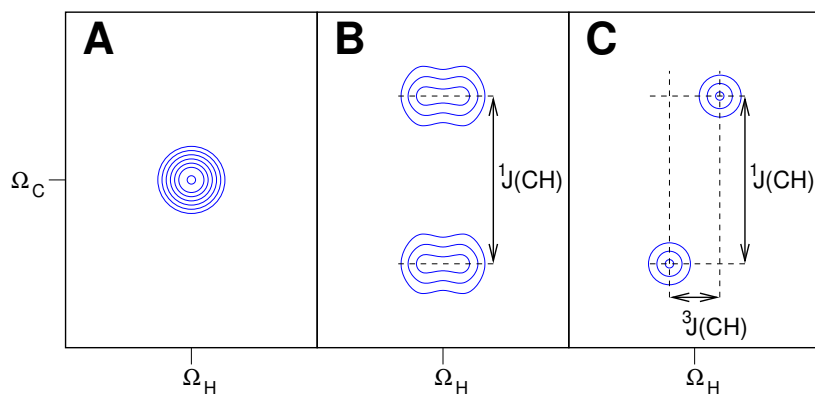

Figure 7.6: Peaks in a slice cut at the ^{15}N frequency from a conventional decoupled HNCA spectrum (A), coupled HNCA spectrum (B), and HNCA-J spectrum (C). The small ($< 10\,\text{Hz}$) three-bond coupling $^3J(H^N H^\alpha)$ is poorly resolved in the coupled HNCA spectrum, but well resolved in the HNCA-J spectrum due to the large ($140\,\text{Hz}$) $^1J(C^\alpha H^\alpha)$ coupling.

The sequence starts to differ from the standard HNCA experiment during t_1. Frequency of $^{13}\text{C}^\alpha$, modulating the signal during t_1, is itself modulated by the large one-bond $^{13}\text{C}^\alpha$–$^1\text{H}^\alpha$ J-coupling in the indirect dimension (by incrementing the delay t_1 without proton decoupling). The developed ^{13}C anti-phase coherence, in terms of correlation with the magnetic moment distribution of the α-proton, can be described by the solid and dashed array introduced in Section 2.5. The solid arrow evolves with the frequency equal to $\Omega_\text{C} - \pi J(\text{C}^\alpha\text{H}^\alpha)$, the dashed one with the frequency equal to $\Omega_\text{C} + \pi J(\text{C}^\alpha\text{H}^\alpha)$. The following INEPT modules transfer the polarization to ^{15}N and finally to amide protons.[3]

When the signal is acquired, the amide protons are coupled to H^α. Therefore, an anti-phase *amide proton* coherence, in terms of correlation with the magnetic moment distribution of the α-proton, evolves during t_3. The pulse sequence is designed carefully, so that it is *the same* distribution of the α-proton magnetic moments as during t_1: the total rotation by all proton pulses between t_1 and t_3 is 360° (shown in cyan in Figure 7.5) returning magnetic moments to their original direction. The oscillation between in-phase and anti-phase proton coherences can be again described by a solid and dashed arrows rotating at frequencies of $\Omega_\text{H} - \pi J(\text{H}^\text{N}\text{H}^\alpha)$ and $\Omega_\text{H} + \pi J(\text{H}^\text{N}\text{H}^\alpha)$. The point is that the evolution of the proton *solid* arrow in t_3 correlates with the evolution of the ^{13}C *solid* arrow in t_1, and the same applies to proton and dashed arrows (the solid arrows in t_1 and t_3 are the same because the $^1\text{H}^\alpha$ magnetic moment distributions are the same, the same applies to the dashed arrows). As a result, two peaks appear in the two-dimensional spectrum (Figure 7.6), one at $\Omega_\text{C} - \pi J(\text{C}^\alpha\text{H}^\alpha), \Omega_\text{H} - \pi J(\text{H}^\text{N}\text{H}^\alpha)$, the other one at $\Omega_\text{C} + \pi J(\text{C}^\alpha\text{H}^\alpha), \Omega_\text{H} + \pi J(\text{H}^\text{N}\text{H}^\alpha)$. In the direct dimension, the peaks are displaced by the small three-bond coupling $J(\text{H}^\text{N}\text{H}^\alpha)$ but this difference can be measured accurately because the peaks are displaced in the indirect dimension by large $J(\text{C}^\alpha\text{H}^\alpha)$.

7.4 Orientation in space and residual dipolar couplings

The direct interaction between two magnetic dipolar moments depends on orientation of the interacting nuclei in the magnetic field, as discussed in Section 2.2 (see Figure 2.1). Energy of this interaction is proportional to $(3\cos^2\Theta - 1)$, where Θ is the angle between the direction of the magnetic induction $\vec{B}_0$ and the vector connecting the nuclei. As the molecule rotates in solution, the angle Θ varies. If the rotation is isotropic, the function $(3\cos^2\Theta - 1)$ averages to zero and no interaction can be measured. However, we can dissolve our macromolecule in a liquid crystal or place it in a strained gel, and restrict rotations in some directions. The liquid crystals can be formed by filamentous viruses, flat discs of phospholipid bilayers ("bicelles"), etc. The partial alignment of the molecule in the liquid crystal does not allow complete averaging of $(3\cos^2\Theta - 1)$ and some residual of the interaction can be measured as splitting in spectra. Technically, these *residual dipolar couplings* cannot be distinguished from the J-couplings between the two interacting nuclei. The value of the residual dipolar coupling can be determined by comparing two experiments, one in regular isotropic buffer, another one in liquid crystal. Apparent coupling measured in the first, isotropic, sample (by one of the methods introduced in the previous section) is just the J-coupling. The difference between values obtained in the two experiments is the residual dipolar coupling.

Residual dipolar couplings are unique because they reflect average orientation of a pair of nuclei with respect to an external coordinate frame (given by the magnetic field orienting components of the liquid crystal or direction of gel compression). Therefore, orientations of two pairs can be compared regardless of the actual distance between these nuclear pairs. Such type of information is very useful in the case of rod-like molecules (e.g., nucleic acid helices). Possible bending of the molecule is clearly manifested in the relative orientation of the residues at the opposite ends of the molecule. Such information is not available from NOESY spectra because NOE can be only measured between nuclei close in space.

Direct geometrical interpretation of the residual dipolar couplings is possible but not straightforward. In order to determine exact mutual orientation of distant nuclear pairs, five independent residual dipolar coupling values need to be measured. Of course, it is not possible to measure more than one coupling for each pair of nuclei. However, information from several nuclear pairs can be put together, if the relative orientations of these pairs is known and fixed. For example, it is possible to determine mutual orientation of two α-helices in a protein if we treat each helix as

---

[3] We know that the first two INEPT modules create a $^{13}\text{C}^\alpha$ coherence that is "twice" anti-phase in terms of correlation with the magnetic moment distribution of amide proton and ^{15}N, and that the last two INEPT steps restore the coherence of amide protons that is in-phase in terms of correlation with the magnetic moment distribution of amide proton and ^{15}N. This fact is not important for the measurement of the J coupling constant and we ignore it for the sake of simplicity (but it must be taken into account when setting phases of the 90° pulses as mentioned when discussing HNHA). We only pay attention to coherences that are anti-phase in terms of correlation with the magnetic moment distribution of the α-proton.
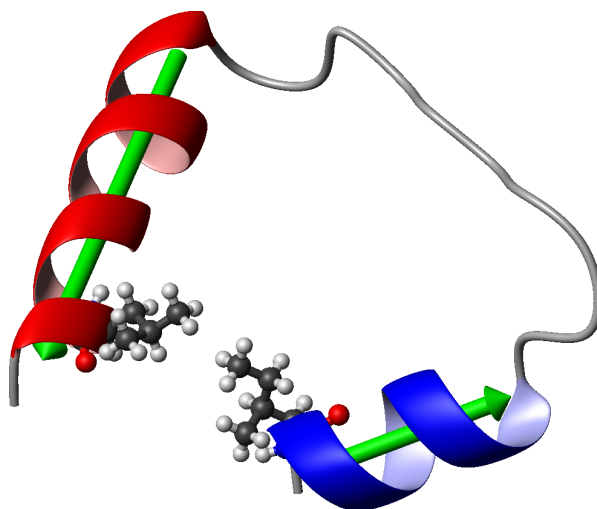
Figure 7.7: Mutual orientation of the blue and red α-helices (green arrows) can be determined by measuring multiple residual dipolar couplings in each helix.

a rigid object of known local geometry (Figure 7.7). Most often, residual dipolar couplings are not interpreted directly but submitted to a computational method as structural *restraints*.

7.5 Building a structural model

There are two possible approaches to interpretation of the NMR data. The first approach is based on human judgment. This approach gives us full control over the interpretation but it is extremely inefficient if large amount of data need to be analyzed and compared. The human interpretation can be successfully applied to prediction of the secondary structure and to critical evaluation of the computer-derived models.

We already mentioned that the human-based data interpretation is often used when the fragments of regular secondary structure are searched for. There are several NMR parameters that can be easily interpreted in terms of secondary structure elements:

- *Rate of proton exchange* with water is slowed down when the proton is involved in a hydrogen bond. Secondary structures are stabilized by regular hydrogen-bond networks and the exchange rates can be used as rough indicators of the presence of such network. The experiment is usually based on a quick exchange of water with deuterium oxide and repeated measurement of quick ^{1}H-^{15}N HSQC spectra. Signals disappear as the protons are replaced with deuterons. Easily accessible protons are replaced within minutes while the protons involved in hydrogen bonds may survive for weeks.

- *Three-bond J-couplings* were already discussed. The *J*-coupling between amide and α protons can be obtained relatively easily. Values larger than 8 Hz indicate β-sheets while values below 6 Hz are typical for helical regions.

- *Nuclear Overhauser effect* is the key structural information. Some NOEs can be inspected separately as indicators of secondary structures (Figure 7.8). In β-sheets, the distance between α protons of the k-th residue and amide protons of $(k+1)$-th residue is much shorter than the distance between two amide protons in neighboring residues. Therefore, an intense NOE between H_k^α and H_{k+1}^N is a strong indication of the β-sheet. On the other hand, NOEs stronger for the H_k^N–H_{k+1}^N pairs than for the H_k^α–H_{k+1}^N are typical for helical structures. Helices can be further characterized by *medium-range* NOEs. Cross-peaks are usually observed for the pairs H_k^α–H_{k+3}^N, H_k^α–H_{k+4}^N, and H_k^α–H_{k+3}^β in α-helices. Presence of a cross peak for the H_k^α–H_{k+2}^N pair but not for the H_k^α–H_{k+4}^N pair indicates a 3_{10}-helix.
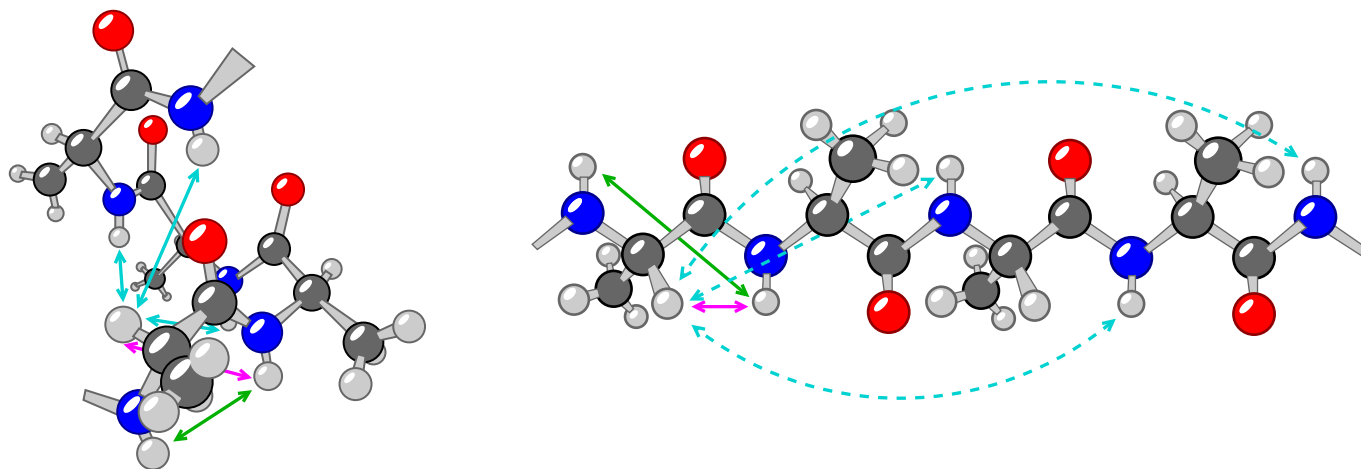
Figure 7.8: Proton-proton distances distinguishing α-helix (left) from β-sheet (right). The distance between H_k^α and H_{k+1}^N is shown in magenta, the distance between H_k^N and H_{k+1}^N is shown in green and the distances between H_k^α and H_{k+2}^N, H_k^α and H_{k+3}^N, H_k^α and H_{k+4}^N are shown in cyan. Hydrogen, carbon, nitrogen, and oxygen atoms are shown in white, black, blue, and red, respectively.

- *Chemical shift* is often difficult to interpret but it works nicely in the secondary structure prediction. Frequencies of carbonyl and alpha ^{13}C are significantly higher in helices than in random coil, on the other hand frequencies of α protons and $^{13}C^\beta$ are elevated in β-sheets. The real beauty of the chemical shifts is that we obtain them for free – as soon as the assignment is finished, the structural information is available.

Direct interpretation of the NOE data can be also applied to determination of the β-sheet topology. The information how the strands of β-sheets are aligned can be obtained from the cross-peaks between backbone protons. It is less straightforward to establish the topology of helices as determination of their relative position requires analysis of side-chain NOE cross-peaks.

The other interpretation approach is using an automated algorithm. With the help of computers, this approach is very efficient but the calculations start to play a role of "black-boxes". The fact that computer simulation was successfully finished does not prove that the obtained structural model is correct. The automated data interpretation is applied when three-dimensional models of biomacromolecules are to be created and refined.

The most obvious way of calculating three-dimensional structure of molecules is solving trigonometric equations defined by the measured interatomic distances. This *distance geometry* approach works fine in civil engineering. Its use in NMR structure calculation is limited. The distances are not measured exactly but roughly guessed from the NOE intensities. The obtained structures have the correct general fold and correct topology of helices and β-sheets, but local geometry looks rather wild. The bond length and angles are far from anything that we learned in the chemistry classes.

Molecular mechanics is the opposite approach. It is based on very good empirical knowledge of local structural parameters such as bond lengths and angles. In structure calculation, it is typically enhanced by introducing molecular motions. As the quantum description is computationally too expensive for large molecules, the molecular motions are mimicked by Newton's equations of motion. Such calculations are usually referred to as *molecular dynamics*. Molecular mechanics suffers from a different disease than distance geometry methods do. It reflects local geometry very well but it has a hard time to find the correct general fold. Methods designed to help to check broader spectrum of conformations have been developed, e.g., simulated annealing (simulation of heating molecules to very high temperatures which gives the molecule enough energy to overcome any energy barrier and adopt any possible conformation). Still, identification of the correct fold is difficult. Computational methods judge the structures based on their energy and the energy difference between various folds is very small (Figure 7.10A). Many macromolecules are even present in two or more conformations under physiological conditions.

The natural solution of the described limitations of distance geometry and molecular dynamics is their marriage. The combined approach, known as *restrained molecular dynamics* uses the NMR data to get the rough general fold ("coarse tuning" of the structure) and the molecular dynamics to refine local geometry ("fine tuning" of the structure).

```
TALOS prediction  .......(∘∘)....(∘∘∘∘∘∘∘∘∘)...⇔.(∘∘∘∘∘∘∘)....(∘∘ ∘∘∘∘∘∘∘∘∘∘∘∘)........................................
³J prediction     .......(∘∘∘).......(∘∘∘∘)..........(∘∘∘∘∘∘∘∘)......  ..∘∘∘∘∘∘∘∘).......⇒..⇐==.........................
NOE prediction    ........(∘∘∘∘)..(∘∘∘∘∘∘∘∘∘∘∘∘∘.∘∘∘∘∘∘∘∘∘∘∘∘)..(∘ ∘∘∘∘∘∘∘∘∘∘∘∘∘∘)..............(∘∘).⇐====⇒........
CSI prediction    .......(∘∘∘)...(∘∘∘∘∘∘∘∘∘∘∘)....(∘∘∘∘∘∘∘∘∘∘∘)..(∘∘ ∘∘∘∘∘∘∘∘∘∘∘∘∘∘)................................
```

```
                    10        20        30        40        50        60        70        80        90
                 GIKQYSQEELKEMALVEIAHELFEEHKKPVPFQELLNEIASLLGVKKEEL GDRIAQFYTDLNIDGRFLALSDQTWGLRSWYPYPDQLDEETQLEHHHHHH
```

Figure 7.9: Identification of secondary structure elements of the N-terminal domain of δ-subunit of RNA polymerase from *Bacillus subtilis* based on direct interpretation of NMR data. Intensity of NOESY cross-peaks between atoms listed in the first column (in residues shown in parentheses) is depicted as thickness of the bars under the sequence. Chemical shifts were interpreted using program TALOS (open and filled circles correspond to predicted helical and extended conformations, respectively) and chemical shift index (CSI). The chemical shift index indicates if the measured chemical shift deviates from the random value to a value typical for helical (shown as open circle) or extended (shown as filled circle) structure. Helical and extended secondary structures predicted from various NMR parameters are depicted above the sequence as ∘ ∘ ∘∘ and <==>, respectively.
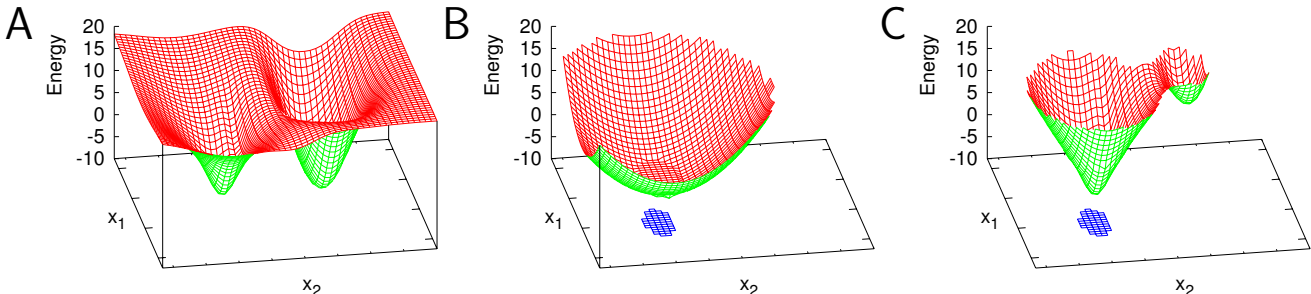
Figure 7.10: Dependence of energy on two coordinates x_1, x_2 of the conformational space (e.g. two torsion angles) in unrestrained molecular dynamics simulation (A), energy penalty for violating the experimental restraints, i.e., deviating from values x_1, x_2 derived from NMR data (B), and dependence of energy on the coordinates x_1, x_2 in restrained molecular dynamics simulation (C).
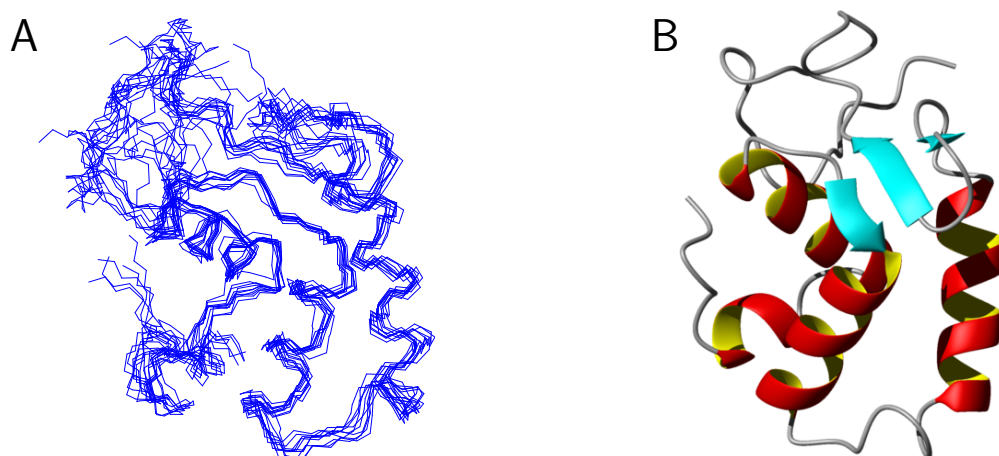
Figure 7.11: Backbone conformations of N-terminal domain of δ-subunit of RNA polymerase from *Bacillus subtilis* calculated by ten independent runs of restrained molecular dynamics simulations (A) and the structure with the lowest energy presented as a cartoon showing the secondary structures (B).

The calculations are mostly based on approximating energy with harmonic potentials (similar to the description of the energy of an ideal spring or a pendulum). For example, bonds are defined as springs having the lowest energy for the length equal to the known distance of the corresponding atoms (this information is obtained from experimental data or quantum calculations of small molecules containing the given functional group). Bond angles are defined in a similar way, planar structures are fixed by artificial potentials, torsion angles are described by periodic functions describing energy minima for the favored conformations. Van der Waals forces are also simulated (typically in a simplified form). The same applies to electrostatic interactions. Their physical description is simple, but their calculation is time-consuming because the electrostatic interactions decrease only slowly with the distance of the interacting atoms. Therefore, each charged atom is in principle influenced by all remaining charges in the molecule, and a lot of attention has to be paid to the decision which interactions can be neglected without biasing the calculated structure.

The NMR data are also introduced through energy. Each value from NMR measurement serves as a *restraint* and is given an artificial potential (Figure 7.10B). For example, a distance between two atoms does not increase the total energy as long as it is in agreement with the intensity of the corresponding NOESY cross-peak. The range of allowed distances is usually broad because the experimental errors are large. If the calculated distance exceeds the rather generous boundaries, energy of the molecule starts to increase rapidly, forcing the atoms to go back closer to each other. The art of NMR structure calculation is based on finding the right combinations of the empirical potentials keeping correct local energy and of the artificial potentials forcing the calculated structure to agree with the NMR data (Figure 7.10C). Usually, the calculations are repeated many times (Figure 7.11A). From the calculated structures, those of the lowest energy and of the best mutual agreement are expected to reflect the actual conformation most accurately (Figure 7.11B). A family of ten or twenty such structures is than deposited and referred to as "the NMR structure" or "the solution structure" of the molecule. Reliability of the obtained structure greatly depends on the quality and quantity of the obtained NMR data and on the correct use of the structure calculation protocol.

Lecture 8
Molecular motions and NMR relaxation

8.1 Real power of biomolecular NMR

We spent a fair amount of time to describe what needs to be done if we want to build a structural model of a large molecule. We learned that many tricks must be used so that our effort is awarded by the ball-and-stick picture on the screen of our computer. Now it is the time to show how far from reality the precious result of our work is. Our model is like a skeleton, but real molecules are not dead. It is not possible to represent a molecule realistically with the model of a single conformation. Fortunately, NMR methodology is sensitive to the motions that make the molecules alive. Actually, among experimental methods designed to investigate molecular motions, NMR is probably the most powerful one Let us now look how can NMR animate our molecular models.

8.2 Connection between molecular motions and NMR relaxation

In general, *relaxation* is a return of some observable quantity to its equilibrium value. In optical spectroscopy (infrared to ultraviolet), the relaxation is usually very fast and dominated by spontaneous emission of a photon at the frequency given by the energy difference between the ground state and the excited state. However, spontaneous emission, proportional to the third power of the photon frequency (and of the energy difference), is completely inefficient in NMR. Yet, magnetic moments perturbed by a radio wave in the NMR experiment return to their equilibrium distribution, although very slowly. The only cause of this process in interaction of magnetic moments with magnetic fields in their surroundings.

Setup of the NMR experiments allows us to study evolution of the *total magnetization* vector $\vec{M}$ in time. When we observe certain type of nuclei, e.g., ^{15}N, precession frequencies of individual ^{15}N magnetic moments in the molecule slightly differ because each nucleus feels a slightly different magnetic field. This would result in the loss of coherence even if the molecules did not move. However, the lost coherence can be gained back by applying an echo if the magnetic field variations do not change in time. Such constant variations have the same effect as changing the magnetic field by the pulsed field gradients (see Section 4.13) or simply having the magnetic field inhomogeneous (in reality, the homogeneity is never perfect).

If the molecule moves, the magnetic fields are not only different for each nucleus but they also change in time. Random motions obviously cause fluctuations of the magnetic field. Relaxation is a consequence of such random fluctuations. As the relation between stochastic molecular motions and NMR relaxation is well defined, relaxation can be used to study dynamics of molecules. It should be emphasized that relaxation is a statistical phenomenon and its analysis requires statistical approaches. We do not build the apparatus of the statistical description of relaxation in this text, we only present its main features.

The qualitative understanding of the effects of fluctuating fields does not require more than knowledge of the roles of the precisely defined external magnetic fields in the basic NMR experiment. It is useful to decompose the magnetic field variations into components parallel to the external field $\vec{B}_0$ (variations of B_z) and perpendicular to it (variations of B_x and B_y).

The variations in the z direction are simply changing the strong static magnetic field of our magnet. As the
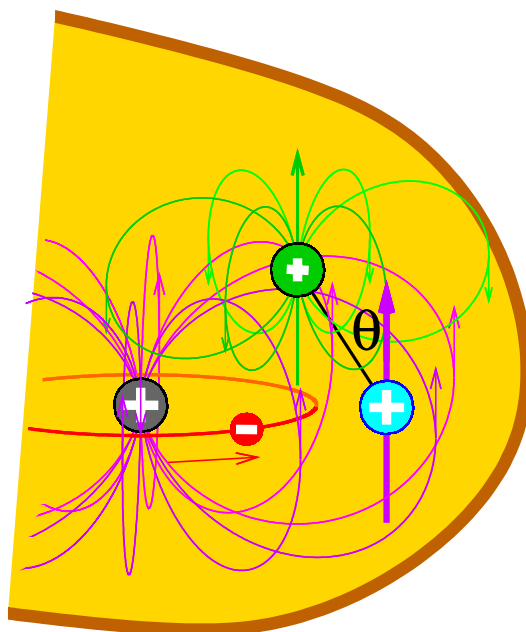
Figure 8.1: Orientations of local magnetic fields influencing the observed nucleus (cyan) are given by the orientation of the whole molecule (if the molecule is rigid). The orientation of the molecule can be described e.g. by a direction of selected chemical bonds. A fragment of a molecule is shown in yellow, other symbols are used as in Figures 2.1A and 2.2B.

precession frequencies of magnetic moments are directly proportional to $\vec{B}_0$ defining the z directions ($\vec{\omega}_0 = -\gamma\vec{B}_0$), variations of B_z cause changes of the precession frequencies of individual magnetic moments. This influences the observed magnetization. The magnetization flipped to the $-y$ direction by a short pulse of a radio wave starts to rotate in the xy plane (perpendicular to $\vec{B}_0$) with the precession frequency of individual nuclei. If the local vertical field B_z at the observed nucleus varies in space, precession frequencies of magnetic moments of the nucleus in different molecules in the sample also vary, as mentioned above. And if the molecular motions randomly change B_z so that it also fluctuates in time, the effect cannot be reversed by an echo. The coherence created by the radio-wave pulse is getting lost and the observed signal decreases. No particular frequency of molecular motions is required, they just have to randomize B_z sufficiently quickly. The total energy of all magnetic moments is preserved, there is no change in M_z. Therefore, there is no energy exchange with the kinetic energy of water molecules hitting our molecule of interest, the process is *adiabatic*.

Fluctuations of the magnetic fields perpendicular to $\vec{B}_0$ resemble the effect of the radio waves. Magnetic induction of the radio waves oscillates in the x direction. If the frequency of the oscillations resonate with the precession frequency, the radio wave rotates magnetization from the vertical direction, changing its orientation from z to $-y \rightarrow -z \rightarrow +y \rightarrow +z$ etc. We can assume that a molecular motion may create accidentally for a short time (between two collisions of molecules changing the speed and direction of the molecular rotation) a horizontal local field rotating with a frequency $\vec{\omega}_{\mathrm{mol}}$ matching the precession frequency $\vec{\omega}_0$. Such a field would rotate the magnetic moment of the given nucleus in a similar manner as the radio wave. This is changing the z components and consequently the average energy of the magnetic moment (the average energy is given by $E = -\mu_z B_0$ because fluctuating components of $\vec{B}$ are averaged to zero). The energy difference is balanced by a change of the kinetic energy of the surrounding molecules (mostly molecules of water). In other words, magnetic moments exchange energy with the surroundings, the process is *non-adiabatic*. Collisions giving the molecule the right rotation frequency are relatively rare, so it takes a long time to see an effect. But in several seconds, the occasional events of energy exchange bring the system to the equilibrium distribution of magnetic moments, given by the Boltzmann law.

The so-far general discussion can be applied to the actual sources of the local fields, namely spin magnetic moments of other nuclei (*dipolar coupling*, described in Section 2.2) and orbital magnetic moments of electrons (*chemical shift*, introduced in Section 2.3). The effects of the local fields depend on

- *magnitude* of the interaction (interaction constant), described below by the parameter b

- *orientation* of the interacting magnetic moments in $\vec{B}_0$, given by the orientation of the whole molecule (see Figure 8.1).

Consequently, the local field fluctuates if the molecular motions vary

- *magnitude* of the interaction

- *orientation* of the molecule (see Figures 2.1A–C and 2.2B,C).

As the relation between the molecular motions and relaxation is not simple, we first discuss a simplified case of a rigid molecule, whose motions do not change the magnitude of the interaction. In other words, we are going to analyze first the effect of random changes of the orientation of the molecule. The orientation of the whole molecule should not be confused with the orientation of the observed magnetic moments. These orientations are almost completely independent, except for the effects discussed in this lecture.

8.3 Rotational diffusion

We now explore the simplest fluctuation of molecular orientation, a random rotation of a rigid molecule, known as *rotational diffusion*. As this is a stochastic process, we must describe it statistically.

First, we identify a geometric parameter Θ describing the actual dependence of local $\vec{B}$ on the orientation of the molecule. In the case of a rigid spherical molecule, it is sufficient to analyze $\Theta = (3\cos^2\theta - 1)/2$, where the angle θ is defined in Figure 2.1. The analysis (not done here) shows that relaxation depends on $\Theta(t)\cdot\Theta(0)$, where $\Theta(t)$ is the actual value of Θ, and $\Theta(0)$ is the value of Θ at the beginning (at the time $t = 0$). $\Theta(t)\cdot\Theta(0)$ changes randomly and differently for different molecules. It is therefore impossible to calculate $\Theta(t)\cdot\Theta(0)$ for a particular molecule. However, the average value for the whole sample $\overline{\Theta(t)\cdot\Theta(0)}$ can by calculated exactly using the statistical approach (solving the diffusion equation, the second Fick's law in spherical coordinates). The result, not derived here, is simply

$$\overline{\Theta(t)\cdot\Theta(0)} \equiv C(t) = \frac{1}{5}\mathrm{e}^{-t/\tau} \tag{8.1}$$

for fluctuations of B_z
and

$$\overline{\Theta(t)\cdot\Theta(0)} \equiv C(t) = \frac{3}{10}\mathrm{e}^{-t/\tau} \tag{8.2}$$

for fluctuations of B_x. The constant τ in Eqs. 8.1 and 8.2 is the *correlation time* and $\overline{\Theta(t)\cdot\Theta(0)}$, or shortly $C(t)$, is the *time correlation function*.

An exact solution can be found for any shape of a rigid molecule, the general solution is a sum of five exponential functions, but we do not need such accuracy in order to understand the basic principles.

8.4 Quantitative description of relaxation

The quantitative knowledge of the relation between the observed relaxation rates and the statistically described molecular motions is necessary for the studies of molecular dynamics by NMR relaxation. We start the quantitative description of relaxation by presenting a general equation defining the desired relation

$$(\text{Relaxation rate}) = \sum_{\omega} (\text{numerical factor}) \times \underbrace{(\text{magnitude})^2}_{b^2} \times \underbrace{\text{spectral density function at } \omega}_{J(\omega)} . \tag{8.3}$$

To avoid a fuzzy general discussion, we rewrite the equation for a particular case of amide ^{15}N in a peptide bond, influenced by the electrons surrounding it and the amide proton attached to it. This is the molecular fragment that is

studied most often because it provides information for all non-proline residues of a protein and cheap selective labeling by ^{15}N makes the measurement accurate and feasible. The following table includes three relaxation rates that are measured most frequently, the *longitudinal relaxation rate* R_1, the *transverse relaxation rate* R_2, and *cross-relaxation rate* R_x, calculated from steady-state NOE and R_1. The subscripts N and H in the table refer to amide ^{15}N and amide proton, respectively.

We start from	we observe	type of R	chemical shift to		contribution of dipolar coupling to				
			B_z	B_x	B_z	B_z	B_x	B_x	B_x
$M_{\mathrm{N},z}$	$M_{\mathrm{N},z}$	$R_1 =$	0	$+\frac{3}{4}b_\mathrm{e}^2 J(\omega_\mathrm{N})$	$+0$	$+0$	$+\frac{3}{4}b_\mathrm{n}^2 J(\omega_\mathrm{N})$	$+\frac{3}{2}b_\mathrm{n}^2 J(\omega_\mathrm{H}+\omega_\mathrm{N})$	$+\frac{1}{4}b_\mathrm{n}^2 J(\omega_\mathrm{H}-\omega_\mathrm{N})$
$M_{\mathrm{N},x}$	$M_{\mathrm{N},x}$	$R_2 =$	$\frac{1}{2}b_\mathrm{e}^2 J(0)$	$+\frac{3}{8}b_\mathrm{e}^2 J(\omega_\mathrm{N})$	$+\frac{1}{2}b_\mathrm{n}^2 J(0)$	$+\frac{3}{4}b_\mathrm{n}^2 J(\omega_\mathrm{H})$	$+\frac{3}{8}b_\mathrm{n}^2 J(\omega_\mathrm{N})$	$+\frac{3}{4}b_\mathrm{n}^2 J(\omega_\mathrm{H}+\omega_\mathrm{N})$	$+\frac{1}{8}b_\mathrm{n}^2 J(\omega_\mathrm{H}-\omega_\mathrm{N})$
$M_{\mathrm{H},z}$	$M_{\mathrm{N},z}$	$R_x =$	0	$+0$	$+0$	$+0$	$+0$	$+\frac{3}{2}b_\mathrm{n}^2 J(\omega_\mathrm{H}+\omega_\mathrm{N})$	$-\frac{1}{4}b_\mathrm{n}^2 J(\omega_\mathrm{H}-\omega_\mathrm{N})$

The symbols in the equations have the following meaning.

- R_1, R_2, and R_x are experimentally determined relaxation rates, input for the analysis of molecular motions. Experiments providing them will be discussed in the next lecture.

- Numerical factors account for differences between correlation functions (cf. Eqs. 8.1 and 8.2) and for the factor of one half multiplying $J(\omega)$ in Eq. 8.10 (see below).

- b_e and b_n are constants describing magnitude of the interaction (interaction constants), known in advance with a relatively high precision and accuracy. For the amide ^{15}N nucleus,

$$b_\mathrm{e} = -\gamma_\mathrm{N} B_0 (\delta_\mathrm{max} - \delta_\mathrm{min}), \tag{8.4}$$

$$b_\mathrm{n} = \frac{\mu_0 h}{8\pi^2} \frac{\gamma_\mathrm{N} \gamma_\mathrm{H}}{r_\mathrm{NH}}, \tag{8.5}$$

where δ_max and δ_min are the amide ^{15}N chemical shifts in orientations providing the highest and lowest values, respectively (the difference is approximately $-160\,\mathrm{ppm}$), r_NH is the distance between the amide ^{15}N and ^{1}H nuclei, μ_0 is the magnetic permeability of vacuum and h is the Planck's constant.

- $J(\omega)$ are most interesting values, representing the actual bridge between molecular motions (described statistically by the time correlation function $C(t)$) and NMR at particular frequencies. As we discuss later, the $J(\omega)$ values provide a deep into the dynamics, but not all researches are used to looking at them. The following section explains how is the dependence of relaxation rates on the molecular motions encoded in $J(0)$.

8.5 Spectral density function

The effect of local field fluctuations on the relaxation can be described as $C(t)\cos(\omega t)$, where the correlation function $C(t)$ describes the molecular motions and $\cos(\omega t)$ accounts for the frequency dependence. It can be derived that the relaxation rates depend on *all values* of $C(t)\cos(\omega t)$ in the whole history of the measurement. The cumulative effect of $C(t)\cos(\omega t)$ can be evaluated by integrating $C(t)\cos(\omega t)$ from the beginning of the measurement until the actual time (Figure 8.2A,B):

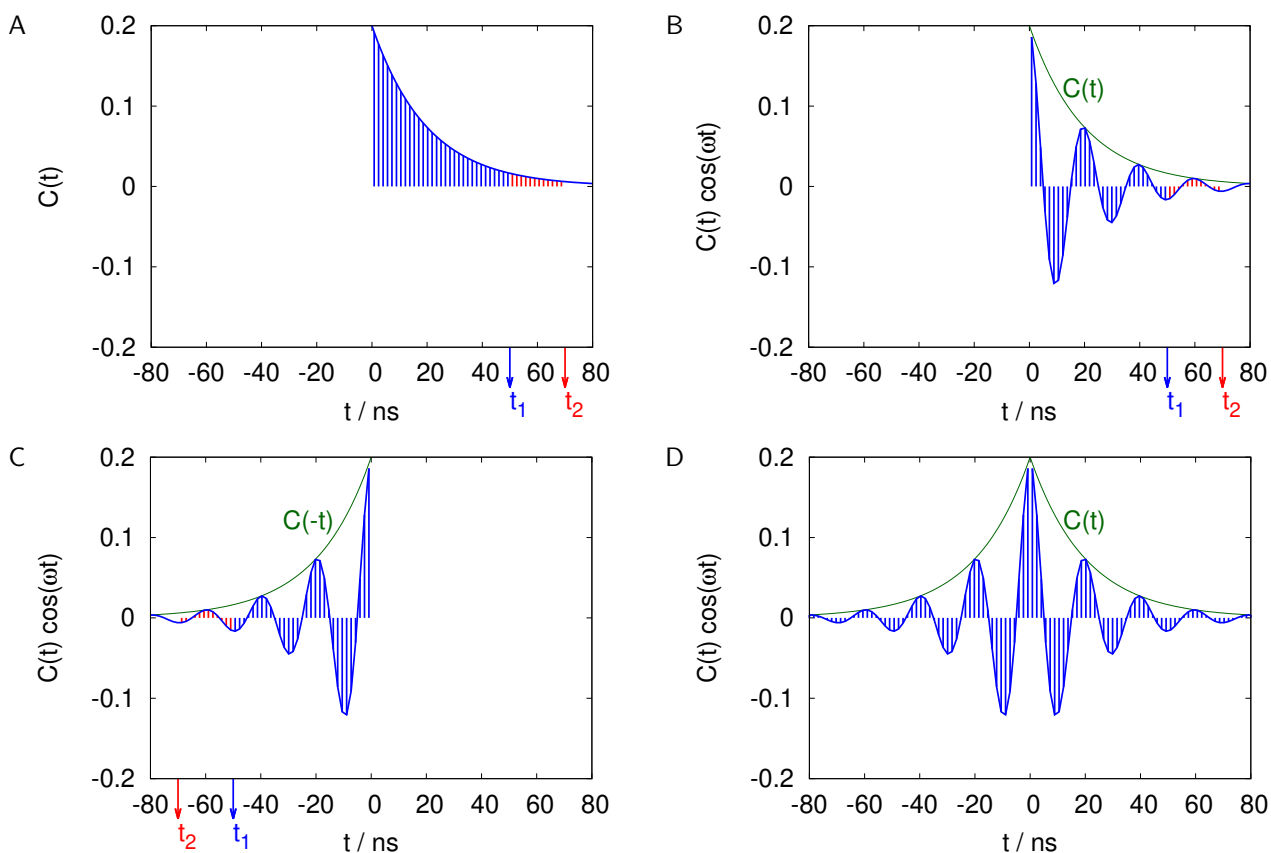$$\int_0^{t_\mathrm{actual}} C(t)\cos(\omega t)\mathrm{d}t. \tag{8.6}$$

Figure 8.2: A, integration of $C(t)$ describes the cumulative frequency-independent effect of fluctuations of B_z. If the upper limit of the integration (t_1) is sufficiently long so that $C(t)$ decays close to zero, further extending the upper limit (e.g. to t_2) does not change the integral significantly. B, integration of $C(t)\cos(\omega t)$ describes the cumulative effect of fluctuations of B_x resonating with the frequency ω. C, for random fluctuations, correlation functions and integrals of $C(t)\cos(\omega t)$ describing the loss of the correlation backward and forward in time are identical. D, for sufficiently long upper integration limit in Panel B, the value of the integral tends to one half of the integral of the sum of backward and forward $C(t)\cos(\omega t)$ functions, calculated from $-\infty$ to ∞. The values are plotted for $\tau = 20\,\text{ns}$ and precession frequency of ^{15}N at $11.75\,\text{T}$ ($500\,\text{MHz}$ spectrometer).

Usually, we integrate for a long time when $C(t)$ already decayed almost to zero. In such a case, extending the time further does not change the value of the integral any more (Figure 8.2B). The integral becomes *constant*, time independent. Therefore, it does not change even if we prolong the integration time to infinity:

$$\int\limits_0^{t_{\text{long}}} C(t)\cos(\omega t)\mathrm{d}t \approx \int\limits_0^\infty C(t)\cos(\omega t)\mathrm{d}t. \tag{8.7}$$

Moreover, we obtain the same integral if we look backwards in the time (Figure 8.2C). As the molecules move randomly, the geometric parameters Θ a nanosecond before we start counting the time are correlated with $\Theta(0)$ exactly like a nanosecond after $t = 0$. Mathematically,

$$\int\limits_{-\infty}^0 C(t)\cos(\omega t)\mathrm{d}t = \int\limits_0^\infty C(t)\cos(\omega t)\mathrm{d}t. \tag{8.8}$$

If we add both integrals, we obtain (Figure 8.2D)

$$\int\limits_{-\infty}^{0} C(t)\cos(\omega t)\mathrm{d}t + \int\limits_{0}^{\infty} C(t)\cos(\omega t)\mathrm{d}t = \int\limits_{-\infty}^{\infty} C(t)\cos(\omega t)\mathrm{d}t = 2\int\limits_{0}^{\infty} C(t)\cos(\omega t)\mathrm{d}t. \tag{8.9}$$

In physics, the integral from $-\infty$ to ∞ is a well established function, labeled $J(\omega)$, and called *spectral density function*. It is therefore convenient to use this already defined function, and express our cumulative effect of local field fluctuations as

$$\int\limits_{0}^{t_{\mathrm{actual}}} C(t)\cos(\omega t)\mathrm{d}t \approx -\frac{1}{2}\int\limits_{-\infty}^{\infty} C(t)\cos(\omega t)\mathrm{d}t.. \tag{8.10}$$

For the correlation function in Eq. 8.1, the integral can be calculated easily

$$\int\limits_{-\infty}^{0} \frac{1}{5}\mathrm{e}^{-t/\tau}\cos(\omega t)\mathrm{d}t = \frac{1}{5}\frac{\tau}{1+\omega^2\tau^2}. \tag{8.11}$$

The graph of the resulting function is the same as the shape of a peak in an NMR spectrum, a typical resonance curve with maximum at $\omega = 0$ (Figure 8.3). It tells us that $J(\omega)$ can be interpreted as a factor integrating the whole history of loosing correlation resonating with five characteristic frequencies ω:

- $\omega = 0$. Molecular motions at any frequency place the amide ^{15}N nucleus in different regions of the fields created by the orbital magnetic moment of the surrounding electrons and by the spin magnetic moment μ_{H} of the attached proton (Figure 8.4A). The resulting fluctuations of B_z causing the loss of coherence have a general randomizing effect, which is not frequency dependent (Section 8.2). The cumulative effect is given by integrating the correlation function for the whole history, without any frequency factor (Figure 8.2A). This missing frequency dependence may be included into the general equation as a multiplication by $1 = \cos(0)$.

- $\omega = \omega_{\mathrm{H}}$. Molecular motions also vary B_z at ^{15}N in another way, not by changing position of the amide ^{15}N nucleus in the field of μ_{H}, but by changing the field of μ_{H} itself. Molecular motions occasionally oscillate B_x with a frequency ω_{mol} resonating with ω_{H}. Such temporary oscillations rotate μ_{H} from the z direction to $-z$ and vice versa (Figure 8.4B). Such a change of μ_{H}, occurring only when ω_{mol} matches ω_{H}, further spreads values of B_z at ^{15}N in different molecules, in addition to the frequency independent variations, discussed above. This is why the contributions to R_2 also include the term $J(\omega_{\mathrm{H}})$.

- $\omega = \omega_{\mathrm{N}}$. As discussed in Section 8.2, the fluctuations of B_x contribute to the relaxation when B_x rotates for a short time with a frequency matching ω_{N} (as a result of a molecular rotation shown in Figure 8.4C). Eq. 8.11 shows that the term $J(\omega_{\mathrm{N}})$ describes resonance with the ^{15}N frequency ω_{N} (for a rigid spherical molecule).

- $\omega = \omega_{\mathrm{N}} \pm \omega_{\mathrm{H}}$. Precession of μ_{H} does not resonate with the precession of the ^{15}N magnetic moment. However, if a molecule rotates for a short time about the vertical axis with an angular frequency ω_{mol} which is accidentally matching a combination of ω_{N} and ω_{H}, the precession of μ_{H} combined with the molecular rotation resonates with the precession of the ^{15}N magnetic moment (see examples in Figure 8.4D,E). This explains why contributions to the relaxation rates also include terms depending on the combinations of the precession frequencies ω_{N} and ω_{H}.
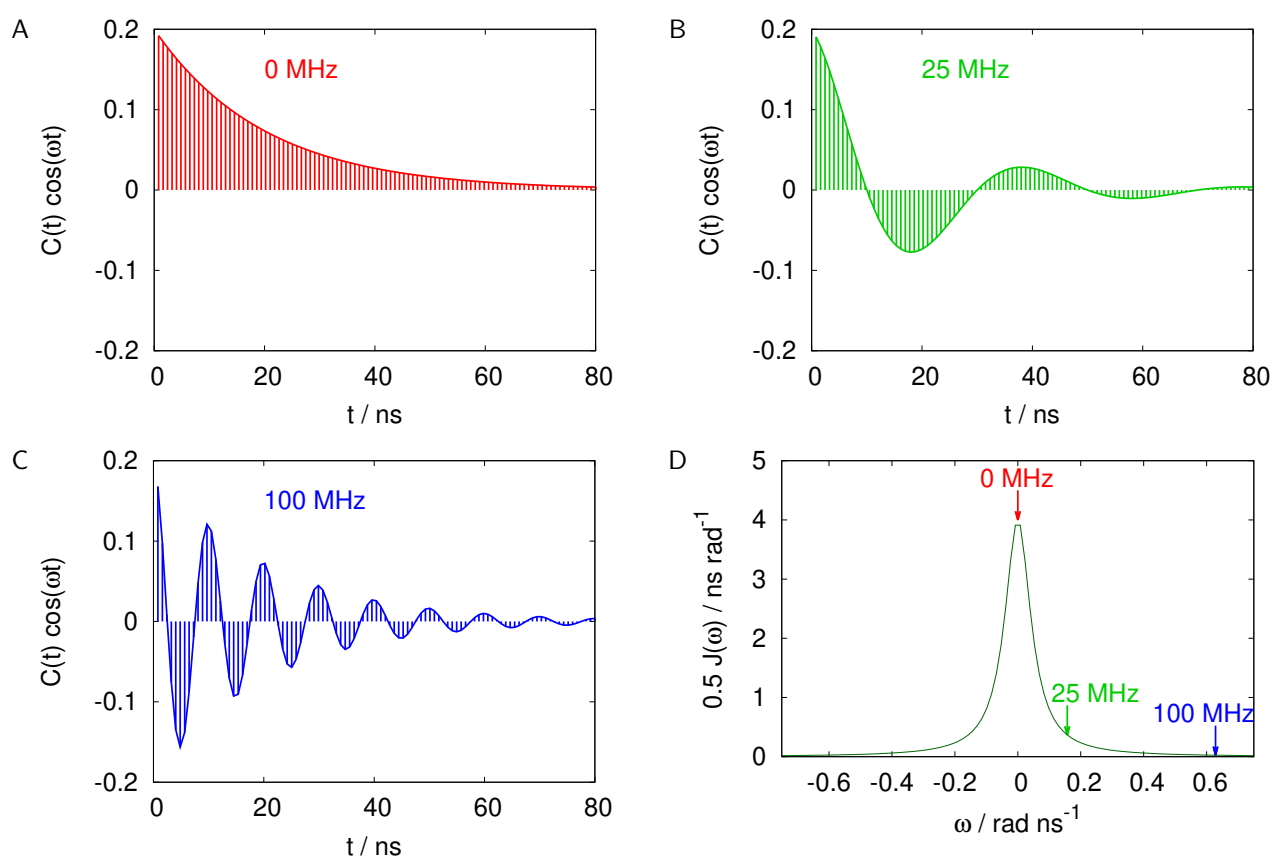
Figure 8.3: Spectral density function. Integrals displayed in Panels A–C represent three values of the spectral density function $J(\omega)$ (D). The data are plotted for $\tau = 20\,\text{ns}$ and precession frequency of ^{13}C and proton at 2.85 T (100 MHz spectrometer).

Figure 8.4: Illustration how random molecular motions resonating with five characteristic frequencies affect $\vec{\mu}_C$ in the CH bond in a 500 MHz spectrometer ($\vec{B}_0 = 11.75$ T). The first diagram in each row shows positions of the nuclei (^{13}C in green, (^{1}H in cyan), the second diagram shows orientation of the coordinate frame, the following diagrams are snapshots of the orientations of magnetic moments shown as arrows (^{13}C in green, (^{1}H in cyan) in a magnetic field of the neighbour (shown as force lines). The red arrow indicates the direction of the change of the orientation of the influenced magnetic moment, but the actual change is very small (not observable in the pictures) in the short depicted period of 4 ns. The molecule is assumed to rotate with a constant frequency for 4 ns. A, $\vec{\mu}_C$ oriented horizontally, $\vec{\mu}_H$ oriented vertically, ^{13}C in the yz plane, ^{1}H in the center of the coordinate system. Rotation at any frequency about a horizontal axis varies precession frequency of $\vec{\mu}_C$ about $\vec{B}_0$ and results in the loss of coherence of ^{13}C. B, $\vec{\mu}_H$ oriented horizontally, $\vec{\mu}_C$ oriented vertically, ^{1}H above the xy plane, ^{13}C in the center of the coordinate system. Rotation at ω_H about a horizontal axis pulls $\vec{\mu}_H$ up (red arrow pointing up in the given coordinate frame) in the magnetic fields of $\vec{\mu}_C$. This reorientation of $\vec{\mu}_H$ (observed only at time much longer than the depicted period of 4 ns) influences the effect of the J-coupling. C, $\vec{\mu}_C$ oriented horizontally, $\vec{\mu}_H$ oriented vertically, ^{13}C above the xy plane, ^{1}H in the center of the coordinate system. Rotation at ω_C about a horizontal axis pulls $\vec{\mu}_C$ up (red arrow pointing up in the given coordinate frame) in the magnetic fields of $\vec{\mu}_H$. D, $\vec{\mu}_C$ oriented horizontally, $\vec{\mu}_H$ oriented horizontally, ^{13}C in the xy plane, ^{1}H in the center of the coordinate system. Rotation at $\omega_H + \omega_C$ about a horizontal axis pulls $\vec{\mu}_C$ up (red arrow pointing up in the given coordinate frame) in the magnetic fields of $\vec{\mu}_H$. E, $\vec{\mu}_C$ oriented horizontally, $\vec{\mu}_H$ oriented horizontally, ^{13}C in the yz plane, ^{1}H in the center of the coordinate system. Rotation at $\omega_H - \omega_C$ about a horizontal axis pulls μ_C up (red arrow pointing mostly up in the given coordinate frame) in the magnetic fields of μ_H. The reorientation of μ_C in Panels C–E (observed only at time much longer than the depicted period of 4 ns) contributes to the return of the distribution of the ^{13}C magnetic moments to the thermal equilibrium.

Lecture 9
Measurement of relaxation rates

9.1 General principle

NMR experiments for measurements of relaxation rates usually follow a general scheme. First, it is necessary to create a starting distribution of magnetic moments defining the type relaxation experiment we are going to run (the first column "we start from" in the table of equations describing relaxation rates R_1, R_2, R_x in Section 8.4. Such magnetic moment distribution is called the *spin state* in the following text. Then the spin state is let to relax for a variable period of time (*relaxation delay*). Typically, some manipulation of the spin system is also necessary during the relaxation delay to suppress coherent evolutions or relaxation pathways which need to be avoided. Finally, the selected spin state is transformed into an observable magnetization detected as an NMR signal which intensity reflects the polarization of the selected spin state at the end of the relaxation delay. The experiment is usually repeated several times, while the relaxation delay is varied. The change of the polarization of the selected spin state is recorded as a dependence on the relaxation time, which is then analyzed to extract the required relaxation rate.

9.2 Inversion recovery experiment

The *inversion recovery* experiment represents probably the simplest NMR relaxation experiment. Usually, it is used to study the relaxation of small molecules and it is also used in magnetic resonance imaging. The experiment is shown in a graphical form in Figure 9.1. In the beginning, the spin magnetization is oriented parallel with the external magnetic field. The experiment starts with a 180° pulse, which inverts the polarization of the studied nuclei. This is the preparation phase of the experiment followed with the variable relaxation delay, during which the spin system returns to the equilibrium in which it was at the beginning of the experiment (before applying the 180° pulse). Therefore, the absolute value of the polarization in the direction opposite to the initial one starts to decrease, later it passes the zero value, switches the sign, and it continues increasing until it reaches its equilibrium value. This process of the return to the equilibrium is interrupted by the application of a 90° pulse which transforms the longitudinal polarization into an observable magnetization and it is detected. The intensity of the signal is proportional to the size of the longitudinal polarization at the end of the chosen length of the relaxation delay. The dependence of the intensity of the detected signal $I(t)$ on the length of the relaxation delay t is described by Eq 9.1:

$$I(t) = I_\infty(1 - 2\mathrm{e}^{-R_1 t}), \tag{9.1}$$

where R_1 is the longitudinal relaxation rate and I_∞ is the equilibrium signal intensity. The example of the dependence is shown in Figure 9.1.

9.3 Measurement of the transverse relaxation rate

A simple experiment for a measurement of the transverse relaxation is discussed in this section and its scheme is shown in Figure 9.2. First, the transverse magnetization is created by the application of a 90° pulse. Then, the relaxation delay follows. It is necessary to keep in mind that magnetization in the transverse plane is a subject of
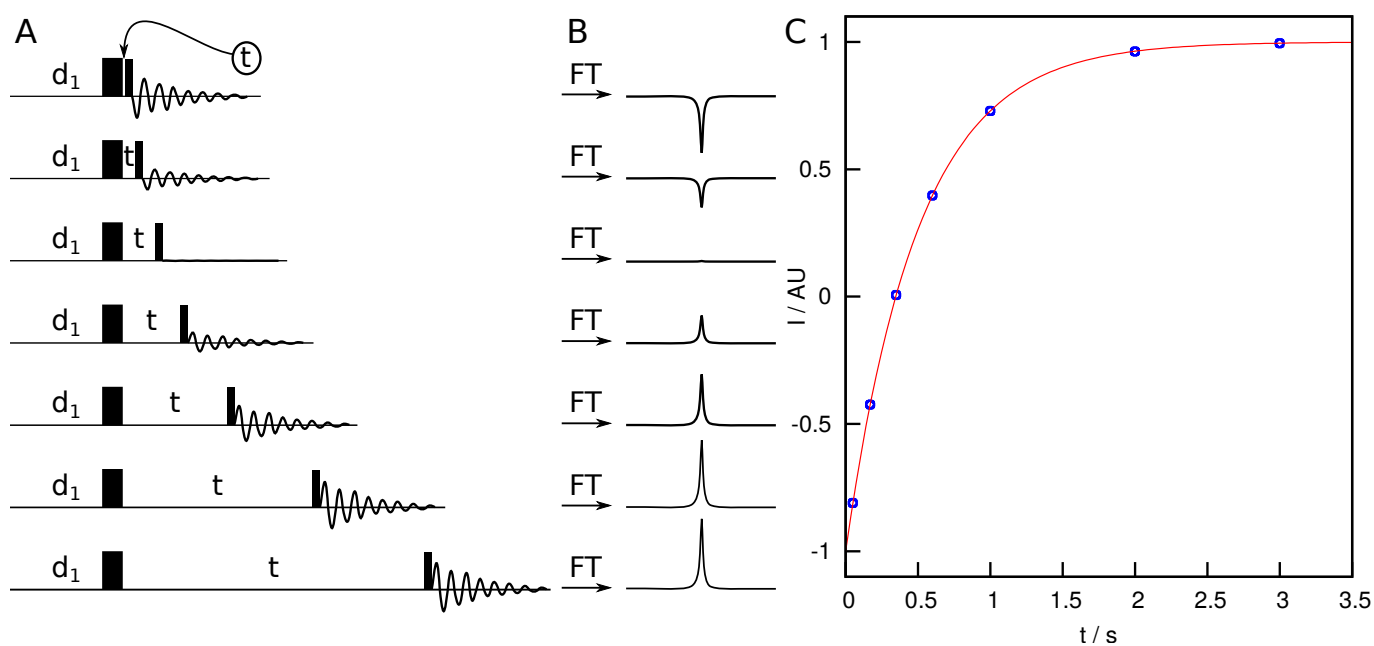
Figure 9.1: A, Scheme of the inversion recovery experiment designed for a measurement of the longitudinal relaxation rate of an isolated spin. The experiment is repeated with variable length of the relaxation delay t, a series of seven experiments is presented in this example. Narrow and wide boxes represent $90°$ and $180°$ degree pulses, respectively. (Note, that the delay d_1 between the scans is not proportional in its length to the rest of the pulse sequence. For the depicted case it should be at least as long as the longest relaxation delay in the last scheme to achieve a state close to the equilibrium.) B, Spectrum obtained after the Fourier transformation of the obtained signal from the series of the inversion recovery experiments (the simplest case of a single peak in the spectrum is presented). C, The dependence of the measured intensities in spectra on the relaxation delay t of the corresponding experiment. The red line shows the theoretical dependence described by Eq. 9.1.
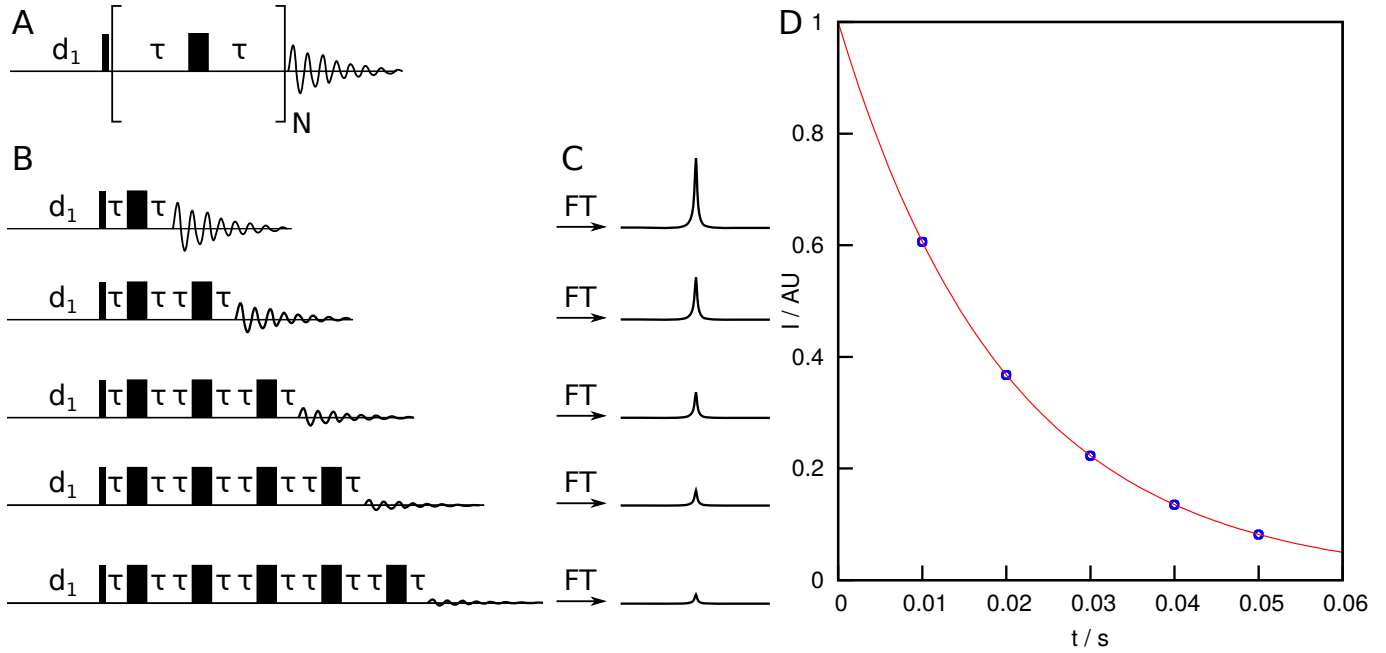
Figure 9.2: A, Scheme of the simple experiment for the measurement of the transverse relaxation rate of an isolated spin. Narrow and wide boxes represent 90° and 180° degree pulses, respectively. Central part in the bracket is a spin echo of the length 2τ and it is repeated N times to achieve variable relaxation time as shown for a series of five experiments in Panel B. Fourier transformation of the obtained signal from each experiment provides a signal with various intensity as shown in Panel C (the simplest case of a single peak in the spectrum is presented). D, The dependence of the measured intensities in spectra on the relaxation delay $t = 2N\tau$ of the corresponding experiments. The red line shows the theoretical dependence described by Eq. 9.2.

coherent evolutions. Even the simplest case, i.e. isolated spin will be subject of effects of evolution due to chemical shift. Therefore, unlike for the inversion recovery experiment, additional spin system manipulation is necessary to be applied during the relaxation delay to suppress this effect. As was already discussed in Section 3.4, the effect of coherent evolution due to the chemical shift can be suppressed by the *refocusing spin echo*. So, the relaxation delay is composed by a spin-echo block which is repeated various number of times to achieve variable relaxation delays. The transverse relaxation causes decrease of the spin coherence until the equilibrium state is reached, which is characterized by a zero coherence and no observable magnetization. The signal can be detected after the end of the relaxation delay without any need of further spin state manipulation (because the transverse magnetization is directly observable). The amount of the transverse magnetization is directly proportional to the detected signal and it decays with the increasing relaxation delay t following the exponential decay:

$$I(t) = I(0)\mathrm{e}^{-R_2 t}, \tag{9.2}$$

where R_2 is the transverse relaxation rate and $I(t)$ is the signal intensity the end of the relaxation delay with the total length $t = 2N\tau$, where τ is the one half of the length of the used spin echo and N is number of repetitions of the spin-echo elements. The example of the experimental data is shown in Figure 9.2.

9.4 Measurement of the steady state Nuclear Overhauser Effect

So far we discussed only the cases when we disturbed a selected spin polarization from equilibrium to create a new spin state and we studied its own return to the equilibrium. This type of relaxation is called auto-relaxation. But it is possible to study also the cases when we disturb one type of polarization and we observe the effect of the consequent perturbation of the equilibrium on another spin state. This type of relaxation is called cross-relaxation, and its
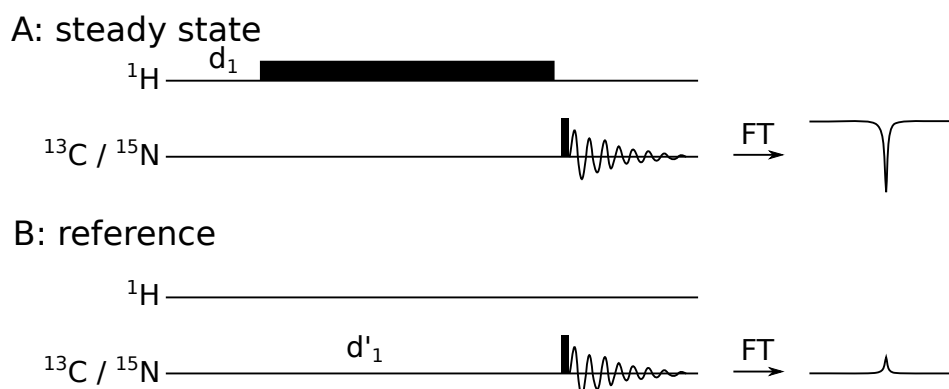
Figure 9.3: Schemes of pulse sequences used to measure the cross-relaxation between proton and heteronuclear polarizations (of ^{13}C or ^{15}N shown in this example). Narrow boxes represent 90° degree pulses. A, Scheme of the simple experiment for the measurement of the steady state NOE with the applied saturation of protons. B, Reference experiment to measure the signal intensity originating from the equilibrium ^{13}C or ^{15}N polarization. Note, that delays between scans in the experiments, d_1' and d_1, have different length: $d_1' \gg d_1$. A long d_1' must be used to let the system reach a state very similar to the equilibrium. C, Fourier transformation is used to obtain spectra in both reference and steady state experiment (only a single peak in the spectrum is presented for the sake of simplicity). The ratio of the intensities of the signals in the spectra originating from the steady state experiment and the reference experiment provides the information about the cross-relaxation rate R_x.

consequence is the nuclear Overhauser effect (NOE). The experiment allowing us to evaluate NOE and to calculate the cross-relaxation rate R_x is explained in this section for a simple spin system: ^{13}C-^{1}H pair or ^{15}N-^{1}H pair. It is important that both nuclei have magnetic moments and are close in space. Then, each of them is affected not only by the external magnetic field, but also by the magnetic field from the other nuclei, i.e., ^{13}C / ^{15}N spin "feels" magnetization of proton, and vice versa (see Section 2.2). The magnetic moments are no longer isolated but they interact with each other via the dipole-dipole interaction (or dipolar coupling). At the beginning of the experiment, magnetic moment distributions of both ^{13}C / ^{15}N and ^{1}H are polarized producing a net magnetization in the direction aligned with the external magnetic field. This equilibrium is then disturbed by a very long irradiation by a radio wave resonating with the precession frequency of one of the nuclei, typically proton. This irradiation may be of various form but its results is the same as shown for solvent suppression by *presaturation* in Section 5.2. The irradiation rotates the polarization out of the z direction so thata coherence is created while relaxation simultaneously has the opposite effect dephasing the coherences and returning the polarization back to the z-direction. As a result, a steady state is achieved characterized by an absence of proton polarization in any direction. Because the proton is not isolated, but it interacts with the carbon, the ^{13}C / ^{15}N polarization is also affected by the change of the proton magnetic moment distribution, and also its polarization is changed as it adapts to the established steady state (different from the equilibrium, where the proton longitudinal polarization is present). Comparison of the equilibrium ^{13}C / ^{15}N polarization and its longitudinal polarization upon the steady state conditions provides the information about the cross-relaxation between the proton and ^{13}C / ^{15}N polarizations. For the quantitative analysis, it is necessary to keep the recovery delay before the acquisition of the reference spectra (when no proton saturation is applied) long enough so that the system is in a state very close to the equilibrium.

9.5 Measurement of the relaxation rates in biomacromolecules

The experiments discussed above in Sections 9.2–9.4 are not suited for the analysis of dynamics of more complex systems like biomacromolecules. But the experiments used for the proteins, nucleic-acids, etc., are derived from the above ones. Usually, dynamics of biomacromolecules is investigated by analysis of relaxation rates of ^{15}N or ^{13}C in isolated ^{15}N-^{1}H or ^{13}C-^{1}H spin pairs which represent the simplest case of interacting magnetic moments. Moreover, it is relatively easy to produce a sample suitable for the relaxation measurements, where the mentioned spin pairs can be considered as isolated. Typical probes of dynamics are amide ^{15}N-^{1}H pairs from the peptide bonds of a protein

enriched with ^{15}N isotopes, ^{15}N-^{1}H spin pairs at position 1 of guanines, or at position 3 of uracils or thymines in nucleic acid samples enriched with ^{15}N isotopes. ^{13}C-^{1}H spin pairs at position 8 in purine bases enriched with ^{13}C isotopes may serve as another example. Although these spin pairs are not completely isolated, other spin magnetic moments are not located very close to them and weak interactions with other nuclei do not corrupt the analysis.

Typically, the relaxation rates are determined from the analysis of peak intensities in 2D spectra, but sometimes a measurement of relaxation rates using a more dimensional spectra is necessary to achieve the desired resolution. It is also very useful to increase the sensitivity of the experiments by polarization transfers between proton and ^{15}N or ^{13}C in a similar way as introduced in Section 3.7. Combinations with the HSQC sequence (Section 3.8) are used most often. Simplified versions of such experiments, emphasizing the basic principles, are discussed in this section.

Our overview of the basic experiments starts with the experiment for the measurement of longitudinal relaxation rates, shown in Figure 9.4A. The spin state preparation step (in the red frame) includes a 90° pulse applied to ^{13}C or ^{15}N followed by a gradient, aimed to destroy longitudinal polarization of ^{13}C or ^{15}N and its correlation with the proton longitudinal polarization (so-called *two spin order*).

Then the INEPT step is used to transfer the polarization from protons to the attached heteronuclei (^{13}C or ^{15}N) to profit from the larger polarization of proton. Unlike in the standard HSQC experiment (and similar to HC(C)H-TOCSY, see Figure 6.3B), a second INEPT transfer is necessary to create a pure in-phase polarization of the heteronucleus.

The preparation step ends with a single 90° pulse used to transform the ^{13}C or ^{15}N in-phase coherence into the polarization aligned with the external static magnetic field. Its absolute value is labeled P_{init} in this paragraph. Depending on the phase of the last applied pulse ($+y$ or $-y$), a longitudinal polarization either parallel or anti-parallel with the external static magnetic field is created, which is distinguished by the sign of the P_{init} in the following equations (positive for parallel orientation). Note that parallel polarization is not equal to the equilibrium polarization of ^{13}C or ^{15}N. It is larger due to the initial polarization transfer from the attached proton, as discussed in Section 3.7.

In the following block (shown in a blue frame), the polarization $P(t)$ decays towards the equilibrium polarization P_∞. The decay of $P(t)$ is exponential with a *longitudinal relaxation rate constant R_1*. For the parallel polarization at the beginning of the relaxation delay we get

$$P_1(t) = (P_{\text{init}} - P_\infty)\mathrm{e}^{-R_1 t} + P_\infty, \tag{9.3}$$

while if we apply the 90° pulse with the opposite phase we start with antiparallel polarization $-P_{\text{init}}$ and the evolution of the polarization $P_2(t)$ towards the equilibrium P_∞ follows the equation

$$P_2(t) = -(P_{\text{init}} + P_\infty)\mathrm{e}^{-R_1 t} + P_\infty. \tag{9.4}$$

It is not convenient to evaluate more unknown variables than necessary, therefore the experiment is measured twice in an interleaved manner and the signals originating from both polarizations $P_1(t)$ and $P_2(t)$ are subtracted, providing a simple mono-exponential decay

$$P_1(t) - P_2(t) = 2P_{\text{init}}\mathrm{e}^{-R_1 t}. \tag{9.5}$$

Compared to the simple inversion-recovery experiment one should notice that the relaxation period is not so simple but there is a proton inversion pulse applied in the middle of the relaxation period. It inverts the effect of the cross-relaxations, so that the cross-relaxations effects before and after this pulse cancel each other.

The third part of the pulse sequence, shown in a green frame in Figure 9.4A, converts the ^{13}C or ^{15}N longitudinal polarization modulated by the exponential decay to a measurable signal. A 90° pulse at the end of the relaxation delay flips the ^{13}C or ^{15}N longitudinal polarization to the horizontal one, corresponding to the ^{13}C or ^{15}N coherence. Its evolution during the incremented delay t_1 introduces modulation of the signal by the ^{13}C or ^{15}N chemical shift. This goal is achieved in the same way as in the HC(C)H-TOCSY, see Figure 6.3B) HSQC experiment 3.8. Finally, the polarization is transferred back to proton using two INEPT steps (like in the HC(C)H-TOCSY experiment, cf. Figure 6.3B). The created proton coherence is detected in the real time t_2. Fourier transformation of the accumulated signal results in a series of two dimensional spectra, with the proton frequency offset in the direct dimension, the ^{13}C or ^{15}N frequency offset in the indirect dimension, and peak intensity decaying exponentially in the series of spectra with the R_1 rate constant.

The experiment for the measurement of the transverse relaxation rate (shown in Figure 9.4B) is very similar to the experiment for the longitudinal relaxation rate, except for the relaxation delay element (shown in a blue frame) and few differences in the central part of the pulse sequence. First, the last 90° pulse applied prior the relaxation period is missing because the desired in-phase polarization is already created at the end of the second INEPT step. The relaxation period for the transverse relaxation has similar form to that one introduced in Section 9.3. It is composed of different numbers of (refocusing) spin echoes. It is necessary to keep in mind that a J-coupled pair of magnetic moments evolves not only due to the chemical shift. The horizontal polarization oscillates between the in-phase and anti-phase coherences as discussed in Section 2.5. This oscillation is refocused at the end of the spin echo, but evolves *during* the echo (see Section 3.4). Therefore, the spin-echoes must be sufficiently short so that the original in-phase coherence is refocused before it has enough time to evolve into an anti-phase coherence, which relaxes differently. If the echo is too long, the measured relaxation rate represents a mixture of the relaxation rates of the in-phase and anti-phase coherences. The length of the spin echo 2τ should be chosen to fulfill the condition: $2\tau\pi J \ll 1$, where J is the J-coupling constant. In addition, it is also necessary to suppress the cross-relaxation between the in-phase and anti-phase coherences. Therefore, additional proton 180° pulses are inserted in the relaxation period, which effectively suppresses the effect of this cross-relaxation.[1]

The relaxation block of the pulse sequence is followed by the incremented delay t_1, when the signal is modulated by the ^{13}C or ^{15}N frequency offset. Because we keep the ^{13}C or ^{15}N transverse magnetization throughout the relaxation delay, the 90° pulse creating the in-phase magnetization in the case of the experiment for the measurement of the longitudinal relaxation rate is missing. The rest of the pulse sequence is identical with the experiment for the measurement of the longitudinal relaxation rate. The dependence of the detected signal on the relaxation delay reflects the relaxation of the coherence during the relaxation delay and it follows Eq. 9.2, where the relaxation delay is calculated slightly differently: $t = 2N\tau + 8\tau$.

Finally, we describe the experiment for the measurement of the steady-state NOE. Its principle is the same as discussed for its simple 1D version in the previous section 9.4. Two experiments are recorded. In the first one, the steady state condition is created by a long irradiation of protons (Figure 9.4C). In the second one, the system is let relax long enough to reach its equilibrium (or a state very close to it) prior to the initial 90° pulse (Figure 9.4D). Therefore, the created coherence is given by the equilibrium longitudinal polarization of ^{13}C or ^{15}N. The final part of both sequences is the same as in the experiment for the measurement of the longitudinal relaxation rate (shown in a green frame).

---

[1] The proton 180° pulses are applied after the first quarter of the relaxation period and at three quarters of the relaxation period. The proton 180° pulses invert the effect of the cross-relaxation, so that the sum of the effects of the cross-relaxation in the outer parts of the relaxation period cancels with the effect in the middle part.
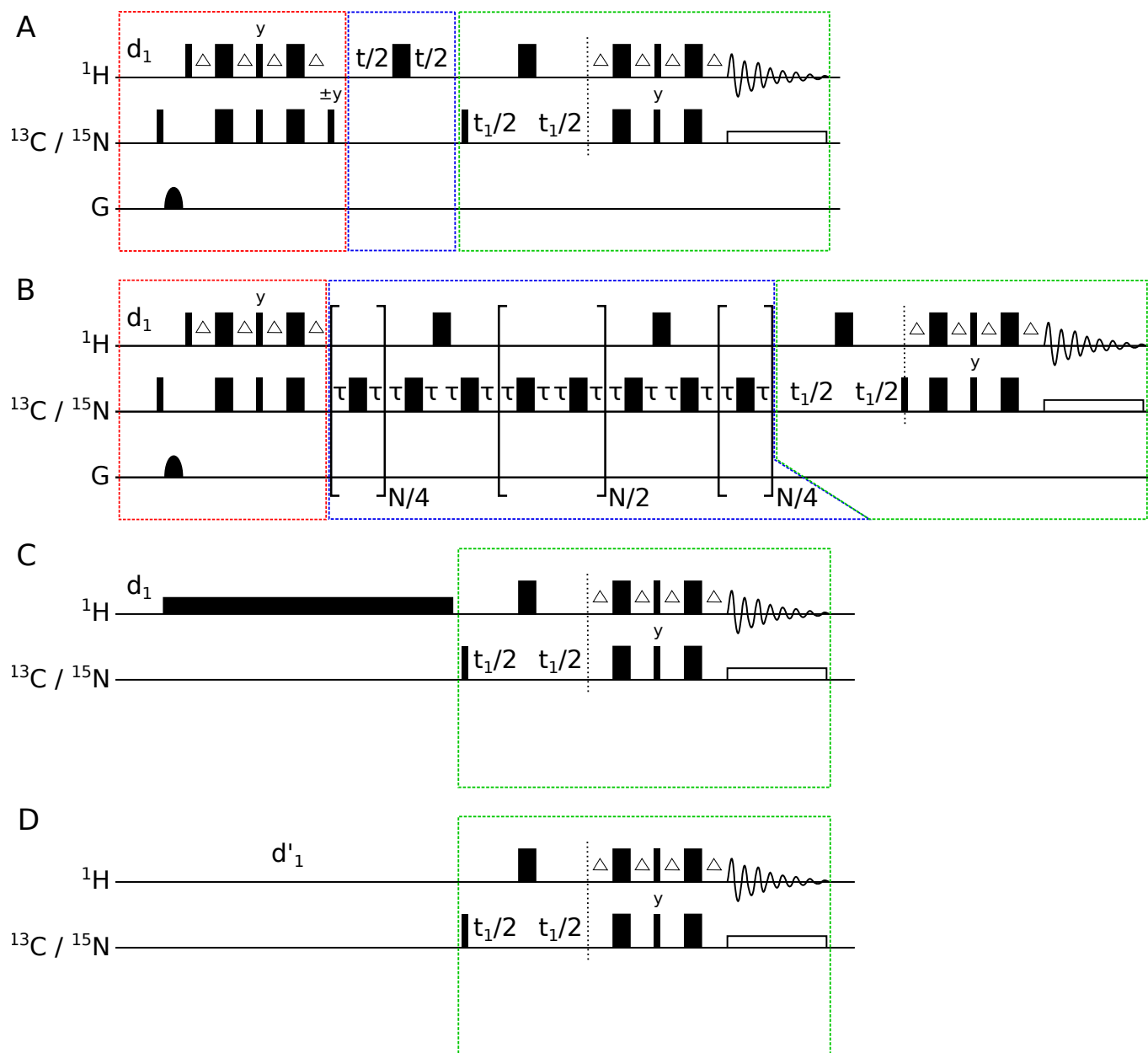
Figure 9.4: Simplified pulse sequences of experiments used to determine heteronuclear longitudinal relaxation rates (A), transverse relaxation rates (B) and steady state NOE (C and D) in biomacromolecules. The examples are provided for ^{13}C-^{1}H or ^{15}N-^{1}H spin pairs. The lines correspond to radio-waves applied at the precession frequency of protons and ^{13}C or ^{15}N, and to the magnetic field gradients (labeled G). Narrow and wide boxes represent $90°$ and $180°$ pulses, respectively. The pulses are applied with x phase unless indicate otherwise. The open rectangles represent decoupling trains. The delay Δ is equal to $1/(4J)$ where J is the J-coupling constant. Two experiments are depicted for the measurement of the steady state NOE: the experiment in which the steady state is created (C) by proton saturation (low rectangle), and the reference experiment (D) in which the equilibrium ^{13}C or ^{15}N polarization is measured. The delays d_1 and d'_1 have different length. A long d'_1 must be used to assure achieve of a state close to the equilibrium. The red, blue, and green frame mark the preparation phases of the experiments, the variable relaxation delays, and the detection elements of the pulse sequences, respectively.

Lecture 10
Analysis of internal motions

10.1 Internal motions

So far, we discussed just the rotational diffusion of the whole molecule. It is much more exciting to study internal motions of the molecule. A brief list of internal molecular motions with their time scales motions is presented in Table 10.1.

Table 10.1: Typical time scales of internal molecular motions

Time scale	type of motion
10^{-15} s	Bond-length fluctuations (stretching vibrations)
10^{-14}–10^{-13} s	Bond angle and torsion angle fluctuations
10^{-12}–10^{-11} s	Helix bending, β-sheet twisting, simultaneous local torsion angle flips,
	conformational changes in disordered regions
10^{-10}–10^{-7} s	Local conformational changes
	(helix growing, sheet breathing, local folding events)
10^{-6}–10^{-3} s	Fast changes of conformation, fast chemical reactions
10^{-2}–10^{0} s	Interconversion of conformational states, slow chemical reactions,
	folding of small proteins (with no prolines and disulfide bridges)
$> 10^{0}$ s	Slow folding events (proline isomerization, S–S bond formation),
	exchange of amide and imino protons with water

We now explore the effect of internal motions on the NMR relaxation, starting with motions that affect only *orientation* of the interacting magnetic moments but do not change *magnitude of the interaction*. In the NMR experiments, we monitor motions of vectors connecting nuclei interaction via the dipole-dipole interaction, or of vectors defining orientation of the electronic environment surrounding the observed nucleus.[1]

We now attempt to describe the internal motions changing orientation of the interacting magnetic moments under some simplifying circumstances. First, we assume that only one type of motion affects the amide bond. Second, we assume that the motion is random and can be described in a fashion similar to the rotational diffusion. Therefore, we expect an exponential decay for the correlation function of the internal motion. We cannot use Eq. 8.1 directly. Eq. 8.1 describes unrestricted random rotation, which is an unrealistic assumption for a motion of a chemical bond in a well-structured molecule. To fix the problem, a so-called *order parameter* can be introduced to describe motional restriction. The single exponential term in Eq. 8.1 is then replaced by the expression

$$C_{\mathrm{I}}(t) = (1 - S^2)\mathrm{e}^{-R_{\mathrm{I}}t} + S^2, \tag{10.1}$$

where S^2 represents the order parameter and R_{I} is a constant describing the rate of loosing the correlation, equal to the inverse value of the correlation time describing the fast motions. Note that $C_{\mathrm{I}}(t)$ decays exponentially from unity (for $t = 0$) to S^2 (for $t \to \infty$). Replacing S^2 with zero gives us back the correlation function from Eq. 8.1. We

---

[1]Technically, the electron distribution influencing observed frequencies of nuclei are described by *chemical shift tensors*.

see that $S^2 = 0$ represents the unrestricted limit. On the other hand, setting $S^2 = 1$ makes $C_I(t)$ equal to one for any t. It shows that $S^2 = 1$ describes complete rigidity, i.e., lack of any internal motion.

The rotational diffusion is always present in solution. So, we need to combine Eqs. 8.1 and 10.1. To do it, we need the last assumption. We expect that the internal motions and overall rotational diffusion are independent and that the whole molecule still behaves as a sphere. Then, we can write

$$C(t) = C_O(t)C_I(t) = \frac{1}{5}S^2 e^{-R_I t} + \frac{1}{5}(1 - S^2)e^{-(R_I + R_O)t}, \tag{10.2}$$

where $R_O = 1/\tau$ from Eq. 8.1 and the subscripts O and I distinguish overall and internal motions, respectively. It is useful to note that the effect of the internal motions cannot be distinguished from the overall rotational diffusion if the internal motions are slower. It can be checked easily by setting $R_I \ll R_O$. Then,

$$C(t) = C_O(t)C_I(t) = \frac{1}{5}S^2 e^{-R_O t} + \frac{1}{5}(1 - S^2)e^{-(R_I + R_O)t} \rightarrow \frac{1}{5}S^2 e^{-R_O t} + \frac{1}{5}(1 - S^2)e^{-R_O t} = \frac{1}{5}e^{-R_O t}. \tag{10.3}$$

Fourier transformation of $C(t)$ gives the spectral density function

$$J(\omega) = S^2 \frac{\frac{2}{5}R_O}{R_O^2 + \omega^2} + (1 - S^2)\frac{\frac{2}{5}(R_O + R_I)}{(R_O + R_I)^2 + \omega^2}, \tag{10.4}$$

which can be used in the equation defining the relaxation rates. Note that we obtain a sum of two functions resembling the description of NMR peaks. Such expressions are known as the *Lorentzian functions*.

Further complexity is introduced if we need more than one type of internal motions to describe the relaxation or if the overall shape of the molecule is far for spherical.

10.2 Motional parameters from NMR measurements

The measured values of R_1, R_2, and R_x (Sections 9.2–9.5) depend on five values of the spectral density function, taken at five different frequencies. If we study relaxation of ^{15}N, these frequencies are zero, ω_N, $\omega_N + \omega_H$, ω_H, and $\omega_N - \omega_H$. Analysis of the form of the spectral density function introduced in the Eq. 10.4 shows that it is a linear combination of Lorentzian functions. An example of its profile is shown in Figure 10.1. Two facts can be noticed. First, the magnetogyric ratio of proton is approximately $10\times$ larger than the magnetogyric ratio of ^{15}N, so the last three frequencies do not differ too much. Second, the dependence does not decay rapidly at frequencies close to ω_H in cases of biomolecules studied by high-field NMR. Therefore, the last three values of spectral density function at frequencies $\omega_N + \omega_H$, ω_H, and $\omega_N - \omega_H$ differ very slightly and they can be replaced by a single "high frequency" value of the spectral density function. We see that the measured three relaxation rates are just linear combinations of three values of the spectral density function. It is easy to calculate the spectral density function values from the relaxation rates. We know that the spectral density functions map the rate of molecular motions. The described analysis of the relaxation data, known as *reduced spectral density mapping*, represents a straightforward way to the information about molecular motions.

If we want to obtain more intuitive description of motions, we can fit the measured relaxation rates to the corresponding equations and obtain directly the correlation rates (or times) and the order parameters. Of course, the number of fitted parameters cannot be larger than the number of measured relaxation rates (can be three, although it is recommended to repeat the measurements at several different magnetic fields to improve the analysis). As a consequence, only one type of internal motions can be fully described by its order parameter (defining range of motion) and correlation rate (defining the rate of the motion) if the relaxation rates were acquired only at a single field. Note that such description of motions is obtained for each residue which amide peak is resolved in the ^{1}H-^{15}N correlation spectrum. The third available parameter may be the rate of overall rotational diffusion, but this parameter is the same for all residues and it is usually obtained in an independent way.[2] The third parameter can be used to partially describe an additional type of motion. The analysis based on fitting correlation rates and order parameters is known as the *model-free approach*. The name reflects the fact that we do not need a mechanistic description of the motion to learn the average range and rate.

---

[2]The average of R_2/R_1 ratios provides a good estimate.
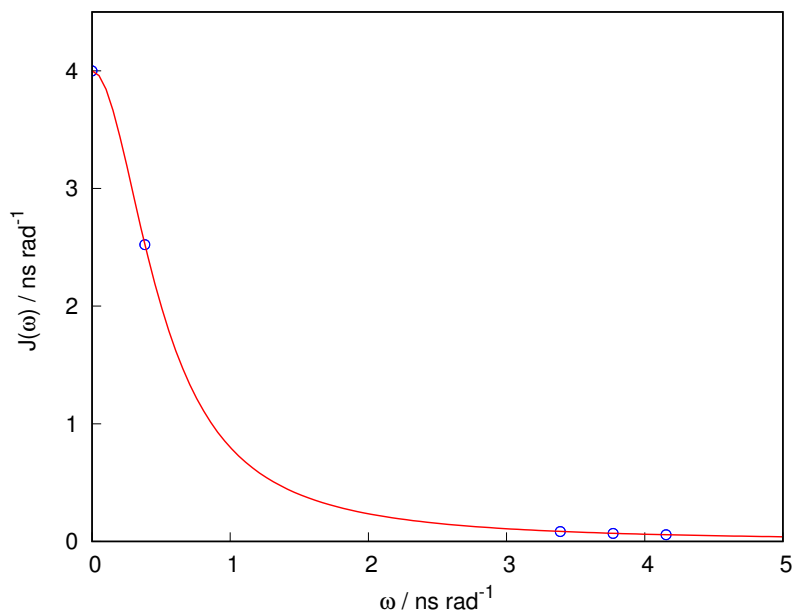
Figure 10.1: Example of the spectral density function with highlighted values of the spectral density values at frequencies that contribute to the relaxation rates of the ^{15}N-^{1}H pair at 14.1 T (600 MHz spectrometer).

10.3 Chemical exchange

We now extend our description of molecular motions to structural changes affecting also the *magnitude of the interaction*. The values of b_{n} and b_{e} vary if the distance between interacting nuclei, or the electron distribution around the observed nucleus change. The causes of such variations can be changes in conformation but also in chemical configuration, including intermolecular interactions and chemical reactions. In NMR spectroscopy, the structural changes are called *conformational exchange* or *chemical exchange*.

We have shown in Eq. 10.3 that the rate constants describing fast relaxation are not sensitive to much slower changes in orientation of vectors describing mutual orientations of interacting magnetic moments. However, slow exchange processes changing *magnitude of the interaction* have impact on the shape of the NMR spectral lines and affect the evolution of the magnetization components parallel and perpendicular to the external magnetic field.

The rate equations describing the chemical exchange are similar to the equations describing evolution of the magnetization components due to the fast relaxation. We just need to treat the magnetization components separately for each state of the molecule, and to add the chemical rate constants to the relaxation rates and precession frequencies in the equations. The description can be also applied to bimolecular processes such as ligand binding, proton dissociation, or enzyme catalysis.

10.4 Effect of chemical exchange on the transverse magnetization

Effects of the chemical exchange on the evolution of the magnetization components perpendicular to the external magnetic field can be studied in a similar fashion as the R_2 relaxation. Direct evaluation of the line-width in the spectrum provides a quick estimate of the exchange contribution to the loss of coherence. Spectra can be simulated for various values of the rate constants and compared to the experimental data. However, the line shape is in reality also influenced by inhomogeneities of the magnetic field. Therefore, the determined relaxation rate may be affected by a systematic error.

More sophisticated methods known as *relaxation dispersion analysis* are used if we want to fully exploit the information hidden in the spectra. There are several methods known as *relaxation dispersion experiments* allowing

us to vary the chemical exchange contribution to apparent R_2 by changing experimental conditions. Here, we briefly introduce a method called by he abbreviation composed of the first letters of its authors: CPMG (Carr-Purcell-Meiboom-Gill). This experiment is derived from the experiment for the measurement of the transverse relaxation rate 9.3. During the description of the experiment for the measurement of the transverse relaxation rate, it was demonstrated that its relaxation delay must be composed from spin-echo elements. The choice of the length of the single spin echo elements is not important as long as we are studying an isolated spin which is not undergoing a chemical exchange. In this case the chemical shift will be same during the whole spin echo and the coherence will be refocused regardless of the length of the delay τ (half of the spin echo). But, the length of the τ becomes important if the studied molecules undergo an exchange affecting the chemical shift of the observed nucleus. Then, the evolutions in the left and right part of the spin echo are different for different molecules depending on when the molecule switched the state during the spin echo. An example of such a case is given in the Figure 10.2C. Consequently, an additional loss of coherence is observed and the measured relaxation rate is elevated by this effect. Clearly, if the difference between the chemical shifts corresponding to the exchanging states is larger, the loss of the signal due to its dephasing is more rapid, because the magnetic moments in different states reorient more quickly. The example given in Figure 10.2 shows a case when the numbers of the studied molecule in both states are equal. However, it is often not the case and the ratio of the molecules in different states is another important factor. It is obvious that if most of the molecules are present in one state and only a relatively small fraction of them is in the other one, the loss of coherence is diminished.

The effect of the loss of coherence can be suppressed if the refocusing pulses are applied faster as it is shown in Figure 10.2D. If we apply pulses sufficiently frequently, we are able to suppress the dephasing effect of the exchange as it is illustrated in Figure 10.2E). Obviously, the slower the exchange is, the less frequent application of refocusing pulses is sufficient to suppress the effects of the exchange. Therefore, the analysis of the dependence of the relaxation rate on the frequency of application of the refocusing pulses during the relaxation delay allows one to extract the information about the rate of the exchange.

The example of the dependence of the transverse relaxation rate on the increasing frequency of the application of the refocusing pulses during the relaxation delay is shown in Figure 10.3. You may notice a decreasing profile, which is becoming flat for higher frequencies, when the refocusing pulses are applied fast enough to suppress dephasing of the signal due to the exchange. Analysis of such a dependence provides information about the rate of the exchange (a kinetic parameter), equilibrium populations of individual states undergoing the exchange (a thermodynamic parameter), and chemical shifts of both (or all) interchanging states (encoded structural information).

Finally, it is important to recall that the experiments for studies of motions of biomolecules (Section 9.5) are slightly more complicated because they are based on the analysis of ^{13}C of ^{15}N nuclei in the ^{13}C-^{1}H or ^{15}N-^{1}H pairs. Therefore, additional effects like cross-relaxation and effects due the J-coupling between these nuclei must be considered. We can for example recall that during the spin echo the in-phase coherence evolves into the anti-phase coherence and back. Consequently, the relaxation reflects the weighted average of the relaxation rates of these two coherences. Because these two rates are not same, the measured relaxation rate depends on the length of the spin-echo element even without the presence of the chemical exchange and this effect would interfere with the measured relaxation dispersion curve, which makes the analysis difficult. Therefore, this effect must be either suppressed or compensated.

The former approach (suppression) is represented by the experiment when continuous proton decoupling is applied during the whole relaxation delay (i) ensuring that the in-phase coherence do not evolve into the anti-phase coherence at all and (ii) suppressing the cross-relaxation effects. The pulse sequence (Figure 10.4A) is very similar to the pulse sequence for the measurement of the transverse relaxation rate in biomolecules (Figure ??B).

The latter approach (compensation) requires also modification of the preparation phase of the pulse sequence. There is only one INEPT step present in order to create the anti-phase ^{15}N coherence. So, it resembles rather the beginning of the HSQC experiment introduced in Section 3.8. The following relaxation delay is split into two parts and a simultaneous echo followed by a 180° pulse is inserted in the middle. This element exchanges the in-phase and anti-phase coherences in the middle of the relaxation delay. The initially created anti-phase coherence evolves into an in-phase coherence and back during each spin-echo in the first part. Then the anti-phase coherence is transformed into the in-phase coherence, which evolves into the anti-phase coherence and back during each spin-echo in the second part of the relaxation delay. Such an approach effectively averages the time when the in-phase and anti-phase coherences are present, regardless of the chosen length of the spin echo. The proton 180° pulse, following the central simultaneous echo, is necessary to suppress the effects of the cross relaxation.[3]

---

[3]A combination of switching between the anti-phase and in-phase coherences by the simultaneous echo with inverting of the cross-
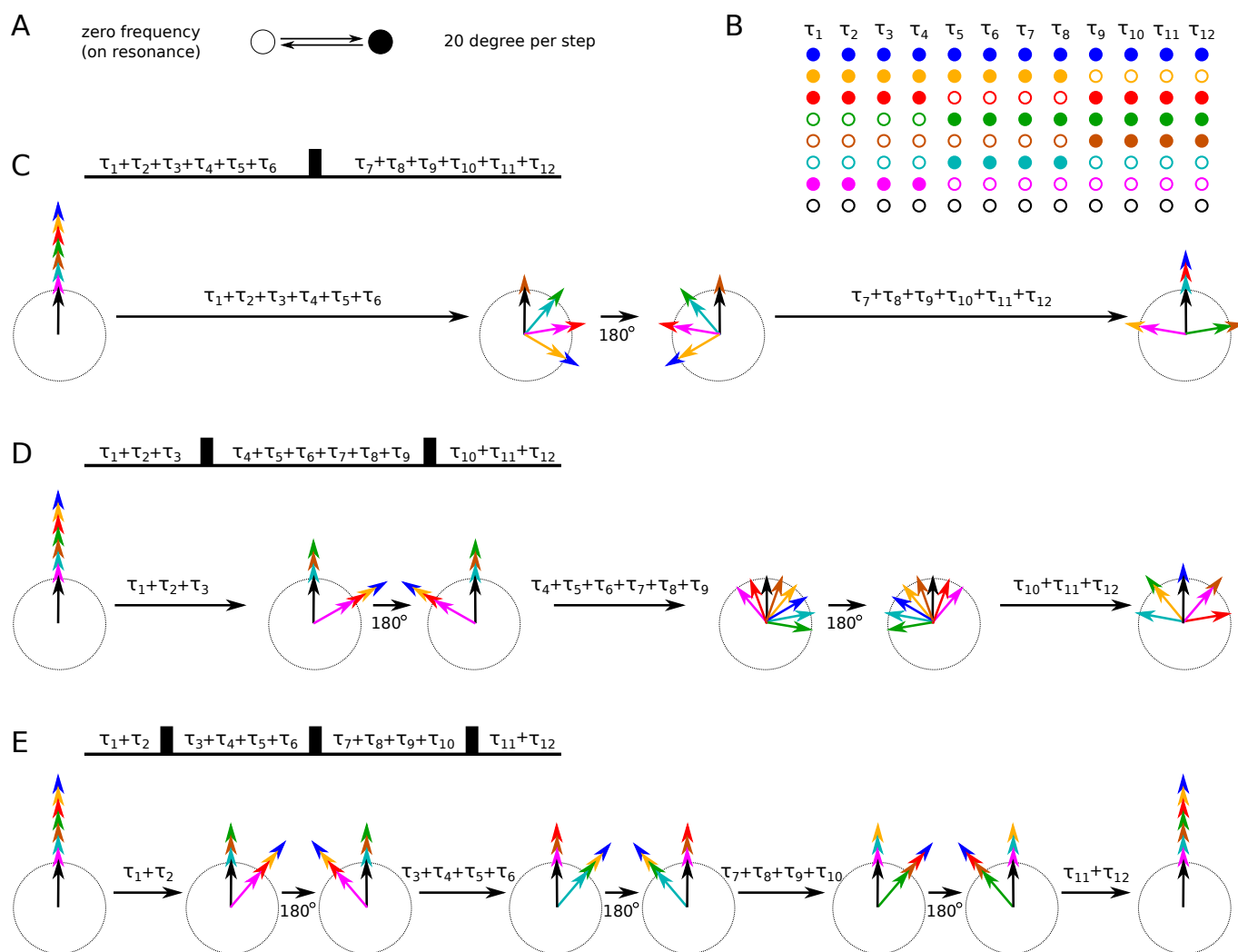
Figure 10.2: Illustration of the effect of various lengths of the spin echo elements on the coherence loss due to an exchange. A, Definition of the system used to explain the function of the CPMG experiment. Open and filled circles represent two states of the molecule undergoing the exchange. B, Variants of the exchange events. The studied system is represented by eight molecules distinguished by colors. Each of them undergoes a unique variant of the exchange events. The relaxation delay is divided into 12 steps τ_1–τ_{12}. The rate of the exchange is limited so that the molecule has to keep its state for at least 4 time steps before it can change the state again. C–E, three variants of the splitting of the relaxation delay by spin echo elements with increasing number of spin echoes. The colored arrows display the orientation of the magnetisation in the transverse plane for each molecule. The arrows allow us to follow the effect of the exchange and refocusing pulses on each molecule. The final sum of the signals increases with the increasing frequency of application of the refocusing pulses.
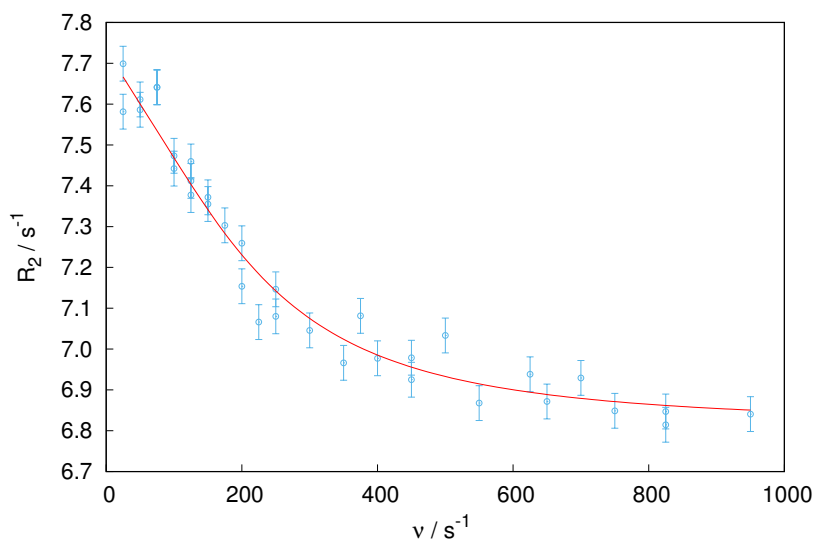
Figure 10.3: Example of the experimental CPMG relaxation dispersion profile. The data eshibit a decay of a transverse relaxation rate with increasing frequency of the application of the refocusing pulses during the relaxation delay. The displayed frequency ν is calculated as $1/(4\tau)$, where τ is the half of the used spin echo element. The red line correspond to the theoretical dependence simulated for the parameters defining the studied exchange.

There is no difference in sensitivity to the chemical exchange between the two methods described above because both in-phase and anti-phase coherences are affected by the chemical exchange. However, in the first case the effect of the chemical exchange increases the pure in-phase relaxation rate, while in the second case it does the same to the average of in-phase and anti-phase relaxation rates.

The last experiment discussed in this section dedicated to the study of slow exchange in biomolecules is called Chemical Exchange Saturation Transfer (CEST). It is designed to investigate the exchange with so highly skewed populations between states so that minor state(s) is not visible in the spectra. It resembles the experiment for the measurement of the longitudinal relaxation rate (Section 9.5), because the ^{13}C / ^{15}N longitudinal polarization is also created prior the beginning of the relaxation delay but the relaxation delay is different. The pulse sequence is shown in Figure 10.4C. A very weak continuous irradiation is applied during the relaxation delay, which has similar a effect as selective presaturation discussed in Section 5.2. It effectively suppresses any signal which is present at the frequency of the irradiating radio wave. The experiment is typically repeated with a fixed length of the irradiation but its frequency is changed step by step throughout the region where the expected chemical shift of the minor state(s) is expected. If the frequency of the irradiating radio wave gets close to the precession frequency of the minor state, magnetic moments of the minor state aadopt distribution of with no polarization. The loss of polarization is transferred via chemical exchange to magnetic moments in the major state. Therefore, intensity of the observable peak (of the major state) decreases. A dependence of the signal intensities on the frequency of the irradiation reveals the position of the minor states in the spectra (typically, an additional spectrum is acquired with the relaxation delay completely omitted to obtain reference peak intensities and the peak intensities relative to this reference is plotted). The dependence is characterized by a major minimum, when the irradiation resonates with the visible peak in the spectrum and other minima showing the positions of frequencies corresponding to the other states as it is shown in Figure 10.5.

---

relaxation effects by the proton 180° pulse is counter-productive for the suppression of the cross relaxation effects. In order to suppress them, we shall not do both at once, therefore the second proton inversion pulse is applied at the end of the simultaneous echo to reverse the effect of the proton inversion pulse in the middle of the echo on the cross-relaxation.
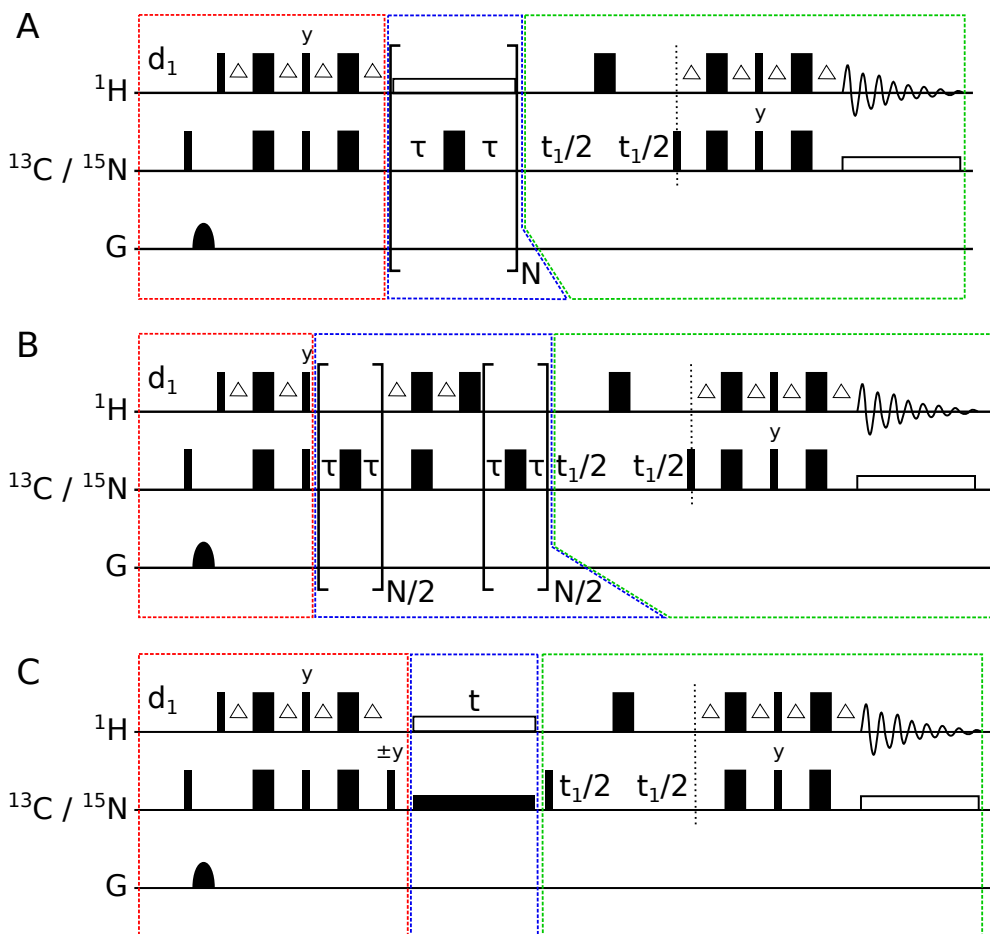
Figure 10.4: Schemes of simplified experiments used to the study chemical exchange in biomolecules. A, CPMG experiment keeping the in-phase coherence during the relaxation delay. B, relaxation compensated CPMG experiment with the inter-exchange of in-phase an anti-phase coherences during the relaxation delay. C, CEST experiment. The examples are provided for ^{13}C-^1H or ^{15}N-^1H spin pairs. Two lines correspond to two channels used to apply radio-wave pulses to proton and to ^{13}C or ^{15}N. The third lines labeled G represents the pulsed field gradients. Narrow and wide filled boxes represent $90°$ and $180°$ degree pulses, respectively. The pulses are applied with the x phase unless indicated otherwise. The lower open rectangle applied during the acquisition is heteronuclear decoupling. The delay Δ is equal to $1/4J$ where J is J-coupling constant. The lower filled rectangle applied in the CEST experiment during the relaxation delay is the CEST irradiation. The lower open rectangle applied during the relaxation delays in Panels A and C is proton decoupling. The red, blue, and green boxes depict the preparation phase of the experiments, the variable relaxation delay, and the detection element of the pulse sequences, respectively.
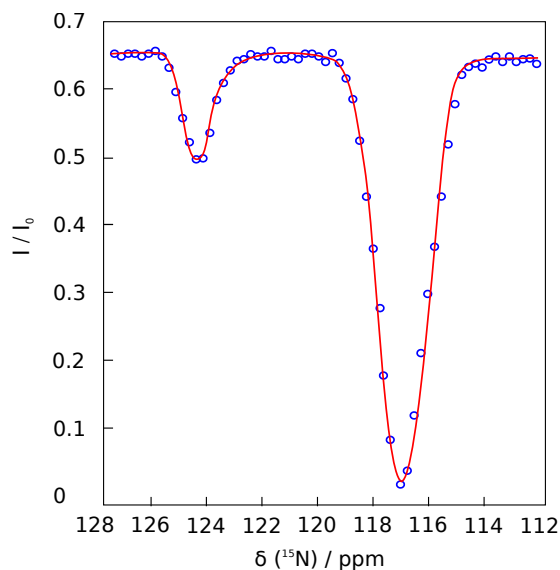
Figure 10.5: Illustration of CEST experimental data displayed as a dependence ratio between peak intensity in the CEST experiment and reference experiment on the frequency of the irradiation during the CEST relaxation delay. The major and minor minima in the profile show the frequencies of the highly populated state and the minor state, respectively.

10.5 Effect of chemical exchange on the longitudinal magnetization

Chemical exchange also affects the z component of magnetization. Experiments similar to the steady-state NOE measurement can be run. Although the results of such *saturation transfer experiments* are similar to the effect of NOE, the physical mechanism is completely different. Signal intensities are changed by NOE because two protons are close in space and their magnetic dipolar moments interact directly. In the saturation transfer experiments, on the other hand, we observe two forms of the same proton. If the form (e.g., conformation) of the molecule changed during the experiment, the proton is measured at the frequency corresponding to the new form but the signal intensity is affected by the magnetic moment distribution in the original form. Saturation transfer experiments are easy to evaluate, but applicable just to the two-site exchange (for technical reasons). Two-dimensional versions of this experiment, resembling NOESY, are also available.

The same principles apply to the *inversion transfer experiment*. Like in the R_1 measurement, longitudinal polarization of a nucleus in one form are selectively inverted and the signal intensity of both forms is monitored. Evaluation of the inversion transfer requires multi-exponential fitting but more information can be obtained compared to the saturation transfer experiments.

Lecture 11
Intermolecular interactions

11.1 Studies of intermolecular interactions

NMR is recognized as a useful tool for binding studies of biomolecules. It allows confirmation of interactions, identification of binding interface and it provides information about binding constant, stoichiometry, and rate of binding events. Methods of fast and cheap identification of binding partners in mixtures of potential ligands have been also developed.

11.2 Titration

We start our discussion of NMR binding studies by describing titration of a biomolecule by its binding partner. This method can be used not only to investigate a simple binding event described in the example below, but it is applicable also to studies of complex binding mechanisms like multistep binding, cooperativity, induced fit or conformational selection, etc. Typically, the sample of the biomolecule is prepared with some isotope enrichment so that heteronuclear experiments can be used. The ^{15}N enrichment of proteins is usually sufficient for titration studies, unless we are working with a protein which ^{15}N-^{1}H HSQC is characterized by a severe signal overlap. The ligand is usually not isotopically enriched and we investigate exclusively the changes in the protein spectrum induced by the binding. The protein spectrum (most often ^{15}N-^{1}H HSQC) is acquired repeatedly, the first spectrum is recorded without any ligand present in the solvent, and then the measurement is repeated after each titration step, i.e., with an increasing content of the ligand. In such manner, we obtain a series of NMR spectra starting from that of the free protein up to the spectrum of the protein fully saturated by the ligand. The titration step must be chosen so that it is possible to follow the changes in the spectra.

Direct comparison of the first spectrum (free protein) and the last spectrum (highest concentration of ligand) allows us to identify binding regions of the protein if the protein assignment is known. If both the assignment and the structure of the protein is known, it is possible to map the changes in frequencies to the structure in order to identify the binding site(s). As multidimensional spectra with different nuclei detected in the individual axis are typically measured, the chemical shift changes of different nuclei must be combined, taking into the account the typical range of frequencies of the nuclei of interest. The resulting value is the *chemical shift perturbation* parameter (CSP). For the experiment applied most often, i.e. for ^{15}N-^{1}H HSQC, CSP is calculated as

$$\text{CSP} = \sqrt{\frac{1}{2}(\Delta\delta_{\text{H}}^2 + (\alpha\Delta\delta_{\text{N}})^2)}, \qquad (11.1)$$

where the scaling factor α is typically chosen based on the observed ranges of chemical shifts of both nuclei. For example, if the range of amide ^{15}N shift is between 131 and 109 ppm and the range of amide protons is between 10.0 and 6.9 ppm, the α factor can be calculated as $\alpha = (10.0 - 6.9)/(131 - 109) = 0.14$. However, one has to keep in mind that each protein has slightly different ranges of chemical shifts. It should be also stressed out that there is no theoretical justification of the assumption that the relative sensitivity of chemical shifts of individual nuclei to the ligand binding is given by the ranges of the chemical shifts.

It is necessary to keep in mind that high values of CSP are not a direct evidence of a binding to that area of the protein. Such simplification can lead to a misinterpretation of data. The chemical shifts may be disturbed for example also by allosteric effects far away from the binding site.

The detailed analysis of the spectra of the whole titration series provides additional information about the binding constant and stoichiometry and kinetic of the binding. Changes in the spectra during the titration depends on the relative size of the rate of the exchange (sum of binding and dissociation rate) and the difference between chemical shifts in the free and bound state. When the exchange rate is much larger than the difference of the chemical shifts ($k_{ex} = k_{assoc} + k_{dissoc} \gg \Delta\omega$), the binding is in the *fast exchange* regime (usually low-affinity binding). On the other hand, if $k_{ex} = \ll \Delta\omega$, the binding is in the *slow exchange* regime (usually strong binding).

The fast exchange regime can be recognized by a subsequent shift of the peak between the initial position (free protein) towards the final position corresponding to the bound form. On the other hand, a progressive loss of the signal intensity at the initial free-state position and increase of signal intensity at the position of the bound state are characteristic for the slow exchange regime. The peak linewidths are not dramatically increased during the titration in the fast or slow exchange regimes. But, the peaks are getting significantly broadened (eventually even beyond the detection limit) in the cases when the exchange rate is similar to the difference of the chemical shifts. This case is called *intermediate exchange* and it provides a bit more complex picture than the slow or fast exchange regime. In the beginning of the titration, the peak starts to shift towards the position of the bound form, but it becomes also broadened and therefore its intensity drops. It might be completely undetectable during the middle phase of the titration, but it gets sharper in the final part of the titration when there is an extent of the ligand and the peak position gets close to its target position. All three cases are illustrated in the Figure 11.1. Note, that if a multiple dimensional spectrum is measured with different nuclei detected in the individual dimensions the discussed regime can be different for each of the dimensions.

In order to quantify the changes in the spectra, different parameters are used in the slow and fast exchange regimes. If the exchange is fast, a gradual increase of CSP can be followed (Figure 11.3). In the case of a simple equilibrium between ligand-free and ligand-bound form of the protein, CSP divided by its maximum value is equal to the fraction of the protein in its bound form:

$$y = \frac{[PL]}{c_P} = \frac{c_P - [P]}{c_P} = \frac{CSP}{CSP_{[L]\gg[P]}}, \tag{11.2}$$

where c_P, $[P]$, $[L]$, and $[PL]$ are the concentrations of total protein, free protein, free ligand, and of the complex, respectively. This allows us to determine the dissociation constant K_d directly from the titration curve (dependence of y on the total concentration of the ligand in each titration step c_L). The shape of the titration curve can be derived as follows.

$$K_d = \frac{[P][L]}{[PL]} = \frac{(c_P - [PL])(c_L - [PL])}{[PL]} \tag{11.3}$$

$$\frac{K_d}{[PL]} = \frac{c_P - [PL]}{[PL]} \frac{c_L - [PL]}{[PL]} = \frac{c_L}{c_P} \left(\frac{c_P}{[PL]}\right)^2 - \left(1 + \frac{c_L}{c_P}\right)\frac{c_P}{[PL]} + 1 \tag{11.4}$$

$$\left(\frac{c_P}{[PL]}\right)^2 - \left(1 + \frac{K_d + c_P}{c_L}\right)\frac{c_P}{[PL]} + \frac{c_P}{c_L} = \left(\frac{1}{y}\right)^2 - \left(1 + \frac{K_d + c_P}{c_L}\right)\frac{1}{y} + \frac{c_P}{c_L} = 0 \tag{11.5}$$

$$\frac{CSP_{[L]\gg[P]}}{CSP} = \frac{1}{y} = \frac{1}{2}\left(1 + \frac{K_d + c_P}{c_L} \pm \sqrt{\left(1 + \frac{K_d + c_P}{c_L}\right)^2 - 4\frac{c_P}{c_L}}\right) \tag{11.6}$$

$$\frac{CSP}{CSP_{[L]\gg[P]}} = y = \frac{2}{\left(1 + \frac{K_d + c_P}{c_L} \pm \sqrt{\left(1 + \frac{K_d + c_P}{c_L}\right)^2 - 4\frac{c_P}{c_L}}\right)}. \tag{11.7}$$

The dependence is plotted in Figure 11.2 for high affinity (red), intermediate affinity (green), and low affinity (blue). Titrating the proteins in six steps (i.e., recording the spectrum of a free protein and of a protein with one to
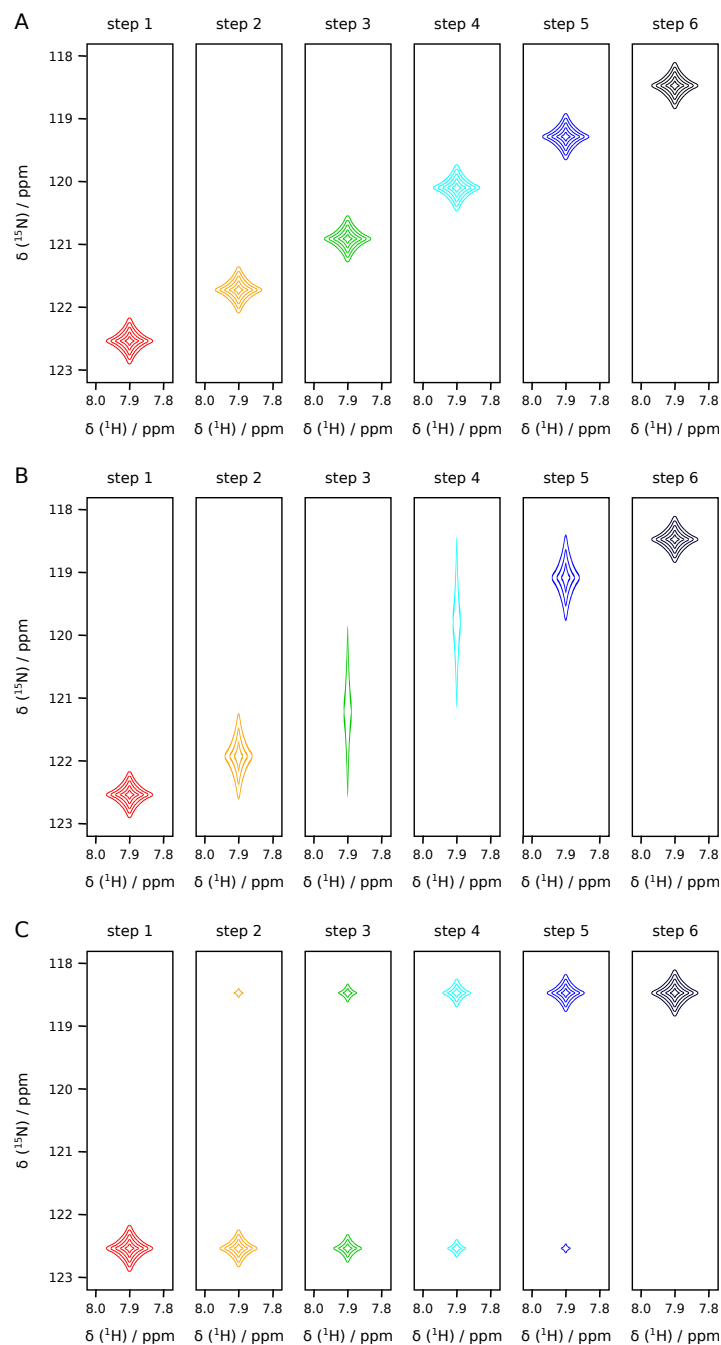
Figure 11.1: Changes observed in the spectra of a protein upon its titration with a ligand. Titration is divided into six steps in this example. The red and black peaks stand for the case of the free protein and protein fully saturated with its ligand. Orange, green, cyan, and blue peaks then represent spectra with increasing ligand concentration, respectively. The intensities of the peaks are depicted by the number of contours. Fast (A), intermediate (B), and slow (C) exchange regimes of the binding (with respect to the ^{15}N chemical shift) are displayed. Note that the regime is fast for proton dimensions in all cases as in this example the binding do not change the proton chemical shift.
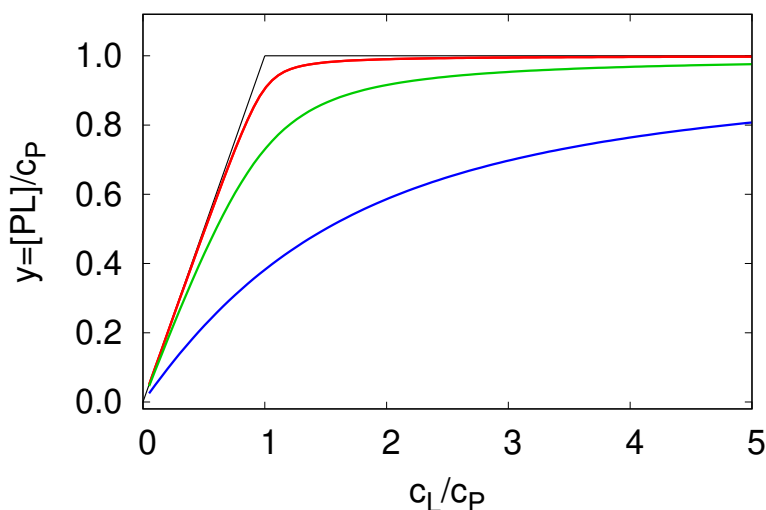
Figure 11.2: Titration curves for three values of the dissociation constant K_d: $K_d = 0.01c_P$ (red), $K_d = 0.1c_P$ (green), and $K_d = c_P$ (blue). The limit for $K_d \to 0$ (irreversible binding) is shown in black. Total concentrations of the added ligand are plotted relative to the total protein concentration.

five aliquots of ligand corresponding to c_L ranging from c_P to $5 \times c_P$) is likely to provide reliable value of K_d for the intermediate-affinity binding (green). In this case, K_d is the only unknown parameter in fitting the experimental data to Eq. 11.7. If the affinity is too low (blue curve), it may be difficult to record a spectrum of protein saturated with the ligand and $\text{CSP}_{[L] \gg [P]}$ must treated as another fitted parameter in fitting the experimental data to Eq. 11.7. In the biologically more interesting case of high affinity (red curve), fitting K_d would be difficult because the curve is close to the limit of tight binding (black lines), when the dependence does not change with decreasing K_d any more.

In the case of the slow exchange, peaks do not move in the spectra and SCP cannot be evaluated. In principle, the intensities (most accurately volumes) of peaks of the free and bound form are in the ratio [P] : [PL]. However, this assumption is true only if the relaxation rates of free protein and of the complex are identical. If the relaxation rates differ, the correct ratio can be obtained only for areas of peaks in one-dimensional experiments where detection immediately follows the 90° excitation pulse. Furthermore, the slow exchange is typical for dissociation constants much lower than concentrations used in NMR experiments (cf. the red curve in Figure 11.2). In such cases, the dependence of y on c_L described by Eq. 11.7 approaches its linear limit (shown in black in Figure 11.2), independent of K_d (because $K_d + c_P \approx c_P$). Therefore, an accurate determination of K_d may not be possible. On the other hand, the linear dependence allows us to precisely determine stoichiometry of binding (equal to one in the example presented in Figure 11.2).

The intermediate exchange represents a case which is most challenging but also richest in information. A careful choice of the ligand:protein ratio, so that the peak broadening due to the exchange occurs but the peak intensity can be still measured reliably (e.g., step 5 in Figure 11.1B), allows us to determine not only K_d, but also the exchange rate k_{ex}, using the methods described in Section 10.4. As $k_{ex} = k_{assoc} + k_{dissoc}$ and $K_d = k_{dissoc}/k_{assoc}$, the rate constants k_{dissoc} and k_{assoc} can be calculated.

11.3 Saturation transfer difference

The saturation transfer difference experiment (STD) is very popular in industry, particularly in the pharmaceutical industry where it is used as a relatively quick, cheap and effective drug screening tool. The experiment is based on comparison of proton spectra, therefore it is not necessary to introduce any isotope labeling of the biomolecule or of the small molecules which are screened for binding to the biomacromolecule. In addition, the price is reduced by the
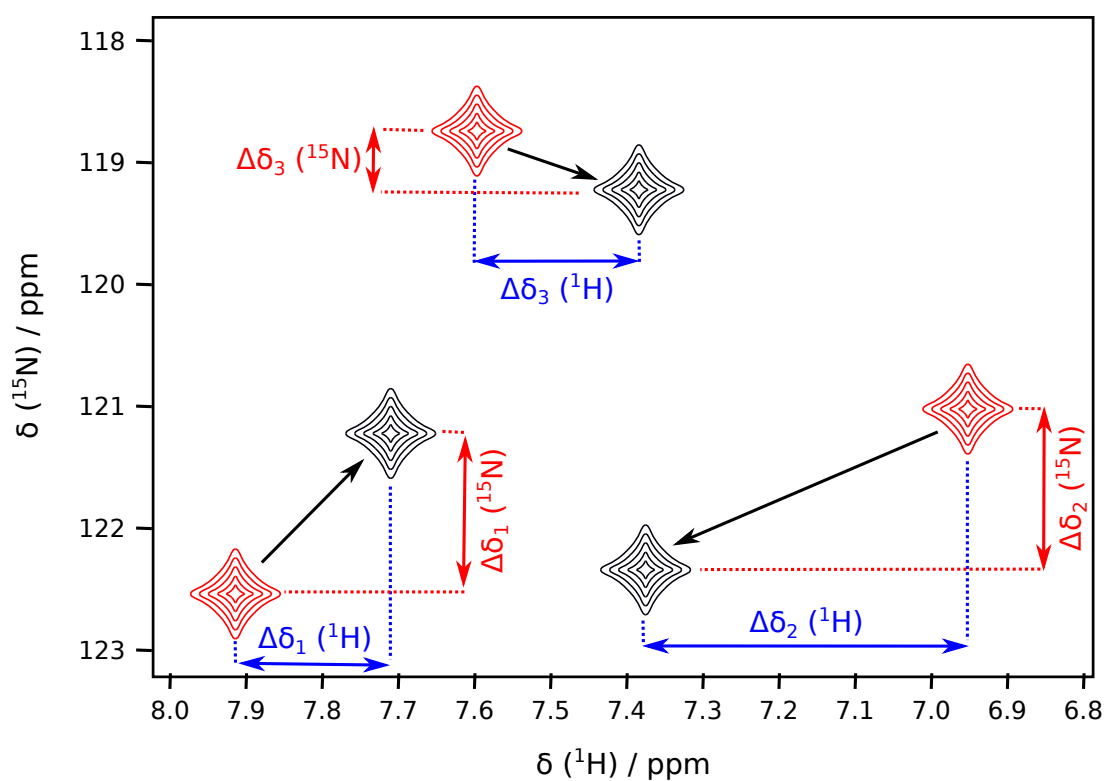
Figure 11.3: Chemical shift perturbation (CSP). An overlay of a region of hypothetical ^{1}H-^{15}N HSQC spectra is shown. The red peaks correspond to the spectrum of a free protein. The black peaks are from a spectrum acquired during titration with the binding ligand. Black arrows represent vectors composed of the chemical shift changes of individual nuclei. Coordinates of the vector are used to calculate CSP for each residue.
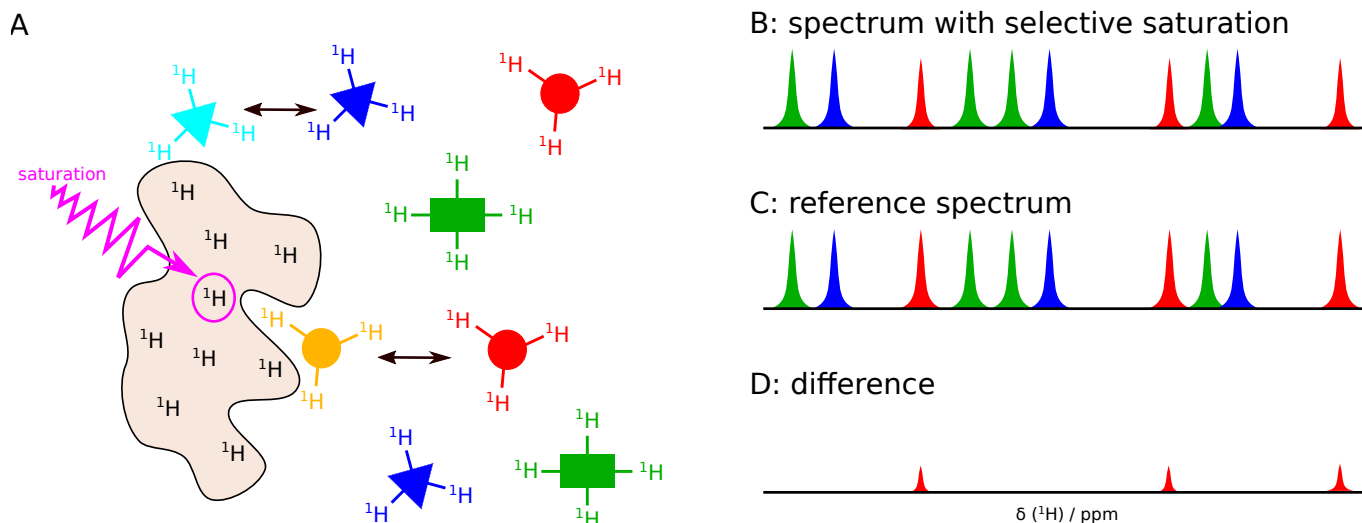
Figure 11.4: Saturation transfer difference experiment. A, illustration of the principle. The signals of the ligand bound to the protein are affected by the saturation of a particular proton in the protein if the binding site is close to them. The ligand is in an exchange between the bound and free form and therefore the effect is transferred to the signals detected for the free ligand. B, an example of a spectrum obtained with saturation, and of the reference spectrum (C). Both spectra contain signals of three potential ligands (distinguished by colors). The signals of the protein and of the ligand bound to the protein are not visible due to their very low concentration. D, difference of the spectra contains only the signals of the interacting molecule (red). Note that the blue molecule also interacts with the protein, but far away from the position of the saturated proton, therefore the interaction of the blue molecule is not observed in the difference spectrum.

fact that the protein sample concentration at the level of $10\,\mu$M is sufficient.

The saturation transfer experiment and its functionality is shown in the figure **??**. Two 1D proton spectra of the mixture of the protein and potential ligands are recorded. At the beginning of the first one, a weak and selective irradiation is applied at protein resonance frequencies to saturate exclusively them. Therefore the signal positions of the ligand must be known to avoid accidental saturation of ligand by this irradiation. The second spectrum is measured with the frequency of the irradiating radio wave far off-resonance to avoid any saturation. The two resulting spectra are subtracted from each other. Considering the very small concentration of the protein, there are no protein signals directly visible. But, if the ligand interacts with the protein at a site close to the proton which was saturated (i.e., with frequency close to the frequency at which the irradiating radio wave was applied), then the saturation influence distribution of magnetic moments that are close in space, including those of the ligand. This is observed as a decrease of the ligand signals compared to their intensity in the reference spectrum. Therefore, the subtraction of the spectrum measured as a reference from the spectrum measured with the saturation reveals only signals of the interacting molecules.

11.4   Isotope-edited and isotope-filtered NOE experiment

We close the chapter dedicated to the interaction studies by an experiment allowing us to calculate structures of intermolecular complexes based on the Nuclear Overhauser effect (NOE). The experiment is applicable to complexes of macromolecules with small ligands, but it is often used in studies of interactions of two large biomolecules.

As discussed in Section 6.6, NOE transfers the polarization between nuclei that are close in space, but not necessarily connected via chemical bonds. Therefore, NOE can be used for investigation of interactions when surfaces of two biomolecules get close to each other. In these cases, the intermolecular NOE cross peaks are observed and provide a direct evidence of the interaction. However, the pulse sequences presented in Figures 6.1C and 6.3C would provide correlations of *all* protons close in space, including those in the same molecule (intra-molecular cross-peaks). The number of intra-molecular cross-peaks is significantly larger than the few inter-molecular peaks we are interested in. Identification of the inter-molecular peaks in spectra of complexes is possible, but challenging.
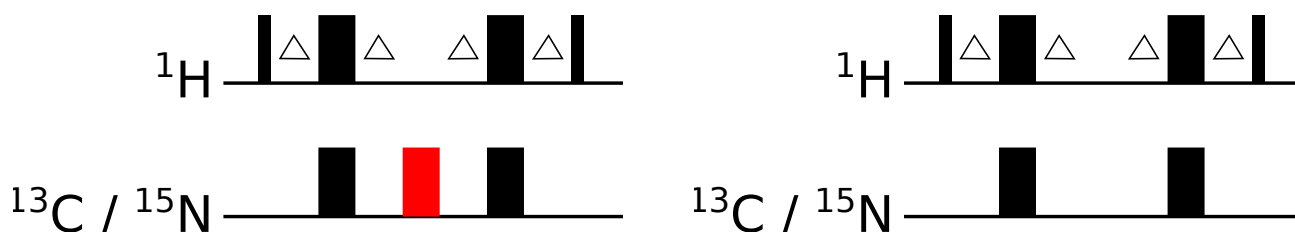
Figure 11.5: Isotope filter/edit pulse sequence element. The narrow and wide boxes represent the 90° and 180° pulse, respectively. All pulses are applied with the x-phase. Delays Δ stand for $1/(4J)$, where J is the J-coupling constant. The red pulse applied to ^{13}C / ^{15}N nucleus is either present (left) or omitted (right). Isotope-filtered and isotope-edited signals are obtained by adding and subtracting the spectra obtained using the individual elements, respectively.

To simplify the spectra, one interaction partner is prepared with ^{13}C or ^{15}N isotope enrichment while the other is unlabeled. The labeled molecule is usually protein as labeling of nucleic acids, oligosaccharides and small organic molecules is more expensive and often technically difficult. The spectra are then measured using a pulse sequence derived from the NOE experiment described earlier 6.6. Either *isotope-filtering* or *isotope-editing* elements are inserted in the sequence. Both element are based on the same phenomena and are shown in Figure 11.5. Below, we describe the ^{13}C isotope-filtering or isotope-editing element, but exactly the same idea can be used for ^{15}N filtering/editing.

Supposing the proton polarization present in the beginning of the sequence, the elements start with a proton excitation pulse followed by a simultaneous echo with the delays optimized for a transfer of a proton in-phase coherence to the proton anti-phase coherence, which actually happens only if the proton is bound to ^{13}C in our case. The natural abundance of these isotopes is negligible and we can assume that they are absent completely in the unlabeled molecule. Therefore, the effect of the same pulse element results only in refocusing the proton chemical shift as the spin echo element always does. Then, the sign of the anti-phase coherence can be altered by application of a 180° pulse applied to ^{13}C, while the application of such a pulse has no effect on the proton in-phase coherence (which was created by the element for the protons not coupled to the heteronucleus). Finally, the proton anti-phase coherence is transferred back to the proton in-phase coherence by the same series of pulses and delays as was used in the first half of the sequence. The proton in-phase coherence can be transformed to the proton longitudinal polarization by the second of the proton 90° pulses. In unlabeled molecules, the proton in-phase coherence is also refocused by the second spin echo and the proton polarization is restored by the second proton 90° pulse as well. So, the result is the same in both labeled and unlabeled molecules. However, the sign of polarization can be altered only for the case of a proton coupled to the ^{13}C nucleus. Therefore, we can perform the experiment twice with and without the 180° pulse applied at the ^{13}C frequency and either sum or subtract both spectra. In the first case, which is called *isotope filtering*, the signal arising from protons not coupled to the ^{13}C are observed, while the signals coming from the protons coupled to the ^{13}C are effectively eliminated. The subtraction will work in the opposite manner. This is called *isotope editing*.

The isotope editing and filtering can be inserted both before and after the mixing element of the NOE experiment. Spectra obtained with two isotope filtering or isotope editing elements contain only in intra-molecular NOE signals of the unlabeled or labeled interaction partner. Applying the isotope filtering element before the NOE mixing time and the isotope editing element after the NOE mixing results in a spectrum containing only the desired inter-molecular NOE cross-peaks created by transferring the proton polarization of the unlabeled molecule to protons of the labeled molecule. Finally, the isotope editing element before the NOE mixing time and the isotope filtering after the NOE mixing result in inter-molecular NOE cross-peaks due to the proton polarization transfer from the labeled molecule to the unlabeled one. Figure 11.6 illustrates the inter-molecular and intra-molecular NOE contants and their selective detection.
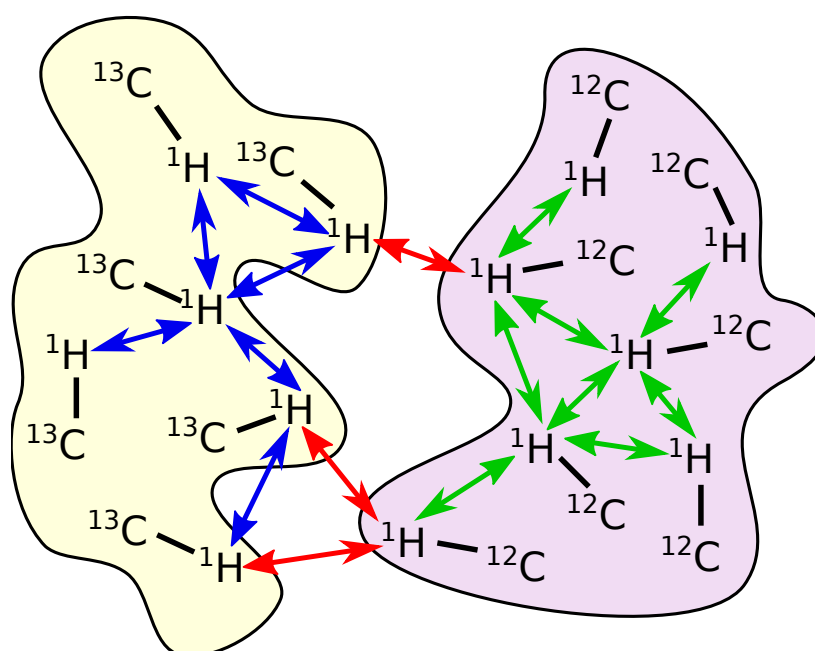
Figure 11.6: Contacts detected by the isotope filtered/edited NOE experiment. The light yellow molecule was prepared with ^{13}C isotope enrichment, unlike the light magenta molecule. The blue arrows mark intramolecular contacts within the ^{13}C labeled molecule that can be selectively detected by inserting the isotope editing element before and after the NOE mixing time. The green arrows mark intramolecular contacts within the ^{13}C unlabeled molecule and can be selectively detected by inserting the isotope filtering element before and after the NOE mixing time. The red arrows show inter-molecular NOE contacts selectively detected if the isotope filtering element is placed before the NOE mixing time and the isotope editing element is placed after it, or vice versa.

Lecture 12
Nucleic acids

12.1 Chemical composition

Chemically, nucleic acids are esters of orthophosphoric acids. This should be kept in mind when considering their chemical properties. For example, they are negatively charged and require a presence of a counter-ion, which is usually either Na^+ or K^+. The other part of the ester is a nucleoside, which itself consists of a sugar and a base bound together by the glycosidic bond (Figure 12.1). The sugars involved in nucleic acids are either ribose in ribonucleic acids (RNA) or 2-deoxy ribose in deoxyribonucleic acids (DNA). This rather small chemical difference however leads to significantly different structural features that are also reflected in NMR spectra. The most common naturally occurring bases in DNA are Adenine, Guanine, Cytosine and Thymine. RNAs contain Uracil instead of Thymine. The glycosidic bond is formed between the sugar atom C1′ (pronounce "one prime") and a nitrogen atom of the base. The symbol prime (′) is used to distinguish the atoms of the sugar part from the base. Note the numbering of the base atoms. Following the principles of chemical nomenclature, the atoms are numbered so that the heavier atoms (N in our case) get the lowest possible numbers and the larger ring is numbered before the smaller ring. As a result of these rules, the nitrogen atom involved in the glycosidic bond is N1 in Pyrimidine bases (Cytosine and Thymine/Uracil), while in Purine bases (Adenine, Guanine) it is the atom N9.

The base combined with the sugar forms a nucleoside, as mentioned above. The nucleoside together with the phosphate form nucleotide (mononucleotide). The phosphate binds the nucleoside either at the position 5′ or at the position 3′. The resulting nucleotides are called, for example, cytidine 5′-monophospahate (shortened to CMP or pC) or 2-deoxyadenosin 3′-monophosphate (dAMP, dAp). Note there is an oxygen atom between the sugar carbon (C5′ or C3′) and phosphorus atoms. By attaching further nucleotides we can form di-, tri-, oligo- (oligo = several), and polynucleotides. Obviously, the chain has to end somewhere. If the is no further nucleotide attached at the 5′sugar, we call it the 5′end. If the chain does not continue after the 3′phosphate, it is called the 3′end. By a convention, the nucleotide sequences are written in the direction from the 5′end to the 3′end. For example, the well-known Dickerson-Drew dodecamer (dodeca = 12) has the sequence d(CGCGAATTCGCG), where d indicates that it is a DNA. Essential for the biological function of nucleic acids is the ability of the bases to form hydrogen bonds. It is the imino and amino hydrogen atoms who play the most important role in the forming of the bonds. Cytosine, Adenine, and Guanine have the amino group and Thymine/Uracil and Guanine have the imino hydrogen. Guanine is thus the only of the bases that have both imino and amino groups. The best known base-pairing patterns are the Watson-Creek base pairs CG and AT. Also important are the Hoogsteen base pairs for which the involvement of Purine N7 is typical. NMR spectroscopy is an excellent tool for studying whether the base pairs are formed and evaluating which type of the base pairs they are.

12.2 Torsion angles

If we have four atoms A, B, C, and D, and look along the BC bond, then the torsion angle along the BC bond is between the vectors AB and CD (Figure 12.2). If the torsion angle is close to $0\,°$, we talk about *syn* or *cis* orientation, if the torsion angle is close to $180\,°$, the orientation is called *trans* or *anti*. For the orientations transient from *syn*
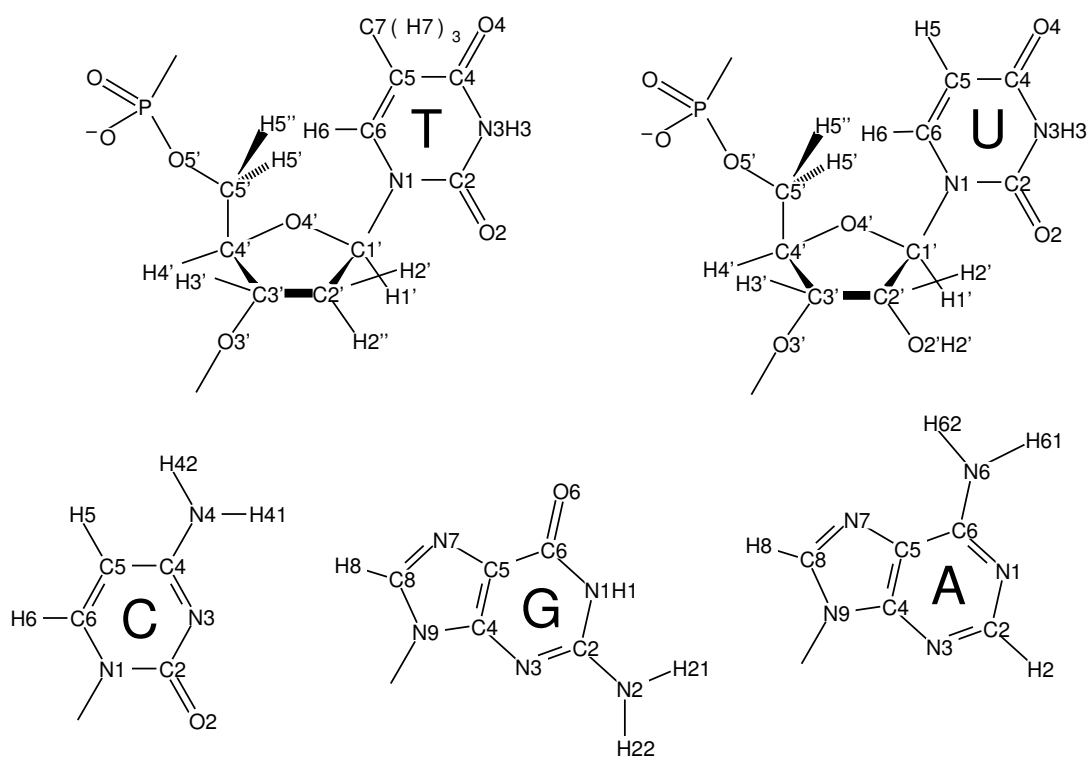
Figure 12.1: Top, chemical structures of DNA (depicted for Thymidine) and RNA (depicted for Uridine). Bottom, bases found in both DNA a RNA (Cytosine, Guanine, and Adenine)

to*anti*, terms synperiplanar (*sp*), synclinal (*sc*), anticlinal (*ac*) and antiperiplanar (*ap*) can be used.

In nucleic acids, the torsion angles significant for characterizing the structure are the torsion angles along the sugar-phosphate backbone (labeled $\alpha, \beta, \gamma, \delta, \epsilon, \zeta$), within the sugar ring (labeled ν_O to ν_4), and the glycosidic torsion angle χ (Figure 12.3).

It should be noted that the sugar ring is not planar. If we choose a plane defined by three atoms, the remaining two can be above or below the plane. As the carbon atoms in the (deoxy)ribose carry bulky substituents, some of the conformations are preferable for steric reasons. The sugar ring conformations are frequently referred to as sugar pucker. If we use the C1′-O4′-C4′plane as the reference, then the atoms occurring on the same side of the plane as the C5′are called *endo* and the atoms on the other side are called *exo*. The two most frequently occurring sugar ring conformations in the nucleic acids are envelope conformations (i.e. conformations with 4 atoms in the plane and only one outside the plane) called C2′-*endo* (prevalent in DNA) and C3′-*endo* (prevalent in RNA).

Additionally, the 5 torsion angles within the ring are not independent. It turns out that the ribose conformation can be characterized by just two parameters. The parameters are called Pseudorotation angle (phase) P (Figure 12.4) and the pucker amplitude $\nu_{\max}$, defined as follows

$$\tan P = \frac{(\nu_4 + \nu_1) - (\nu_3 + \nu_O)}{2\nu_2 \cdot (\sin 36° + \sin 72°)}, \tag{12.1}$$

$$\nu_{\max} = \nu_2 / \cos(P). \tag{12.2}$$

Expressed using the Pseudorotation angle P, the C3′-*endo* conformation corresponds to $P = 18°$ and the C2′-*endo* conformation corresponds to $P = 172°$. When depicted on a sphere, the positions resemble North and South on the globe, therefore the C3′-*endo* and C2′-*endo* are also referred to as North (N) and South (S) conformations, respectively. The torsion angle χ around the C1′–N glycosidic bond is defined by atoms O4′–C1′–N1–C2 in pyrimidines and O4′–C1′–N9–C4 in purines. The *trans* conformation is sterically preferable as the bulky bases need space. However, if the chain changes the direction like in the loops or quadruplexes, a *cis* conformation becomes inevitable at some residue. Most frequently, the *cis* conformation occurs at guanosines.

12.3 Helical parameters

In nucleic acids, several terms are used to characterize the position of the base with respect to the helix axis or the distances and angles between the bases or base pairs.

Specifically, the axis-base or axis-base pair relations can be characterized by X-displacement, Y-displacement, Inclination and Tip. The distance and shift relation within the base-pair can be described by Shear, Stretch and Stagger, while the intra-base pair angles are described by Buckle, Propeller twist, and Opening. For the base-pair distance and shift relations we have Shift, Slide, and Rise and the inter-base pair angles are characterized as Tilt, Roll, and Twist. The meaning of these terms is best described by diagrams in Figures 12.5 and 12.6.

12.4 A and B double helix

There are many tertiary structures into which nucleic acids can fold, for example hairpins, triplexes, quadruplexes, i-motifs, to name a few. However, the most typical structures for nucleic acids are A and B helices. The A-type helix is more typical for RNA while DNA usually forms the B-type helix. The difference between these two types of helices becomes most obvious when we look along the helical axis. In the A helix, the base-pairs are wrapped around the axis forming a hole in the middle with no atoms in the place of the axis. In the B-helix, the axis goes right through the atoms forming the hydrogen bonds between the bases. In the A-helix, the base pairs are conspicuously inclined with respect to the helical axis by about 21°, while in the B-type helix the base-pairs are almost perfectly perpendicular to the axis. The A-helix with 11 base-pairs per a single turn is also a little bit more twisted that the B-helix with 10 base-pairs per a turn.
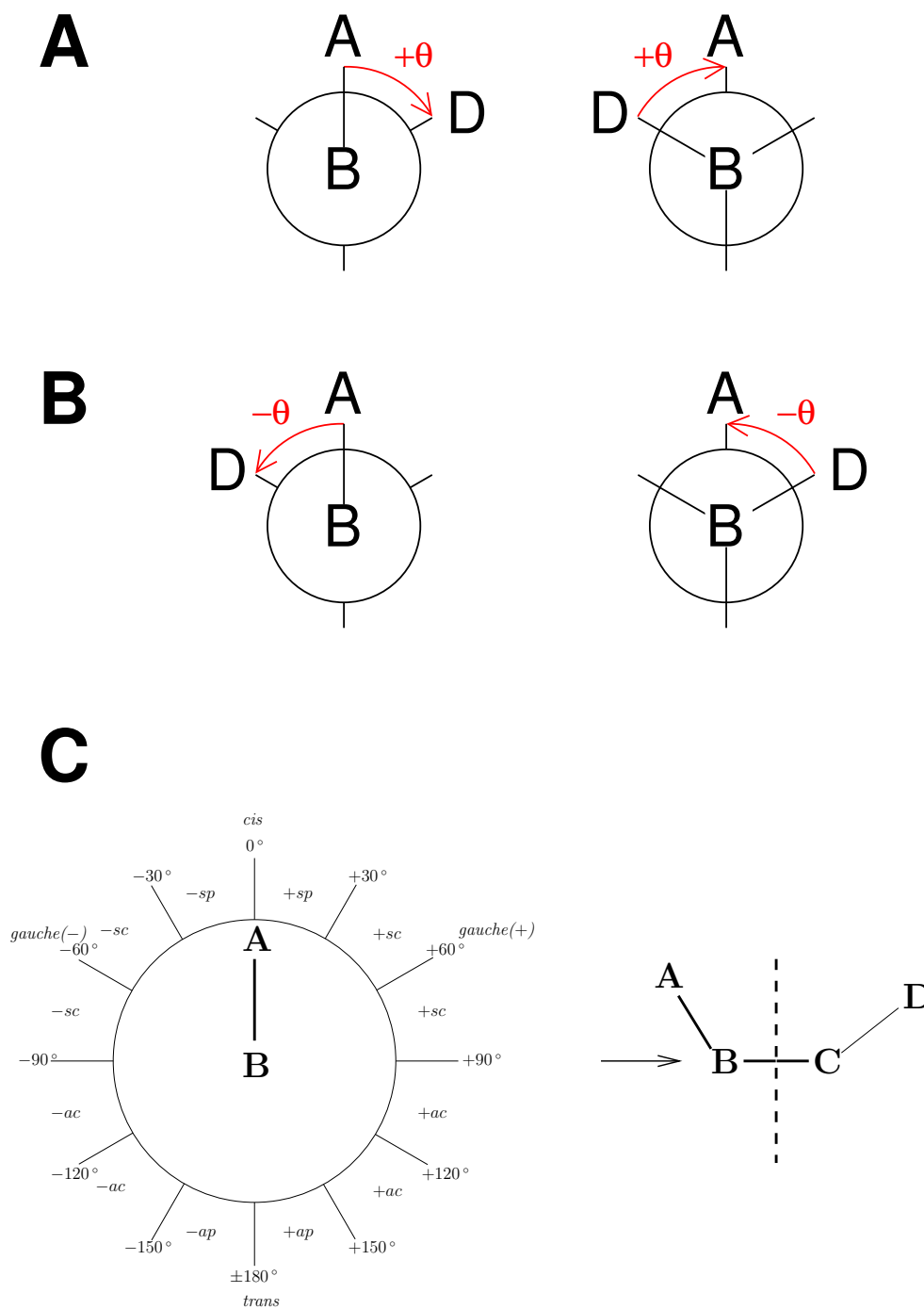
Figure 12.2: Torsion angles in a general sequence of four atoms A, B, C, and D. A, two views of the atoms with a positive value of the torsion angle about the B–C bond. B, two views of the atoms with a negative value of the torsion angle about the B–C bond. C, various descriptions of torsion angles.
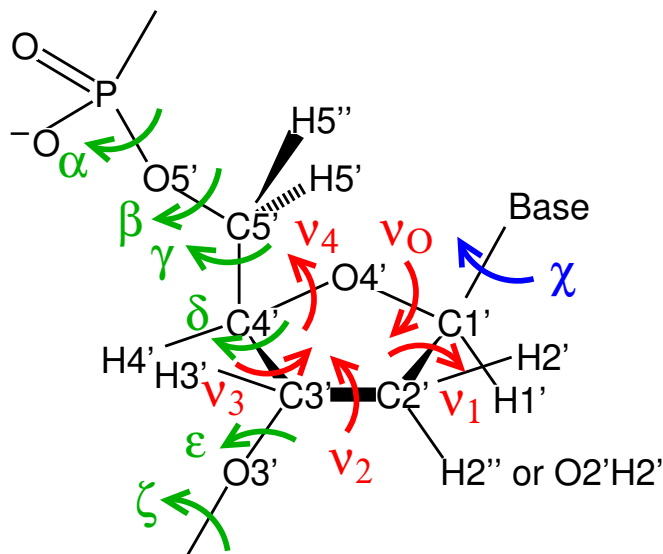
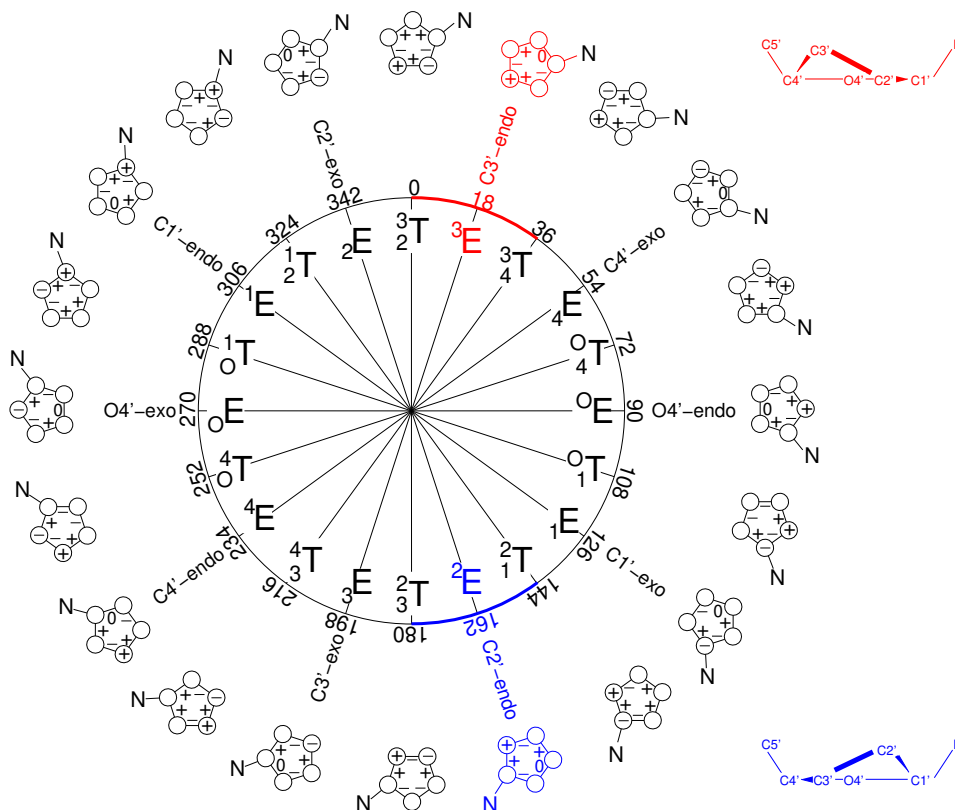Figure 12.3: Torsion angles in nucleic acids.

Figure 12.4: Values of P displayed using the *pseudorotation wheel*. All envelope and twisted conformations are marked (starting form the center by one-letter symbol, value of P, verbal description, and depicted schematically (circles symbolize atoms in the furanose ring, plus and minus signs mark atom s in the *endo* and *exo* positions, respectively, and signs of the angles ν_i are displayed next to the bonds). Conformations C2'-*endo*- and C3'-*endo* are shown in blue and red, respectively.
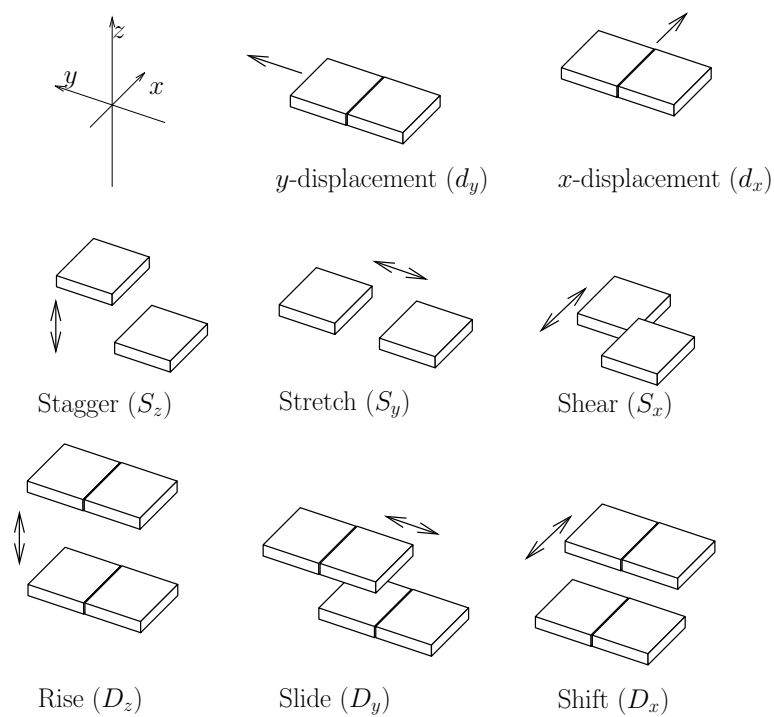
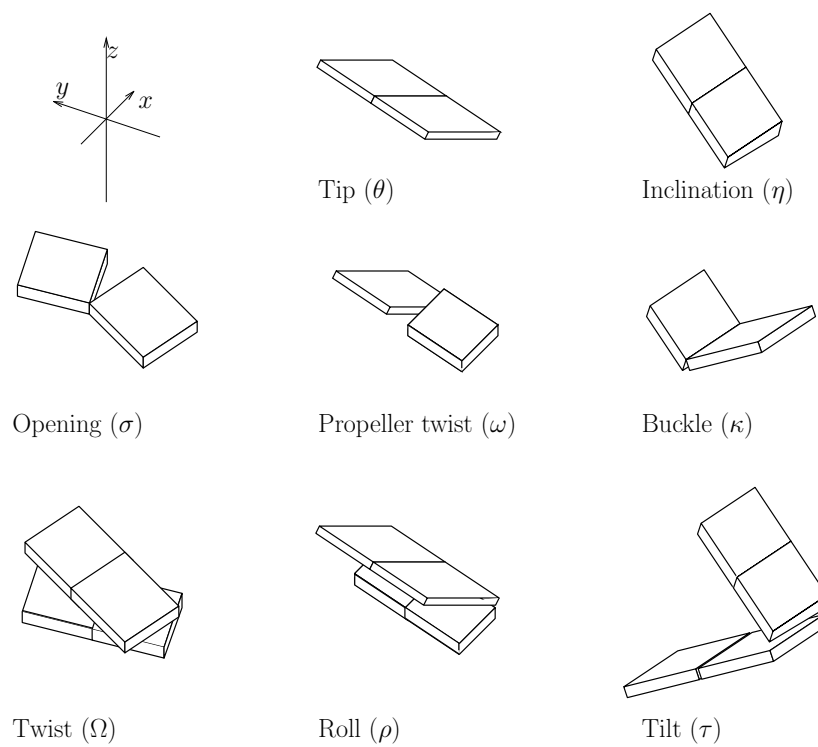Figure 12.5: Distance and shift relations between the nucleic acid bases and base pairs.

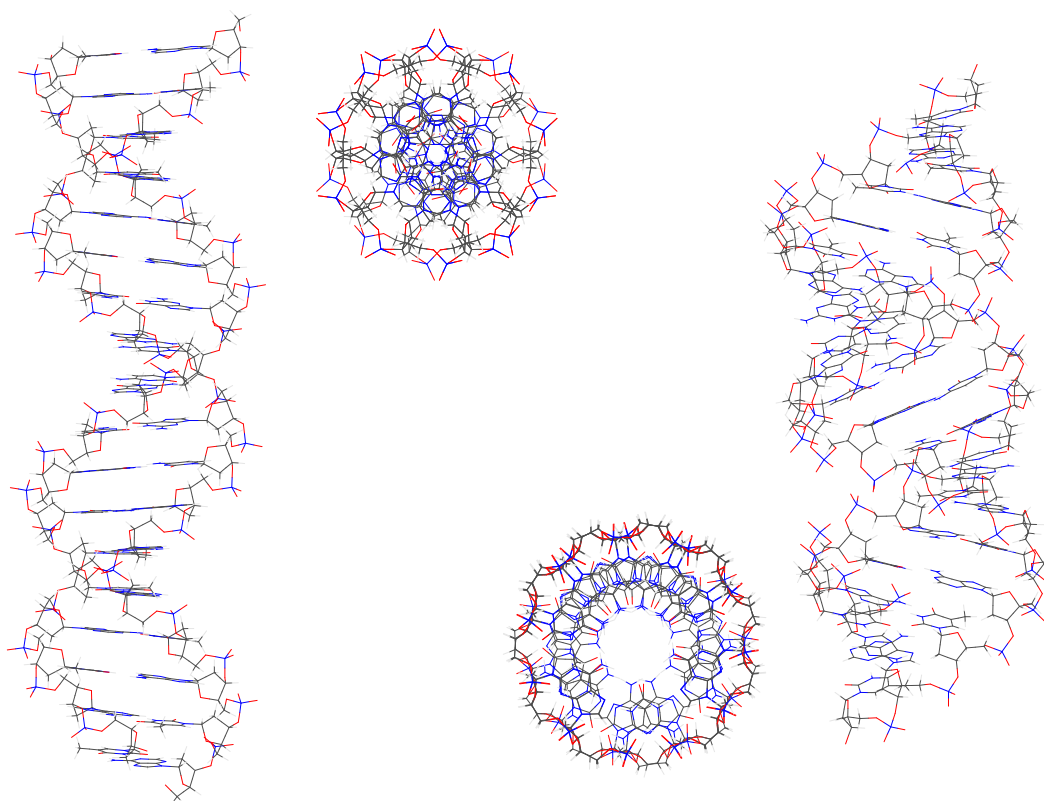Figure 12.6: Angular relations between the nucleic acid bases and base pairs.

Figure 12.7: Stick models of B- and A-type double helix (left and right, respectively).

Table 12.1: Properties of isotopes available for studying nucleic acids.

Isotope ($I = 1/2$)	$10^{-7}\gamma$ $\mathrm{rad\,s^{-1}T^{-1}}$	ν at 11.74 T MHz	Natural Abundance %	Sensitivity relative[a]	absolute[b]
^{1}H	26.75	500.0	99.98	1.00	1.00
^{13}C	6.73	125.7	1.1	1.6×10^{-2}	1.8×10^{-4}
^{15}N	−2.71	50.7	0.4	1.0×10^{-3}	3.8×10^{-6}
^{31}P	10.83	202.4	100	6.6×10^{-2}	6.6×10^{-2}

[a] Relative sensitivity at constant field for equal number of nuclei.
[b] Product of relative sensitivity and natural abundance.

12.5 Atoms in nucleic acids

Out of five elements constituting nucleic acids (H, C, N, O, P), four have isotopes suitable for NMR spectroscopy, i.e. ^{1}H, ^{13}C, ^{15}N, and ^{31}P. While all naturally occurring phosphorus is ^{31}P and overwhelming majority of hydrogen is ^{1}H, in the case of carbon and nitrogen, we have to rely on low natural abundance isotopes ^{13}C and ^{15}N (Table 12.1). This means that for samples with natural isotopic abundance we have to rely primarily on proton spectra and only simple heteronuclear correlation experiments (HSQC, HMQC) are possible. Even though ^{31}P has 100% natural abundance and a high frequency, there is another complication. ^{31}P has a large value of chemical shift anisotropy that causes fast relaxation leading to broad lines in 1D ^{31}P spectra and poor sensitivity in correlation experiments. The relaxation rate increases with the magnetic field. Therefore, moderate magnetic fields (not higher than 11.75 T corresponding to 500 MHz proton resonance frequency) are preferable for measuring ^{31}P spectra.

12.6 Exchangeable an non-exchangeable protons

The protons bound to oxygen and nitrogen atoms are in water solution in a fast exchange regime with the solvent. The exchange rate of the protons in -OH groups is usually too fast for the protons to be detected at all. The nitrogen bound protons in imino and amino groups are observable in most cases. It often helps to lower the temperature to slow down the exchange rate. Also, the methods of measurement that saturate the water signal should be avoided as the nuclei with the saturated spin levels from the solvent that enter the nucleic acid molecules by the exchange process do not produce any signal.

Note the low proton density in the bases. Except for the Guanine, there are only two signals from non-exchangeable protons (the protons in thymine methyl group are equivalent) and one signal from either imino or amino group. Guanine has only one non-exchangeable proton and both the imino and amino groups (Figure 12.8).

On the other hand, the spin system in the sugar part of the molecule are much more complicated. It is especially the case of RNA where the carbons C2′, C3′, and C4′ all carry a proton and -OH group, and consequently, the chemical shifts from their protons are very similar, falling in the range of 3.5–5.0 ppm. In DNA, the absence of the -OH group at the position 2′ makes a significant difference. The chemical shifts of the methylene group protons are in the range of 1.8–3.0 ppm and the resolution of the sugar protons in DNA is thus much better. The signals of H2′,H2″ protons together with the methyl proton of Thymine between 1 and 2 ppm makes the DNA spectrum clearly different from the RNA spectrum (Figure 12.9).
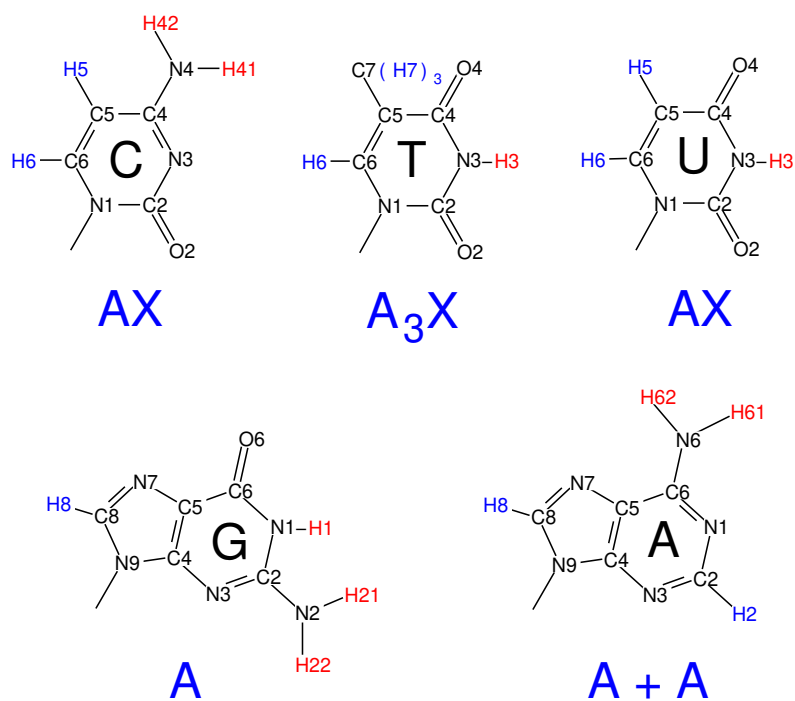
Figure 12.8: Spin systems in nucleic acid bases (blue). The exchangeable protons are shown in red.
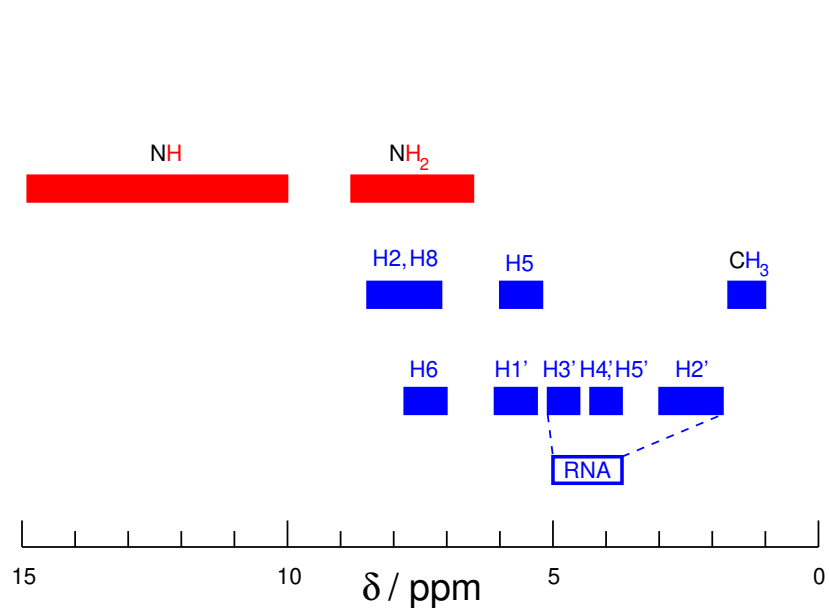

Figure 12.9: Proton chemical shifts in nucleic acids. The exchangeable protons are shown in red.